CARL
VON
OSSIETZKY
universität OLDENBURG

Time-Resolved Spectroscopy of Rydberg Electrons at a Gold Nanotip and Calcium Sensor Proteins

An der Fakultät für Mathematik und Naturwissenschaften
der Carl von Ossietzky Universität Oldenburg
zur Erlangung des Grades und Titels eines
Doktors der Naturwissenschaften (Dr. rer. nat)
angenommene

Dissertation

von
Jörg Robin, M. Sc.
geboren am 14.09.1983
in Haselünne

Januar 2017

Erstgutachter:	Prof. Dr. Christoph Lienau, Universität Oldenburg
Zweitgutachter:	Prof. Dr. Walter Pfeiffer, Universität Bielefeld
Tag der Disputation:	23.12.2016

Kurzfassung

In dieser Arbeit wird die Methode der zeitaufgelösten Spektroskopie auf zwei unterschiedliche Forschungsfelder angewandt. Zum einen lässt die zeitaufgelöste Fluoreszenz-Spektroskopie Rückschlüsse auf die differentielle Funktion zweier strukturell homologer Ca^{2+} Sensor-Proteine zu. Zum anderen wird die ultraschnelle Dynamik von Rydberg-Elektronen an einer Gold-Nanospitze mit Hilfe der Zwei-Farben-Pump-Probe-Spektroskopie untersucht.

Sich ändernde Lichtverhältnisse beeinflussen die intrazelluläre Konzentration an Ca^{2+} in den Photorezeptor-Zellen unserer Augen. Dies wird von den neuronalen Sensor-Proteinen GCAP1 und GCAP2 detektiert. Sie aktivieren ihr Ziel-Protein über eine Konformations-Änderung in einem sequentiellen Mechanismus, welcher die präzise Antwort einer Photorezeptor-Zelle in einer negativen Rückkopplungs-Schleife formt. In dieser Arbeit wurden dazu GCAP1-Mutanten untersucht, die ortsspezifisch mit einem Fluoreszenz-Farbstoff markiert waren. Messungen der Fluoreszenz-Lebensdauer des Farbstoffs in seiner lokalen Umgebung und die Analyse der Rotationsdiffusion des Farbstoff-Protein-Komplexes ließen einen Rückschluss auf die Konformations-Änderung von GCAP1 zu, welche sich bildlich als verdrehtes Akkordeon beschreiben lässt. Dies steht im Gegensatz zu einer kolbenartigen Bewegung einer Alpha-Helix in GCAP2, welche aus einer früheren Studie geschlossen wurde. Diese beiden strukturell homologen Sensor-Proteine ändern ihre Konformation daher auf unterschiedliche Weise, welche ihre differentielle zelluläre Reaktion und physiologische Spezifität widerspiegelt.

Während in dieser Studie die relativ langsame Neuordnung von Atomen untersucht wurde, laufen Elektronen-Dynamiken auf einer schnelleren Zeitskala ab. Die Untersuchung ultraschneller Prozesse erfordert die Entwicklung fortgeschrittener Techniken, zu denen diese Arbeit hauptsächlich beiträgt. Hierfür steht ein abstimmbarer, zweistufiger nicht-kollinearer optischer parametrischer Verstärker zur Verfügung, welcher mit Signal-Impulsen aus dem Prozess der Weißlichterzeugung und frequenzverdoppelten Pump-Impulsen eines regenerativen Titan:Saphir-Verstärkers betrieben wird. Das Laser-System stellt breitbandige Wenig-Zyklen-Lichtimpulse im sichtbaren und schmalbandige Lichtimpulse im infraroten Spektralbereich zur Verfügung, welche über Differenzfrequenz-Erzeugung in Zwei-Zyklen-Lichtimpulse im nahinfraroten (NIR) Spektralbereich umgewandelt werden, deren Träger-Einhüllenden-Phase passiv stabilisiert ist. Diese Stabilität wurde in dieser Arbeit durch ein optimiertes Temperatur-Management verbessert und im Besonderen Schuss-zu-Schuss mit Hilfe von spektraler f-zu-2f-Interferometrie charakterisiert.

Eine Anwendung von Wenig-Zyklen-Lichtimpulsen ergibt sich in Kombination mit einer Metall-Nanospitze. Diese ist ein konisch zulaufender Draht, der am Apex zu einem Radius von wenigen Nanometern konvergiert. Die hohe Dichte an elektrischen Feldlinien führt hier zu einer starken Überhöhung eines schwachen Eingangsfeldes, wodurch die Elektronen-Emission räumlich auf die Apex-Region und zeitlich auf ein Fenster von wenigen Femtosekunden beschränkt werden kann. Hierdurch wird eine Metall-Nanospitze eine ideale Quelle für die ultraschnelle Elektronen-Mikroskopie.

Metall-Nanospitzen erlauben die Anwendung eines elektrischen Feldes unterhalb der Zerstörschwelle, welches mit Hilfe der Feldüberhöhung eine Stärke vergleichbar mit der Bindungsenergie eines Elektrons erreicht. Hierdurch haben sich Metall-Nanospitzen als Modell-Systeme zur Untersuchung von Starkfeld-Phänomenen wie der Above-Threshold-Ionisation (ATI) entwickelt, welche üblicherweise in atomaren Systemen beobachtet wird. Allerdings resultiert die Elektronen-Emission im Falle eines Festkörpers aus einer breiten kinetischen Energieverteilung vom Fermi-Niveau, so dass im Vergleich zu stark durchmodulierten ATI-Spektren atomarer Systeme, welche eine direkte Signatur von Attosekunden-Dynamik sind, ein relativ schwacher Modulations-Kontrast erzielt wird. Atomähnliche Zustände sind in Festkörpern von Zwei-Farben-Photoemissions-Studien an metallischen Filmen als schwach gebundene, langlebige Bildladungszustände bekannt, wurden bisher aber noch nicht an einer Metall-Nanostruktur beobachtet.

In dieser Arbeit wurden die bislang nicht näher studierten zweidimensionalen Rydberg-Wellenfunktionen in der gekrümmten Geometrie einer Metall-Nanospitze mit Hilfe der numerischen Lösung der Schrödinger-Gleichung näher untersucht. Ihre Projektion auf die Spitzenachse ähnelt der eindimensionalen Lösung, so dass ihre Dynamik im Folgenden mit Hilfe der eindimensionalen zeitabhängigen Schrödinger-Gleichung berechnet wurde. Hieraus ergaben sich stark durchmodulierte ATI-Spektren und die Bildung eines Zuges von Attosekunden-Elektronen-Pulsen.

Dies motiviert den konzeptionell neuen Ansatz, Elektronen in atomähnlichen Bildladungszuständen und damit entkoppelt vom Fermi-Niveau zu speichern, um sie im Folgenden im stark überhöhten Lichtfeld am Apex einer Gold-Nanospitze zu treiben und atomähnliche ATI-Spektren zu gewinnen. Hierzu wurde der Apex einer Gold-Nanospitze mit einer präzisen Sequenz von sichtbaren und NIR Femtosekunden-Lichtimpulsen beleuchtet. Im Zeitüberlapp wurden stark durchmodulierte kinetische Energiespektren mit bis zu 12 Maxima im Abstand der NIR Photonen-Energie gemessen, welche sich mit der Erhöhung der NIR-Intensität verbreiterten. Die Elektronenzählrate stieg linear mit der NIR-Intensität an, was auf eine Photoemission aus schwach gebundenen Zwischenzuständen hindeutet und eine effektive Reduktion der Austrittsarbeit bedeutet, wodurch das Starkfeld-Regime leichter erreicht wird.

Bei Veränderung der zeitlichen Verzögerung der Lichtimpulse stieg die Elektronenzählrate auf das Fünffache an und klang monoexponentiell mit einer Zeitkonstanten von bis zu 130 Femtosekunden ab. Überlagert war das Signal von einem Schwingungsmuster, welches auf die Schwebung von Wellenfunktionen von langlebigen, diskreten Zwischenzuständen hindeutet, die sich Bildladungszuständen zuordnen lassen. Diese Beobachtungen wurden durch die numerische Lösung der Schrödinger-Gleichung unterstützt, in welcher ein ähnliches Schwingungsmuster nach Präparation des Quantensystems in einer kohärenten Superposition von Bildladungszuständen berechnet wurde. Im zweidimensionalen Raum wurde eine weitere Quantisierung der Wellenfunktionen berechnet, was auf ein komplexeres Schwingungsmuster hindeutet und über Folge-Experimente aufgelöst werden kann.

Die in dieser Arbeit gewonnenen Erkenntnisse motivieren weitere Experimente. Die Erzeugung eines Attosekunden-Elektronen-Pulses vom Apex einer Gold-Nanospitze verspricht beispielsweise eine Verbesserung der Zeitauflösung der ultraschnellen Elektronen-Mikroskopie. Eine mögliche Rekombination des Elektronen-Wellenpakets mit der Spitze kann den Grundstein für die Erzeugung höherer Harmonischer an einer Metall-Nanospitze legen und erlaubt unter anderem möglicherweise die Erzeugung

eines Attosekunden-Lichtimpulses von einer Festkörper-Nanostruktur. Darüber hinaus kann die hohe räumliche Ausdehnung der Rydberg-Elektronen-Wellenfunktionen dazu genutzt werden, um Nanostrukturen kohärent miteinander zu koppeln. Schließlich kann die Zwei-Farben-Pump-Probe-Spektroskopie mit der Detektion von Elektronen auf eine neue Diade angewandt werden, um den ultraschnellen Ladungstransfer in einem organischen Solarzellen-Material zu kontrollieren.

Abstract

In this thesis, the toolbox of time-resolved spectroscopy is applied to two different areas of research. First, the differential function of two structurally homologous Ca^{2+} sensor proteins is concluded from time-resolved fluorescence spectroscopy. Second, the ultrafast dynamics of Rydberg electrons at a gold nanotip is investigated by two-colour pump-probe spectroscopy.

Changing light conditions alter the intracellular Ca^{2+} concentration in the photoreceptor cells of our eye, which is sensed by specific neuronal sensors, GCAP1 and GCAP2. They operate via a conformational change on their target protein in a sequential relay mechanism to precisely shape the response of the photoreceptor cell in a negative feedback loop. In this thesis, GCAP1 mutants, site-specifically labelled with a fluorescent dye, were investigated. Measuring the fluorescence lifetime of the dye in its local environment and analysing the rotational diffusional motion of the protein-dye complex, a conformational change of GCAP1 was concluded, pictorially described as a twisted accordion movement. This contrasts the piston-like movement of an alpha-helix in its cellular cognate GCAP2 concluded from a previous study. This shows that these structurally homologous neuronal calcium sensor proteins undergo a distinctly different conformational change, which may mirror their differential cellular responsiveness and more generally tune physiological specificity.

In this study the rather slow dynamics is governed by the rearrangement of atomic nuclei. In contrast, the dynamics of electrons occurs on a much faster time scale. Capturing such ultrafast phenomena requires the development of sophisticated tools, to which this thesis mainly contributes. For this, a home-built widely tuneable two-stage non-collinear optical parametric amplifier (NOPA) system, seeded by white light generation and pumped by the frequency-doubled driving laser pulses from a Ti:sapphire regenerative amplifier, provides broadband, few-cycle laser pulses in the visible (VIS) and narrowband laser pulses in the infrared. Subsequent difference frequency generation (DFG) results in two-cycle laser pulses in the near-infrared (NIR), which are passively carrier-envelope phase (CEP) stabilised. In this thesis, the CEP stability of this laser system was improved by optimising its temperature management after tracing back instabilities to the regenerative amplifier. Importantly, this scheme of passive CEP stabilisation was experimentally characterised shot-to-shot by spectral f-to-2f interferometry.

An intriguing application of few-cycle laser pulses arises from their combination with a metallic nanotip. This is a thin wire converging conically to an apex radius of curvature of few nanometres, where the high density of electric field lines gives rise to a strong enhancement of a low incident electric field. As such, electron photoemission may be confined spatially to the nanometre-sized apex region and temporally to a femtosecond time window, rendering metallic nanotips an ideal source for ultrafast electron microscopy. Moreover, permitting the application of an incident electric field with a strength below the damage threshold of the solid, but enhanced to a strength comparable to the binding energy of an electron, metallic nanotips have emerged as model systems to study strong-field phenomena usually observed in atomic systems such as above-threshold ionisation (ATI). However, the emission of electrons in a one-step process from a broad distribution of states near the Fermi level results in a weak modulation contrast as compared to deeply modulated atomic ATI spectra, which are a direct signature of attosecond electron dynamics. In solids, atomic-like states are well-known from two-photon photoemission studies on metallic films as weakly-bound, long-lived image potential (IP) states, but have not been observed at a metallic nanostructure so far.

In this thesis, so far unknown two-dimensional (2D) Rydberg wave functions in the curved geometry of a nanotip were found by numerically solving the Schrödinger equation to yield the one-dimensional (1D) solutions when projected onto the taper axis. This allows for calculating the Rydberg electron dynamics in a computationally feasible 1D model, yielding deeply modulated ATI spectra and the formation of a train of attosecond electron pulses.

This motivates the conceptually new approach of storing electrons in atomic-like IP states, decoupled from the Fermi level, and subsequently driving them in the strongly enhanced field at the apex of a metallic nanotip to yield atomic-like ATI. For this, the apex of a single gold nanotip was illuminated in this thesis by a precisely timed sequence of femtosecond VIS and NIR laser pulses. In the time overlap of both pulses deeply modulated kinetic energy spectra with up to 12 peaks separated by the NIR photon energy were observed, broadening with increasing NIR electric field strength. A linear scaling of the electron yield with the NIR intensity points to photoemission from weakly bound intermediate states, constituting an effective reduction of the work function, which enables an easier access to the strong-field regime.

Furthermore, varying the time delay between the VIS and NIR pulses resulted in a five-fold increase in electron yield, which decayed exponentially with a time constant of up to 130 fs. Superimposed on the decay curve an oscillatory pattern was measured, pointing to beating of long-lived, discrete states leaving IP states as the most likely candidate. These findings were supported by preparing a coherent superposition of IP states in the 1D Schrödinger equation model giving rise to an oscillatory electron yield. This may be more complex in 2D, in which a further quantisation of the wave functions was found calling for their spatial resolution in future experiments.

Moreover, an attosecond electron pulse emerging from the nanometre-sized apex of a metallic nanotip may extend ultrafast electron microscopy to the attosecond time domain. The recombination of an electron with the metallic nanotip during its oscillatory motion may further lay the foundation for high harmonic generation, possibly enabling the generation of an attosecond optical pulse from a nanometre-sized solid-state device. Furthermore, the large spatial extent of the Rydberg electrons may enable coherent coupling of metallic nanostructures. Finally, the established two-colour pump-probe spectroscopy setup with electron detection may be applied to a novel dyad designed to control ultrafast charge transfer in an organic solar cell material, possibly to be investigated further in an ultrafast optical-pump electron-probe experiment.

Table of Contents

1. Introduction 1
2. Nanosecond Dynamics of Calcium Sensor Proteins 5
   2.1. Phototransduction 5
   2.2. Guanylate Cyclase Activating Protein (GCAP) 6
   2.3. Fluorescent Dye 9
   2.4. Time-Resolved Fluorescence Spectroscopy 14
   2.5. Conformational Change of the Calcium Sensor Protein GCAP1 15
3. Femtosecond Laser System 21
   3.1. Theoretical Background of an Ultrashort Laser Pulse 22
   3.2. Chirped Pulse Amplification System 26
   3.3. Non-collinear Optical Parametric Amplifier (NOPA) 27
   3.4. Passive Carrier Envelope Phase (CEP) Stabilisation 33
4. Metallic Nanotips 39
   4.1. Fabrication and Properties 40
   4.2. DC Field Emission 43
   4.3. Linear Photoemission 44
   4.4. Multiphoton Photoemission 45
   4.5. Strong-Field Photoemission 47
5. Above-Threshold Ionisation in Atomic Systems 59
6. Image Potential States 63
7. Numerical Model: The Schrödinger Equation 67
   7.1. Stationary Wave Functions in 1D 68
   7.2. Stationary Wave Functions in 2D 70
   7.3. Time Evolution in 1D and Kinetic Energy Spectra 74
8. Two-Colour Pump-Probe Spectroscopy 81
   8.1. Experimental Setup 81
   8.2. Above-Threshold Ionisation of Rydberg Electrons 85
9. Outlook 95
   9.1. Charge Transfer in Solar Cell Materials 95
   9.2. Ultrafast Point Projection Electron Microscopy 97
   9.3. High Harmonic Generation from a Metallic Nanotip 99
   9.4. Coherent Coupling of Nanostructures 102
10. Appendix 105
   10.1. In Situ Laser Pulse Characterisation 105
   10.2. Image Correction 109

10.3. Numerical Implementation of the Schrödinger Equation 114
11. References 119
12. Publications and Conference Contributions 129

1. Introduction

Not only since the development of quantum mechanics at the beginning of the last century has it been a dream to gain insight into fundamental processes in nature such as watching the evolution of an electronic wave packet at an atomic length and time scale. The observation of electronic motion stretches far beyond our classical perception of the world by our human senses and requires sophisticated tools at the cutting edge of modern technology. For example, in the hydrogen atom the electronic wave packet oscillates between the 1s and 2p orbitals with a period of about ~400 as. An attosecond (as) is a billionth of a billionth of second, which is a billion times faster than the rate at which a common computer processes data. Moreover, investigating matter at an atomic scale does not only involve extreme time scales, but also extreme forces. For example, the electron bound to the proton experiences an electric field strength of $\sim 500\ \mathrm{V/nm}$. Providing a comparable electric field strength with an optical laser pulse corresponds to an enormous light intensity on the order of $10^{16}\ \mathrm{W/cm^2}$. For comparison, focussed sunlight would ignite a piece of paper at an intensity on the order of $10^{2}\ \mathrm{W/cm^2}$.

Nevertheless, using femtosecond technology strong field laser physics has enabled the manipulation of electron trajectories in and around atomic systems and thereby laid the foundation of modern attosecond science [1,2] and emerging technologies such as light wave electronics [3,4]. In the strong-field regime, the electron dynamics is not solely governed by the light intensity anymore, but driven by the light field itself. For example, exposing noble gas atoms to sufficiently strong ultrashort laser pulses, strong-field phenomena such as above-threshold ionisation (ATI) [5-7] and high harmonic generation (HHG) [8,9] have been observed.

In ATI, an electron is liberated from its parent ion and subsequently performs a quiver motion in the oscillatory potential created by the incident electric field. At the outermost points of its oscillatory motion, a fraction of the electron wave packet is released in time intervals spaced by the optical period of the driving laser pulses. The interference of this freely propagating train of electron wave packets leads – in the energy domain – to photoelectron kinetic energy spectra modulated by the photon energy of the driving laser pulses. In the time domain it translates into a train of attosecond electron pulses [10].

HHG is related to this concept by considering the return of the electron to its parent ion. Depending on the overlap of the wave functions associated with the quivering electron and the bound state, recombination may occur, which results in the emission of phase-locked high harmonics [11]. In particular, ultrashort bursts of coherent extreme ultraviolet (XUV) radiation were obtained from an ensemble of noble gas atoms, which lasted less than a femtosecond [12,13]. Attosecond optical pulses are now routinely applied to image molecular wave packets [14,15]. They further enable attosecond chronoscopy of both atomic systems [16] and condensed matter [17], which provides a deeper insight into the photoelectric effect [18] by not merely considering the release of an electron wave packet from a quantum system, but also measuring the time of its propagation after being launched from different states inside the quantum system, i.e. charge migration. The concept of HHG may further be extended to solid state systems by mimicking an atomic system in a semiconductor with its valence and conduction band [19-21] or investigating rare-gas solids [22].

Further strong-field phenomena in solids [23] such as optically inducing a current in a dielectric [24] and manipulating its electronic structure [25] have been observed, but are mostly restricted to atomic systems, as low damage thresholds of solids set a limit to a sufficiently high light intensity to access the strong-field regime.

Here, metallic nanotips, primarily investigated in this thesis, have emerged as model systems to study electron dynamics on a femtosecond time and nanometre length scale. A metallic nanotip is a thin wire, which conically converges down to an apex radius of curvature of few nanometres. The high density of electric field lines in the apex region gives rise to a local enhancement of an incident electric field [26,27]. As a consequence, the photoemission of electrons is localised to the apex region, rendering metallic nanotips a nano-localised source of ultrafast electron pulses, for example, when their apex is illuminated with femtosecond laser pulses [28-30]. In contrast to electron diffraction experiments with ultra-bright electron sources [31,32], metallic nanotips are usually operated in point projection electron microscopy setups [33-35] in the ultra-dim regime, that is with a single electron emitted per laser pulse. Furthermore, exploiting the enhanced optical near field [27] at the apex of the metallic nanotip, strong-field phenomena have been observed, including sub-cycle electron dynamics [36,37], control of the electron motion via the carrier-envelope phase [38] and above-threshold photoemission [39,40].

In particular, the latter experiments are of profound importance for the work presented in this thesis. They raise the question how we can we transfer the atomic concepts of strong-field laser physics to a single solid state nanostructure. Such experiments are currently limited, because the emission of electrons occurs in a one-step process from a broad distribution of states near the Fermi level. An electron emitted from a deeper lying state will arrive at a detector will less residual kinetic energy than an electron originating from a higher lying state. Thereby, the broad distribution of states maps directly onto a kinetic energy spectrum and smears out distinct features such as ATI peaks. In contrast, the origin of electrons from a discrete state with a well-defined energy gives rise to deeply modulated ATI spectra as observed in atomic systems.

In condensed matter, atomic-like states are well-known from two-photon photoemission studies on extended metallic films [41]. Here, a negatively charged electron in front of the surface induces a positive image charge inside the bulk, such that the electron is bound to its own, hydrogen-like image potential. Consequently, it occupies a Rydberg series of weakly bound states and is characterised by a hydrogen-like wave function with a reduced spatial overlap with the bulk resulting in a long lifetime [42,43]. However, such image potential states have not been observed at a metallic nanostructure so far.

This raises the more specific question addressed in this thesis, whether we can devise a concept to facilitate atomic-like ATI from a metallic nanotip, i.e. from a solid-state device rather than a gaseous medium, by storing electrons in long-lived, atomic-like image potential states and subsequently photoionising and driving them in the oscillatory potential created by the electric field of an ultrashort laser pulse. Such a conceptually new approach might allow for the generation of an attosecond electron pulse and may also lay the foundation for an attosecond optical pulse obtained by HHG [44]. This would place metallic nanotips firmly into the context of attosecond science, providing a nano-localised solid-state source of ultrafast electron and optical pulses to be applied in ultrafast pump-probe spectroscopy or ultrafast electron microscopy experiments.

In contrast to attosecond physics, our classical perception of the world takes place on fundamentally different scales. For example, our eye is a sensory system, by which we perceive light stimuli as a clue to interpret our surroundings. The complex molecular signalling cascade, which facilitates our sense of vision, adapts to light signals as high as bright sunlight and as low as a single photon [45,46]. It is initiated by highly responsive proteins located in the photoreceptor cells, which photoisomerise on a femtosecond timescale [47,48], followed by a second messenger cascade, which limits the overall response time of a photoreceptor cell to about a millisecond [45]. Specifically, changing light conditions alter the intracellular Ca^{2+} concentration, to which our eye responds in a negative feedback loop, that is by shutting off the photoreceptor cells in response to an increase in light intensity. Here, structurally homologous neuronal calcium sensor proteins [49] are involved in sensing the intracellular Ca^{2+} concentration and precisely shaping the response of a photoreceptor cell. Specifically, they are believed to operate sequentially in a relay mechanism on their target protein undergoing a conformational change [50]. Here, a question of interest addressed in this thesis arises, whether differential cellular responsiveness and thereby physiological specificity is reflected in the structural dynamics, i.e. a differential conformational change despite structural homology. This may point to a more general concept in Ca^{2+} mediated signal processing, which is widely found in further physiological processes such as fertilisation, apoptosis, muscle contraction and sensory perception [51-53] and may specifically affect the treatment of neuropsychiatric disorders [54].

This thesis will be structured as follows:

Chapter 2 retraces the path of photon from its point of absorption in our eye to its conversion into a chemical signal in the phototransduction cascade. In particular, the role of the neuronal calcium sensor proteins, GCAP1 and GCAP2, which sequentially activate their target protein via a conformational change, is elucidated via time-resolved fluorescence spectroscopy of GCAP1 mutants, site-specifically labelled with a fluorescent dye. Its relevant properties such as its fluorescence lifetime and anisotropy will be discussed. Furthermore, the experimental setup and the outcome of the GCAP1 study are presented and put into context.

Chapter 3 introduces ultrashort laser pulses both theoretically and experimentally. In particular, a femtosecond laser system is introduced, starting from a regenerative Ti:sapphire amplifier, which drives a home-built two-stage non-collinear optical parametric amplification (NOPA) system providing passively carrier-envelope phase (CEP) stabilised laser pulses. The necessary theoretical background of these processes is provided, before the experimental realisation of this laser system is characterised in further detail.

Chapter 4 deals with metallic nanotips, which are both a nano-localised, ultrafast electron source for ultrafast electron microscopy and a model system to study strong-field phenomena usually observed in atomic systems. Their fabrication, their properties and different regimes of electron (photo)emission are discussed, particularly focussing on strong-field phenomena such as sub-cycle dynamics, CEP effects and ATI.

Chapter 5 focusses on ATI in more depth from the perspective of an atomic system. In particular, effects such as peak shifting, channel closing, Freeman resonances and CEP effects are highlighted.

Chapter 6 introduces the concept of image potential states from the perspective of extended metallic films. Their properties such as their wave functions and lifetimes are described. Furthermore, experimental techniques such as two-photon photoemission spectroscopy and quantum beat spectroscopy are outlined.

Chapter 7 gives an account on various theoretical models, such as the time-independent Schrödinger equation in one and two dimensions as well as the one-dimensional time-dependent Schrödinger equation and a two-dimensional density functional theory model. The stationary wave functions associated with image potential states in the curved geometry of a metallic nanotip are calculated and compared to the well-known solutions from extended metallic films. Furthermore, the electron dynamics and kinetic energy spectra arising from electrons originating from image potential states are simulated.

Chapter 8 addresses the experimental strategy to facilitate a conceptually new approach to transfer the atomic concept of ATI to a single gold nanotip. A dedicated two-colour pump-probe spectroscopy setup is introduced, with which the population of image potential states and the subsequent observation of ATI has been conducted.

Chapter 9 gives an outlook on possible experiments to be carried out in the future. The optical two-colour pump-probe setup with electron detection may be extended to investigate controllable ultrafast charge transfer in a novel organic solar cell material. An attosecond electron pulse emerging from a metallic nanotip may be measured and applied in an ultrafast (point projection) electron microscopy setup. An attosecond optical pulse may be generated at a metallic nanotip from high harmonics, which may yield valuable information on their own. In the far-fetched future one may also think of building a quantum logic network based on Rydberg electrons localised at metallic nanostructures.

Chapter 10 briefly outlines technical procedures important for the results presented in this thesis such as the in situ characterisation of ultrashort laser pulses, an image correction procedure and the numerical implementation of the Schrödinger equation.

2. Nanosecond Dynamics of Calcium Sensor Proteins

Our eye is a sensory system, which governs our classical perception of the world by interpreting light stimuli as a clue to our surroundings. In fact, the complex molecular signalling cascade, which facilitates our sense of vision, adapts to light signals as high as bright sunlight and as low as a single photon [45,46]. At various stages it is triggered by the conformational change of proteins, which results in the well-balanced production, consumption or exchange of messengers. Specifically, changing light conditions alter the intracellular Ca^{2+} concentration, to which our eye responds in a negative feedback loop, that is by shutting off the photoreceptor cells in response to an increase in light intensity. To gain an insight into the molecular signalling cascade enabling light adaption, we will specifically investigate the role of a member of the family of neuronal calcium sensor proteins, GCAP1. It senses the intracellular Ca^{2+} concentration and, in combination with its cellular cognate GCAP2, sequentially triggers the activation of its target protein by a conformational change [50]. Importantly, this relay mechanism involves two sensor proteins to shape the precise response of our photoreceptor cells to changing light conditions. The study presented in this chapter sheds light onto the question whether the differential cellular responsiveness mediated by these structurally homologous calcium sensor proteins manifests itself in a differential conformational dynamics tuning physiological specificity [JR4].

2.1. Phototransduction

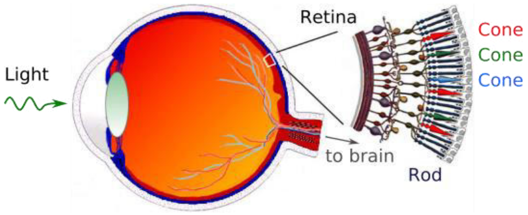

Figure 2.1: Schematic illustration of a human eye. The various cell types of the retina are shown in magnification, in particular the photoreceptor cells, rods and cones. Modified from [55].

Vision is one of our most important senses, in which light is used as a clue to perceive our surroundings. To understand how an incoming photon is eventually converted into a chemical signal, which our brain is able to interpret, let us first trace its path from the point of entering our eye, schematically shown in Figure 2.1.

Photoreceptor Cells

When light from an object enters our eye, it is focussed by a lens onto the retina, where an image of the object forms. The retina consists of layers of various cell types, which are mostly transparent to light, and two distinct photoreceptor cell types, rods and cones, which absorb light [56]. Exemplary, a rod cell is shown in Figure 2.2.

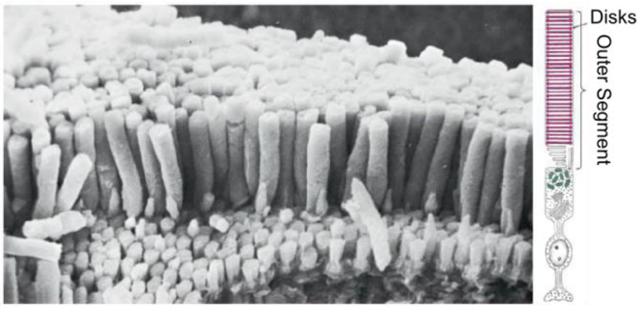

Figure 2.2: Scanning electron microscopy image of rod cells (left) and their schematic representation (right). Modified from [56].

The process of light absorption occurs in the outer segment of a photoreceptor cell. Here, transmembrane light-sensitive opsins are located in a stack of membranous disks, which collect about 90% of the incoming photons [45]. Cone cells facilitate colour vision [56] and typically host three photopsins in humans, which predominantly absorb light in the blue ($\lambda_{max} \approx 420\ \mathrm{nm}$), green ($\lambda_{max} \approx 534\ \mathrm{nm}$) and yellow ($\lambda_{max} \approx 564\ \mathrm{nm}$) spectral region [57]. In contrast, rod cells are responsible for dark-adapted vision [56] and harbour rhodopsin, which absorbs predominantly in the green spectral region ($\lambda_{max} \approx 498\ \mathrm{nm}$) [57].

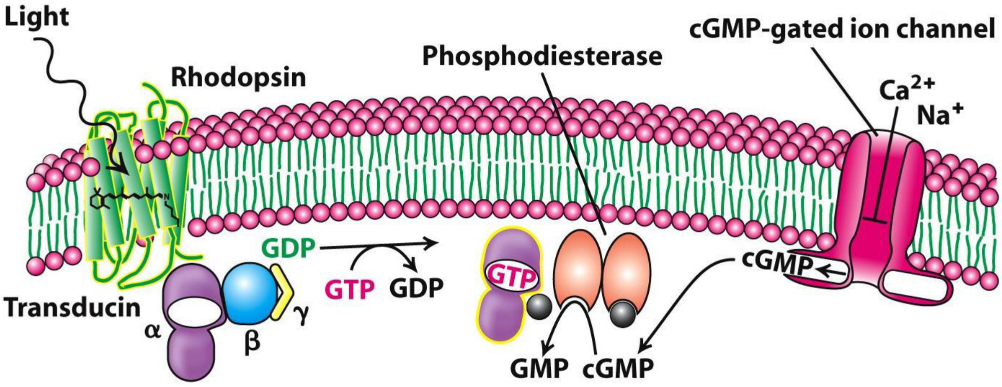

Figure 2.3: Phototransduction cascade. The photoisomerisation of rhodopsin starts a signalling cascade, which results in a decrease in the intracellular concentration of the second messenger cGMP, causing a closure of ion channels and thereby stopping the Ca^{2+} influx into the cell. Modified from [56].

Phototransduction Cascade

To understand the effect of the absorption of a photon on the response of a photoreceptor cell, let us now investigate its further conversion into a chemical signal in more depth. Specifically, the rhodopsin in a rod cell contains the chromophore 11-*cis* retinal, which upon absorption of light undergoes a conformational change to an all-*trans* form [45]. This photoisomerisation starts the phototransduction cascade, sketched in Figure 2.3, which may be triggered by a single photon [45]. With the chromophore in all-*trans* configuration the opsin can now activate hundreds of the regulatory protein transducin. This heterotrimeric G-protein [58] splits off its α-subunit, at which the nucleotide guanosine diphosphate (GDP) is exchanged for the nucleotide guanosine-5'-triphosphate (GTP). This active form of the G-protein can now bind to the γ-subunit of the effector protein phosphodiesterase (PDE), which relieves its inhibitory function [45]. The enzyme PDE breaks down the second messenger cyclic guanosine monophosphate (cGMP) into 5'-GMP. Each PDE molecule may split up to 1000 cGMP molecules, completing the remarkable amplification and detection efficiency of an incoming light signal. The consumption of cGMP causes the cGMP-gated ion channels [59] to close, eventually preventing the Ca^{2+} influx into the cell. Overall, the intracellular concentration of cGMP and Ca^{2+} has changed from a high level in the dark state to a low level in the light state, in which the rod cell has become inactive.

2.2. Guanylate Cyclase Activating Protein (GCAP)

At this stage, the calcium binding guanylate cyclase activating proteins (GCAPs) come into play to shape the precise response of the photoreceptor cell to changing light conditions [50]. As the intracellular Ca^{2+} concentration decreases, these neuronal calcium sensors release their Ca^{2+} into the cell. This process triggers a conformational change of the GCAPs, which activates the guanylate cyclase (GC) to which the GCAPs are bound. As illustrated in Figure 2.4, both GCAPs are believed to bind to different sub-units of the GC, yet there is still controversy on this topic [60]. In its active state the GC replenishes cGMP by synthesising it from GTP. As the intracellular cGMP concentration increases, the cGMP-gated ion channels re-open and the rod cell returns to its active state. Experiments further indicate, that not simply the cation-free form the GCAPs, but the replacement of Ca^{2+} ions by Mg^{2+} ions at the binding sites of the GCAPs constitutes the physiological activator state [61].

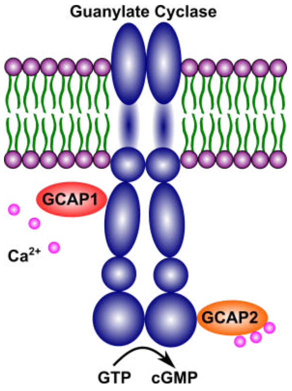

Figure 2.4: Schematic illustration of the GC with two GCAPs attached. The GCAPs sequentially activate the GC by undergoing a conformational change upon release of Ca^{2+} ions in response to an intracellular decrease in the Ca^{2+} concentration.

Calcium-Relay Mechanism

Depending on the species several forms of GCAPs may be found. For example, humans have three and zebrafish six forms of GCAPs [62]. In the study presented here [JR4], bovine GCAP was used, of which there exist two forms, GCAP1 and GCAP2. Importantly, they are believed to operate in a relay mechanism [50]. Fast response kinetics have been observed for GCAP1, from which Ca^{2+} ions dissociate at an intermediate level of intracellular Ca^{2+} concentration. Thereby, GCAP1 facilitates a fast response to an incoming light signal and effectively shuts down the photoreceptor cell. At later times and a lower intracellular Ca^{2+} concentration, GCAP2 releases its Ca^{2+} ions. Thereby, GCAP2 enables fine tuning of the response of the photoreceptor cell. The common feature of both GCAPs is their activation of the GC by undergoing a conformational change. The question addressed in [JR4] is therefore, whether their differential activation mechanism is reflected in a differential conformational change. This may suggest a more general concept, in which differential cellular responsiveness and physiological specificity are tuned by differential conformational dynamics despite structural homology.

Protein Structure of the GCAPs

In order to describe a conformational change of a protein, its structure must be known. Generally, a protein is described by its primary, secondary, tertiary and quaternary structure [56]. Its primary structure is its polypeptide chain formed by a sequence of amino acids, which is terminated by a carboxyl group at one end (C-terminus) and an amine group at the other end (N-terminus). Hydrogen bonds between different amino acids support the folding of this chain, by which alpha helices or beta sheets may form. These are secondary structure elements. The protein as a whole may be described by its geometric shape, which is referred to as its tertiary structure. For example, globular proteins such as myoglobin consist of solvent-exposed hydrophilic residues and a core of hydrophobic residues [56]. Finally, a protein may have a quaternary structure, which describes a particular arrangement of sub-units or dimerisation of the protein. For example, the guanylate cyclase is a dimer [50].

Specifically, in case of the GCAPs, there exists a crystal structure of myristoylated Ca^{2+}-bound GCAP1 obtained by X-ray diffraction (PDB: 2R2I) and a nuclear magnetic resonance structure (NMR) of GCAP2 in the non-myristoylated, Ca^{2+}-bound form (PDB: 1JBA). They are shown in Figure 2.5, which highlights their structural homology. The GCAPs belong to the family of neuronal calcium sensor proteins [49] and therefore share common features. For example, both GCAPs have four EF-hand motifs, which consist of two alpha helices linked by a loop region, where Ca^{2+} is bound. In both GCAPs, three of them are active in binding Ca^{2+}.

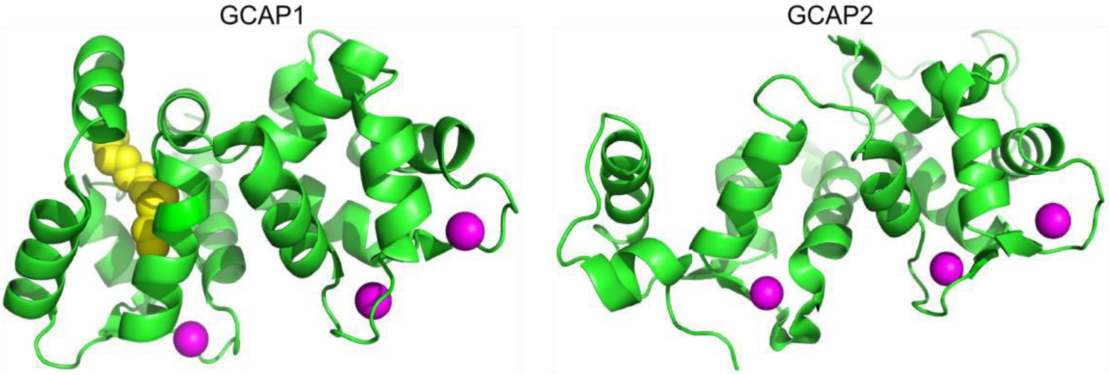

Figure 2.5: Protein structures of GCAP1 (left) and GCAP2 (right), highlighting their structural homology. Both GCAPs harbour four EF hand motifs, of which three are active in binding Ca^{2+} ions (magenta spheres). The structure of GCAP1 also shows the location of the myristoyl group (yellow spheres).

Furthermore, a fatty acid in form of a myristoyl group is attached to the N-terminus of the GCAPs. For GCAP1 the myristoyl group was found to be buried inside the protein and has been assigned a stabilising function [63]. Thereby the GCAPs differ from recoverin, another member of the family of neuronal calcium sensor proteins, in which the myristoyl group acts as molecular switch, becoming solvent-exposed upon binding of Ca^{2+} and anchoring the protein to a membrane or hydrophobic site of a target protein [64]. In this study, the conformational change was deduced by directly resolving the structure of the protein. However, such structural information is not always available. For example, for crystallography high amounts of protein would be needed, whereas GCAP1 in its Ca^{2+}-free form does not crystallise at all. Thus, information on the conformational change of the polypeptide chain due to the release of bound Ca^{2+} is not directly accessible.

Site-specific Labelling

In this case, a strategy adopted in [JR4] to investigate the conformational change of a protein is time-resolved fluorescence spectroscopy of site-specifically labelled mutants. For this technique, our colleagues from the biochemistry group of Professor Karl-Wilhelm Koch modified specific amino acids in the polypeptide chain of the protein by attaching a fluorescent dye, which is sensitive to a change in its local environment. For example, cysteine is an amino acid with a thiol group. Such a residue can be labelled with a dye like Alexa647. As can be seen from its chemical structure shown in Figure 2.6 this dye contains a maleimide group (left) with reacts with the thiol group of the cysteine to form a stable thioether bond [65].

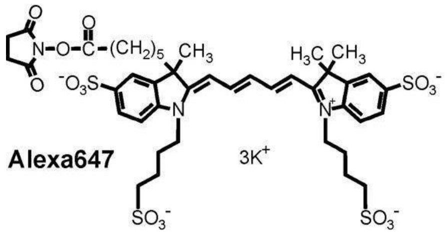

Figure 2.6: Chemical structure of the fluorescent dye Alexa647. Modified from [66].

Specifically, GCAP1 has four cysteine residues in its polypeptide chain, marked in Figure 2.13. Site-specific labelling is only possible, if there exists only one cysteine residue in the protein. Here, this was achieved by synthesising mutants of the protein, in which cysteine residues were replaced by the amino acid alanine. Further details of this biochemical procedure can be found in [JR4]. It results in GCAP mutants with only one cysteine residue left, to which the Alexa647 dye is covalently bound. If the protein changes its conformation, the dye will automatically move as part of the polypeptide chain into a new local environment. For example, it may be buried inside the protein or become more exposed to the solvent. This will change its fluorescence properties like lifetime and anisotropy, which may be probed by time-resolved fluorescence spectroscopy. To gain a better understanding of the outcome of such an experiment presented in [JR4], these properties of a dye molecule are discussed in further depth in the next section.

2.3. Fluorescent Dye

The following discussion will illustrate the main concepts of fluorescence with the scope of giving a background for the time-resolved fluorescence spectroscopy measurements carried out on the Alexa647 dye attached to GCAP1 mutants [JR4].

Absorption and Fluorescence Spectra

To gain an understanding of the absorption and fluorescence spectra of a dye molecule, let us consider its energy diagram [67], as shown in Figure 2.7. This one-dimensional representation is a simplification of the multidimensional molecular configuration of the nuclei. In the Born-Oppenheimer approximation, their positions are fixed. For this molecular configuration the energy of an electronic state is calculated. This results in an effective potential, which is described by a short-range repulsive and a long-range attractive interaction term. The region around its potential minimum may be further approximated by a harmonic oscillator potential.

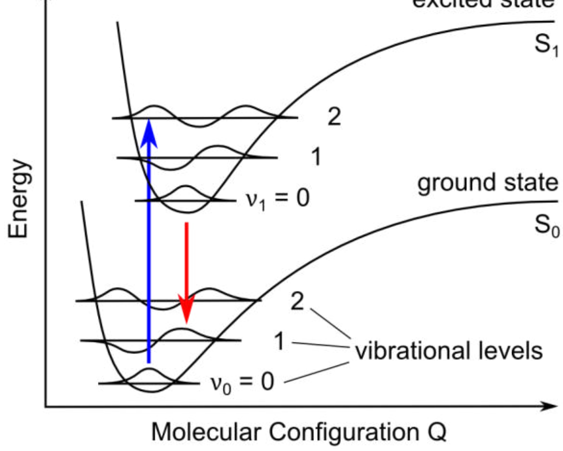

Figure 2.7: Energy level diagram of a dye molecule. The absorption of light (blue arrow) promotes an electron to an upper vibrational level of an excited state, from where it relaxes to the lowest vibrational level. The subsequent radiative decay to the ground state (red arrow) is accompanied by the emission of a fluorescence photon. Adapted from [67].

Specifically, the dye molecule may be described by an electronic ground and excited state [68], as sketched in Figure 2.7. In each of these states the electron can occupy vibrational levels. The excitation of a dye molecule may occur via absorption of light, which promotes an electron usually occupying the lowest vibrational level of the ground state to an upper vibrational level of the excited state. The probability of the population of a specific vibrational level is governed by the overlap of the corresponding wave functions.

After being promoted to the upper vibrational level of the excited state an electron usually decays to the lowest vibrational level of the same state via intramolecular vibrational relaxation [68]. From there, the electron usually decays to an upper vibrational level of the ground state via the emission of a fluorescence photon, from where it finally relaxes to the lowest vibrational level in the absence of thermal excitation. Overall, energy is partially converted into other channels, such that the fluorescence photon will have a longer wavelength than the photon absorbed. This difference in wavelength is known as the Stokes shift [68].

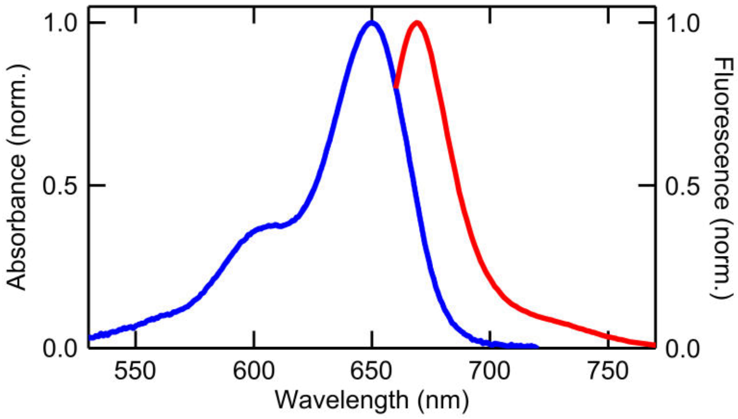

Figure 2.8: Measured absorption (blue) and fluorescence (red) spectrum of the Alexa647 dye. The absorption maximum occurs at 650 nm, the fluorescence maximum at 669 nm.

The measured absorption and fluorescence spectra of the Alexa647 dye are shown in Figure 2.8. Specifically, Alexa647 has its absorption maximum near 650 nm and a weaker second peak near 605 nm. When excited with 656 nm light, the fluorescence maximum occurs at 669 nm, corresponding to a Stokes shift of about 19 nm.

Fluorescence Lifetime

A property of fluorescence, which holds a clue to the local environment of the dye is the fluorescence lifetime. It is therefore important, to understand this quantity in more depth and define its precise meaning. In particular, the excited state population $n(t)$ decays according to [68]:

$$\frac{d}{dt}n(t) = (k_r + k_{nr})n(t) \tag{2.1}$$

Here, k_r is the radiative decay rate (i.e. via fluorescence) and k_{nr} is the non-radiative decay rate. As the decay of the excited state occurs at random, for example, radiatively via spontaneous emission (stimulated by a virtual photon created by quantum fluctuations of the vacuum background), and with the same probability for each dye molecule in a given time interval, the excited state population decays exponentially [68] according to $n(t) = n_0 e^{-t/\tau}$, where n_0 is the initial population and

$$\tau = (k_r + k_{nr})^{-1} \tag{2.2}$$

is the fluorescence lifetime. Experimentally, the population of the excited state is proportional to the measured fluorescence intensity $I(t) = I_0 e^{-t/\tau}$.

Importantly, an increase in the non-radiative decay rate will shorten the measured fluorescence lifetime. For example, internal twisting of the molecule provides a de-excitation pathway of the excited state via non-radiative internal conversion to the ground state [69,70]. This process is more likely for a molecule, which is less constrained in its motion, for example, for a dye molecule exposed to a solvent. In contrast, a dye molecule in the interior of a protein will be more constrained in its motion, limiting non-radiative decay via internal conversion and favouring radiative decay via fluorescence. This will result in a longer measured fluorescence lifetime. If the diffusive rotational motion of the dye is constrained, the local viscosity is large. Quantitatively, the fluorescence lifetime of a dye depends on the local viscosity η of its environment via the Förster-Hoffmann relation $\tau \propto \eta^{\beta}$, where β is a dye-dependent positive constant [71]. In particular, this relationship has been shown for cyanine dyes [69], to which the Alexa647 dye used in this experiment is similar [72]. Specifically, the polymethine backbone of these dyes allows for cis/trans isomerisation, such that their fluorescence lifetime strongly depends on viscosity by the mechanism of internal conversion to the ground state as described above [72]. Consequently, the Alexa647 dye is a well suited probe for changes in local viscosity. Note, that the natural lifetime of a dye molecule, that is the measured fluorescence lifetime in the absence of such de-excitation pathways, would be given by the Strickler-Berg equation, which relates the Einstein A coefficient to the refractive index of the surrounding medium [73].

Fluorescence Anisotropy

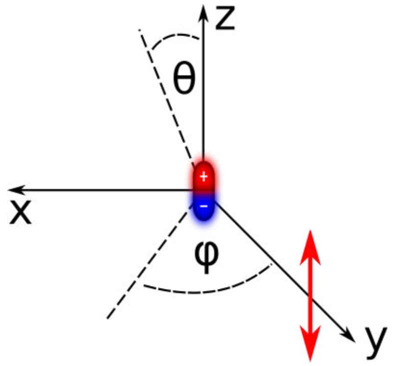

Figure 2.9: Photoselection. Molecules oriented with their electric dipole moment parallel to the polarisation axis of the excitation light (red arrow) are preferentially excited. Adapted from [68].

Further information on the local environment of the dye due to rotational diffusion may be deduced from the polarisation of the fluorescence. To account for this property the dye molecule is modelled as a radiating dipole [68,74]. For a fixed polarisation of the excitation light dye molecules with their electric dipole moment oriented parallel to the polarisation axis of the light will be preferentially excited. This is called photoselection [68].

From Figure 2.9 it can be seen that the component of the fluorescence light parallel to the excitation light (red arrow) is:

$$I_{\parallel} = I_0 \cos^2 \theta \tag{2.3}$$

The perpendicular component is given by:

$$I_{\perp} = I_0 \sin^2 \varphi \sin^2 \theta = \frac{1}{2} I_0 \sin^2 \theta \tag{2.4}$$

Here, $\langle \sin^2 \varphi \rangle = 1/2$, as molecules in the range from $\varphi = 0$ to $\varphi = 2\pi$ are excited with equal probability in case of a fixed excitation polarisation, as depicted Figure 2.9. The total intensity is then given by:

$$I_0 = I_{\parallel} + 2I_{\perp} = I_0(\cos^2 \theta + \sin^2 \theta) \tag{2.5}$$

The ratio of the polarised component of the fluorescence to the total fluorescence intensity can by quantified by the anisotropy [68]:

$$r = \frac{I_{\parallel} - I_{\perp}}{I_0} \tag{2.6}$$

By inserting Equations 2.3 and 2.4 into this expression the initial anisotropy of a sample is obtained as:

$$r_0 = \frac{3\langle \cos^2 \theta \rangle - 1}{2} \tag{2.7}$$

In solution molecules are usually randomly oriented. Consequently, the number of molecules excited by vertically polarised light in the process of photoselection is limited. Specifically, for an ensemble of molecules, $\langle \cos^2 \theta \rangle = 3/5$ [68]. This gives an initial anisotropy $r_0 = 0.4$.

It is also worth noting, that at $\theta = 54.7°$ the anisotropy becomes $r = 0$. This is called the magic angle [68]. It does not imply, however, that all molecules are oriented at $54.7°$. Rather, at this angle both polarisation components contribute equally to the total intensity as given by Equation 2.5. Hence, a fluorescence decay measurement will not be influenced by anisotropy effects and the correct fluorescence lifetime can be determined.

Spherical Rotor

The anisotropy will change over time due to rotational diffusion of the dye molecules. In this process, Brownian motion randomises the orientation of the dye molecules. It depends on the size of the dye molecules. Large dye molecules will rotate slower than small ones. To account for its size, the dye is modelled as spherical molecule [68], from which a simple description of its rotational motion arises. In particular, for a spherical rotor the anisotropy decay following pulsed excitation is given by [68]:

$$r(t) = r_0 e^{-t/\phi} \tag{2.8}$$

In combination with Equation 2.6, the intensity of fluorescence light polarised parallel to the excitation light will decrease over time, while for perpendicularly polarised fluorescence light more photons will be emitted at later times as depicted in Figure 2.10a. Overall, the depolarisation caused by rotational diffusion leads to a final anisotropy $r_\infty = 0$, as illustrated in Figure 2.10b.

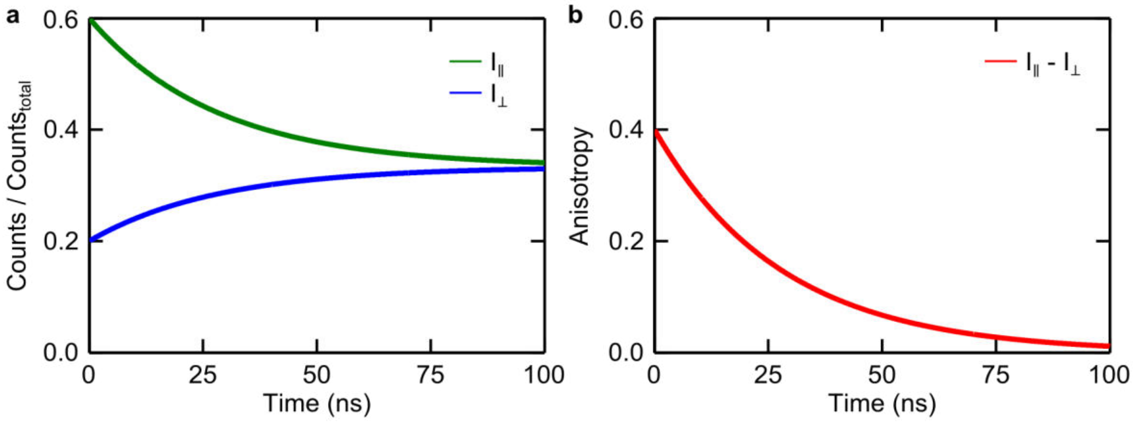

Figure 2.10: (a) The contribution of the parallel (perpendicular) component of the fluorescence light decreases (increases) over time. (b) Overall, the anisotropy of the fluorescence light approaches 0, as rotational diffusion randomises the orientation of the molecules.

The decay of the anisotropy yields information on the size of the dye molecule. The larger the dye molecule is, the longer it takes to rotate and the longer it takes for the anisotropy to decay. For a spherical rotor, the rotational correlation time ϕ is related to its hydrodynamic radius r_{st}, i.e. the radius of a hypothetical hard sphere with the same diffusion coefficient as, for example, a protein in a viscous medium, by the Stokes-Einstein-Debye equation [68,75].

$$\phi = \frac{4\pi\eta r_{st}^3}{3k_B T} \tag{2.9}$$

Here, k_B is Boltzmann's constant, T is the temperature of the solution and η is the viscosity of the solvent.

If the rotation of the dye molecule is restricted, for example, as sketched in Figure 2.11 by the surface of the protein to which it is bound, the final anisotropy r_∞ will tend to a non-zero value. This information can be used in a wobbling-in-a-cone model [76]. In this model, the dye is assumed to exert a rapid diffusive rotational motion in its local environment as a (hindered) spherical rotor [68]. In addition, a slower global rotational motion is assigned to the protein-dye complex. The surface of the protein restricts the motion of the dye to the interior of a cone defined by a semicone angle

$$\theta = \cos^{-1}\left(\sqrt{2\sqrt{\frac{r_\infty}{r_0}+\frac{1}{4}}-\frac{1}{2}}\right) \tag{2.10}$$

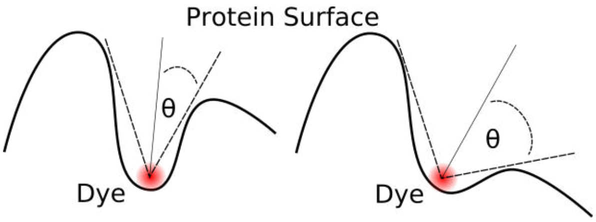

Figure 2.11: Wobbling-in-a-cone model. A dye attached to a protein is hindered in its rotational motion by the protein surface. The motional restriction of the dye is quantified by the semi-cone angle θ.

2.4. Time-Resolved Fluorescence Spectroscopy

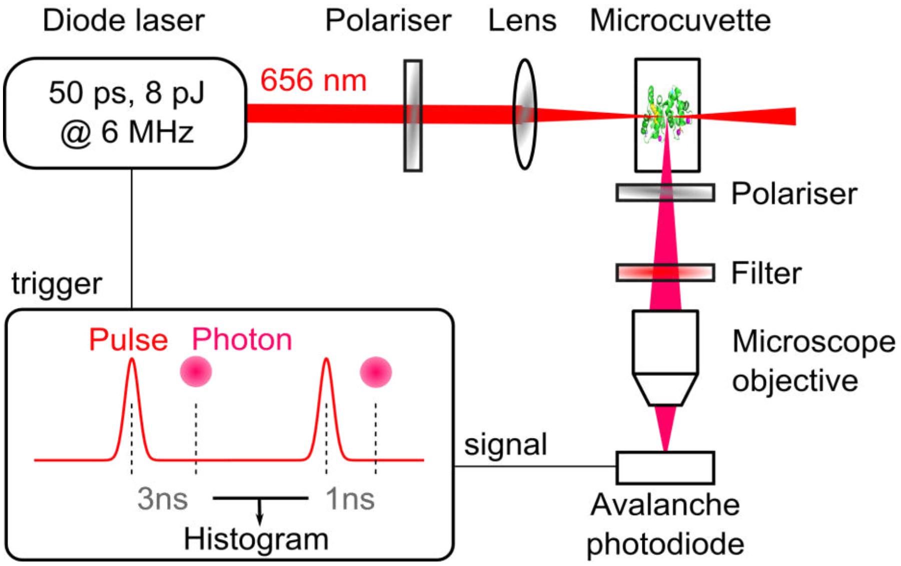

Figure 2.12: TCSPC setup. Vertically polarised light at 656 nm from a pulsed laser diode excites the dye molecules attached to the GCAP1 mutants, hosted in solution in a microcuvette. The fluorescence light is separated from the excitation light by a filter, analysed in polarisation and recorded with an avalanche photodiode. The time between the emission of an excitation pulse from the laser diode and the arrival of a fluorescence photon at the detector is sorted into a histogram.

The fluorescence properties of the Alexa647 dye in its local environment, site-specifically attached to the protein GCAP1 as discussed in Section 2.2, were probed by time-resolved fluorescence spectroscopy [JR4]. Specifically, the technique of time-correlated single photon counting (TCSPC) [68,77] was employed.

In this setup schematically shown in Figure 2.12 a laser diode (LDH 8−1−060 with PDL 800, PicoQuant) provides the excitation light in the form of ~50 ps pulses centred around 656 nm at a repetition rate of 6 MHz and with an average power <5 μW. This excitation wavelength is close to the absorption maximum of the Alexa647 dye, as shown in Figure 2.8. A polariser ensures a well-defined vertical polarisation of the laser pulses. They are weakly focussed into a microcuvette with an optical path length of 1.5 mm (105.252-QS, Hellma Analytics) containing the protein solution, where they excite the Alexa647 dye attached to a GCAP1 mutant. This results in the isotropic emission of fluorescence light, which is collected with an efficiency of about 2% and analysed with respect to its polarisation by a further polariser. Scattered excitation light in this path is eliminated by an optical filter, such that only the longer wavelength fluorescence light is focussed by a microscope objective (Nikon, NA=0.7) onto an avalanche photodiode (ID Quantique 100) with an active area with a diameter of 20 μm.

The arrival of a fluorescence photon on the detector stops the charging of a capacitor, which was electronically triggered by the release of an excitation light pulse from the laser diode. The charge on the capacitor is proportional to the time between the absorption of an excitation photon and the emission of a fluorescence photon. The recorded time intervals are sorted into a histogram with a timing resolution of 4 ps (PicoHarp 300, PicoQuant). This process is repeated until data with a sufficient signal-to-noise ratio has been taken. To prevent bias towards short arrival times, the count rate was kept in the range of 1% to 5% of the repetition rate of the laser diode [77]. This gives a fluorescence decay curve, exemplary displayed in Figure 2.14a, which is obtained by setting the polariser in the detection arm to magic angle conditions as discussed in Section 2.3.

The fluorescence lifetime is extracted by fitting the measured fluorescence decay curve with the software FluoFit (PicoQuant) to an exponential decay model by reconvolution with the instrument response function (IRF):

$$I(t) = \int_{-\infty}^{t} IRF(t') \sum_{i=1}^{n} A_i e^{-\frac{t-t\prime}{\tau_i}} dt' \tag{2.11}$$

Here, A_i corresponds to the amplitude of the decay component with fluorescence lifetime τ_i. The IRF is governed by the response time of the electronics and the temporal width of the excitation pulses. In our setup, it was recorded with scattered light from diluted milk and found to have a width of ~100 ps (FWHM).

The anisotropy decay curves, exemplary displayed Figure 2.15a, are calculated from Equation 2.6 from the fluorescence decay curves with the polariser in the detection arm set to either transmit vertically or horizontally polarised light and are fitted with the software FluoFit (PicoQuant) to:

$$r_{fit}(t) = r_\infty + \sum_{i=1}^{n} r_i e^{-\frac{t}{\phi_i}} \tag{2.12}$$

Here, r_∞ is the final anisotropy and r_i corresponds to the amplitude of the decay component with rotational correlation time ϕ_i.

2.5. Conformational Change of the Calcium Sensor Protein GCAP1

As discussed above the time-resolved fluorescence spectroscopy study, with its key findings achieved in this thesis presented here and closely following the associated publication [JR4], investigates the question, whether differential cellular responsiveness mediated by the structurally homologous calcium sensor proteins GCAP1 and GCAP2 is reflected in their differential conformational protein dynamics, triggered by a change in intracellular Ca^{2+} concentration.

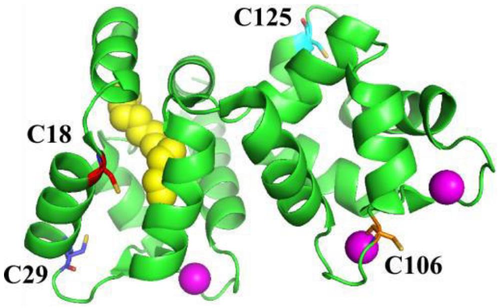

Figure 2.13: Protein structure of GCAP1. The four cysteine residues are labelled according to their position in the polypeptide chain. Modified from [JR4].

For this, mutants of GCAP1 were prepared by our colleagues from the biochemistry group of Professor Karl-Wilhelm Koch, site-specifically labelled as discussed in Section 2.2 with the Alexa647 dye at each of the four cysteine residues displayed in Figure 2.13 and checked for biochemical functionality. To investigate the effect of myristoylation discussed in Section 2.2 the protein was supplied both in its myristoylated (myr) and non-myristoylated (nmyr) form. Thus in this thesis eight GCAP1 mutants were investigated by time-resolved fluorescence spectroscopy in four different solutions each, i.e. either in the presence of the chelating agent EGTA (corresponding to a Ca^{2+}-free protein, also termed apo), Ca^{2+} ions, Mg^{2+} ions or a combination of Ca^{2+} and Mg^{2+} ions. The solutions containing Mg^{2+} ions probed their role in the physiological activator state of the protein as discussed in Section 2.2. In total 960 fluorescence decay curves were measured.

First, the fluorescence lifetime of the Alexa647 dye in all 32 configurations of the protein was measured. An example of a fluorescence decay curve is displayed in Figure 2.14a. The data was fitted to a bi-exponential decay model given by Equation 2.11, which yields good agreement with the data as judged from the equally distributed residuals. A fast component ranging from $1.3\ \mathrm{ns}$ to $2.0\ \mathrm{ns}$ typically exceeded a slow component ranging from $0.6\ \mathrm{ns}$ to $1.2\ \mathrm{ns}$ in amplitude by a factor of 3 and is therefore displayed in Figure 2.14b. In particular, it was found, that the lifetime of the dye attached to the cysteine residue at position 106 in the polypeptide chain increased significantly by about 30% from $1.4\ \mathrm{ns}$ in the Ca^{2+}-bound form to $1.8\ \mathrm{ns}$ in the Ca^{2+}-free protein. As explained in Section 2.3 an increase in lifetime corresponds to a more viscous local environment of the dye. From this measurement it was therefore concluded that the loop region around position 106 moves towards the interior of the protein upon release of Ca^{2+} ions by the GCAP1 [JR4].

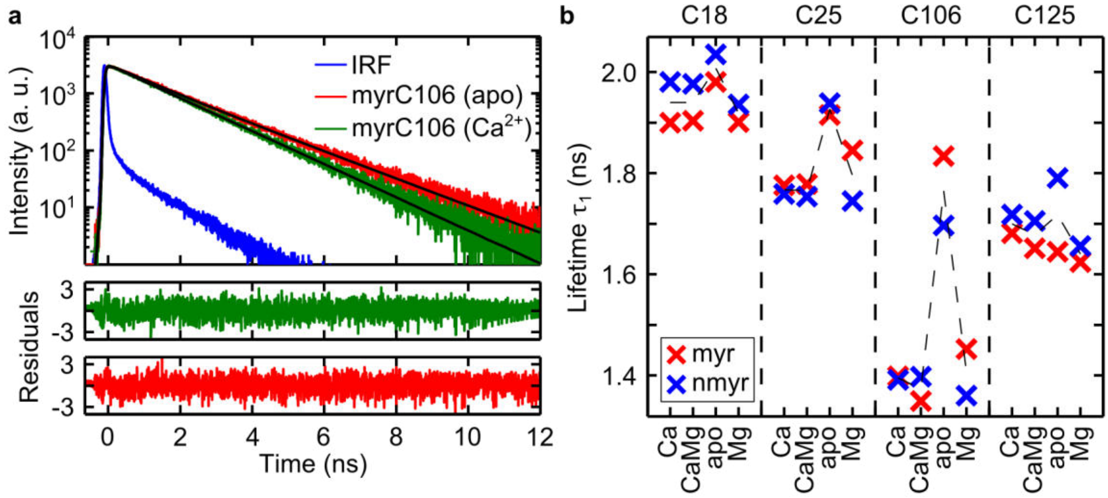

Figure 2.14: (a) Exemplary fluorescence decay curves of the GCAP1 mutant myrC106 in its Ca^{2+} bound (green) and Ca^{2+} free (red) state and the instrument response function (blue). Equally distributed residuals arise for bi-exponentially fitted curves (black). (b) The dominant lifetime component is displayed as the weighted average of 10 measurements with a weighted fitting error <5 ps (not shown) for all mutants in all cation configurations, either myristoylated (red) or nonmyristoylated (blue). Modified from [JR4].

Second, the fluorescence anisotropy was measured in all 32 configurations of the protein-dye complex. An example of an anisotropy decay curve is displayed in Figure 2.15a. The data was fitted to a bi-exponential decay model given by Equation 2.12 yielding equally distributed residuals. In this model, a fast component ranges typically from $0.43\ \mathrm{ns}$ to $0.82\ \mathrm{ns}$ and may be associated with the rapid diffusive motion of the dye within its local environment. Furthermore, a slow component ranges from $19\ \mathrm{ns}$ to

$43\,\mathrm{ns}$ for the mutants with the dye located at positions C18 and C29. It may be associated with the global rotational motion of the protein-dye complex. In particular, the slow component of the rotational correlation time of the protein-dye complex with the dye located at position C18 increased from $33\,\mathrm{ns}$ in the myristoylated Ca^{2+}-bound form to $43\,\mathrm{ns}$ in the Ca^{2+}-free protein as displayed in Figure 2.15b. At this position of the dye, also the longest fluorescence lifetime as shown in Figure 2.14b was measured, which indicates its position in the interior of the protein. Thus, the attachment of the dye to the protein will most likely have the least influence on its hydrodynamics radius, such that the rotational correlation time measured for the protein-dye complex most closely resembles that of the unlabelled protein. By Equation 2.9 it was found to increase from $r_{st} = 2.98 \pm 0.05\,nm$ in the Ca^{2+}-bound form to $r_{st} = 3.48 \pm 0.10\,nm$ in the Ca^{2+}-free protein. It was therefore concluded that GCAP1 enlarges upon release of Ca^{2+} ions [JR4]. This conclusion agrees with dynamic light scattering measurements of myristoylated wild-type GCAP1 [78].

Moreover, a similar behaviour, but an overall reduced rotational correlation time of the protein-dye complex with the dye located at position C18 is measured in the non-myristoylated form of the protein. This translates into a smaller hydrodynamic radius and thereby into a more compact form of the protein as compared to its myristoylated form.

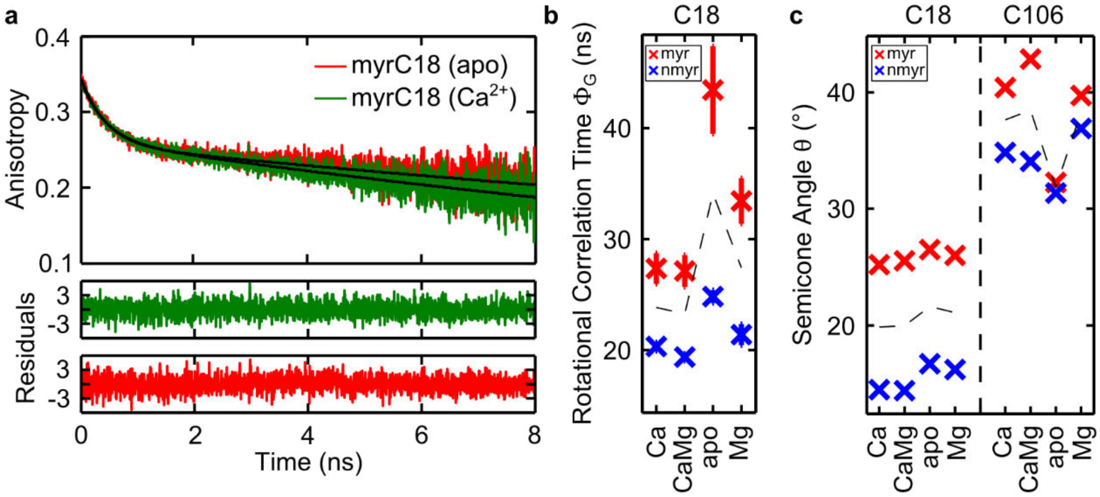

Figure 2.15: (a) Exemplary anisotropy decay curves of the GCAP1 mutant myrC18 in the Ca^{2+} bound (green) and the Ca^{2+} free state. Equally distributed residuals arise for bi-exponentially fitted curves (black). (b) The slow rotational correlation time component is displayed as the weighted average of 10 measurements with weighted fitting errors ranging from 0.33 to 4.0 ns for the mutant C18 in all cation configurations, either myristoylated (red) or nonmyristoylated (blue). (c) The semicone angle obtained from a wobbling-in-a-cone model is displayed as the weighted average of 10 evaluations with weighted errors ranging from 0.15° to 0.57° (not shown) for the mutants C18 and C106 in all cation configurations, either myristoylated (red) or nonmyristoylated (blue). Modified from [JR4].

Third, the initial and final anisotropy obtained from fitting the anisotropy decay curves were analysed in the framework of the wobbling-in-a-cone model described in Section 2.3, which yields information on the diffusional motion of the dye restricted by a semicone angle θ given by Equation 2.10. As displayed in Figure 2.15c, this semicone angle increases for a dye located at position C106 from 32° in the Ca^{2+}-free to 41° in the Ca^{2+}-bound protein. As a dye in the interior of the protein should also be more restricted in its motion, this model relying on the anisotropy measurements thereby supports the movement of the dye at position C106 towards the interior of the protein upon release of Ca^{2+} ions as also concluded from the lifetime measurements above [JR4].

Moreover, a decrease in the semicone angle from 26° in the myristoylated to 15° in the nonmyristoylated protein was calculated for the dye located at position C18. This points to a movement of the region around position C18 into a hydrophobic pocket of the protein, when the myristoyl group is missing. This is further supported by a measured increase in fluorescence lifetime by ~0.1 ns at this position displayed in Figure 2.14b. It also correlates with the more compact form of the nonmyristoylated protein concluded before. This points to the stabilising function of the myristoyl group in GCAP1 [63].

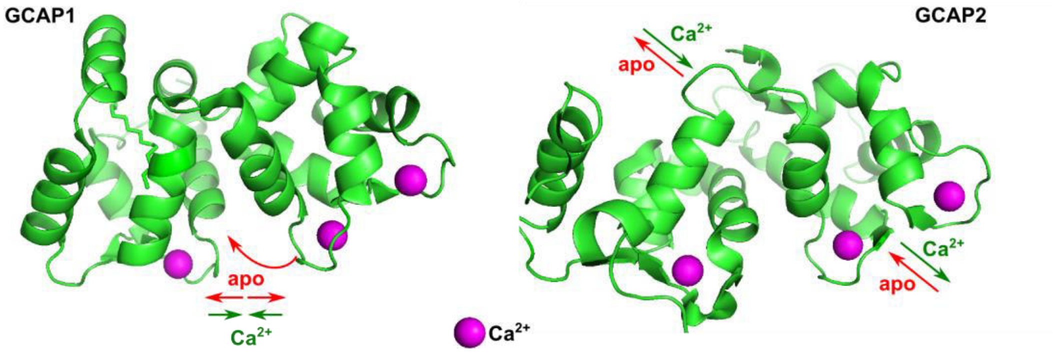

Figure 2.16: The comparison of the protein structures of GCAP1 and GCAP2, as discussed in Section 2.2, shows the distinctly different switching mechanisms upon Ca^{2+} release. Modified from [JR4].

Taken together, all observations suggest the movement of the loop region near position 106 towards the interior of the protein combined with a simultaneous enlargement of the protein upon release of Ca^{2+} ions. These conclusions are additionally supported by molecular dynamics simulations [JR4] performed by our colleagues from the group of Professor Daniele Dell'Orco, which point to an overall increase in hydrodynamic volume of GCAP1 in its Ca^{2+} free state [79]. Furthermore, the angle between the EF-hand motifs increases upon release of Ca^{2+} ions, which opens up a cavity, into which the loop region around position C106 may move towards the interior of the protein as concluded from the time-resolved spectroscopy measurements presented above. Pictorially, this rearrangement of the polypeptide chain may be seen as a twisted-accordion motion as depicted in Figure 2.16. It contrasts the piston-like movement of an alpha helix in GCAP2 concluded from a similar time-resolved fluorescence study [80]. In summary, these structurally homologous calcium sensor proteins are distinctly different in the conformational change they undergo to activate the guanylate cyclase. This differential conformational change may therefore reflect their differential action on the guanylate cyclase in the context of the calcium relay mechanism discussed in Section 2.2, in which GCAP1 ensures a fast response and GCAP2 enables fine regulation. Moreover, the conclusions drawn from this study may even point to a conceptually new concept in Ca^{2+} mediated signal processing beyond the retina, in which differential cellular responsiveness is mediated by differential conformational dynamics despite structural homology. For example, another pair of related neuronal calcium sensors was recently found to differentially modulate a signalling pathway, which may be relevant in the treatment of neuropsychiatric disorders [54].

In this time-resolved fluorescence study the rather slow dynamics of the conformational change of a protein is governed by the rearrangement of its constituent atomic nuclei. In contrast, the dynamics of electrons occurs on a much faster time scale. Capturing these phenomena requires sophisticated tools such as ultrafast two-colour pump-probe spectroscopy, which will be discussed in the remainder of this thesis.

3. Femtosecond Laser System

The remainder of this thesis concerns the investigation of the ultrafast dynamics of Rydberg electrons at a gold nanotip in the strong-field regime by two-colour pump-probe spectroscopy. Specifically, a gold nanotip, as discussed in more depth in Chapter 4, is a thin piece of wire, which converges conically to an apex radius of curvature of few nanometres. The high density of electric fields at its apex gives rise to an enhancement of an incident electric field [26,27]. This sets a scale for the requirements, which need to be fulfilled for a laser system facilitating two-colour pump-spectroscopy on a gold nanotip.

First, to access the strong-field regime the laser system needs to provide pulses of sufficient strength. Typically, as discussed in more depth in Chapter 4, this requires a laser intensity on the order of $10^{11}\ \mathrm{W/cm^2}$, which is then enhanced at the apex of the metallic nanotip by about two orders of magnitude [38]. Second, in the strong-field regime the electron dynamics is not solely governed by the intensity envelope of the laser pulses anymore, but driven by the light field itself [24,38,81]. Their phase difference is the carrier-envelope phase (CEP). Control over the motion of electrons in the strong-field regime therefore requires a controllable, stable CEP. In particular, the CEP varies most strongly under the envelope for few-cycle laser pulses. Such pulses will be in the domain of few femtoseconds and thus also provide the necessary time resolution to study ultrafast dynamics. Finally, their wavelength should be tuneable, for example, to the near-infrared in order to exploit the field enhancement at the apex of the gold nanotip [26,27,82], avoid damage due to absorption and enable an easier access to the strong-field regime as discussed in more depth in Chapter 4. For two-colour pump spectroscopy femtosecond laser pulses in a different spectral range are additionally required. In particular, the requirement for a pump pulse to prepare an electron wave packet in the gold nanotip is substantially different from that for a probe pulse to subsequently photoionise and strongly drive the electron wave packet in its oscillatory light field. Furthermore, using laser pulses of a different colour avoids, for example, interference effects, which would result in a change in intensity, which thereby could not be controlled independently.

Wavelength tuneability and sub-100-fs pulses may be achieved with dye lasers [83]. However, this requires an exchange of the dye as the laser medium followed by a lengthy re-adjustment. An easy-to-handle, solid-state alternative is provided by Ti:sapphire [84,85]. Here, mode-locking techniques have pushed the pulse duration down to few femtoseconds [86,87]. Moreover, the pulse energy can be increased by chirped pulse amplification [88,89] to several joule, which allows for subsequently driving a cascade of nonlinear processes such as optical parametric generation [90,91] to achieve wavelength tuneability. Here, the techniques of white light generation in bulk materials [92,93] or nonlinear fibres [94,95] are a focus of current research. They provide a seed for subsequent optical parametric amplification achieving few-cycle laser pulses tuneable from the visible to the far-infrared spectral region [96-99], thereby covering the range of transparency of common nonlinear crystals such as beta-barium borate (BBO) [100,101]. These techniques have further been shown to preserve the CEP [102,103] and may therefore be used in combination with an actively CEP stabilised laser system [104-107], which, however, requires a feedback loop built into the laser system and is powered by electronics. The stabilisation of the CEP may also be realised passively in an all-optical scheme, which predominantly employs the technique of difference frequency generation (DFG), in which two laser pulses carrying the same CEP fluctuations are mixed [108-114].

In particular, our group chose to follow a design pioneered by the group of Professor Giulio Cerullo [108]. Here, a home-built widely tuneable two-stage non-collinear parametric amplifier (NOPA) provides broadband, few-cycle laser pulses in the visible (VIS) and narrowband laser pulses in the infrared (IR). Their subsequent mixing by DFG additionally provides few-cycle laser pulses in the near-infrared (NIR), which are passively CEP stabilised. The system is seeded by the process of white light generation and pumped by frequency-doubled laser pulses from a regenerative Ti:sapphire amplifier.

To provide a more general understanding of ultrashort laser pulses and their characterisation this chapter will first introduce the theoretical framework of an ultrashort laser pulse, focussing particularly on its duration. The discussion will then shift to the experimental generation of ultrashort laser pulses as realised in our group. It will start with a short description of the regenerative Ti:sapphire amplifier, which was modified as part of this thesis to optimise the performance of the NOPA system. Next, the NOPA technique will be explained, followed by an experimental characterisation of the NOPA and DFG stages as implemented in our laser system. Finally, the scheme of passive CEP stabilisation will be introduced. In particular, the CEP stability was improved as part of this thesis and, importantly, characterised shot-to-shot by spectral f-to-2f interferometry.

3.1. Theoretical Background of an Ultrashort Laser Pulse

To understand how an ultrashort laser pulse is described and, in particular, its pulse duration is characterised and optimised, this section will look into its theoretical background in more depth. For this, the electric field of an ultrashort laser pulse will be discussed in the time-frequency domain, whereas its spatial dependence is neglected and linear polarisation is assumed. In general, the electric field of an ultrashort laser pulse may be written in the time domain as a complex valued function with an amplitude and a phase [67]:

$$E(t) \propto \sqrt{I(t)}e^{i\varphi(t)} \tag{3.1}$$

Here, $\varphi(t) = \varphi_{CE} + \omega_0 t + \varphi_a(t)$ is the temporal phase of the laser pulse.

Similarly, the ultrashort pulse is described in the frequency domain by

$$E(\omega) \propto \sqrt{S(\omega)}e^{i\psi(\omega)} \tag{3.2}$$

Here, $S(\omega)$ is the spectral intensity, which is usually referred to as the optical spectrum measured with a spectrometer. Furthermore, $\psi(\omega) = \psi(\omega_0) + \psi'(\omega_0) * (\omega - \omega_0) + \frac{1}{2}\psi''(\omega_0) * (\omega - \omega_0)^2 + \ldots$ is the spectral phase [67], assuming a well-behaved ultrashort laser pulse centred around the angular frequency ω_0. In the time domain, the zeroth order term $\psi(\omega_0)$ corresponds to the carrier-envelope phase φ_{CE}. The first order term translates the laser pulse in time. It is known as the group delay, i.e. the delay experienced by an ultrashort laser pulse as a whole, as it travels through a dispersive medium. The quadratic term is called the group delay dispersion and describes the dependence of the group delay on frequency, i.e. the delay experienced by each individual spectral component. It may occur, if an ultrashort laser pulse travels through an optical medium with a frequency-dependent refractive index and is known as chromatic dispersion. Common optical materials exhibit positive dispersion [67]. That is, the refractive index increases with decreasing wavelength, which results in red spectral components travelling faster than blue ones. This causes an ultrashort laser pulse to broaden in time, also referred to as linear chirp.

The representations of an ultrashort laser pulse in the time and in the frequency domain are related to each other by the Fourier transform pair [115]:

$$E(t) = \frac{1}{2\pi} \int_{-\infty}^{+\infty} E(\omega)\, e^{-i\omega t}\, d\omega \tag{3.3}$$

and

$$E(\omega) = \int_{-\infty}^{+\infty} E(t)\, e^{i\omega t}\, dt \tag{3.4}$$

Specifically, if the ultrashort laser pulse is assumed to be described by a Gaussian profile in the time domain as in Section 3.1, its Fourier transform will be a Gaussian profile in the frequency domain. In particular, a broad spectral profile provides the basis for a narrow temporal profile. Quantitatively, the equations above may be converted into a single number by expressing them in terms of FWHM quantities. These are the measurable spectral bandwidth $\Delta\omega/2\pi = \Delta\nu$ and the measurable pulse duration $\Delta\tau$, defined as the intensity FWHM. Their relationship is known as the time-bandwidth product [67], which for a Gaussian-shaped pulse gives:

$$\Delta\tau\Delta\nu = \frac{c}{\lambda^2}\Delta\lambda\Delta\tau \geq 0.441 \tag{3.5}$$

Here, the equality holds for a Fourier limited pulse duration, assuming a flat spectral phase.

Dispersion Management

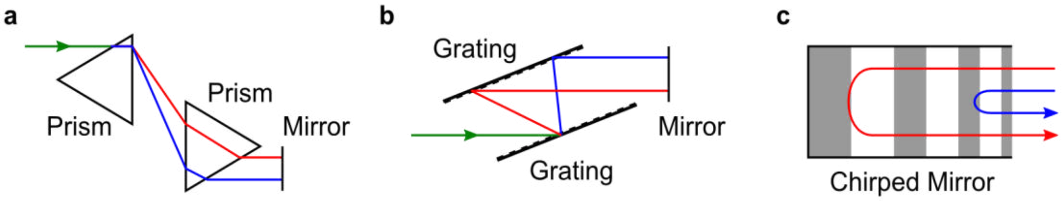

Figure 3.1: Common setups for dispersion management, explained in the main text: (a) Prism compressor. (b) Grating compressor. (c) Chirped mirror.

In order to maintain a pulse duration as close as possible to the Fourier limit, one has to compensate for chromatic dispersion. Here, the general idea is to introduce negative dispersion, that is delaying the red spectral components with respect to the blue ones. This may be achieved in a prism compressor [67], shown in Figure 3.1a, in which the red spectral components are forced to travel a longer distance through the prisms than the blue ones. However, the blue spectral components travel a longer distance through air in this setup, which needs to be balanced. Furthermore, the relatively low change in refractive index of the prism material introduces only little negative dispersion. A higher amount of negative dispersion can be achieved using a grating compressor [67], as shown in Figure 3.1b. Here, however, the losses due to diffraction efficiency are comparatively high. A third option is the use of chirped mirrors [67], shown in Figure

3.1c. They are made of different layers of dielectric material. Light of a different wavelength is reflected at a different layer. Thus, the red spectral components propagate more deeply into the stack of layers than the blue ones. Hence, they are delayed more in time. Thereby, spectral components advancing a dispersed optical pulse can be synchronised in time with the lagging components of the same pulse, such that overall the dispersed pulse is compressed, ideally to its Fourier-limited pulse duration as given by the time-bandwidth product.

Pulse Duration Measurement

To confirm these theoretical considerations in an actual experiment, one needs to measure the duration of an ultrashort laser pulse. Usually, the pulse duration is in the femtosecond time domain. Such a short event cannot be resolved with electronic equipment, which would be limited to the picosecond time domain. For example, the instrument response function of the TCSPC setup discussed in Chapter 2 was ~100 ps. To measure an ultrashort laser pulse, one needs something, which is as short. This is usually the ultrashort laser pulse itself.

Thus, in the most common technique a replica of the ultrashort laser pulse is created in a Mach-Zehnder interferometer [67]. The original pulse and its replica travel on different paths, before they are recombined and spatially overlapped onto the same path. In one arm of the interferometer the path length and thereby the time delay between the original pulse and its replica may be varied. In this way, the replica can be scanned across the original pulse and the interference signal between the two pulses is observed. Specifically, the highest signal will be recorded, when the maxima of the electric fields of the original pulse and its replica coincide.

As information on the spectral phase is lost in the interference of the fundamental light beams, a nonlinear process such as second-harmonic generation in a beta-barium borate (BBO) crystal is employed [91]. The second-harmonic signal is recorded by a spectrometer. In this way, an interferometric frequency-resolved autocorrelation (IFRAC) trace is obtained:

$$I(\omega, \Delta t) = \left| \int_{-\infty}^{+\infty} [E(t) + E(t - \Delta t)]^2 e^{-i\omega t} \, dt \right|^2 \tag{3.6}$$

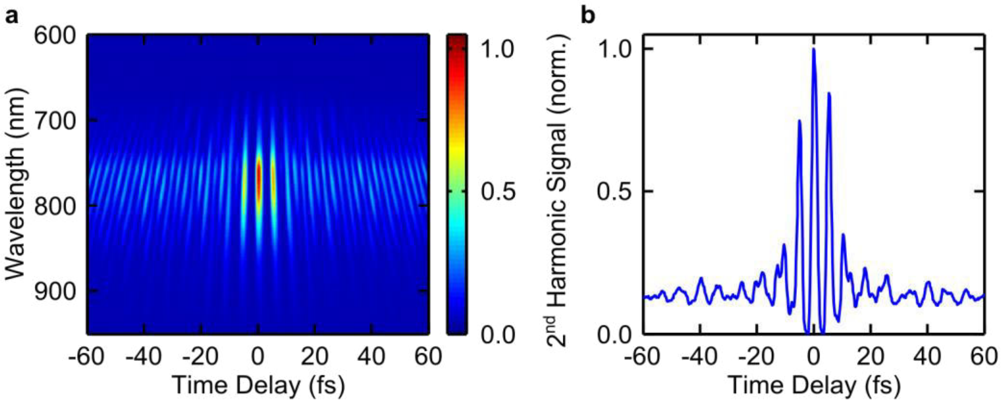

Figure 3.2: (a) An IFRAC and (b) an IAC trace of a few-cycle laser pulse, centred at $\lambda = 1600$ nm. The pulse duration was determined as $\tau_{FWHM} = 10.6$ fs [JR1].

An example of an IFRAC trace is shown in Figure 3.2a. Integrating over the frequency domain gives an interferometric autocorrelation (IAC) trace, displayed in Figure 3.2b.

Experimentally, integration over the frequency domain is equivalent to replacing the spectrometer by a photodiode.

By Fourier transformation along the time delay axis, extracting the dc component with a super-Gaussian filter and back transformation, an IFRAC trace can be converted to a FROG trace [116], which is the abbreviation for frequency resolved optical gating [117]:

$$I_{FROG}(\omega, \Delta t) = \left| \int_{-\infty}^{+\infty} E(t)E(t-\Delta t)e^{-i\omega t} \, dt \right|^2 \tag{3.7}$$

An example of a FROG trace is shown in Figure 3.3a. Integrating over the frequency domain yields an intensity autocorrelation, displayed in Figure 3.3b.

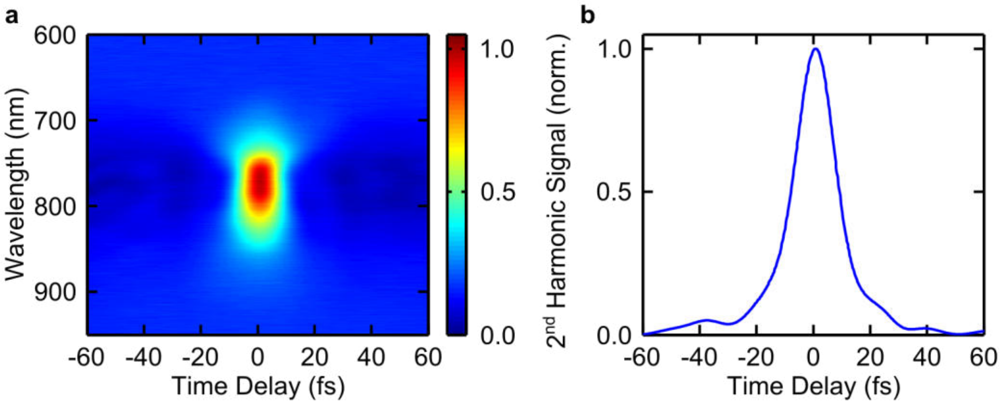

Figure 3.3: (a) A FROG and (b) an intensity autocorrelation trace of a few-cycle laser pulse, centred at $\lambda = 1600$ nm. The pulse duration was determined as $\tau_{FWHM} = 10.6$ fs [JR1].

Experimentally, the FROG trace and the corresponding intensity autocorrelation may also be recorded directly without the need of post-processing the data. This is achieved by letting the original pulse and its replica propagate parallel at a distance to each other [67]. A focussing element then results in both pulses propagating towards each other in directions $\vec{k}_1$ and $\vec{k}_2$, before they cross at one point, at which a BBO crystal is placed. Here, the sum-frequency is generated and emitted in the direction of $\vec{k}_1 + \vec{k}_2$. This signal is observed, while the signal from each individual beam is filtered out by an optical aperture.

The traces shown in Figure 3.2 and Figure 3.3 correspond to the laser pulse published in [JR1]. It was centred at 1600 nm. A nearly Fourier-limited pulse duration of 10.6 fs was concluded, corresponding to two cycles of the electric field and a nearly flat spectral phase. Here, the spectral phase was retrieved using an iterative FROG algorithm [117]. Note, that the direct reconstruction of the electric field is also possible via spectral phase interferometry in a technique called SPIDER [118].

Electron Autocorrelation

While these techniques are useful to characterise an ultrashort laser pulse itself, their major disadvantage is that they use an optical medium for generating a nonlinear signal. This is necessarily different from the actual sample to be probed by the ultrashort laser pulse. Hence, it is much more useful to employ the nonlinear signal from the sample itself and characterise the ultrashort laser pulse in situ. In this thesis, predominantly photoemission of electrons from a gold nanotip is investigated. As we shall learn in Chapter 4, this is a nonlinear process. It can be employed to characterise both the temporal and spatial properties of an ultrashort laser pulse. This method of characterisation will be presented in Chapter 10.

3.2. Chirped Pulse Amplification System

We have now developed the theoretical description of an ultrashort laser pulse and explored how its pulse duration is influenced, optimised and eventually measured. The next step is to look into the experimental generation of ultrashort laser pulses, tuneable over a wide wavelength range. In this thesis, this is achieved in a home-built two-stage NOPA system with a further DFG stage for passive CEP stabilisation. The limited conversion efficiency of this cascade of nonlinear processes requires input pulses of sufficient strength to achieve output pulses suitable for strong-field experiments [96,99,108,119]. Therefore, the NOPA system is pumped by a commercially available regenerative Ti:sapphire amplifier (Spectra-Physics, Spitfire Pro XP), which was modified as part of this thesis to optimise its performance and shall therefore be briefly sketched here.

Its setup is schematically shown in Figure 3.4. Here, a diode-pumped Ti:sapphire oscillator (Spectra-Physics, Mai Tai) provides pulses with a duration of 100 fs and a pulse energy of 10 nJ at a repetition rate of 80 MHz corresponding to a cavity round-trip time $T = 12.5\ \mathrm{ns}$. The associated optical spectrum is centred around 795 nm with a bandwidth of 10 nm. For amplification, they pass a Ti:sapphire crystal, in which the population inversion is created by optically pumping with an intra-cavity doubled, diode-pumped Nd:YLF laser (Spectra-Physics, Empower-30) operating at 527 nm.

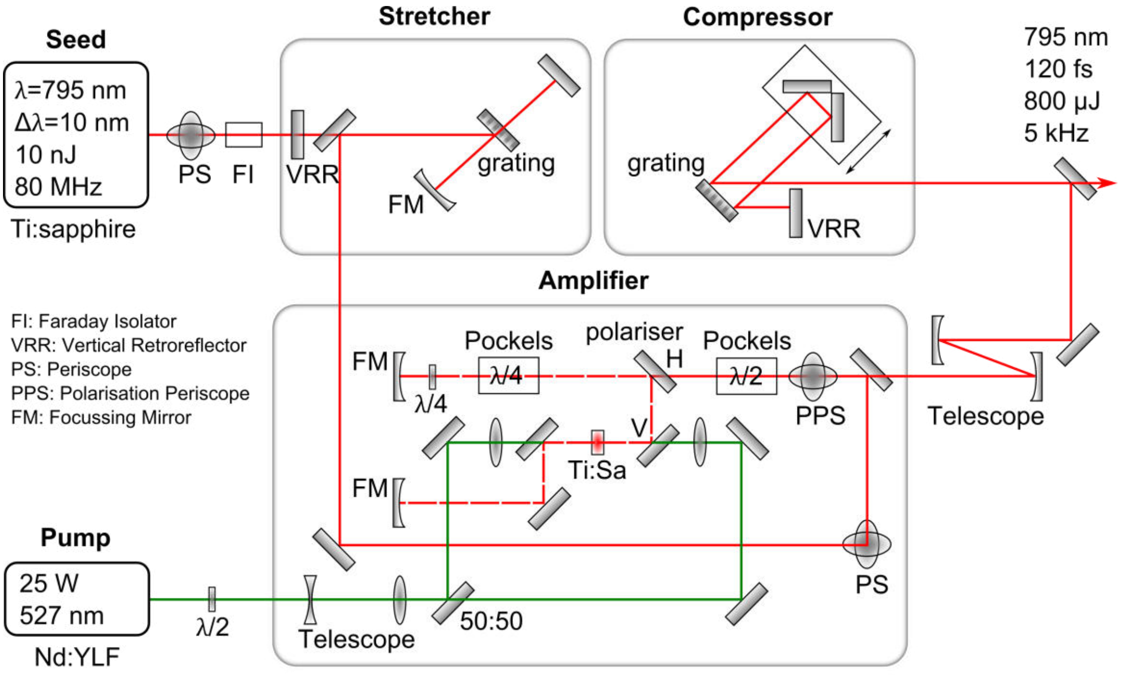
Seed
λ=795 nm
Δλ=10 nm
10 nJ
80 MHz
Ti:sapphire
PS
FI
VRR
Stretcher
grating
FM
Compressor
grating
VRR
795 nm
120 fs
800 µJ
5 kHz
Amplifier
FI: Faraday Isolator
VRR: Vertical Retroreflector
PS: Periscope
PPS: Polarisation Periscope
FM: Focussing Mirror
FM
Pockels
λ/4
λ/4
polariser
H
Pockels
λ/2
PPS
Telescope
V
Ti:Sa
FM
Pump
25 W
527 nm
Nd:YLF
λ/2
Telescope
50:50
PS

Figure 3.4: Regenerative Ti:sapphire amplifier (Spitfire Pro XP, Spectra Physics). The seed laser pulses are provided by a Ti:sapphire oscillator. The pump pulses originate from a Nd:YLF laser. In a chirped pulse amplification scheme described in the main text the seed laser pulses are stretched, amplified and recompressed.

The oscillator pulses to be amplified are selected by Pockels cells, which down-convert the repetition rate of the laser system from 80 MHz to 5 kHz. A first, extra-cavity Pockels cell turns the polarisation of the incoming pulses by 90°, such that the pulses are allowed to enter the amplifier cavity defined by two focussing mirrors (FM). In the amplifier cavity, a second, intra-cavity Pockels cell in combination with a $\lambda/4$ wave plate turns the polarisation again by 90° to vertical, such that the pulses are kept in the amplifier cavity. After several round trip times, the intra-cavity Pockels cell is switched off, such that the amplified pulses may now exit the amplifier cavity. The horizontally polarised output pulses are separated in height from the vertically polarised input pulses by a polarisation sensitive periscope (PPS).

To avoid damage to optical components the system employs the technique of chirped pulse amplification [88,89]. Before passing the amplifier medium the oscillator pulses are first stretched by a grating assembly. The amplified output pulses are recompressed in another grating assembly, as explained in the context of Section 3.1. Here, a movable horizontal retroreflector allows for fine tuning of the optical path length to ensure optimal compression of the output pulses. Overall, this system provides horizontally polarised pulses at a repetition rate of 5 kHz with a pulse energy of 0.8 mJ, a centre wavelength 795 nm and a pulse duration of around 120 fs, switchable to 30 fs. For pumping the NOPA system as shown in Section 3.3 their linear, horizontal polarisation is turned to vertical by a periscope, sketched in Figure 3.5. This is followed by a telescope, which reduces the beam diameter.

3.3. Non-collinear Optical Parametric Amplifier (NOPA)

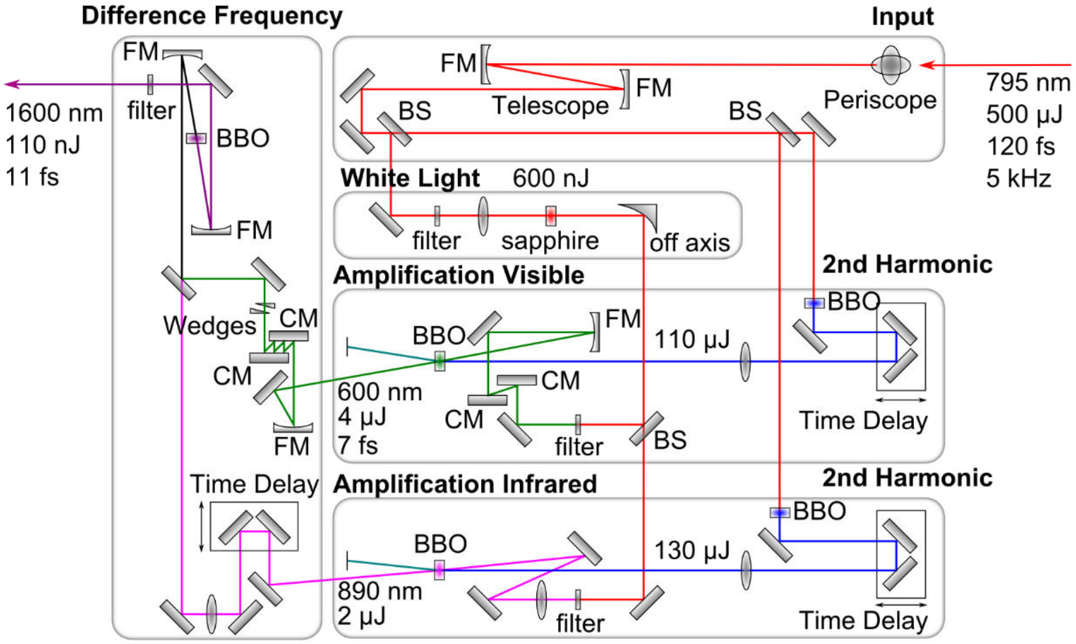
Difference Frequency
Input
FM
FM
FM
1600 nm
110 nJ
11 fs
filter
BBO
FM
BS
Telescope
BS
Periscope
795 nm
500 µJ
120 fs
5 kHz
White Light
600 nJ
filter
sapphire
off axis
Amplification Visible
2nd Harmonic
BBO
Wedges
CM
CM
FM
BBO
FM
110 µJ
600 nm
4 µJ
7 fs
CM
CM
filter
BS
Time Delay
Time Delay
Amplification Infrared
2nd Harmonic
BBO
BBO
130 µJ
890 nm
2 µJ
filter
Time Delay

Figure 3.5: Setup of the NOPA system for the generation of passively CEP stabilised two-cycle NIR laser pulses, as described in the main text. CM: Chirped Mirror. FM: Focussing Mirror. BS: Beam splitter.

As Ti:sapphire lasers are restricted in the wavelength range around 800 nm [85], this section will focus on the requirement of wavelength tuneability as outlined in the introduction to this chapter. In our laser system, this is achieved by further manipulating the output pulses from the regenerative Ti:sapphire amplifier introduced in Section 3.2

by the process of optical parametric generation [90,91] / amplification [96-99] and subsequent difference frequency generation [108,113]. The experimental setup is schematically sketched in Figure 3.5, whereas a more compact, but technically identical illustration may be found in [JR1]. The NOPA technique requires seed pulses, which are obtained by white light generation [92,93] for broadband wavelength tuneability, and pump pulses, obtained by frequency-doubling [91,120,121], to cover the visible spectral range in the amplification process.

This process is similar to optical parametric generation [90,91], in which an input beam of high-frequency ω_p, usually referred to as pump, in converted into two output beams of lower frequencies ω_s and ω_i, usually referred to as signal and idler. Usually, the output beam is weak, so in an experimental setup, the related technique of optical parametric amplification [96-99] is employed. Here, there are two input beams, the pump and the signal. The signal beam acts as a seed and is amplified at the expense of the pump beam.

White Light Generation (Seed)

In order to achieve broadband amplification, the signal beam to be amplified needs to cover a broad spectral range in the first place. This is achieved in the process of white light generation [92,93]. In this method, an ultrashort laser pulse is focussed into an optically transparent nonlinear medium such as sapphire or an optical fibre [94,95]. According to the optical Kerr effect [67] the refractive index of the optical medium depends on the laser intensity $I(t)$

$$n(t) = n_0 + n_2 I(t) \tag{3.8}$$

Here, n_0 is the linear and n_2 is the nonlinear refractive index. Consequently, self-focussing of the laser pulse sets in. This enforces other nonlinear processes such as optical shock wave formation and self-phase modulation [122-124]. As the refractive index now varies in the time-dependent electric field of the laser pulse, the phase of the laser pulse also becomes time-dependent:

$$\varphi(t) = \omega_0 t + kz = \omega_0 t + \frac{2\pi L}{\lambda_0} n(t) \tag{3.9}$$

Here, ω_0 is the centre angular frequency, λ_0 is the associated wavelength, k is the wave vector, z is the propagation distance and L is the length of the nonlinear medium. As the instantaneous frequency is related to a change in phase by $\omega(t) = \partial\varphi/\partial t$, this leads to the generation of new frequencies, with the lower frequencies generated at the front and the higher frequencies trailing the laser pulse. The polarisation of the incident laser pulses is preserved in this process.

In our setup, white light is generated by focussing a small fraction of the pulses from the regenerative Ti:sapphire amplifier, that is with a pulse energy of 600 nJ, into a 2-mm thick sapphire plate. This results in a white light spectrum, plotted in Figure 3.6, which extends from the blue to the infrared spectral range, where it is limited in this measurement due to the silicon (Si) detector of the spectrometer. The fundamental at 795 nm dominates the visible part of the white light spectrum by five orders of magnitude. Specifically, the spectral components of the white light are inhomogeneously distributed and peak around 500 nm.

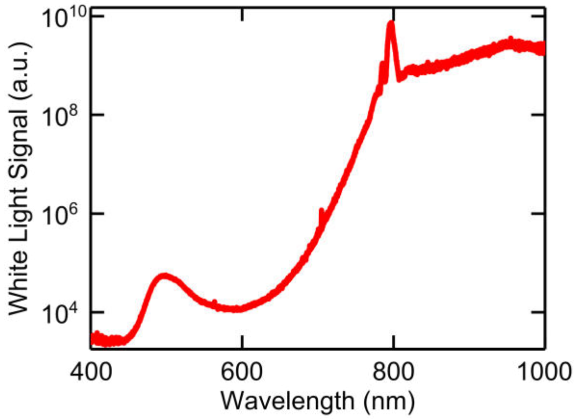

Figure 3.6: White light spectrum, corrected for the response of the Si detector of the spectrometer. The fundamental at 795 nm dominates the spectrum by several orders of magnitude. New spectral components appear in the visible and in the infrared. The detected wavelength range is limited by the spectral response of the Si detector.

Second Harmonic Generation (Pump)

Energy conversion implies that the seed pulses are amplified at the expense of a pump beam. Specifically, the photon energy and thereby the frequency of the signal beam cannot be higher than that of the pump beam. Consequently, to achieve optical parametric amplification in the visible spectral range, for example, from 500 nm to 750 nm, a pump with a shorter wavelength is required. This is supplied by frequency-doubling the pulses from the regenerative Ti:sapphire amplifier. This process of second harmonic generation is the non-linear response of an optical medium, which may be induced by a sufficiently strong electric field [91,120,121]:

$$\boldsymbol{P} = \epsilon_0\left(\chi_{(1)}\boldsymbol{E} + \chi_{(2)}\boldsymbol{E}^2 + \ \ldots\right) \tag{3.10}$$

This results in an additional electric field, which oscillates with twice the frequency of the fundamental electric field. In our setup, type I phase matching in a BBO crystal results in horizontally polarised pump pulses centred around ~400 nm derived from the vertically polarised pulses from the regenerative Ti:sapphire amplifier centred around ~800 nm. Second-harmonic generation is a special case of the more general sum-frequency generation (SFG) [91].

Optical Parametric Amplification

The next step is now to amplify the white light seed at the expense of the pump pulses by the technique of optical parametric amplification [96-99]. This process obeys energy and momentum conservation [96]:

$$\hbar\omega_p = \hbar\omega_s + \hbar\omega_i \tag{3.11}$$

$$\hbar k_p = \hbar k_s + \hbar k_i \tag{3.12}$$

The requirement of momentum conversion, Equation 3.12, is also known as the phase matching condition [91]. From a microscopic point of view, the individual atomic dipoles of the optical medium, through which the light propagates, then oscillate in phase, such that their individual contributions to the output wave from different locations add constructively in the direction of propagation resulting in a high conversion efficiency [91]. Moreover, group velocity mismatch [67] would prevent the interaction between light beams of different frequencies due to chromatic dispersion and thereby limits the interaction length in the optical medium.

The light beams therefore need to experience the same refractive index. This requirement is achieved by using a birefringent material such as beta-barium borate (BBO), in which the refractive index depends on the polarisation and the direction of the incident light [100,101]. BBO is a negative uniaxial crystal, with two ordinary axes and one extraordinary axis. Light propagating with its polarisation perpendicular to the optic axis will experience the ordinary refractive index n_o, while light propagating with its polarisation parallel to the optic axis will experience the extraordinary refractive index n_e. The attribute negative in case of BBO means that $n_e < n_o$. For type I phase matching the signal and the idler will have the same polarisation, whereas for type II phase matching they are orthogonally polarised [125]. For a particular type of phase matching the orientation of the crystal is then chosen, such that the phase matching condition is fulfilled. This technique is called angle tuning [91] or critical phase matching, as it depends critically on the phase matching angle.

Non-collinear Geometry

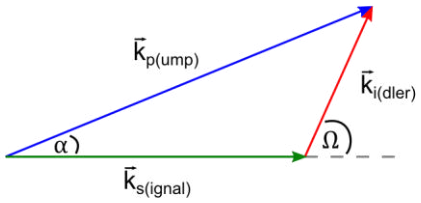

Figure 3.7: Definition of the angle α between the pump and the signal as well as the angle Ω between the signal and the idler wave vectors in the process of non-collinear optical parametric amplification.

In an optical parametric amplification process with a given pump wavelength the phase matching angle depends strongly on the signal wavelength [96]. Consequently, if the pump and signal beams propagate collinearly, optical parametric amplification only occurs over a narrow bandwidth, which would prevent the generation of ultrashort pulses from this process. However, if the angle between the signal and the pump beams is varied, the phase matching condition can be fulfilled over a much larger bandwidth [96,97,108]. The phase matching condition is a two-dimensional vector equation, schematically illustrated in Figure 3.7:

$$\vec{k}_p - \vec{k}_s - \vec{k}_i = 0 \tag{3.13}$$

Here, $\vec{k}$ is the wave vector of the pump (p), signal (s) and idler (i), respectively. The projection parallel and perpendicular to $\vec{k}_s$ gives [96]:

$$\Delta k_{\parallel} = k_p \cos\alpha - k_s - k_i \cos\Omega = 0 \tag{3.14}$$

and

$$\Delta k_{\perp} = k_p \sin\alpha - k_i \sin\Omega = 0 \tag{3.15}$$

Here, Ω is the angle between the signal and the idler and α is the angle between the signal and the pump wave vectors. These conditions are fulfilled, if [96]:

$$v_{gs} = v_{gi} \cos\Omega \tag{3.16}$$

That is, the group velocity of the idler v_{gi} along the signal direction must match the group velocity of the signal v_{gs}. It also implies $v_{gi} > v_{gs}$, which is satisfied in type I phase matching in negative uniaxial crystals such as BBO. Whereas the angle Ω is required for broadband phase matching, it is the angle α, which is adjusted in an experimental setup. It may be calculated according to [96]:

$$\alpha = \sin^{-1}\left(\sqrt{\frac{1-\left(v_{gs}/v_{gi}\right)^2}{1+2\left(v_{gs}/v_{gi}\right)(n_s^o\lambda_i/n_i^o\lambda_s)+(n_s^o\lambda_i/n_i^o\lambda_s)^2}}\right) \tag{3.17}$$

Here, λ_i is the idler wavelength, λ_s is the signal wavelength and n_i^o and n_s^o are the corresponding (ordinary) refractive indices.

In this non-collinear geometry, the phase matching angle θ depends on the signal wavelength λ_s and the internal non-collinear angle α between the pump and the signal beams as [126]:

$$\theta = \cos^{-1}\left(\sqrt{\left[\frac{\left(n_p^e/\lambda_p\right)^2}{Y}-1\right]\Bigg/\left[\frac{\left(n_p^e/\lambda_p\right)^2}{\left(n_p^o/\lambda_p\right)^2}-1\right]}\right) \tag{3.18}$$

with

$$Y = (n_s^o/\lambda_s)^2 + (n_i^o/\lambda_i)^2 + 2(n_s^o/\lambda_s)(n_i^o/\lambda_i)\cos(\alpha+\beta) \tag{3.19}$$

where

$$\beta = \sin^{-1}\left(\frac{n_s^o/\lambda_s}{n_i^o/\lambda_i}\sin\alpha\right) \tag{3.20}$$

is the angle between the idler beam and the pump beam at wavelength λ_p and n_p^o and n_p^e denote the corresponding ordinary (o) and extraordinary (e) refractive indices. The values for the refractive indices may be found in [100,101] and have been used here to calculate the phase matching angle given by Equation 3.18 as a function of signal wavelength, which is shown in Figure 3.8. For example, using a pump beam at $\lambda_p = 400\ \mathrm{nm}$ a non-collinear angle $\alpha = 3.7°$ (corresponding to an angle of 6.2° outside the BBO) gives broadband phase matching over a signal wavelength range from about 500 nm to 750 nm for a phase matching angle $\theta = 31.3°$ [96]. The non-collinear geometry results in an idler beam, which is angularly dispersed. In an experimental setup, femtosecond laser pulses sustained by broadband spectra tuneable over the visible range have been achieved [96,98,99,127], which by mixing with the output from a second NOPA stage translate into broadband spectra sustaining femtosecond NIR laser pulses by DFG [108,111,113].

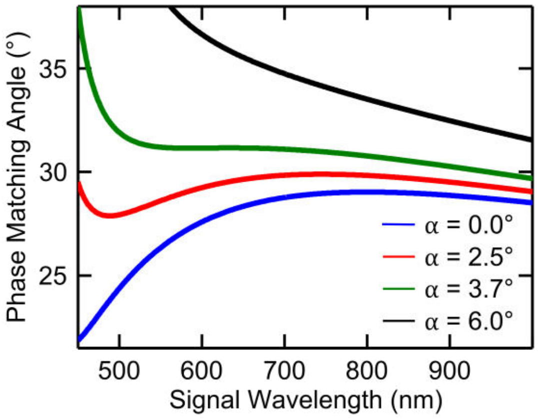

Figure 3.8: Phase matching angle as a function of signal wavelength for various non-collinear angles α given by Equation 3.18. Broadband phase matching in the visible spectral region is achieved for $\alpha = 3.7°$.

In our setup [JR1], broadband amplification of the seed pulses in the VIS spectral range according to the scheme above and narrowband amplification in the IR is performed in two NOPA stages. For this, the vertically polarised seed pulses in each stage are focussed into a BBO crystal at a non-collinear angle as explained above to the horizontally polarised pump pulses, with which they are spatially and temporally overlapped. Specifically, the beam diameters of the seed and pump pulses inside the BBO crystal are 320 µm and 650 µm, respectively. Whereas the seed pulses have a pulse energy of few nJ each, the pump pulses are provided with a pulse energy of 110 µJ in the VIS stage and 130 µJ in the IR stage.

In the VIS stage a coloured glass filter (2 mm of BG39, Schott) suppresses the driving pulses from the regenerative Ti:sapphire amplifier otherwise dominating the seed as shown in Figure 3.6 and allows for amplification over a wide tuning range from 475 nm to 675 nm [JR1], as displayed in Figure 3.9a. Typically, the NOPA system is operated with the spectrum from the VIS stage centred around 600 nm with a ~100-nm bandwidth (FWHM), which sustains a pulse duration down to 7 fs and was as part of this thesis further measured in situ as 9 fs by an electron autocorrelation shown in Chapter 10. The corresponding pulse energy is 4 µJ. In the IR stage a bandpass filter (FB890-10, Thorlabs) limits the spectrum to a centre wavelength of 890 nm. Here, the pulse energy is 2 µJ.

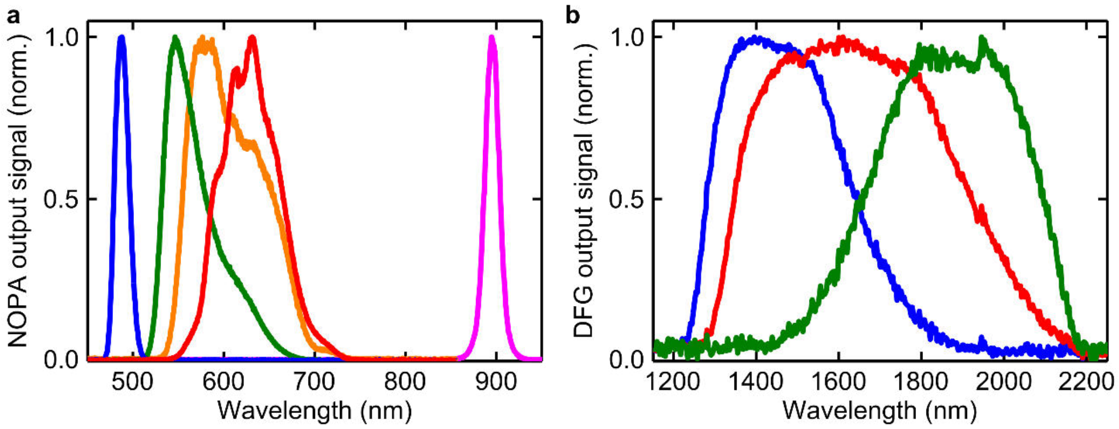

Figure 3.9: (a) Spectra obtained from the VIS stage of the NOPA system are widely tuneable between $\lambda = 475\ \mathrm{nm}$ and $\lambda = 675\ \mathrm{nm}$ by changing the time delay between seed and pump pulses. The spectrum of the IR stage is centred at $\lambda = 890\ \mathrm{nm}$. Modified from [JR1]. (b) Spectra obtained from the DFG stage are widely tuneable between $\lambda = 1200\ \mathrm{nm}$ and $\lambda = 2100\ \mathrm{nm}$. The detected wavelength range is limited by the spectral response of the InGaAs detector.

The output signals of the two NOPA stages are then spatially and temporally overlapped in a BBO crystal to facilitate DFG. Here, the broad spectral bandwidth and the wide tuneability of the spectra from the VIS stage directly translates into broad NIR spectra tuneable between 1200 nm and 2100 nm [JR1], as displayed in Figure 3.9b. Typically, the NOPA system is operated with the spectrum from the DFG stage centred around 1600 nm with a ~500-nm bandwidth (FWHM), which sustains nearly Fourier-limited 10.6-fs laser pulses shown in Section 3.1. The pulse energy of the corresponding output pulses is 110 nJ. Their generation involves the propagation through dispersive optical components, which requires dispersion management, as explained in Section 3.1. In our NOPA system, this is realised after the VIS stage with 3 bounces between a pair of chirped mirrors (DCM9, Venteon) followed by fused silica wedges for dispersion fine tuning. In a comparable NOPA system [113] operated at a higher repetition rate of 100 kHz, a prism compressor in the VIS stage ensures dispersion management. Similar to our NOPA system, ~10-fs pulses centred around ~1800 nm are achieved by DFG with a pulse energy of ~100 nJ.

3.4. Passive Carrier Envelope Phase (CEP) Stabilisation

An important consequence arising from mixing the output from two NOPA stages in order to generate their difference frequency is the passive stabilisation of the carrier-envelope phase (CEP) of the resulting ultrashort laser pulses [108]. To understand this concept, let us first illustrate the CEP with the help of a simple description of an ultrashort laser pulse by a sinusoidal wave, multiplied by a temporal envelope function $A(t)$. Assuming linear polarisation, the electric field strength as a function of time is given by:

$$E(t) = A(t)\cos(\omega_0 t + \varphi_{CE}) \tag{3.21}$$

Here, φ_{CE} is the CEP, $\omega_0 = 2\pi c/\lambda_0$ is the centre carrier angular frequency, c is the speed of light and λ_0 is the centre wavelength. Assuming a Gaussian envelope gives:

$$E(t) = E_0\cos(\omega_0 t + \varphi_{CE})e^{-2\ln 2(t/\tau_{FWHM})^2} \tag{3.22}$$

Here, E_0 is the peak electric field strength and τ_{FWHM} is the pulse duration, defined as the intensity FWHM. To illustrate the CEP, an example of an ultrashort laser pulse with $\tau_{FWHM} = 10\ \text{fs}$ and $\lambda_0 = 1600\ \text{nm}$ is plotted in Figure 3.10 for two different settings of the CEP, $\varphi_{CE} = 0$ and $\varphi_{CE} = \pi$.

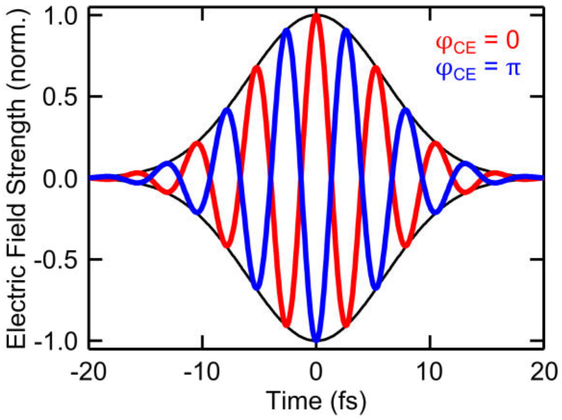

Figure 3.10: The envelope (black curve) and the carrier electric field of a few-cycle laser pulse, centred at $\lambda = 1600\ \text{nm}$ and with a pulse duration $\tau_{FWHM} = 10\ \text{fs}$, is shown for a CEP $\varphi_{CE} = 0$ (red) and $\varphi_{CE} = \pi$ (blue).

In general, the CEP of a laser system is not stabilised. An instability of the CEP arises, because the envelope of an ultrashort laser pulse travels at the group velocity [67,115]:

$$v_g = \frac{\partial\omega}{\partial k} = \frac{c}{n(\omega)} - \frac{ck}{n(\omega)^2}\frac{dn}{dk} \tag{3.23}$$

Here, k is the angular wavenumber and n is the refractive index. However, each spectral component of the wave packet defining an ultrashort laser pulse travels at its phase velocity [67,115]:

$$v_p = \frac{\omega}{k} = \frac{c}{n(\omega)} \tag{3.24}$$

These relationships imply, that the group velocity is only equal to the phase velocity, if $dn/dk = 0$, i.e. for a constant refractive index corresponding to a non-dispersive medium. Thus, letting an ultrashort laser pulse propagate through a dispersive medium, such as glass or even air, will influence the offset between the carriers travelling at the phase velocity and the envelope travelling at the group velocity, i.e. the CEP illustrated in Figure 3.10.

However, to study CEP dependent processes such as switching a current in a dielectric [24], steering the motion of electrons in the vicinity of a metallic nanotip [38], above-threshold ionisation [81] or high harmonic generation [128], a scheme of CEP stabilisation is required. This may be done actively [104-107], which requires a built-in feedback loop powered by electronics, or passively in an all-optical scheme [108-114], which was chosen here.

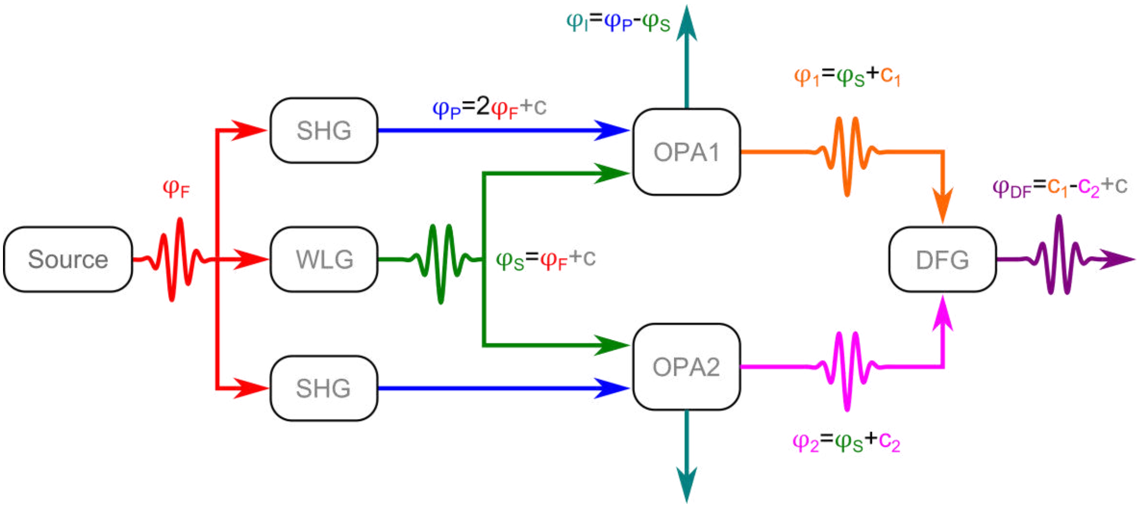

Figure 3.11: Passive CEP stabilisation scheme. The CEP fluctuations of an unstabilised source are inherited by the processes of white light generation (WLG) and optical parametric amplification (OPA). They cancel out in the process of difference frequency generation (DFG).

The scheme of passive CEP stabilisation, sketched in Figure 3.11, is the following [108]. Let us assume an initial source with a fluctuating CEP φ_F. The white light generation process inherits the CEP of the driving pulses apart from a constant phase shift and an additional phase shift due to propagation. For the seed, this gives a CEP $\varphi_s = \varphi_F - \pi/2 + c_{WL}$, which it carries on after amplification apart from a further phase shift due to propagation, i.e. $\varphi_1 = \varphi_s + c_1$. The CEP of the idler is coupled to the phase of the pump via $\varphi_i = \varphi_p - \varphi_s - \pi/2 + c_1$. Combining both NOPA stages the shot-to-shot fluctuations from the driving laser pulses cancel out in theory. In particular, the CEP is given by $\varphi_{DF} = c_1 - c_2 - \pi/2 + c_{DF}$. Experimentally, it will depend on phase shifts, which result, for example, from propagation of the two laser pulses in the separate NOPA stages. This is influenced by the refractive index of the medium, through which the laser pulses propagate. For example, this medium may be air. Its refractive index depends on fluctuations in temperature and pressure, which contribute to the instability of the CEP.

Measurement of the CEP Stability

Having devised a scheme to passively stabilise the CEP, the next step is now to confirm its performance experimentally. A tool for measuring the CEP stability is a common-path f-to-2f interferometer [129], schematically sketched in Figure 3.12 in its realisation as part of this thesis. Here, the NIR output pulses from the DFG stage of our NOPA system are focussed by an off-axis parabolic mirror into a combination of an 8-mm thick yttrium aluminium garnet (YAG) crystal followed by a 100-µm thin BBO crystal, which are mounted as close as possible to each other. In the YAG crystal the NIR laser pulses are first spectrally broadened in the process of white light generation [92,123] preserving their horizontal polarisation. Next, their second harmonic is generated in the BBO crystal, which will be polarised vertically [91]. A polariser is then used to balance both pulses in intensity. The interference pattern of the spatially overlapped pulses is finally recorded by a spectrometer equipped with a nitrogen-cooled charge-coupled device (CCD) camera.

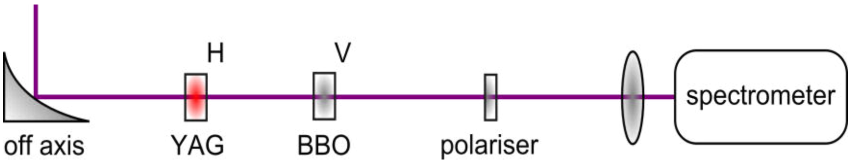

Figure 3.12: Common-path f-to-2f interferometer. The output pulses from the NOPA system are focussed into a YAG crystal for white light generation and a BBO crystal for second harmonic generation. A polariser balances both pulses in intensity, before their interferogram is recorded with a spectrometer.

On the detector, an interference pattern is observed, which is given by [108]:

$$I(\omega) = I_{WL}(\omega) + I_{SH}(\omega) + 2\sqrt{I_{WL}(\omega) + I_{SH}(\omega)} * cos(\omega\Delta\tau + \varphi_{CE}) \tag{3.25}$$

Here, I_{WL} is the intensity of the white light generated in the YAG crystal, I_{SH} is the intensity of the second harmonic generated in the BBO, $\Delta\tau$ is the time delay between them and φ_{CE} is the CEP, which does not drop out because the spectrally broadened fundamental NIR pulses and their second harmonic are overlapped.

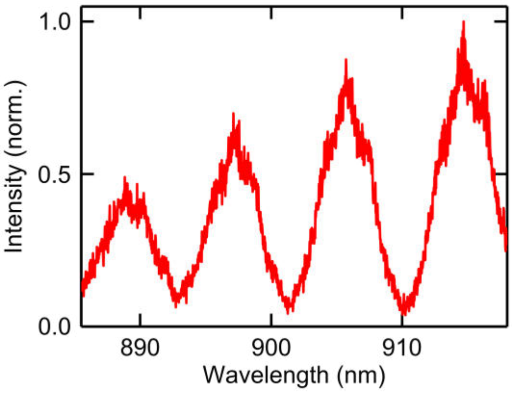

Figure 3.13: Interference fringes resulting from the interference of the spectrally broadened fundamental NIR pulses and their second harmonic, here recorded for an integration time of 100 ms. The position of the peaks is analysed to deduce the CEP instability, as described in the main text.

A typical interferogram, recorded at an integration time of 100 ms, is shown in Figure 3.13. It can be seen from Equation 3.25, that the sinusoidal pattern and thereby the interference maxima will move, if the CEP changes [108]. In particular, for a CEP shift of $\Delta\varphi_{CE} = 2\pi$ the interference maxima would move by one period, whereas for a stable CEP, i.e. $\Delta\varphi_{CE} = 0$, they would not move. To extract information on the CEP instability the positions of the interference maxima are recorded for each consecutive measurement. Their standard deviation divided by the period of the interference fringes and multiplied with 2π then gives a measure of the CEP instability. Alternatively, the CEP instability can be extracted by taking a Fourier transform [108].

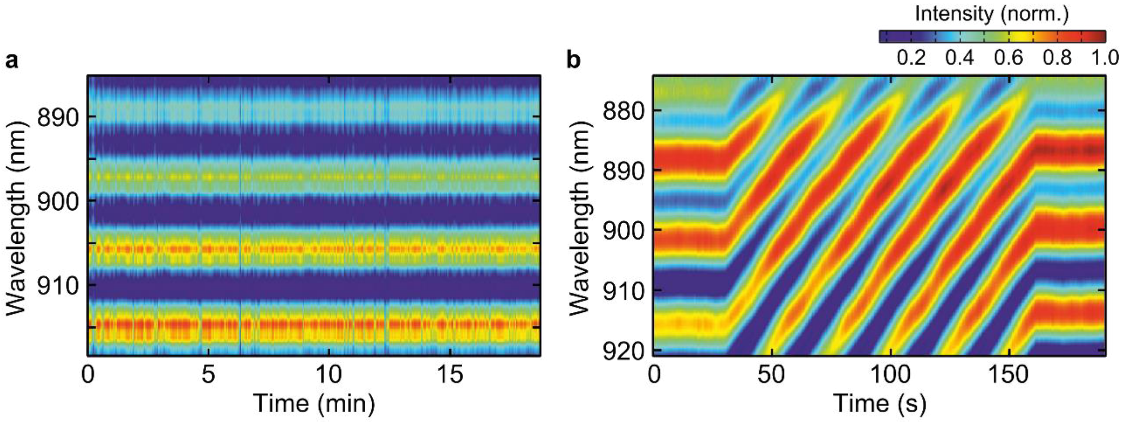

Figure 3.14: (a) Interference fringes recorded by spectral f-to-2f interferometry over a time interval of 18 minutes and averaging over 100 pulses. From this measurement a CEP instability of ~50 mrad was extracted. (b) Control of the CEP over a range of 10π is achieved by inserting dispersive material. Modified from [JR1].

The interference fringes corresponding to a measurement over a long-term interval of 18 minutes and averaging over 100 pulses are displayed in Figure 3.14a. From this measurement a residual CEP instability of ~50 mrad was extracted. Furthermore, controllable adjustment of the CEP over a range of 10π was demonstrated as displayed in Figure 3.14b by inserting dispersive material in the form of fused silica wedges. This measurement constitutes an improvement of a previously obtained CEP instability of 66 mrad averaging over 1000 pulses [38] from this laser system and compares favourably to a passive CEP instability of 79 mrad averaging over 100 pulses obtained from a similar system over a short-term interval of 0.5 s [113].

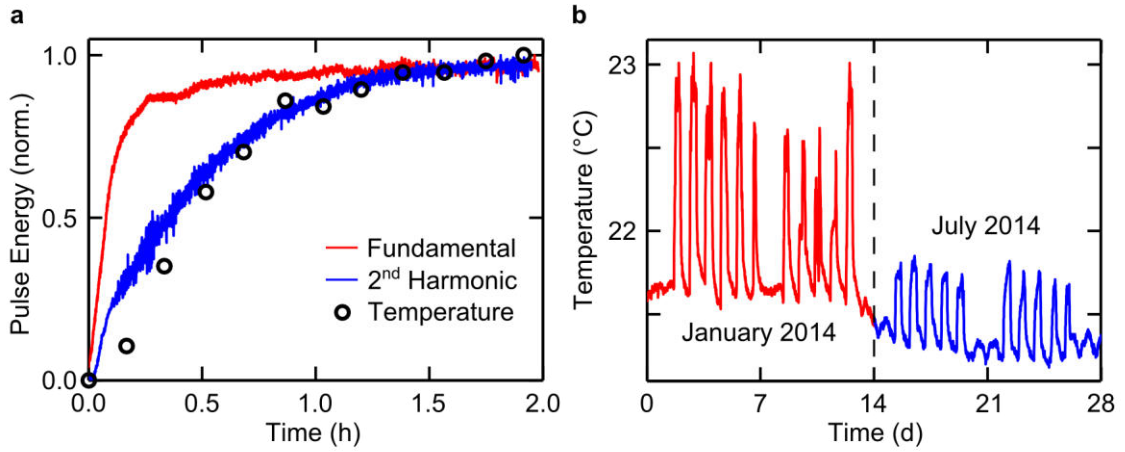

Figure 3.15: Temperature management. (a) After switching on the laser system the pulse energy of the fundamental (red) has reached its maximum after about 15 minutes, whereas the pulse energy of the second harmonic (blue) follows the temperature (black circles) in the laboratory. (b) Removing the chillers from the laboratory resulted in a decrease of the temperature fluctuations from 1.5 °C (red) to only 0.5 °C (blue).

The excellent performance shown here is primarily attributed to an improvement of the temperature management in the laboratory as implemented as part of this thesis. For this, a designated housing was built around the NOPA system to decouple it from the surroundings. Furthermore, correlations between the CEP instability and the second harmonic generation process in the NOPA system were found, which were traced back to an instability of the duration of the driving pulses originating from the regenerative Ti:sapphire amplifier Spectra-Physics Spitfire Pro XP described in Section 3.2. Hence, heat shields were introduced into the regenerative Ti:sapphire amplifier to enclose the stretcher and compressor units, sketched in Figure 3.4. This corresponds to an upgrade to the Spectra-Physics Spitfire Ace configuration and reduced the instability in the duration of the driving pulses from 2.6 fs RMS to 1.3 fs and thereby the correlation with the CEP instability [JR1]. Additionally, as can be seen in Figure 3.15a, the second harmonic generation efficiency follows the increase in room temperature by switching on the laser system. Therefore, the chillers were moved into a separate room outside the laboratory. As can be seen from Figure 3.15b this measure reduced the temperature fluctuations in the laboratory. Specifically, switching on the laser system now results in an increase in temperature of only 0.5 °C, as compared to a previous variation of 1.5 °C. This improved temperature performance is achieved even in the summer months, when the climate conditioning unit has to cope with higher temperatures outside.

Importantly, a further advancement in the characterisation of the passive CEP stabilisation scheme was made in this thesis by a shot-to-shot measurement. So far, measurements of the CEP stability from this [38] and a comparable [113] system have only been performed by averaging over pulses. However, if one would like to put a reported CEP stability into context with other measurements, the effect of averaging over pulses needs to be taken into account. It arises from the law of large numbers, which implies that the average of a large number of trials will tend to the expectation value. Here, the CEP is as likely to vary in one direction as in the other, so that this expectation value would be zero. Hence, by averaging over pulses the reported CEP stability will seemingly improve. Experimentally, this was shown in a stereo above-threshold ionisation measurement capable of deducing the CEP shot-to-shot [130]. This is an important observation, because in an experiment any CEP-dependent response of a sample will necessarily occur for each single laser pulse. Therefore, a shot-to-shot measurement of the CEP stability, as achieved as part of this thesis, constitutes a significant experimental progress in the characterisation of the passive CEP stabilisation scheme.

A shot-to-shot measurement will necessarily be limited by the acquisition speed of the detector. In our setup, the interference fringes are captured with a nitrogen-cooled charge-coupled device (CCD) camera (Princeton Instruments Pro EM512B-EX), which due to its electron-multiplying technology is particularly suitable for low-light applications. To acquire the CEP stability shot-to-shot, the time required for its read out process must be shorter than the time interval between two pulses. Experimentally, such a shot-to-shot measurement as shown in Figure 3.16 was achieved by reducing the read out time to 0.9771 ms and setting its shutter time to 10 µs. Operating the NOPA system at a repetition rate of $f_{rep} = 1\,\mathrm{kHz}$ corresponding to a time delay between consecutive pulses of $T = 1/f_{rep} = 1\,\mathrm{ms}$, optimising the processes of white light generation and second-harmonic generation in the f-to-2f interferometer as well as their spatial overlap for a measurable signal then allowed single-shot acquisition of the interference fringes. In particular, the detector recorded 15000 photons per pulse, such that shot-noise induced phase jitter only amounted up to ~10 mrad [131].

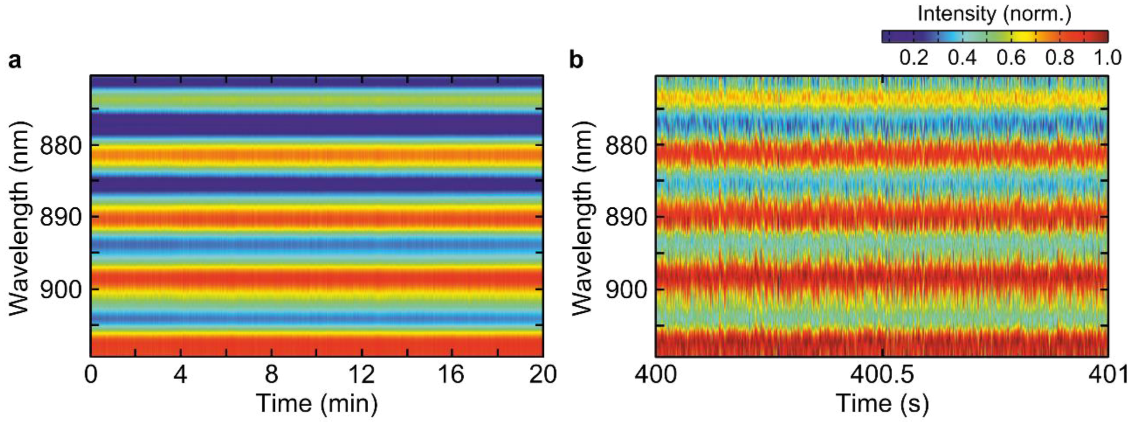

Figure 3.16: (a) Interference fringes recorded shot-to-shot by spectral f-to-2f interferometry over a time interval of 20 minutes. From this measurement a CEP instability of ~800 mrad was extracted (b) A zoom into a time interval of 1 s reveals the fluctuations between adjacent single spectra. Modified from [JR1].

The interference fringes corresponding to a shot-to-shot measurement over a long-term interval of 20 minutes are shown column by column in Figure 3.16a. In particular, a residual shot-to-shot CEP instability of ~800 mrad was extracted, which agrees with an indirect approach via the visibility of the interference pattern [JR1]. Looking into a shorter time interval of 1 s as displayed in Figure 3.16b the residual fluctuations of the CEP between adjacent spectra are revealed. Such fluctuations would average out by capturing a larger number of pulses with the CCD camera, as shown in Figure 3.17 below. Overall, the measured shot-to-shot CEP instability compares favourably to previously reported results of ~2.5 rad from a system operating at 100 Hz [129] and ~1 rad from a system operating at 1 kHz [132].

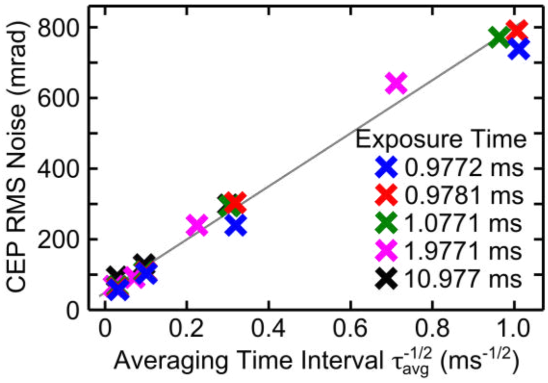

Figure 3.17: The residual CEP instability is plotted as a function of spectrometer exposure time. The two outermost right data points mark measurements of the shot-to-shot CEP instability. The grey line serves as a guide to the eye. Modified from [JR1].

To further demonstrate the effect of averaging on the measured CEP instability, the interference fringes were recorded for different exposure times of the spectrometer in the range from <1 ms to 11 ms. From these measurements the CEP instability was extracted as before, which is plotted in Figure 3.17 as the outermost right data point for each exposure time. In addition, the data was post-processed to simulate the averaging over pulses, which gives the other data points for each exposure time. For example, averaging over 100 spectra obtained in a shot-to-shot measurement, which had led to a shot-to-shot CEP instability of ~800 mrad, gives a result similar to the measured CEP instability of ~50 mrad with the spectrometer exposure time set to 100 ms corresponding to averaging over 100 pulses. Overall, the value for the reported CEP instability reduces with the square root of the number of averaged pulses, which is in agreement with the expectation from the law of large numbers.

4. Metallic Nanotips

A particularly intriguing application of the femtosecond laser pulses discussed in Chapter 3 arises from their combination with a metallic nanotip, rendering it a nano-localised source of electrons for ultrafast electron microscopy [28-30].

An electron microscope is a powerful tool to obtain structural information with a resolution below an optical microscope owing to the shorter de Broglie wavelength of an electron as compared to the wavelength of a photon in the visible spectral range. It was developed in the 1930s [133] and nowadays achieves an atomic resolution below 50 pm [134,135]. Common modes of operation are thermionic emission, that is by heating a thin metallic filament, or field emission, i.e. by applying a DC bias voltage to a sharp metallic nanotip. In both cases a continuous beam of electrons is emitted, which is collimated and focussed onto a sample by the use of electrostatic lenses. However, both techniques lack the dimension of time, such that functional information on the sample remains unresolved.

To realise ultrafast electron microscopy or diffraction a pulsed electron source is required [136,137]. Triggering the release of an electron wave packet from a photocathode with femtosecond optical pulses has allowed for ultrafast electron diffraction with a sub-picosecond time resolution [136,138-140]. This technique has been further miniaturised and improved to a time resolution of ~300 fs [31]. Here, an ultra-bright electron source provided sufficient structural sensitivity to observe the non-reversible process of non-thermal melting of aluminium, while the ultrafast electron pulses allowed taking snapshots before the onset of blurring due to diffusive motion. Recently, the phase transition of the molecular crystal $Me_4P[Pt(dmit)^2]^2$ from an electrical insulator to a metal under illumination with light could be attributed to a rearrangement of individual atoms on a femtosecond time scale [32]. So far, electron pulses with a duration of ~100 fs have been experimentally demonstrated [141].

However, electron pulses generated by these techniques suffer from two major drawbacks. First, electrons are emitted from a broad area given by the µm-sized focal spot of the illuminating light source [136]. Second, Coulomb repulsion leads to broadening of electron bunches [142]. This may be overcome by going to the single electron pulse regime [143-145] or sophisticated electron pulse compression schemes possibly promising attosecond electron pulses [146-148].

To improve the temporal resolution and the spatial coherence of the electron wave packet, an alternative compact ultrafast electron source is provided by a sharp metallic nanotip. This is a thin wire conically converging down to an apex radius of curvature of few nanometres. The high density of electric field at its apex gives rise to a strong enhancement of an incident electric field [26,27], such that electron emission is localised to the nanometre-sized apex region. In particular, illuminating the apex of a sharp metallic nanotip with ultrashort laser pulses from a femtosecond laser system as presented in Chapter 3 enables the release of an electron wave packet in an ultrashort interval of time from its nanometre-sized apex region [28-30]. For example, by combining laser-triggered electron emission from a metallic nanotip with a point projection electron microscopy setup [33-35], a time resolution of ~100 fs has been shown [34]. In fact, as also suggested in this thesis [JR5], the duration of an electron pulse may even be confined to an attosecond time window [29,40,149].

To understand laser-triggered emission of electrons from a metallic nanotip, the process of photoemission needs to be elucidated in more depth. Specifically, it is subdivided into different regimes. Its first observation was the well-known photoelectric effect [18], which was generalised from a single- to a multiphoton picture [150,151] after the advent of the laser [152,153]. In particular, exposing atomic systems to an increasingly stronger laser intensity, the description of the photoemission of electrons in the perturbative multiphoton picture broke down and a much richer electron dynamics was revealed. In reaching the non-perturbative strong-field regime control over the electron motion gave access to concepts such as above-threshold ionisation (ATI) [5-7,81,154] and high harmonic generation (HHG) [8,9,155,156] providing the foundation of modern attosecond science [1,2]. Specifically, this led to the generation of attosecond optical pulses [12,13], which are accompanied by attosecond electron pulses [10]. An increasing number of experiments exists to transfer the concept of HHG to solids [19,20,22,23], whereas ATI on solid surfaces has been limited to low photon orders [157-163], possibly due to low damage thresholds. This limitation is naturally overcome by the use of sharp metallic nanotips owing to their property of field enhancement [26,27]. Consequently, first evidence of strong-field phenomena at solid state nanostructures was obtained [36-40], starting to bridge a gap between the concepts of atomic and solid state physics. Moreover, in contrast to bulk materials metallic nanotips further provide directivity, as electron emission does not occur from an area defined by the focal spot of the illuminating laser pulse, but is confined to a single, well-defined point in space, i.e. the nanometre-sized apex. Metallic nanotips have therefore emerged not only as candidates for ultrafast electron microscopy [28-30,34,149,164,165], but also as model systems to study strong-field phenomena at the nanoscale [36-40,166-168].

This chapter will introduce the properties of metallic nanotips and relevant experimental observations. In the first sections the fabrication and properties of metallic nanotips will provide a background for the different regimes of electron emission discussed in the following sections. This chapter will conclude with key experimental observations, part of which require concepts from atomic physics, to be further discussed in Chapter 5.

4.1. Fabrication and Properties

In the experiments presented in this thesis the photoemission of electrons from gold nanotips is investigated. To meet their advanced specifications such as sharpness and a clean and smooth surface they are fabricated in a dedicated home-built electrochemical etching setup, which is outlined in the following.

Electrochemical Etching

The starting point of this process is a 125-μm thin gold wire. It is commercially available (Advent Research Materials) in a polycrystalline form, which would result in an inhomogeneous surface structure. Therefore, the gold wire is annealed to render it monocrystalline. For this procedure, the gold wire is cut into small pieces of approximately ~10-cm length, which are put into a ceramic boat. The ceramic boat is placed into an oven, where it is surrounded by a glass tube filled with a constant flow of argon. The gold wires are then heated over eight hours to a temperature of 800°C, kept at this temperature for eight hours and cooled down to room temperature for eight hours.

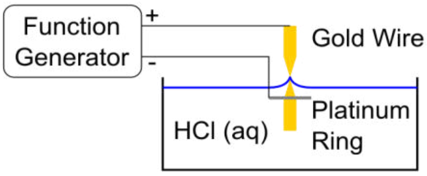

Figure 4.1: Etching setup (not to scale). Voltage pulses are applied between a platinum ring and a gold wire, immersed in hydrochloric acid (HCl (aq)). A meniscus travels down the wire, resulting in its progressive sharpening.

The gold wire is then electrochemically etched in 37% concentrated grade hydrochloric acid. This is the solution of hydrogen chloride in water, in which positively charged hydronium ions and negatively charged chloride ions form:

$$HCl + H_2O \longrightarrow H_3O^+ + Cl^-$$

As shown in Figure 4.1, the gold wire serves as one electrode and a platinum ring is the second electrode. The platinum ring resides just below the surface of the hydrochloric acid. The gold wire is then centred in the middle of the platinum ring and immersed perpendicularly to the surface plane into the hydrochloric acid by a length of ~500 µm. Rectangular voltages pulses with a frequency of $3\ \mathrm{kHz}$, a peak-to-peak voltage $V_{pp} = 7.5\ \mathrm{V}$, a DC offset of $-250\ \mathrm{mV}$ and a duty cycle of 10% are then applied to the electrodes. This results in the following chemical reactions between the gold wire and the hydrochloric acid:

$$Au + 4Cl^- \longrightarrow AuCl_4{}^- + 3e^-$$

$$Au + 2Cl^- \longrightarrow AuCl_2{}^- + 1e^-$$

In effect, gold from the wire is transformed into the chloroaurate anions $AuCl_2{}^-$ and $AuCl_4{}^-$. To keep up the etching reaction, the consumed Cl^- ions need to be resupplied to the etching region. This is achieved by setting the duty cycle to 10% and may be additionally supported by stirring. By immersion of the gold wire into the hydrochloric acid a meniscus forms due to the surface tension. In each etching cycle this meniscus moves further down the wire and gets narrower, until the lower part of the wire drops offs. This process is monitored on a camera. The upper part of the wire should now be well above the surface of the hydrochloric acid. Furthermore, the drop-off should be abrupt, and the etching process should not have taken longer than ~20 s in total. These conditions increase the chance of having a tip with a small radius of curvature.

Characterisation in a Scanning Electron Microscope

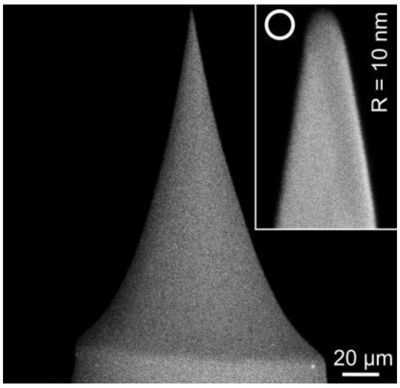

Figure 4.2: Scanning electron microscopy image of a gold nanotip. The annealing and etching process results in a smooth and conical surface. The magnification of the apex region reveals a radius of curvature $R = 10\ \mathrm{nm}$ and a (full) opening angle $\theta = 20°$.

To select sharp and clean tips to be used in an experiment they are inspected under a scanning electron microscope (SEM). In this device, a primary beam of electrons ejects secondary electrons from the sample, which are sensitive to its topography. Depending on the angle of incidence, a different number of secondary electrons may be emitted, such that steep surfaces appear brighter. Furthermore, insulating material such as oxides will be positively charged resulting in less emitted secondary electrons and will therefore appear darker. To prevent damage to the nanotips the brightness of the electron beam is set to a low value of 11 pA and a moderate acceleration voltage of 10 kV. Furthermore, the nanotips are illuminated as short as possible, typically with an integration time of 100 ns, especially in high magnification operation, in which there is a high density of electrons in the imaged region of the nanotip. Figure 4.2 shows a SEM image of a tip typically used in an experiment. It has a radius of curvature $R = 10\ \mathrm{nm}$, a (full) opening angle $\theta = 20°$ and is characterised by a clean and smooth conical surface.

Field Enhancement

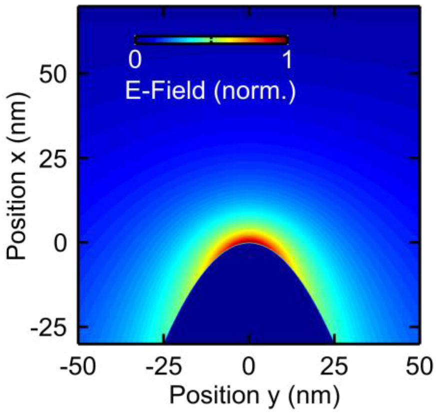

Figure 4.3: Field enhancement. Illuminating a metallic nanotip with light polarised along its axis, here along the x-direction, results in a strongly enhanced field at the apex, which was calculated according to [27]. The nanotip is modelled as a hyperboloid with the parameters deduced from the SEM image in Figure 4.2.

The geometry of the nanotip results in an enhancement of an electric field at its apex due to the quasi-static lightning rod effect [26]. The apex approaches a singularity, which is finite for a real tip and results in an increased density of electric field lines. In case of an external static electric field, the highly localised density of surface charge at the apex is responsible for the emission of electrons [82]. In case of an optical excitation, assuming the light field to be polarised along the tip axis, the field enhancement may be calculated in a quasi-static approximation [27]. Here, as shown in Figure 4.3, the nanotip is modelled as a hyperboloid, with the parameters chosen to match the geometry of a gold nanotip as deduced from the SEM image in Figure 4.2, and assumed to be illuminated with near-infrared light (NIR) around 1600 nm.

The enhanced electric field is spatially inhomogeneous. Outside the nanotip, it decays exponentially on a length scale roughly given by the apex radius of curvature. Inside the bulk material, the electric field switches sign [169] and its field strength is reduced. Explicitly, for illumination with the NIR laser pulses presented in Chapter 3, the electric field inside the nanotip becomes negligible, as may be inferred from the large and negative real part of the dielectric function of gold, i.e. $\varepsilon_{Au}(1600\ \mathrm{nm}) = -120 + 12i$.

Furthermore, the field enhancement depends on the material. For example, a field enhancement factor $f = 9$ is observed for a gold nanotip [38], whereas for a tungsten nanotip only a reduced value $f = 5$ is reported [40]. The higher field enhancement for the plasmonic material gold with its negative real part of the dielectric function arises from the surface plasmon mode localised to the apex of the nanotip [170]. Hence, gold nanotips are favourable for the strong-field experiments presented in this thesis, because a low incident electric field may be enhanced to a stronger effective electric field as compared to tungsten. This outweighs concerns about possible damage due to heating of the nanotip as a consequence of the deposited laser energy, considering the lower melting point of gold (1300 K) as compared to tungsten (3700 K). Furthermore, as the field enhancement in the quasi-static approximation depends on the conductivity of the material, it increases towards the infrared spectral region [27,82,171], in which gold hardly absorbs any light. However, an intense laser field will still excite the electron gas, which transfers energy via electron-phonon scattering to the lattice eventually causing the nanotip to disintegrate [172-175].

In contrast, the field enhancement and localisation to the apex are suppressed in the visible (VIS) spectral region due to interband absorption in gold [176]. This is also indicated by investigating typical gold nanotips used in our experiments by electron energy-loss spectroscopy (EELS) performed by our colleagues from the group of Professor Peter van Aken [177], in which the coupling of electrons to the optical modes of the nanotip is probed. In particular, above energies of 2 eV corresponding to the VIS spectral region the EELS signal is spatially homogeneous, whereas for energies of 0.75 eV corresponding to the NIR spectral region a spatially well-localised EELS signal is measured.

4.2. DC Field Emission

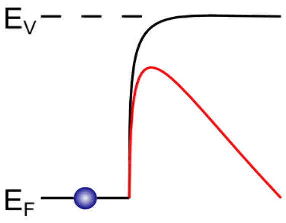

Figure 4.4: DC field emission. To leave a metallic nanotip electrons need to overcome the energy difference between the Fermi level E_F and the vacuum level E_V. The potential barrier (black curve) is bent down by a static electric field. Electrons may tunnel through the lowered potential barrier (red curve).

Due to the high density of electric field lines at the apex of a metallic nanotip with a radius of curvature R the extraction of electrons can be facilitated by applying a bias potential U_{DC}, which leads to a local electric field strength [178]:

$$E_0 = \frac{U_{DC}}{kR} \tag{4.1}$$

Here, $k \approx 5$ is a geometrical factor, which accounts for the geometry of the emitter and the anode, for example, resulting in a shielding of the electric field due to the tip shank [39,178]. Due to the presence of a strong electric field the potential barrier sketched in Figure 4.4 is bent down, such that electrons will begin to tunnel out from their continuous Fermi-Dirac distribution [179] of states with energy E given by:

$$F(E) = \left(e^{(E-E_F)/k_B T} + 1\right)^{-1} \tag{4.2}$$

Here, E_F is the Fermi level, k_B denotes Boltzmann's constant and T is the temperature of the electron gas. At $T = 0\,\mathrm{K}$, the Fermi level is a sharp edge, whereas for $T > 0\,\mathrm{K}$ and at thermodynamic equilibrium the Fermi level is the hypothetical energy level, which is occupied by an electron with a probability of 50%.

The phenomenon of DC field emission was first reported in 1897 by Wood [180] and theoretically described in 1928 by Fowler and Nordheim [181]. In particular, the current density of field emitted electrons is calculated by considering the transmission probability $T(E)$ of an electron through a triangular barrier of height ϕ due to the presence of an electric field of strength E_0 in the Wentzel-Kramers-Brillouin (WKB) approximation [178]:

$$T(E) = \frac{4\sqrt{E(\phi - E)}}{\phi + E_F} \exp\left(-\frac{4\sqrt{2m_e}(\phi - E)^{3/2}}{3e\hbar E_0} v(z) \right) \tag{4.3}$$

Here, m_e and e are the mass and charge of an electron and $\hbar$ is the reduced Planck constant. Furthermore, the slowly varying Nordheim function [182]

$$v(z) = 1 - z^2 + \frac{1}{3} z^2 \ln(z) \tag{4.4}$$

with

$$z = \sqrt{e^3 E_0 / (4\pi\varepsilon_0 E_F^2)} \tag{4.5}$$

accounts for the modification of the triangular barrier by the image potential of the released electron. The current density as a function of applied electric field strength E_0 is then given by the Fowler-Nordheim law of field emission [181]:

$$j(E_0) \propto \exp\left(-\frac{4\sqrt{2m_e}\phi^{3/2}}{3e\hbar E_0} v(z) \right) \tag{4.6}$$

4.3. Linear Photoemission

While applying a static DC bias voltage results in a well-defined emission of electrons from the nanotip, it lacks the possibility of electron emission in a femtosecond or even attosecond time window. This may be achieved by illuminating the apex of a metallic nanotip with a time-dependent electric field, for example, associated with an ultrashort laser pulse as described in Chapter 3. More generally, the photoemission of electrons may be classified into different regimes, of which the well-known photoelectric effect may be seen as a starting point.

It was first found by Hertz in 1887, who observed the enhancement of an electric spark under illumination of UV light [183]. His assistant Hallwachs continued this experiment in 1888 and could charge an isolated metallic plate by UV light [184]. Lenard found in 1902 [185] that the light intensity I determined the number of photoemitted electrons:

$$P(I) \propto I \tag{4.7}$$

The kinetic energy, however, was found to depend only on the (angular) frequency ω of the light, as later quantified by Einstein [18] as:

$$E_{kin} = \hbar\omega - \phi \tag{4.8}$$

Here, $\hbar$ is the reduced Planck constant and ϕ is the work function of the metal, which for gold is $\phi \approx 5.5\ \mathrm{eV}$ [43]. To remove an electron from the metal this energy must be provided by a photon, which in this case would be in the UV spectral region with a wavelength $\lambda \leq 225\ \mathrm{nm}$. Clearly, these experiments deviate from classical intuition. Their underlying mechanism was explained theoretically by Einstein in 1905 [18], who adapted Planck's hypothesis of the quantisation of light [186]. Einstein's prediction was quantitatively confirmed in 1916 by the experiments of Millikan, who determined a value for Planck's constant [187].

Nowadays, the photoelectric effect is widely understood as a coupling between a discrete bound state and a continuum, which is mediated by a time-dependent sinusoidal perturbation due to an electric field, i.e. treating only matter as quantised, but making no assumption on the quantisation of the light field [188]. In fact, Equation 4.8 follows from calculating the matrix element responsible for transitions between the bound and an ionised state, whereas the transition rate is proportional to the square of the electric field strength and thereby to the intensity as given by Equation 4.7.

Moreover, the simple picture of the release of an electron wave packet from a solid after excitation by light must be extended by a further step. Usually, the electron wave packet is launched from a quantum state lying beneath the surface of the solid. Consequently, the electron wave packet must propagate through the solid and may experience a delay as compared to electron wave packets launched from other quantum states. This phenomenon of charge migration has recently been elucidated by means of attosecond spectroscopy [17]. In particular, a delay in photoemission of ~100 as between electron wave packets launched from localised core states and delocalised conduction band states in a tungsten crystal was found.

4.4. Multiphoton Photoemission

In his 1905 paper [18], Einstein further hinted at lifting the restriction of electron photoemission as a single photon process. A multiphoton process would be achieved, if the photon flux of the illuminating source was high enough. In the language of that time this would result in the probability of a multiple number of photons being absorbed by an electron to overcome the work function of a metal or the ionisation potential of an atom, which nowadays can also be explained in a wave picture as shown at the end of this section and calculated in Chapter 7. Technically, such a source was not feasible at that time. This situation changed after 1960 with the advent of the laser [152,153]. Multiphoton photoemission [151] had already been predicted as early as 1931 [189] and was first observed in 1961 by illuminating a CaF_2:Eu^{2+} crystal with red light from a ruby optical maser [150]. Here, a two-photon excitation process was concluded from measuring a quadratic dependence on the applied laser intensity I. In general, for a multiphoton process of order N the photoemission rate $P(I)$ is given by a power law

$$P(I) \propto I^N \tag{4.9}$$

The kinetic energy of the emitted electrons follows:

$$E_{kin} = N\hbar\omega - \phi \tag{4.10}$$

Setting $N = 1$ yields the equations for the well-known photoelectric effect introduced in the previous section.

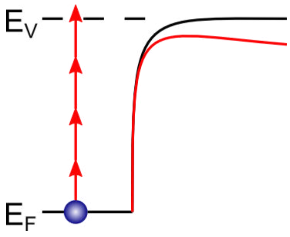

Figure 4.5: Multiphoton photoemission. An electron overcomes the energy difference between the Fermi level E_F and the vacuum level E_V by absorbing a multiple number of photons. The light field perturbs the potential barrier (black curve) only weakly (red curve).

In the multiphoton regime, the potential barrier set by the work function of the metal is hardly bent down, as illustrated in Figure 4.5, such that effects like tunnelling of electrons as seen in Section 4.2 for DC field emission are negligible. Instead, the multiphoton regime is known as the perturbative regime, in which the laser field is only seen as a weak perturbation. This results in the emission of electrons, which – in a photon picture commonly found in the literature – absorb a multiple number of photons to overcome the potential barrier and keep the remainder as kinetic energy. In this regime, the kinetic energy spectra are dominated by the origin of electrons from the distribution of energies near or below the Fermi level, convoluted with the spectral width of the illuminating light source, electron temperature and spectrometer resolution [37].

Making use of multiphoton photoemission allows for electron emission, for example, from a gold nanotip by illuminating it with light in the infrared spectral range, at which gold hardly absorbs. Damage to the nanotip is further avoided by exploiting the field enhancement at its apex, which allows for illumination with a low incident laser intensity. In particular, with an easy-to-handle solid-state Ti:sapphire femtosecond laser system multiphoton photoemission of electrons from metallic nanotips has been established [28-30]. Specifically, for an ultrashort laser pulse described by a temporal intensity distribution $I(t)$ and a pulse duration τ_{FWHM} the process of multiphoton electron emission is limited by Equation 4.9 to a temporal window $\tau_{FWHM}/\sqrt{N}$ measured at FWHM. However, originating from a broad Fermi-Dirac distribution of energies some electrons travel faster than others, such that the electron pulse would disperse. Nonetheless, electron emission from metallic nanotips contributes an alternative approach to the field of ultrafast electron microscopy and diffraction, providing a point-like electron source [33-35] in contrast to other concepts [31,32,136,142-146,148,190] with the goal of approaching the regime of attosecond electron pulses [142,148,191] as outlined in the introduction to this chapter.

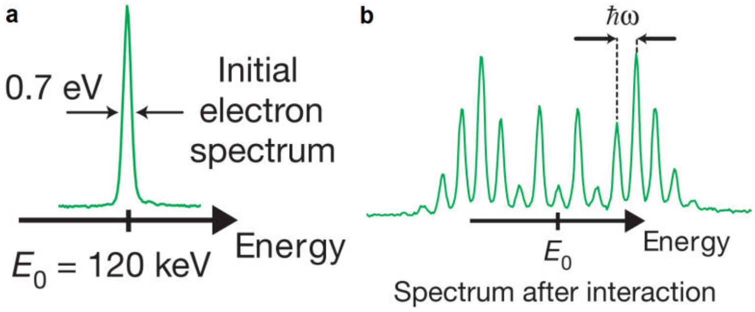

Figure 4.6: (a) The incident kinetic energy spectrum of a free ultrashort electron pulse becomes (b) phase-modulated after traversing an optical near-field at the apex of a gold nanotip as described in the main text. The electron wave packet exchanges energy with the optical near-field in integer multiples of the photon energy. Modified from [149].

Within this field of research a particularly neat method of generating attosecond electron pulses recently [149] emerged in a series of experiments in the sub-field of photon-induced near-field microscopy (PINEM) [192-194] and demonstrates the interpretation of multiphoton absorption in a wave picture as theoretically predicted [195]. In this experiment [149], a fine beam of free electrons is obtained by photoemission from a needle-shaped tungsten emitter and traverses an optical near-field excited at the apex of a gold nanotip. The optical near-field may be approximated as a harmonic oscillator. Their interaction induces Rabi oscillations between the optical near-field and the freely propagating electron wave packet, such that the initial momentum state of the electron wave packet is modulated resulting in a population of multiple sidebands separated by the photon energy as exemplary shown in Figure 4.6. This periodically phase-modulated electron wave packet may recompress itself in its subsequent propagation to an attosecond electron pulse [149].

A different concept followed in this thesis, which may possibly lead to an attosecond electron pulse, stems from the field of strong-field physics. In atomic systems the use of strong ultrashort laser pulses has enabled the control of electron trajectories and led to the generation of attosecond optical pulses via high harmonic generation [12,13], which by the closely linked phenomenon of above-threshold ionisation, further explained in Chapter 5, are accompanied by an attosecond electron pulse [10]. As we shall explore in the next section, metallic nanotips have emerged as model systems to study such strong-field phenomena usually observed in atomic systems, while also features in the strong-field regime unique to metallic nanostructures have been found.

4.5. Strong-Field Photoemission

As the light field becomes strong enough to periodically bend down the potential barrier, the probability of electrons tunnelling through the lowered barrier increases. As illustrated in Figure 4.7, these electrons may now get accelerated in the oscillatory potential created, for example, by the electric field of an ultrashort laser pulse. Thus the motion of the electrons may be driven by the light field itself, which at the apex of a metallic nanotip is strongly enhanced and spatially inhomogeneous. Importantly, the light field can no longer be seen as a small perturbation and the simple description of the photoemission process by the photon picture breaks down. Evidently, it needs to be extended to account for much richer electron dynamics expected to be observed. Specifically, the strong-field electron dynamics may be described in the semiclassical Simple Man's Model [8,196], which consists of two steps, that is the adiabatic tunnelling of an electron through the lowered potential barrier and its subsequent classical propagation as a point-like particle.

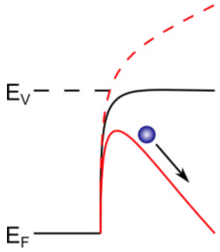

Figure 4.7: Strong-field photoemission. An electron may tunnel through the potential barrier, bent down by a strong electric field of a laser pulse. It may receive an acceleration in the light field, before it is driven back, when the oscillating electric field changes sign.

Keldysh Parameter

To start with let us consider the first step of the Simple Man's Model, i.e. the adiabatic tunnelling of an electron through a lowered potential barrier. Its contribution to the photoemission process will gradually increase with the strength of the incident light field, such that there will be a smooth transition from the multiphoton regime discussed in Section 4.4 to the strong-field regime presented here. Quantitatively, it may be expressed in terms of the Keldysh parameter [197,198], which relates the tunnelling frequency of an electron of mass m_e and charge e through a barrier of height ϕ lowered by the presence of an electric field of strength E_0

$$\omega_t = \frac{eE_0}{\sqrt{2m_e\phi}} \tag{4.11}$$

to the optical driving frequency ω via

$$\gamma = \frac{\omega}{\omega_t} = \frac{\sqrt{2m_e\phi}}{eE_0}\omega \tag{4.12}$$

Here, the work function ϕ of a metal may be replaced by the binding energy I_P of an atomic system in its ground state [197,198].

As the presence of a strong electric field bends down the potential barrier and thereby enables electrons to tunnel out, one may expect a deviation from the multiphoton photoemission rate in the strong-field regime. This deviation has, for example, been measured in non-sequential multiple ionisation of rare gas atoms by high-intensity laser pulses from a Ti:sapphire laser [199]. Quantitatively, this transition to the strong-field regime may be understood both for atomic systems and solids by considering the photoemission rate as a function of the Keldysh parameter [197,198], which is plotted in Figure 4.8 and given by:

$$P(\gamma) \propto \exp\left(-\frac{2\phi}{\hbar\omega}\left[\left(1+\frac{1}{2\gamma^2}\right)\mathrm{arcsinh}(\gamma) - \frac{\sqrt{1+\gamma^2}}{2\gamma}\right]\right) \tag{4.13}$$

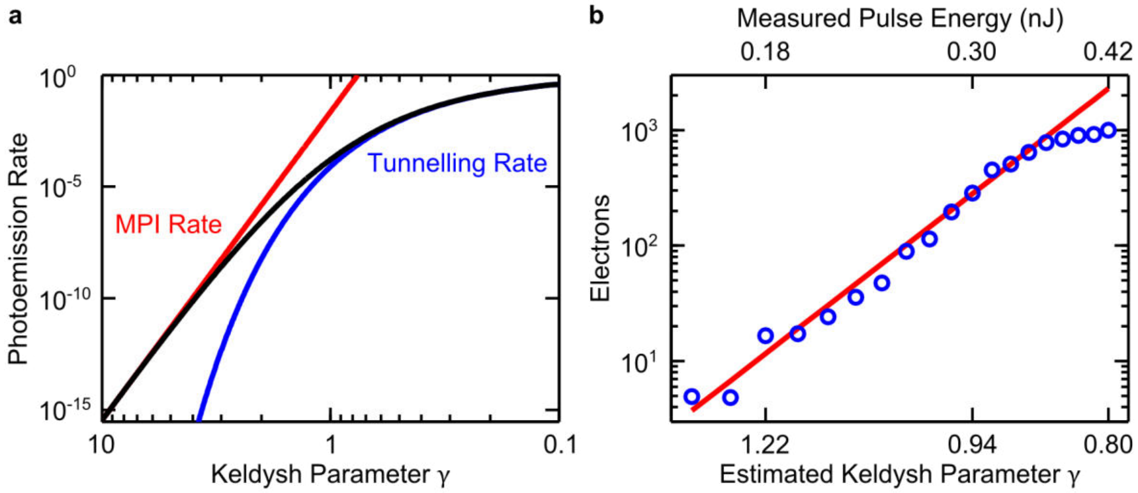

Figure 4.8: (a) Photoemission rate (black curve) for a photon energy $\hbar\omega = 0.78\ \mathrm{eV}$ as calculated according to Equation 4.13. The transition from the multiphoton to the strong-field regime is characterised by the Keldysh parameter γ. For $\gamma \gg 1$ the photoemission rate is described by the nonlinearity of the process (red line). For $\gamma \ll 1$, it approaches the tunnelling rate (blue curve). (b) Experimentally measured electron yield from the apex of a gold nanotip illuminated with 18-fs laser pulses centred at 1600 nm. A soft kink in the electron yield is observed by increasing the pulse energy, i.e. lowering γ. It occurs roughly at $E_{pulse} = 0.30\ \mathrm{nJ}$, for which by Equation 10.6 an electric field strength $fE_0 = 10\ \mathrm{V/nm}$ is estimated.

In the limit of a weak electric field and/or high frequency, $\gamma \gg 1$, so that $\mathrm{arcsinh}(\gamma) \approx \ln(2\gamma)$. Furthermore, $1/2\gamma^2 \to 0$ and $\sqrt{1+\gamma^2}/2\gamma \to 0.5$. This gives:

$$P(\gamma) \propto \exp\left(-\frac{2\phi}{\hbar\omega}\ln(2\gamma)\right)\exp\left(\frac{\phi}{\hbar\omega}\right) \tag{4.14}$$

Noting that $\ln(2\gamma) = \ln 2 + \ln \gamma$, this further simplifies to:

$$P(\gamma) \propto \left(\frac{1}{\gamma^2}\right)^{\phi/\hbar\omega} \propto I^N \tag{4.15}$$

Hence, in this limit the multiphoton photoemission rate, given by Equation 4.9, is retrieved. Here, the photoemission rate is governed by the nonlinearity N of the process. Plotted against intensity on a double logarithmic plot, this nonlinearity is indicated by the slope of a straight line, as shown in Figure 4.8a.

In the limit of a strong electric field and/or low frequency, $\gamma \ll 1$, so that $\mathrm{arcsinh}(\gamma) \approx \gamma - \frac{\gamma^3}{6}$. This results in:

$$P(\gamma) \propto \exp\left(-\frac{2\phi}{\hbar\omega}\cdot\frac{2\gamma}{3}\right) \propto \exp\left(-\frac{4\sqrt{2m}\phi^{3/2}}{3e\hbar E_0}\right) \tag{4.16}$$

This limit corresponds to the tunnelling regime. Here, the photoemission rate follows the tunnelling rate as also found by Fowler and Nordheim [181] in the case of DC field emission, explained in Section 4.2. Thus, the tunnelling regime in strong-field photoemission is also called the quasi-static regime. In particular, the photoemission rate is no longer governed by the nonlinearity of the process. The slope of a straight line fitted to the photoemission rate would therefore not indicate the nonlinearity anymore, but would give a lower value.

In particular, for a fixed wavelength the Keldysh parameter is varied with the pulse energy, which translates by Equation 10.4 linearly into an intensity. Increasing the pulse energy lowers the Keldysh parameter. Specifically, focussing 18-fs laser pulses centred around 1600 nm onto the apex of a gold nanotip with a Cassegrain objective and recording the number of photoemitted electrons as a function of pulse energy, a soft kink in the electron yield is observed, as shown in Figure 4.8b. It occurs roughly for a measured pulse energy $E_{pulse} = 0.30\ \mathrm{nJ}$, which translates by Equation 10.6 into an estimated electric field strength $fE_0 = 10\ \mathrm{V/nm}$, and thereby agrees with previous measurements [38].

Note, that for a sharp tip illuminated with few-cycle NIR laser pulses centred around 1600 nm electron emission may set in at a pulse energy of about 0.06 nJ. For typical experimental parameters, characterised in more detail in Chapter 10, this pulse energy corresponds to a Keldysh parameter $\gamma \approx 2$. From Figure 4.8a it can be seen that even at such a low pulse energy the photoemission rate is not solely governed by multiphoton emission. Hence, the expected nonlinearity of $\phi/\hbar\omega = 5.5\ \mathrm{eV}/0.78\ \mathrm{eV} = 7.1$ is not observed. Instead, a slightly reduced nonlinearity $N \approx 6$ is usually measured.

Quiver Motion

To gain an understanding of the subsequent electron dynamics, let us now consider the second step of the Simple Man's Model [8], i.e. the motion of an electron in an oscillatory electric field. Specifically, a time-dependent, monochromatic, continuous-wave light field with angular frequency ω and peak electric field strength E_0 exerts a force on a free electron of mass m_e, charge e and initially at rest at $x = 0$, such that its acceleration is given by:

$$\frac{d^2x}{dt^2} = \frac{e}{m_e} E_0 \cos(\omega t) \tag{4.17}$$

Integrating once yields the speed of the electron:

$$\frac{dx}{dt} = \frac{e}{m_e \omega} E_0 \sin(\omega t) \tag{4.18}$$

Integrating twice gives the time evolution of its position:

$$x(t) = \frac{e}{m_e \omega^2} E_0 \cos(\omega t) \tag{4.19}$$

Hence, the electron performs an oscillatory motion with a quiver amplitude

$$l_q = \frac{eE_0}{m_e \omega^2} \tag{4.20}$$

Its mean kinetic energy is:

$$U_p = \langle E_{kin} \rangle = \langle \frac{1}{2} m_e \left(\frac{dx}{dt} \right)^2 \rangle = \frac{e^2 E_0^2}{4 m_e \omega^2} \tag{4.21}$$

This quantity is called the ponderomotive energy U_p. If this energy gained by an electron in a light field becomes comparable to its binding energy, i.e. the ionisation potential I_P of an atomic system or the work function ϕ of a metal, strong-field phenomena may be observed. Quantitatively, the Keldysh parameter given by Equation 4.12 may be expressed in terms of the ponderomotive energy as:

$$\gamma = \sqrt{\frac{\phi}{2U_p}} \tag{4.22}$$

Sub-Cycle Dynamics

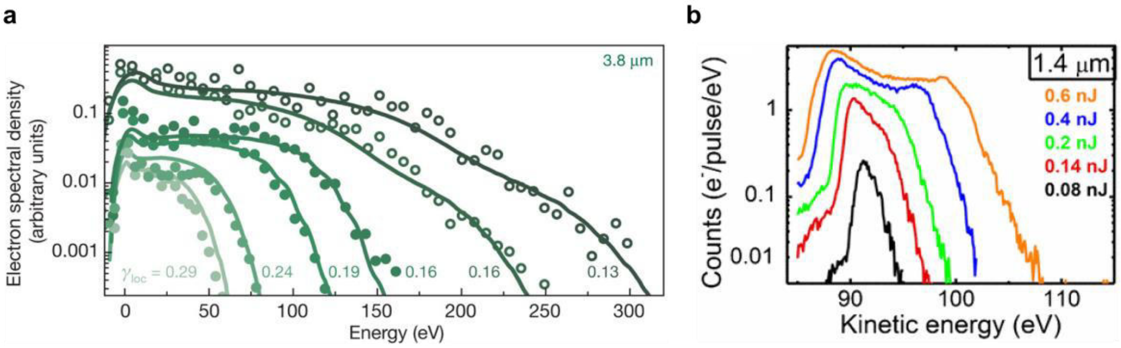

Figure 4.9: Sub-cycle dynamics. In the strong-field regime photoelectron kinetic spectra show a plateau, whereas narrow kinetic energy spectra are seen in the multiphoton regime (black curve). Modified from [36] and [37].

As the electrons are not just emitted, but also their motion is influenced in the oscillatory potential created by a strong electric field, one may expect the transition from the multiphoton to the strong-field regime to be further accompanied by a change in the kinetic energy distribution of the photoemitted electrons. Experimentally, this effect was demonstrated for gold nanotips using low-frequency electric fields associated with femtosecond laser pulses centred around the near-infrared and mid-infrared spectral range [36,37]. As evident from Equations 4.21 and 4.22 the use of low-frequency laser fields enables an access to the strong-field regime at a lower laser intensity, which avoids damage to the nanotip. Furthermore, a gold nanotip provides a higher field enhancement than, for example, a tungsten nanotip, as mentioned in Section 4.1.

As shown in Figure 4.9 the photoelectron kinetic energy spectra in the strong-field regime are characterised by a distinct plateau region. The plateau extends to electron kinetic energies of ~300 eV. This contrasts the narrow kinetic spectra observed in the multiphoton regime, such as depicted in Figure 4.9b (black curve). There, an electron performs a quiver motion as explained above, in which the oscillatory potential created by a weak light field causes the electron to accelerate away from the nanotip and upon reversal of the electric field to decelerate. This limits the kinetic energy attained by quivering electrons. However, if the light field is strong enough to bend down to the potential barrier, electrons tunnelling through the lowered potential barrier are born, before the electric field reverses. In consequence, they may receive an acceleration from the electric field, which is strongly enhanced at the apex region, into which the electrons are born. This may result in such a high acceleration, that the electrons may leave the near-field region within less than one cycle of the oscillating electric field, i.e. within one sub-cycle, before the reversal of the electric field would cause them to decelerate. Consequently, these sub-cycle electrons gain a higher kinetic energy than electrons quivering in front of the nanotip, such that the spectra substantially broaden and develop a plateau-like region [36,37]. In the absence of a nanostructure the transition into such a regime would require relativistic electrons [36].

Spatial Adiabaticity Parameter

Evidently, such sub-cycle effects depend on the spatial-temporal vectorial field distribution in the region, into which electrons are born after tunnelling. The quiver length l_q of their subsequent motion is determined by the electric field strength, with which it scales linearly as given by Equation 4.20. If this quiver length is longer than the decay length l_F of the spatially inhomogeneous near-field, electrons may escape from this near-field region within less than one cycle of the oscillating electric field as described above. In analogy to the Keldysh parameter given by Equation 4.12, which describes the adiabaticity of the photoelectron emission process in time, the observed sub-cycle effects on the kinetic energy of photoelectrons originating from metallic nanotips may be quantitatively described by a spatial adiabaticity parameter [36]:

$$\delta = \frac{l_F}{l_q} \tag{4.23}$$

The limit $\delta \gg 1$ corresponds to the atomic case, in which electrons quiver in a homogeneous laser field. In this case, the width of the photoelectron kinetic energy spectra approaches $2U_p$ [196]. In contrast, if $\delta \ll 1$, the quiver length is longer than the near-field decay length. In this case electrons may escape from the spatially inhomogeneous near-field region within one sub-cycle. Thereby the quiver motion of an electron is quenched. In this scenario the width of the photoelectron kinetic energy is given by αU_p with $\alpha < 2$ [36]. Whereas $\alpha \approx 2$ for weak spatial field gradients like in an atomic system, it was found to take a reduced value $\alpha \approx 1.2$ in case of a sharp gold nanotip [38].

These findings for direct electrons, to be further explained in the context of electron trajectories below, were supported by a model assuming a one-dimensional free-electron gas confined by a crystalline potential and calculating the temporal evolution of a single-electron wave function under the influence of an oscillatory electric field by numerically solving the time-dependent Schrödinger equation [167]. It was further found that electrons scattering back from a nanotip do not gain a maximum kinetic energy of $10U_p$, as observed in a homogeneous electric field in the case of an atomic system [200]. Instead, a reduced maximum kinetic energy of $3U_p$ was calculated, assuming a near-field decay length $l_F = 10\ \mathrm{nm}$ corresponding to a spatial adiabaticity parameter $\delta = 0.7$ [167].

In addition, a narrowing of the cone, into which electrons are emitted from the nanotip, was observed [37], which indicates the steering of electrons by the electric field of an ultrashort laser pulse in the strong-field regime. This may be explained by sub-cycle electrons escaping the near-field region directly on well-defined trajectories. In contrast, quiver electrons describe a more complicated, less directional zig-zag trajectory involving deflection during back acceleration and possibly rescattering from the nanotip. To gain a deeper understanding of the sub-cycle regime, let us now focus more deeply onto these electron trajectories.

Electron Trajectories

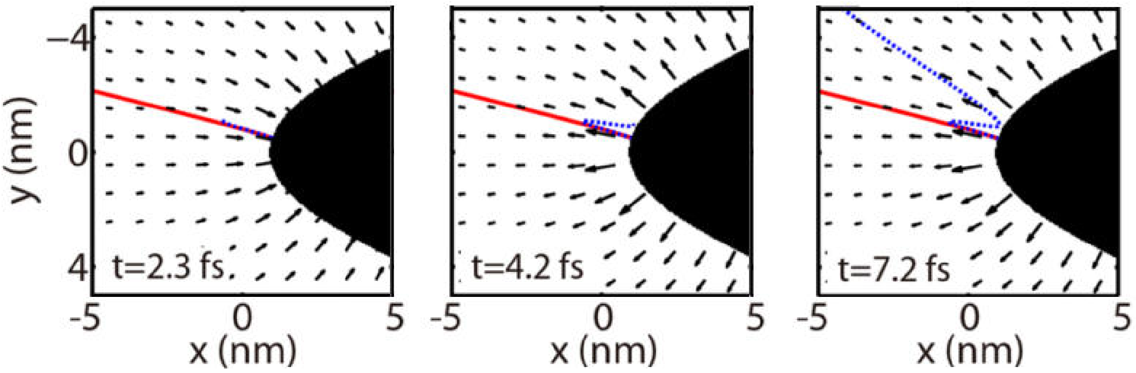

Figure 4.10: Snapshots of the trajectories of a sub-cycle electron (red) emitted at $\varphi = -0.5\pi$ reaching a kinetic energy $E_{kin} = 25\ \mathrm{eV}$ and a quiver electron (blue) emitted at $\varphi = 0.18\pi$ reaching a kinetic energy $E_{kin} = 3.5\ \mathrm{eV}$. The black arrows indicate the vectorial electric field distribution in the vicinity of the nanotip's apex. Illumination with a 30-fs laser pulse centred at $\lambda = 1500\ \mathrm{nm}$ and with an enhanced peak electric field strength $fE_0 = 28\ \mathrm{V/nm}$ is assumed. A decay length $l_F = 1.5\ \mathrm{nm}$ is taken. Modified from [37].

In particular, the shape of the plateau-like spectra in the sub-cycle regime is well understood in an extended semi-classical Simple Man Model [36,37,40,166]. This takes an analytical solution for the spatially inhomogeneous optical near-field at the apex of the gold nanotip into account, which is modelled as a two-dimensional hyperboloid [27,201], as also shown in Figure 4.3. Electron emission is calculated as a function of emission site and birth time $t_B = \varphi/\omega$ according to a Fowler-Nordheim tunnelling probability [36,181,202], assuming electron emission in negative half cycles only (i.e. away from the tip) and neglecting the field-dependent barrier suppression.

Here, φ is the emission phase and ω is the carrier angular frequency of the oscillatory, time-dependent electric field associated with an ultrashort laser pulse. Electron trajectories are simulated by treating electron motion classically under the action of the force field $\vec{F}(\vec{r},t) = e\vec{E}(\vec{r},t)$, assuming perfect elastic collisions with the tip [40].

Exemplary electron trajectories are shown in Figure 4.10 for two different types of electron motion at different instants in time [37]. Initially, both electrons are accelerated along the electric field lines, whereas they describe distinctly different trajectories thereafter depending on their birth time. Sub-cycle electrons, emitted for emission phases $\varphi < 0.12\pi$, are accelerated out of the strongly enhanced near-field region in the first half cycle of the electric field of the near-infrared laser pulse and are weakly affected in their trajectory by subsequent half cycles. In contrast, quiver electrons, emitted for emission phases $\varphi > 0.12\pi$, do not escape from the near-field region. They are back-accelerated to the nanotip, where they possibly recollide. Local magnetic fields hardly affect the electron trajectories, as they are weak [37].

To exemplify the spatially inhomogeneous near-field at a metallic nanostructure as a distinguishing feature from the homogeneous field distribution around atomic systems, the nanotip's radius of curvature was varied within the framework of this model [166]. As shown in Figure 4.11a, the trajectories of sub-cycle and quiver electrons differ substantially from each other, if a small tip radius $R = 1\,\mathrm{nm}$ is assumed, corresponding to a spatial adiabaticity parameter $\delta = 0.28$. Specifically, a quiver electron hardly traverses the near-field region within one cycle of the oscillatory electric field and is driven away from the taper axis by a backwards pointing electric force. In contrast, a sub-cycle electron escapes from the near-field region within one half cycle of the oscillatory electric field and follows the strongly curved electric field lines during its motion. Such an electron is therefore steered towards the taper axis. However, assuming a tip radius $R = 100\,\mathrm{nm}$ corresponding to a spatial adiabaticity parameter $\delta = 28$ the difference between the trajectories of sub-cycle and quiver electrons is negligible [166], as shown in Figure 4.11b.

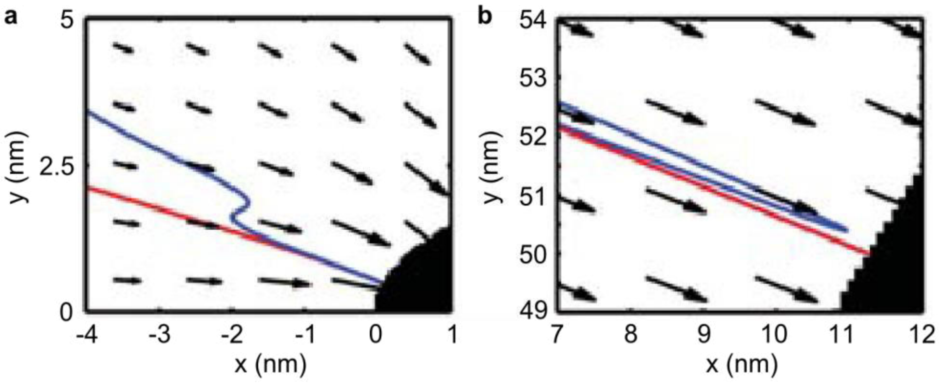

Figure 4.11: Trajectories of a sub-cycle (red) and a quiver electron (blue), calculated for different tip radii (a) $R = 1\,\mathrm{nm}$ and (b) $R = 100\,\mathrm{nm}$. The black arrows indicate the vectorial electric field distribution in the vicinity of the nanotip's apex. Illumination with a 30-fs laser pulse centred at $\lambda = 1500\,\mathrm{nm}$ and with an enhanced peak electric field strength $fE_0 = 25.4\,\mathrm{V/nm}$ corresponding to a quiver amplitude $l_q = 2.8\,\mathrm{nm}$ is assumed. Modified from [166].

The findings presented so far are summarised in Figure 4.12 as follows [38]:

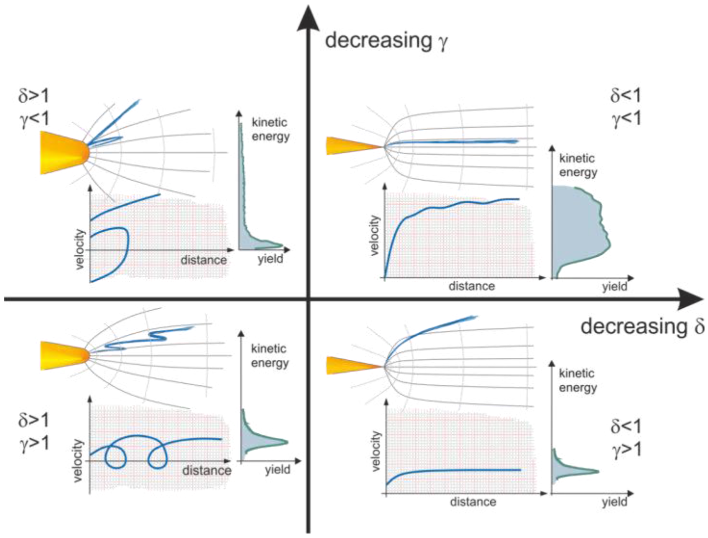

Figure 4.12: Schematic illustration of electron trajectories and photoelectron kinetic energy spectra as a function of Keldysh parameter γ and spatial adiabaticity parameter δ, as described in the main text. Taken from [38].

For $\gamma > 1$ and $\delta > 1$, both the ponderomotive energy U_p as compared to the work function of, for example, a gold nanotip and the spatial gradients of the optical near-field are weak. This regime is known as multiphoton ionisation (MPI) [28] and characterised by exponentially decaying spectra, possibly superimposed by above-threshold ionisation (ATI) peaks [39,40,167], further elucidated at the end of this chapter.

For $\gamma < 1$ and $\delta > 1$, photoemitted electrons quiver in a strong, spatially homogeneous electric field similar to an atomic system. Recollisons, for example, with a gold nanotip, give rise to a plateau extending up to a high-energy cut-off at $10U_p$ [38], similar to atomic systems [200].

For $\gamma > 1$ and $\delta < 1$, spatial field gradients are present, but electrons are only weakly accelerated along the field lines. This regime may be reached with low-frequency (THz) radiation [147,173].

For $\gamma < 1$ and $\delta < 1$, electrons are emitted by strong-field tunnel ionisation and strongly accelerated along the field lines. This regime of photoemission is known as the sub-cycle regime [36,37,166,167] described in the main text above. In contrast to atomic systems, recollisions are suppressed and plateau-like spectra characteristic for photoemission from a metallic nanostructure arise.

CEP Effects

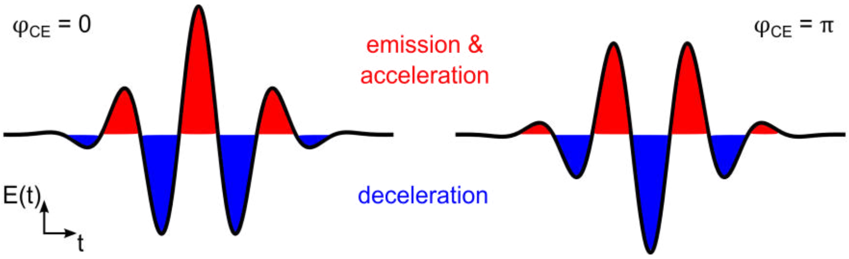

Figure 4.13: Illustration of different settings of the CEP. For $\varphi_{CE} = 0$ mainly one, high-amplitude half-cycle contributes to electron emission and subsequent acceleration. For $\varphi_{CE} = \pi$ electron emission occurs within two half-cycles, which are lower in amplitude.

As electrons are driven by the light field itself in the strong-field regime, their dynamics is expected to depend on the exact form of the carrier electric field beneath the intensity envelope of an ultrashort laser pulse, i.e. the carrier-envelope phase φ_{CE}. As illustrated in Figure 4.13 electrons emitted for $\varphi_{CE} = 0$ may gain a higher kinetic energy than for $\varphi_{CE} = \pi$ due to being acceleratd in an electric field of higher amplitude in the former case. Electrons born at the beginning of the main half cycle gain the highest kinetic energy, as they receive an acceleration for the maximum duration. In this way, the high-energy cut-off of photoelectrons originating from a metallic nanotip may be controlled via the CEP [38]. Specifically, this was achieved by illuminating a gold nanotip with an apex radius of curvature $R \approx 10\,\mathrm{nm}$ by 15-fs laser pulses centred around 1600 nm originating from a previous version of the laser system explained in Chapter 3. An additional observation in this experiment was the variation of the electron yield with the CEP in the transition region from the multiphoton to the strong-field regime. Assuming electron emission in negative half cycles only, this dependence on the CEP arises, because most electrons will be emitted at the highest electric field strength, which additionally scales with the high nonlinearity of the photoemission process. Specifically, the measured electron yield doubled for two different settings of the CEP offset from each other by $\Delta\varphi_{CE} = \pi$ [JR1]. Such CEP effects become pronounced for few-cycle laser pulses, for which the CEP varies more strongly from one optical cycle to another.

Above-Threshold Photoemission

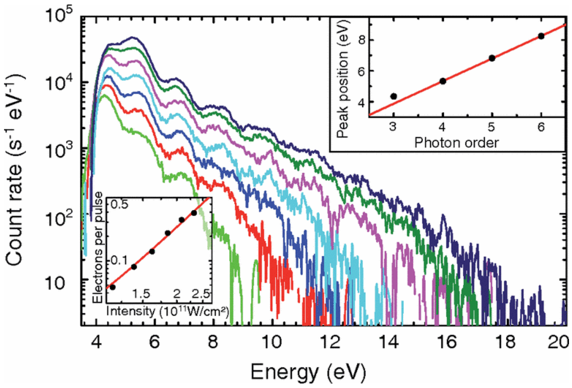

Figure 4.14: Above-threshold photoemission. Photoelectron spectra are characterised by peaks separated by the photon energy of the laser pulses illuminating a tungsten nanotip. Taken from [39].

So far photoelectron kinetic spectra have been discussed, which were either narrow as in the multiphoton regime or broad with a distinct plateau pointing to sub-cycle dynamics in the strong-field regime. In contrast, a distinctly different observation, that is a periodic modulation of the photoelectron kinetic energy spectra displayed in Figure 4.14, was made by illuminating the apex of a tungsten nanotip with 6-fs laser pulses from a Ti:sapphire oscillator centred around 800 nm [39,40]. In contrast to the gold nanotips investigated in the experiments presented above, a tungsten nanotip provides a comparatively weak field enhancement, as discussed in Section 4.1. Additionally, the tungsten nanotips had a slightly larger apex radius of curvature $R \approx 20\,\mathrm{nm}$. Overall, these conditions point to an increased spatial adiabaticity parameter, i.e. $\delta \approx 100$ in the case of [39], and thereby away from the sub-cycle regime discussed above, but towards a quiver regime.

The periodic modulation arises, as further illustrated in Chapter 5, because the wave function representing a quivering electron partially leaks out at the outermost points of its oscillatory motion. The interference of these freely propagating electron wave packets released in temporal slits spaced by the optical period of the driving laser pulses corresponds in the energy domain to peaks in the photoelectron kinetic energy spectrum separated by the photon energy. This strong-field phenomenon is well-known as above-threshold ionisation (ATI) from atomic systems. This experiment provided the first clear signature of this concept, here termed above-threshold photoemission, from a solid, after numerous attempts had been made before [157-163]. Yet, they were limited to low photon orders as recently also reported for a measurement of an Au(111) surface, in which electron emission has been attributed to occur from the Shockley surface state [203]. Using metallic nanotips, however, also higher photon orders were achieved by exploiting the field enhancement at the apex of the metallic nanotip, which allowed for reaching the strong-field regime, while staying below the damage threshold of the solid-state nanostructure.

In particular, control over the CEP determined the cut-off and increased the modulation contrast in the high-energy part of the photoelectron kinetic energy spectrum to up to 30% [40]. This observation is explained by the notion of ATI as an interference phenomenon. For a few-cycle laser pulse used in this experiment, the photoemission of electrons may either occur in one or in two half cycles, depending on the CEP, as also illustrated in Figure 4.13. The contribution of two half cycles corresponds to the presence of two arms in an interferometer. Hence, the highest modulation contrast is observed in this case. If only one half cycle contributes to electron emission, no interference is possible and hence no modulation in the photoelectron kinetic energy spectrum is seen.

While the origin of ATI peaks separated by the photon energy of the driving laser pulses may be seen as the interference of electron wave packets released in temporal slits spaced by the optical period [204], the width of each slit may be estimated from the width of the region of higher-order ATI peaks. Specifically, this region was shown to extend over a range in energy $\Delta E \approx 9\,\mathrm{eV}$, so that the width of a temporal slit was estimated as $\Delta t \approx h/\Delta E \approx 450\,\mathrm{as}$ [40].

However, in contrast to the deeply modulated photoelectron kinetic energy spectra obtained from atomic systems [6], as displayed in Figure 5.2 and further discussed Chapter 5, the modulation contrast in the low energy part of the ATI spectrum from the metallic nanotip amounted to few percent only. This is a consequence of the one-step photoemission strategy employed in this experiment, in which electrons are emitted from a broad distribution of states near or below the Fermi level. Specifically, an electron emitted from a deeper lying state will arrive at a detector will less residual kinetic energy than an electron originating from a higher lying state. Thereby, the broad distribution of states maps directly onto a kinetic energy spectrum and smears out distinct features such as ATI peaks.

These findings were reconciled with the quantum mechanical model used to elucidate the sub-cycle regime before [167]. Instead of plateau-like spectra characteristic for the sub-cycle regime, peaks separated by the photon energy appear in this case, which are pronounced by considering the contribution of electrons from a single level, but wash out when a higher number of states near the Fermi level contributes to electron emission. Furthermore, it could be confirmed that the high-energy tail extending up to $\sim 10\,U_p$ in this experiment originates from electrons, which were backscattered at the nanotip. In contrast, such recollisions are suppressed in the sub-cycle regime.

Here, the question now arises whether the limitation of the weak modulation may be overcome. In particular, one would need to achieve a similar situation as in the theoretical simulation, in which ideally a single level contributes to electron emission like in an atomic system. This requires the decoupling of electrons from the broad distribution of states near and below the Fermi level. In this thesis, a conceptually new approach of bridging the gap between an atomic system and a solid-state device is suggested, which involves atomic-like image potential states at metallic surfaces to be introduced in Chapter 6. First, however, to provide a deeper understanding of the concept of ATI it will be discussed from the perspective of an atomic system in Chapter 5.

5. Above-Threshold Ionisation in Atomic Systems

Exposing noble gas atoms to strong laser intensities has facilitated modern attosecond science [1,2], which relies on the closely linked concepts of high harmonic generation (HHG), further elucidated in the outlook in Chapter 9, and above-threshold ionisation (ATI) as investigated as part of this thesis. In particular, the strong-field phenomenon ATI [6,7,205] was first observed in 1979 by exposing xenon atoms to a strong electric field associated with a nanosecond laser pulse [5]. In the framework of the Simple Man's Model [8] introduced in Chapter 4 the action of a strong laser pulse results in the release of a bound electron from a discrete atomic state, followed by its subsequent acceleration and quiver motion in the spatially homogeneous light field, as depicted in Figure 5.1. At its outermost points of its oscillatory motion, a freely propagating electron wave packet separates from the bound state electron wave packet. The interference of the released electron wave packets in temporal slits spaced by the optical period of the driving laser pulses results in a photoelectron kinetic spectrum, which is characterised by peaks separated by the photon energy, which form a plateau for higher orders and abruptly cut off [81,154,200].

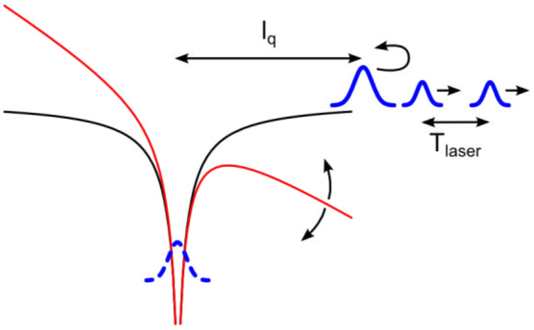

Figure 5.1: ATI. An electron wave packet bound (dashed blue curve) in an atomic potential (black curve) is released by the action of an oscillatory light field, which modifies the potential barrier (red curve). The wave packet representing the released electron quivering in one half cycle by a length l_q partially leaks out at its outermost point of its oscillatory motion in temporal slits spaced by the optical period T_{laser} of the driving laser pulses.

In particular, a deeply modulated comb-like ATI photoelectron kinetic energy spectrum in the energy domain, as displayed in Figure 5.2, may correspond to a train of attosecond electron pulses in the time domain [10,11]. This feature may be understood in terms of an analogy to mode-locking [67,115]. There, phase-locking of longitudinal modes oscillating in a laser cavity results in the generation of an ultrashort laser pulse. Here, the oscillatory motion of the electron wave packet defined by the optical period of the driving laser pulses may yield an ultrafast electron pulse. Specifically, a deeply modulated photoelectron kinetic energy spectrum with $N_{modes} = 10$ ATI peaks separated by a photon energy of $0.78\,\mathrm{eV}$ corresponding to a centre wavelength $\lambda = 1600\,\mathrm{nm}$ and an optical period $T_{laser} = 5\,\mathrm{fs}$, as provided by the ultrashort laser pulses in the near-infrared presented in the Chapter 3, may sustain a train of electron pulses with an individual pulse duration roughly given by $T_{laser}/N_{modes} = 500\,\mathrm{as}$.

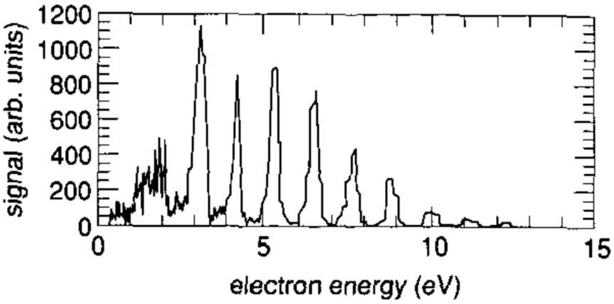

Figure 5.2: ATI spectrum obtained by illuminating xenon atoms at an intensity of $2 * 10^{13}\,\mathrm{W/cm^2}$ with 100-ps laser pulses centred around 1060 nm. Taken from [6].

It would be particularly interesting to transfer such a concept to a metallic nanotip, because such an attosecond electron pulse would controllably emerge from its nanometre-sized apex instead of an extended volume defined by the focal spot of the illuminating laser pulses in case of an atomic system. It is therefore important to understand the concept of ATI in further depth. In particular, apart from its characteristic modulation by the photon energy of the driving laser pulses the photoelectron kinetic energy spectra in the ATI regime display further properties, which are of relevance in understanding the tungsten nanotip experiment [39,40] and the ATI spectra presented in this thesis [JR5].

Peak Shifting and Channel Closing

The position of the ATI peaks may not remain at a constant kinetic energy, but may change with laser intensity. This arises, because the ionisation potential upshifts by the ponderomotive energy [206], which increases linearly with the laser intensity. Consequently, the initial kinetic energy of an electron is reduced:

$$E = N\hbar\omega - I_P - U_p \tag{5.1}$$

This equation does not only predict, that the ATI peaks will shift towards lower energies, but also implies that at some point the kinetic energy for the lowest photon order would become negative. Experimentally, the lowest-order ATI peak will diminish in magnitude until it disappears. This effect has been termed channel closing [207]. Both effects, peak shifting and channel closing, have also been observed in the tungsten nanotip experiment [39] described in Chapter 4. In particular, by increasing the laser intensity the first order peak was found to exceed the lowest order peak in electron yield. Furthermore, the peaks shifted to lower energies. In fact, this shift was larger than expected. This discrepancy was attributed to the enhancement of the electric field at the apex of the tungsten nanotip, which in a quantitative evaluation translated into a field enhancement factor $f = 4$ [39].

Peak shifting, however, is not observed in the long pulse regime [6], that is for laser pulses with a duration above ~1 ps. Here, the kinetic energy of an electron is initially reduced by an amount equal to the ponderomotive energy as described above. The electron then propagates in the slowly varying electric field of the laser pulse, leaves the focal spot and reaches the field-free region of the detector, before the interaction with the laser pulse is over. Pictorially, the electron “surfs down” the ponderomotive potential [206]. In this process, the electron converts the ponderomotive potential energy U_p into kinetic energy exactly compensating for the upshift in ionisation potential. Consequently, ATI peaks will not shift and are narrow, as displayed in Figure 5.3 below. In the short pulse regime, however, the electron’s quiver motion in the time-dependent electric-field of the laser pulse stops, once the laser pulse is over. Hence, the initially lost energy is not regained by the electron and the ATI peaks will shift as described above.

Freeman Resonances

Furthermore, as shown in Figure 5.3, the narrow ATI peaks observed in the long pulse regime were observed to split up into a finer structure in the short pulse regime [190], with sharp features occurring at

$$E = N\hbar\omega - I_P - (M\hbar\omega - E_i) \tag{5.2}$$

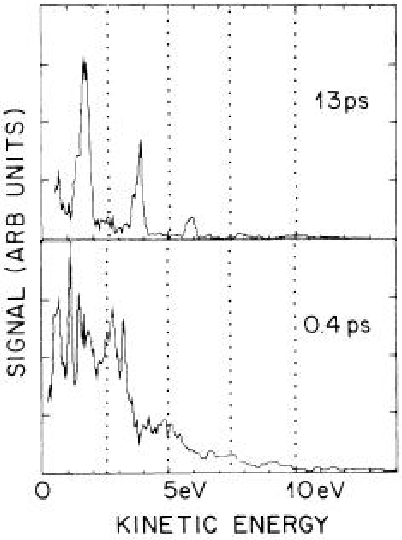

Figure 5.3: Freeman resonances. In the long-pulse regime, narrow ATI peaks are observed. However, in the short-pulse regime, the ATI peaks split up and display a finer structure due to Freeman resonances. Modified from [190].

This fine structure is explained by the resonant excitation of weakly bound excited states of the atom at an intermediate energy level E_i with M photons. As not only the ionisation potential, but all states are upshifted by the ponderomotive energy, these states will eventually sweep into a multiphoton resonance. This situation arises, because the ponderomotive energy as given by Equation 4.21 increases linearly with the laser intensity, which is governed by the temporally varying envelope of the laser pulse. Exciting a multiphoton resonance causes an enhancement of the ionisation rate and hence the appearance of sharp features in the photoelectron kinetic energy spectrum. These sharp features are called Freeman resonances, named after their discoverer [190].

CEP Effects

A further characteristic feature of an ATI spectrum is a low-energy part, in which the magnitude of the photon orders rapidly decreases, and a high-energy part, in which the number of detected electrons stays almost constant and abruptly drops in a cut-off region [154,200]. The low-energy part of an ATI spectrum is ascribed to direct electrons, which do not return to its parent ion. The high-energy plateau region consists of electrons, which have elastically rescattered from the ionic core, and are subsequently accelerated in the laser field to kinetic energies up to $10U_p$. The effect of rescattering has also been predicted for solids [208] and has been assigned to the development of a plateau region of higher-order ATI peaks in the tungsten nanotip experiment [39,40,167].

In particular, the high-energy plateau region of an ATI spectrum is sensitive to the CEP [81]. High-energy electrons, tunnelling through the potential barrier at a time t_0, may only be created at the highest electric field strength, on which their probability of tunnelling depends exponentially. They return at a later time t_1 to their parent ions. Here, they may rescatter and receive an efficient acceleration only, if the electric field strength during the subsequent optical cycle is high. As the time of photoionisation of an electron at t_0 and its return time t_1 to its parent ion differ by approximately three quarters of an optical cycle, the requirement of fulfilling both conditions is hard to meet and results in a strong dependence on the CEP. In particular, the CEP of a few-cycle laser pulse may be determined in a so called stereo-ATI measurement [130]. In an atomic system every half cycle contributes to electron emission in opposite directions.

The left-right asymmetry in the ATI spectra yields information on the CEP, as shown in Figure 5.4. Specifically, a CEP $\varphi_{CE} = 0$ yields a higher high-energy cut-off in one direction than in the other, whereas this argument is reversed for $\varphi_{CE} = \pi$. Without control over the CEP of a few-cycle laser pulse no difference is seen between the ATI spectra detected on opposite sides [81].

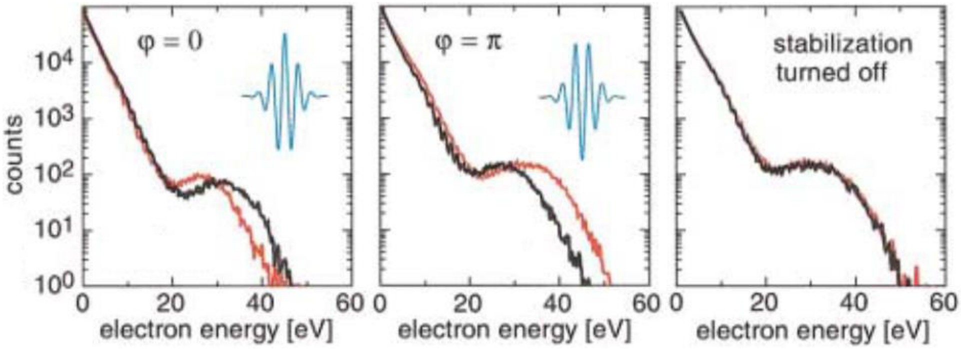

Figure 5.4: Photoelectron kinetic spectra for different settings of the CEP obtained in a stereo-ATI measurement by illuminating xenon atoms with 5-fs laser pulses centred at 760 nm with a peak intensity $\sim 10^{14}\,\mathrm{W/cm^2}$. The black (red) curves correspond to photoemission to the right (left). Modified from [81].

6. Image Potential States

The discussion in Chapters 4 and 5 has elucidated on the atomic concept of above-threshold ionisation (ATI), which in conjunction with the related concept of high harmonic generation (HHG) has found numerous applications in the rapidly growing field of attosecond science [1,2]. Different approaches exist to transfer these concepts to solid-state materials [23], for example, by exploiting the field enhancement at the apex of a metallic nanotip to reach the strong-field regime [39,40] as shown in Chapter 4 or by mimicking an atomic system in a semiconductor material [19-21], as sketched in the outlook in Chapter 9.

In this thesis, the gap between an atomic system and a solid-state nanostructure is suggested to be bridged in a conceptually new approach by the well-known concept of image potential states [41,42]. These are long-lived states, which have been extensively studied on extended metallic films [43,209]. Here, a negatively charged electron in front of the surface induces a positive image charge inside the bulk, such that the electron is bound to its own, hydrogen-like image potential. Consequently, it occupies a Rydberg series of weakly bound states and is characterised by a hydrogen-like wave function with a reduced spatial overlap with the bulk [42,43]. This results in a long lifetime of up to few picoseconds [41], as rapid dephasing processes such as electron-electron scattering, electron-phonon scattering or scattering with defects such as impurity atoms [210] typically occurring in a solid due to the high density of electrons are suppressed. It also allows for the observation of long-lived coherences by quantum beat spectroscopy [41,211].

Image potential states have widely served as a probe of the properties of surfaces [43]. For example, a Rydberg series of image potential states with the finite penetration of their associated wave functions into the bulk corresponds either to the surface itself or an adsorbate, depending on the number of monolayers of the adsorbate. A particularly interesting situation arises for free-standing graphene, which is a single monolayer of graphite and thus has two surfaces in close proximity. It has been predicted, that in this situation a double Rydberg-like series of image potential states exists, resulting from a symmetric or antisymmetric superposition of the eigenstates of each surface [212]. Moving such a layer of graphene closer to a metal surface should eventually result in single Rydberg series corresponding to the metal surface [213]. Other examples of the observation of image potential states at nanostructures include related materials such as carbon nanotubes [214] or fullerenes [215,216] and also metal nanoclusters [217,218].

However, strong-field phenomena known from atomic systems such as ATI have so far not been observed arising from the atomic-like image potential states at an extended metallic film. This is most likely due to the low damage threshold, which is exceeded when increasing the laser intensity required to reach the strong-field regime. Here, metallic nanotips provide a solution, as they permit the application of a weak incident electric field, which is enhanced by the geometry of the nanotip, as explained in Chapter 4. However, image potential states have not been reported for metallic nanotips so far and strong-field photoemission from metallic nanotips has been mainly facilitated from the broad distribution of states near the Fermi level [36-40]. It would be particularly intriguing to decouple an electron from this continuous distribution and store it in a discrete image potential state at the apex of a metallic nanotip. This might open the possibility for subsequently photoionising and driving the electron in the strongly enhanced electric field of an ultrashort laser pulse and hence provide a conceptually new approach to observe ATI from a metallic nanotip.

To introduce the concept of image potential states, their properties will be discussed in this chapter in the context of well-established experiments on extended metallic films. A deeper understanding, especially of the so far unknown nature of image potential states at a metallic nanotip, will then be gained in Chapter 7 from a numerical model based on solving the Schrödinger equation, which will account for specific properties of a metallic nanotip such as its curved geometry and the spatially inhomogeneous electric field at its apex.

Energy Levels

In the following, the physical concept of image potential states will be explained [41-43]. As illustrated in Figure 6.1, an electron in front of or emitted from a metallic surface will induce a positive image charge inside the metal. This image charge is located at an equal distance inside the surface, as the electron is at a distance in front of the surface. Specifically, if the electron is at a distance x from the surface, the distance between the negatively charged electron and its positive image charge is $2x$. Hence, the magnitude of the electric force between them is $F \propto -1/(2x)^2$, which by the relation for a conservative force, $F = -\mathrm{grad}\, V$, gives rise to an attractive Coulomb-like potential of the form $V \propto -1/4x$. Thus, outside the metal the electron will experience a potential, which is similar to the potential created by the positively charged proton in a hydrogen atom, but scaled by a factor $1/4$.

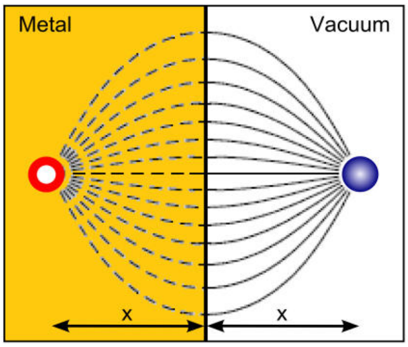

Figure 6.1: Image charge. A negatively charged electron, a distance x in front of a metallic surface, induces a positive image charge, at an equal distance x inside the bulk. Adapted from [41].

In this potential the electron may occupy a discrete set of states. Like in a hydrogen atom, their energy levels follow a Rydberg series

$$E_n = -0.85\ \mathrm{eV}/n^2\,, \qquad n = 1,2,3,\ldots \tag{6.1}$$

In the case of image potential states, the ground state energy is a scaled down Rydberg energy. Specifically, $-0.85\ \mathrm{eV} = -13.6\ \mathrm{eV}/4^2$.

Wave Functions

The associated electron wave functions are the s-like radial wave functions of the hydrogen atom $R_n^{l=0}$ with $n = 1,2,3,\ldots$, expanded by a factor of $1/4$ and multiplied by the distance x to the surface [42]. Analytically, the wave functions outside the metal are described by:

$$\psi_n(x) = x R_n^{l=0}(x/4) \tag{6.2}$$

As shown in Figure 6.2, with increasing principal quantum number n their probability density peaks further away from the surface. Inside the metal, the wave functions decay exponentially. This part has been obtained from a well-established one-dimensional model [43,219,220] by matching the Coulomb-like potential given above to equally spaced potential wells representing the ionic cores of the bulk and solving the time-independent Schrödinger equation. This calculation is discussed in Chapter 7, where also a comparison to the analytical solution is given. Overall, the wave functions are predominantly located outside the metal. This reduced spatial overlap of the wave functions with the bulk results in a long lifetime associated with an electron occupying an image potential state.

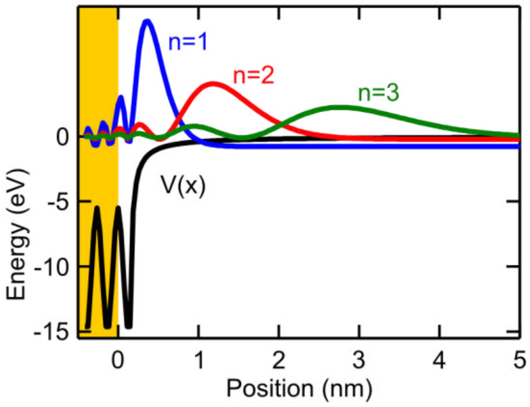

Figure 6.2: Wave functions associated with the first three image potential states, resulting from a potential $V(x)$ described by equally spaced potential wells inside the metal matched to a Coulomb-like potential outside. The wave functions are described by an exponentially decaying tail inside the bulk, which is modulated by the periodicity of the lattice, and a dominant hydrogenic part outside, increasing in extent with the principal quantum number n.

Lifetime

Experimentally, the lifetime of an image potential state may be determined by two-photon photoemission (2PPE) spectroscopy [43]. Here, a first laser pulse excites electrons from the Fermi level into an image potential state, which is then probed by a time-delayed second laser pulse. Specifically, in an exemplary experiment [41] 70-fs IR probe pulses and frequency-tripled 95-fs UV pump pulses were used to investigate image potential states on the Cu(100) surface. Lifetimes of up to $\tau_6 = 2.0\,\mathrm{ps}$ were found, which scaled according to $\tau_n \propto n^3$, in agreement with theoretical expectations [42].

The lifetime τ of an image potential state may also be inferred from the width Γ of a Lorentzian shaped peak in the photoelectron spectrum via the relation $\Gamma \cdot \tau = \hbar$. In this way, the lifetime of the $n = 1$ image potential state of an Au(111) surface has been experimentally deduced as $\tau_1 = 4\,\mathrm{fs}$ [43], which was in agreement with theoretical calculations [221].

Quantum Beats

A coherent superposition of multiple states may be excited by an ultrashort laser pulse with an associated spectral width spanning across several image potential states. This results in oscillations, which reflect the beating of the associated wave functions with a period corresponding to the energy spacing of the states involved. The observation of such quantum beats manifests the involvement of a set of discrete states and clearly distinguishes the electron signal from electrons originating from a continuous distribution.

Specifically, the wave function associated with a particular state with principal quantum number n evolves in time as

$$\Psi_n(x,t) = \psi_n(x)\exp(-i\omega_n t) \tag{6.3}$$

Here, $\omega_n = E_n/\hbar$ with E_n given by Equation 6.1.

A wave packet of multiple states excited by a pump pulse into a coherent superposition is then given by:

$$\Psi(x,t) = \sum_n a_n \psi_n(x) e^{-i\omega_n t} \tag{6.4}$$

The electron will perform an oscillatory motion in the image potential. A probe pulse maps the image potential states onto continuum states, which propagate as a coherent wave packet partially towards the detector. In particular, if two states are involved and provided there is no loss in coherence, the electron count on this detector will evolve in time as [41]:

$$I(t) \propto |a_n(t)\Psi_n(t) + a_{n+1}(t)\Psi_{n+1}(t)|^2 \tag{6.5}$$

Inserting the expressions for the wave function above and retaining only the real part corresponding to the measured observable yields:

$$I(t) \propto a_n^2 + a_{n+1}^2 + 2a_n a_{n+1} \cos(\omega_{n,n+1} t) \tag{6.6}$$

Here, a_n is the coefficient of the wave function corresponding to the image potential state with principal quantum number n. This coefficient will decay exponentially over time due the limited lifetime of the electron in the image potential state. Superimposed on this decay a beating pattern will be observed, with a beating frequency given by

$$\nu_{n,n+1} = \frac{\omega_{n,n+1}}{2\pi} = \frac{(E_{n+1} - E_n)}{h} \tag{6.7}$$

An example of such a quantum beat measurement on an extended metallic film is shown in Figure 6.3.

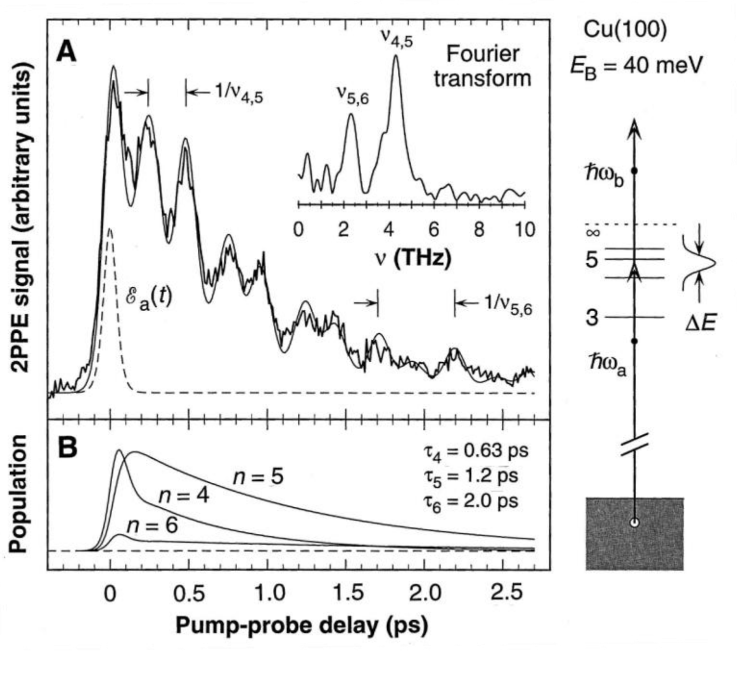

Figure 6.3: Quantum beats associated with the population of image potential states on an extended metallic film. The Fourier transform reveals an oscillatory pattern on top of an overall exponential decay. Here, the decay and the beating periods are associated with the $n = 4$, $n = 5$ and $n = 6$ image potential states. Modified from [41].

7. Numerical Model: The Schrödinger Equation

To gain a deeper understanding of image potential states beyond their well-known properties on extended metallic films, a numerical model has been developed in this thesis, which accounts for the specific features of a metallic nanotip such as its curved geometry and the field enhancement at its apex. For such a nanostructure, image potential states have not been observed so far.

Commonly, image potential states on extended metallic films are calculated in a one-dimensional (1D) model [43,219,220,222] assuming equally spaced potential wells representing the ionic cores of the bulk matched to a Coulomb-like potential outside, as for example displayed in Figure 6.2. Specifying such a potential sets a framework, which the quantum system needs to obey according to the Schrödinger equation. Specifically, to find its stationary eigenstates and their associated electron wave functions, the Schrödinger equation has been solved numerically in this thesis using the software package Matlab.

To draw a comparison between the known properties of image potential states on extended metallic films [41-43] and the numerical implementation developed here, the stationary wave functions corresponding to image potential states are first calculated by solving the time-independent Schrödinger equation in 1D, which is presented in Section 7.1.

In contrast to an extended metallic film, a metallic nanotip exhibits a curved geometry. The spatial variation of the potential perpendicular to the nanotip's axis may influence the nature of the wave functions associated with image potential states. Consequently, in this thesis the time-independent Schrödinger equation model was extended to a two-dimensional (2D) model, as discussed in Section 7.2. The obtained 2D stationary wave functions are compared to the 1D solutions and the possibility of a further quantisation of the wave functions is discussed. However, this approach lacks the enormous density of states in the solid-state material as well as many-body interactions of the electrons. To check the validity of our model, the results are compared to a model based on density functional theory (DFT), which was developed by our colleagues from the theoretical physics groups of Professor Angel Rubio and Professor Esa Räsänen, and makes no initial assumption on the potential.

Having found the stationary states of the quantum system, the next step is to perturb it, for example, by an ultrashort laser pulse. This modifies the potential barrier and induces bound-state and freely propagating electron dynamics. In this thesis, good agreement between the 2D stationary wave functions projected onto the taper axis and the 1D solutions was found, so that a computationally feasible calculation of solving the 1D time-dependent Schrödinger equation was performed in a Crank-Nicolson scheme [223,224], which is presented in Section 7.3. Specifically, this allows for obtaining kinetic energy spectra to be compared to an actual experiment and investigating the temporal structure of the freely propagating electron packet, separated from the bound state electron wave packet by the action of the ultrashort laser pulse. In particular, it is found that preparing the quantum system in a discrete image potential state results in a deeply modulated ATI spectrum, which would indeed support an attosecond electron pulse, as envisaged in Chapter 5.

Furthermore, interesting electron dynamics arise, if a coherent superposition of states is excited leading the quantum beats introduced in Chapter 6. In this section the numerically obtained results are verified by comparison to the analytical solution given in Chapter 6, before they are applied to provide a background vital for the understanding of the experimental observation of discrete image potential states at the apex of a single gold nanotip presented in Chapter 8.

7.1. Stationary Wave Functions in 1D

To relate the results of our numerical model to the well-known properties of image potential states [41,42], let us first calculate the stationary electron wave functions associated with image potential states in a 1D model similar to that commonly used for a metallic film [43,219,220]. The stationary wave functions $\psi(x)$ of a quantum system and their associated energies E are found by solving the time-independent Schrödinger equation:

$$E\psi(x) = H\psi(x) \tag{7.1}$$

Here,

$$H = \left(-\frac{\hbar^2}{2m_e}\frac{\partial^2}{\partial x^2} + V(x)\right) \tag{7.2}$$

is the Hamiltonian of the quantum system, where $V(x)$ is the potential, $\hbar$ is the reduced Planck constant and m_e is the mass of an electron.

1D Potential Representing a Metallic Nanotip

In particular, the potential $V(x)$ is characteristic of the quantum system to be investigated and determines both its stationary eigenstates as well as its further evolution. Here, the system under investigation is a metallic nanotip, which will be modelled in this section in 1D as equally spaced potential wells representing the ionic cores inside the metal matched to a Coulomb-like potential outside. This simplification proposed by Chulkov et al. [219,220] has been shown to resemble realistic surface electron dynamics, which would otherwise require a complex and computationally hardly feasible 3D model [210,222]. It assumes that the charge density and the one-electron potential are constant in a plane parallel to the surface and vary only in the perpendicular direction. This approach has been shown to work well for image potential states on extended metallic films [43,210,222] and shall be adopted here as a first step, before its validity in the case of the curved 2D geometry of a metallic nanotip is investigated in the next section.

Specifically, the 1D potential inside the metal is taken as, similar to [43]:

$$V_c(x) = \phi + \frac{V_c - \phi}{2}\left[1 - \cos\left(\frac{2\pi}{d}x\right)\right], \qquad x \le \frac{d}{2} \tag{7.3}$$

Here, ϕ is the work function, V_c is the crystal potential and d is the spacing of the ionic cores. The gold surface terminates with the last potential well of the bulk, where it is matched to a Coulomb-like potential accounting for the image potential of an electron [42,43]:

$$V_c(x) = -\frac{1}{4}\frac{e^2}{4\pi\varepsilon_0 x}, \qquad x > \frac{d}{2} \tag{7.4}$$

Here, e is elementary charge and ε_0 is the permittivity of free space.

Specifically, the parameters in this model were chosen to match an Au(111) surface, which has been indicated by a detailed analysis of SEM images in our group [225] to represent the surface of the facets converging to the apex of a typical gold nanotip [226] used in our experiments, though different types of facetting may occur at the apex. Furthermore, for an Au(111) surface, specific values are known from the literature as $\phi = -5.55\ \mathrm{eV}$ [43], $V_c = -14.6\ \mathrm{eV}$ [43] and $d = 0.29\ \mathrm{nm}$ as the nearest-neighbour distance in gold with a face-centred cubic (FCC) lattice and lattice constant $a = 407.82\ \mathrm{pm}$ [227]. These values may be different for another surface [220] due to the different work function, which may affect details such as the exact values of the calculated binding energies. Nevertheless, this model shall convey an understanding of the essential physics such as the nature of image potential state wave functions and their subsequent temporal evolution treated in Section 7.3. Furthermore, as sketched in Section 7.2, these assumptions are not made in a DFT model developed by our colleagues from the theoretical physics groups of Professor Angel Rubio and Professor Esa Räsänen supporting the following calculations.

1D Stationary Wave Functions

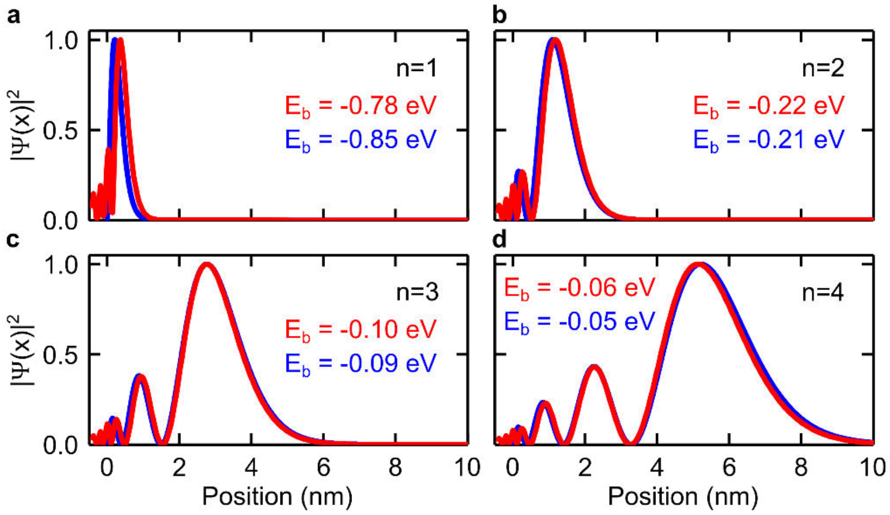

Figure 7.1: Comparison between the analytical (blue) and the numerical (red) wave functions associated with the first four image potential states, here plotted as a probability density. Overall, good agreement is achieved, both qualitatively and quantitatively, including the binding energies E_b. The numerical solutions also account for the bulk potential.

The stationary wave functions are now numerically obtained by discretising the Hamiltonian, writing it in matrix form as outlined in Chapter 10 and solving the eigenvalue equation by Matlab, which is optimised for calculations involving matrices. The probability density of the wave functions is plotted in Figure 7.1 (red curves). It shows a pronounced maximum, which peaks at a further distance away from the surface for increasing principal quantum number n. The numerical wave functions compare well to the analytical solutions (blue curves) associated with image potential states [41,42], as given by Equation 6.2. In contrast to the analytical expression, the numerical model also accounts for the bulk potential. This results in a small deviation of the numerical results from the analytical solution for distances closer to the surface. Furthermore, also the binding energies agree well with theoretical expectations [41-43], as given by Equation 6.1.

7.2. Stationary Wave Functions in 2D

Image potential states are usually calculated in a 1D model potential [43,219,220] as shown in the previous section. In fact, a 3D calculation of image potential states on extended metallic films gives electron wave functions, which resemble those obtained in a 1D approach when averaged over the surface plane [222]. However, such a model does not account for the 2D curvature of a metallic nanotip, which results in a variation of the potential perpendicular to the axis of the nanotip. Consequently, the properties of electron wave functions associated with image potential states in this geometry have not been analysed in detail, yet. In this thesis, the model was therefore extended to 2D to investigate the nature of image potential states at a metallic nanostructure, which have not been observed so far.

2D Potential Representing a Metallic Nanotip

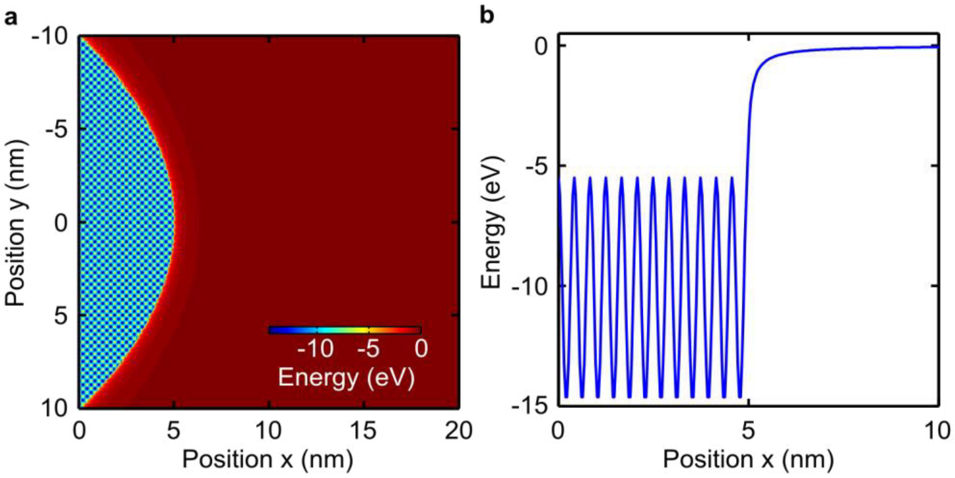

Figure 7.2: Potential of the nanotip in 2D. (a) The ionic cores of the bulk are represented by equally spaced potential wells, terminated by a curved surface, where the bulk potential is matched to a Coulomb-like potential. (b) The potential along the axis of the nanotip, i.e. at $y = 0$, is shown. Modified from [JR5].

In 2D the time-independent Schrödinger equation to be solved is:

$$E\psi(x,y) = H\psi(x,y) \tag{7.5}$$

Here,

$$H = \left(-\frac{\hbar^2}{2m_e}\left(\frac{\partial^2}{\partial x^2} + \frac{\partial^2}{\partial y^2}\right) + V(x,y)\right) \tag{7.6}$$

Specifically, the potential $V(x,y)$ now describes a 2D arrangement of potential wells representing the ionic cores of the bulk:

$$V(x,y) = \phi + \frac{V_c - \phi}{2}\left[1 - \cos\left(\frac{2\pi}{a}x\right)\cos\left(\frac{2\pi}{a}y\right)\right] \tag{7.7}$$

Here, the periodicity is chosen as the lattice spacing a, such that the spacing of potential wells along the diagonal of the 2D grid is equal to the nearest neighbour distance $d = a/\sqrt{2}$. The bulk potential is terminated by a surface describing a hyperboloid, where it is matched to a Coulomb-like potential similar to Equation 7.4, but here with its isopotential lines running parallel to the surface.

To account for the specific geometry of a metallic nanotip its surface is calculated in prolate spheroidal coordinates $1 \leq \xi \leq \infty$ and $-1 \leq \eta \leq 1$ [27]. Here, the surface of the nanotip is assumed to be described by a rotationally symmetric hyperboloid with an apex radius R and a full opening angle θ. In particular, the surface of the nanotip is located at $\eta_0 = \cos(\theta/2)$. This surface is converted into Cartesian coordinates according to the relationships [27]:

$$x(\xi) = k\eta_0\xi \tag{7.8}$$

and

$$y(\xi) = \pm k\sqrt{1-\eta_0{}^2}\sqrt{\xi^2-1} \tag{7.9}$$

In the simulation, $1 \leq \xi \leq 1.1$. Furthermore, $k = \frac{\eta_0 R}{1-\eta_0^2}$ is a scaling parameter influenced by the apex radius of the nanotip. Specifically, the properties of the nanotip are chosen as $R = 10\ \mathrm{nm}$ and $\theta = 20°$, as deduced from the SEM image of a typical gold nanotip used in the experiments, displayed in Figure 4.2.

2D Stationary Wave Functions

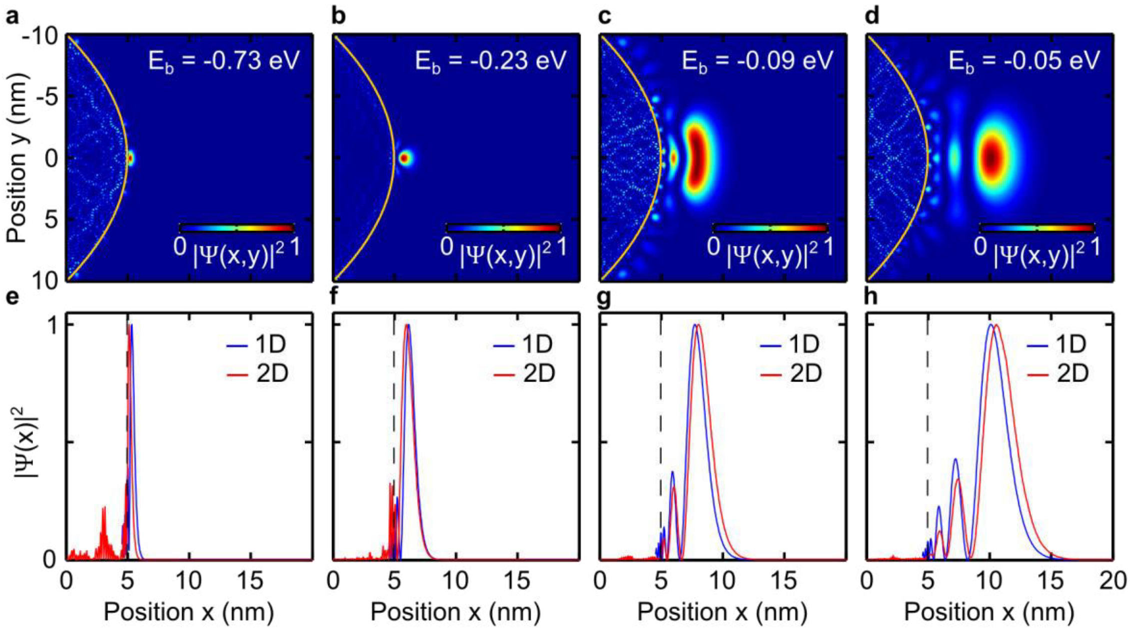

Figure 7.3: (a-d). The probability densities of 2D wave functions arising from the potential described in the main text are shown, which are predominantly located in front of the surface of the nanotip (yellow curve) and display only nodes parallel to the axis of the nanotip, increasing in number from 0 to 3. The highest probability density is found at the outermost maximum. (e-f) The comparison between the probability densities of these 2D wave functions projected onto the taper axis (red curves) and the 1D wave functions obtained in Section 7.1 (blue curves) yields good agreement. Modified from [JR5].

The 2D stationary wave functions are now numerically obtained by discretising the Hamiltonian, writing it in an appropriate matrix form as outlined in Chapter 10 and solving the eigenvalue equation by Matlab. Their probability density is shown in Figure 7.3a-d. Overall, they are localised to the apex region of the nanotip. The number of nodes parallel to the axis of the nanotip increases from 0 to 3, with the outermost maximum located at an increasing distance from the nanotip for increasing principal quantum number n, as for the stationary wave functions obtained in the 1D model in Section 7.1. In fact, a projection of the wave functions onto the axis of the nanotip at $y = 0$ (red curves) closely agrees with the 1D stationary wave functions (blue curves), as shown in Figure 7.3e-h, where the probability density of the wave functions is plotted. Furthermore, also the binding energies obtained from the 2D and the 1D model, as shown in Figure 7.1, closely agree.

Quantisation of the Wave Functions Perpendicular to the Axis of the Nanotip

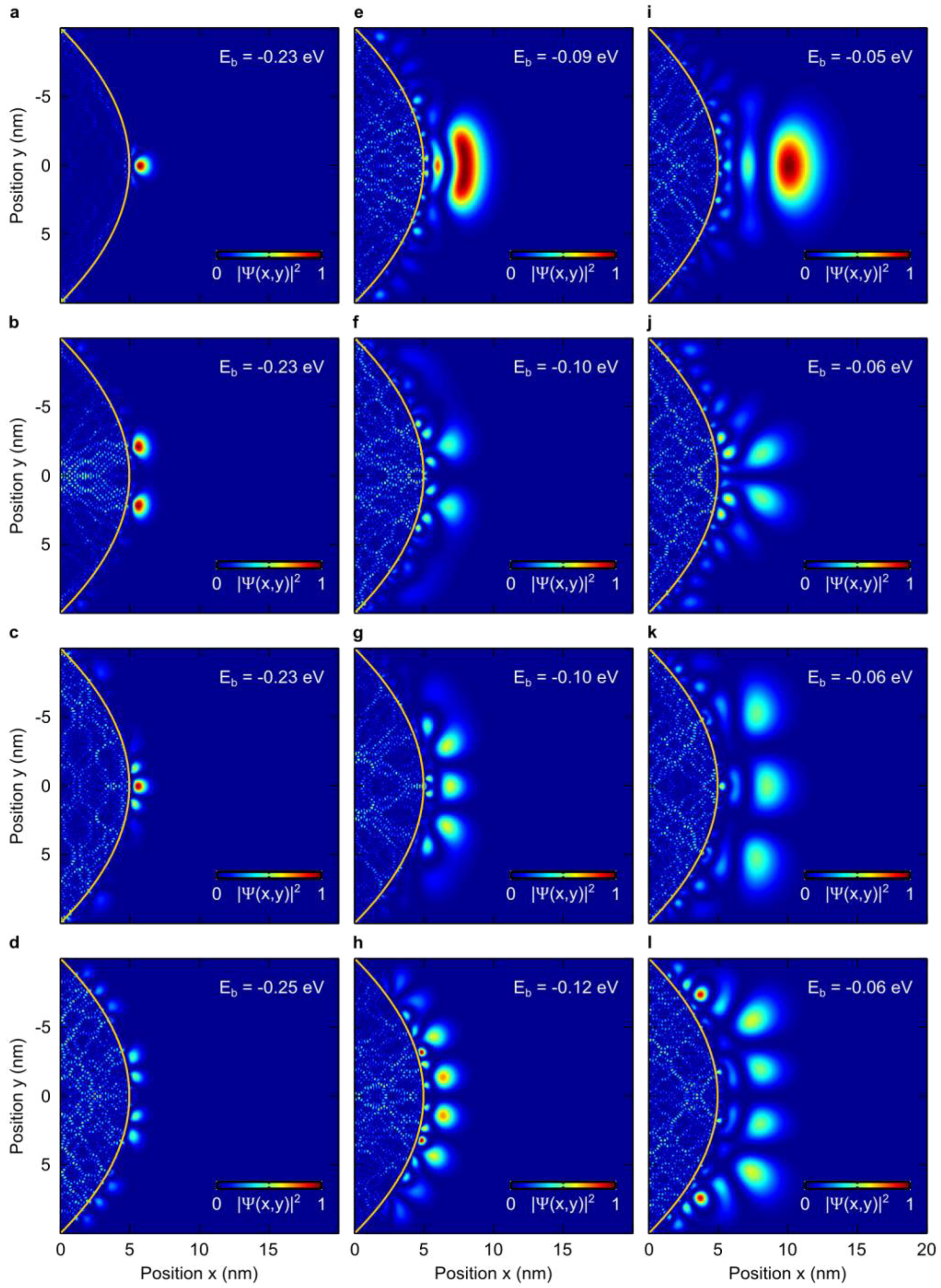

Figure 7.4: Quantisation perpendicular to the tip axis. All panels show the probability density of 2D wave functions predominantly located in front the surface of the nanotip (yellow curve), associated with image potential states. Column wise, the principal quantum number increases from $n = 2$ via $n = 3$ to $n = 4$. Row wise, the number of nodes perpendicular to the tip axis increases from 0 to 3, and with the number of these nodes also the binding energies E_b. Taken from [JR5].

In contrast to an extended metallic film the potential of the metallic nanotip is not constant along the surface. Hence, apart from a principal quantum number n a further quantisation is expected arising from the nanotip's circular symmetry and the variation of the potential perpendicular to the axis of the nanotip. For the investigation of the circular symmetry, a 3D calculation would be required, which is beyond the scope of this thesis. However, in this thesis the influence of the potential variation perpendicular to the axis of the nanotip on the quantisation of the electron wave functions could be deduced. In particular, wave functions were found, which do not only show a quantisation parallel to the axis of the nanotip as displayed in Figure 7.3, but also perpendicular to it. This is shown column for column in Figure 7.4 for the wave functions with principal quantum number $n = 2$, $n = 3$ and $n = 4$, where the probability density of the wave functions is plotted. Row for row, the number of nodes perpendicular to the axis increases from 0 to 3. The binding energies appear to depend only weakly on the number of these nodes and hence only weakly on the component of angular momentum around the axis of the nanotip. In our current experimental setup, described in further detail in Chapter 8, the corresponding energy splitting is too small to be resolved. However, the results of this simulation point to future experiments, in which the momentum distribution of an electron wave function is projected onto a suitable detector, for example, a velocity map imaging [228,229] spectrometer or a delay line detector as currently set up as part of another project in our group. This may result in a direct imaging of electron wave functions associated with individual image potential states.

Stadium Wave Functions

The 2D wave functions shown so far represent only a subset of several hundreds of wave functions corresponding to bound states of the metallic nanotip. The probability density of an exemplary wave function of a further subset of solutions is displayed in Figure 7.5. It shows a complex structure within the nanotip, but no localisation in front of the surface. It resembles a highly excited resonator mode of the metallic nanotip, which is reminiscent of stadium wave functions [230]. The lifetime of a state associated with such a wave function is, however, expected to be extremely short, as the wave function is located mainly inside the nanotip, where it is subject to rapid dephasing processes.

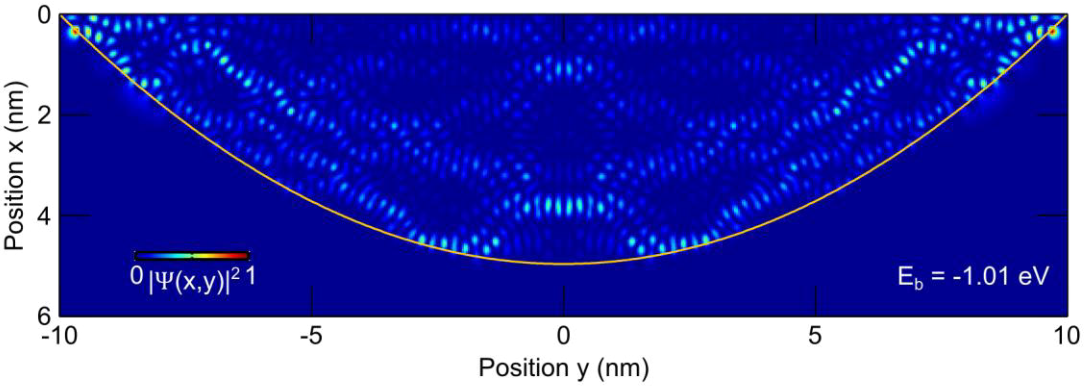

Figure 7.5: Probability density of a 2D wave function corresponding to a bound state of the metallic nanotip with binding energy $E_b = -1.01\ \mathrm{eV}$.

2D Density Functional Theory Model

The Schrödinger equation model presented above, however, is based on making an assumption on the model potential, which inevitably influences the electron dynamics. Furthermore, it neglects the many-body interactions of the electrons within the nanotip. To support the validity of the Schrödinger equation model, our colleagues from the theoretical physics groups of Professor Angel Rubio and Professor Esa Räsänen have developed a 2D density functional theory (DFT) model of the metallic nanotip, which is described in further detail in [JR5]. The DFT is based on the Hohenberg-Kohn theorem [231], which states that the ground state of a many-electron system is determined by the local electron density. As such, this model makes no initial assumptions on the potential, which distinguishes it conceptually from the Schrödinger equation model and makes calculations of many-electron systems computationally feasible. The interaction of the electrons with each other, for example via Coulomb forces or the Paul exclusion principle, is modelled via an exchange-correlation potential in the local density approximation [232-234]. For example, the number of electrons determines the work function, which in this case matches ~5 eV in the case of 5000 electrons. The metallic nanotip is described in a jellium model [235] as a background of positive charge contained in a hyperbolic shape, which is softened at the tip-vacuum boundary and thereby gives rise to a Coulomb-like potential. In this potential weakly bound states have been found with their associated electron wave functions displaying a pronounced electron probability density in front of the nanotip, exemplary shown in Figure 7.6.

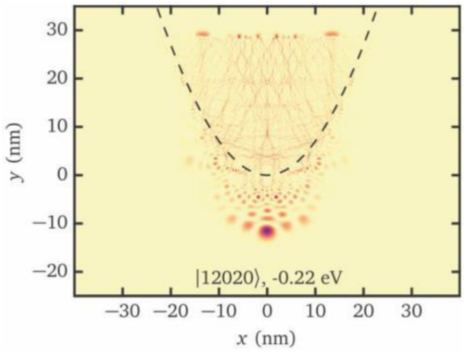

Figure 7.6: Electron density of a weakly bound excited state with binding energy $E_b = -0.22\,\mathrm{eV}$ obtained from the 2D jellium model. Modified from [JR5].

They show an increased number of nodes and a larger spatial extent than the wave functions found in the Schrödinger equation model, but may nevertheless be identified as Rydberg electron wave functions. As such, both models independently confirm the existence of image potential states at the apex of a gold nanotip.

7.3. Time Evolution in 1D and Kinetic Energy Spectra

So far only the stationary properties of wave functions associated with image potential states have been considered. To investigate the electron dynamics induced by the perturbation of the quantum system by an ultrashort laser pulse, the model is now extended in this thesis in order to solve the time-dependent Schrödinger equation. In particular, this extension of the model allows us to investigate the temporal structure of the freely propagating electron wave packet, which is separated from the bound state electron wave packet by the action of the ultrashort laser pulse, and to obtain its kinetic energy distribution, which can be compared to an experimental kinetic energy spectrum.

For this, having established the stationary wave functions in the previous sections, the quantum system is prepared in one of the associated states or a superposition of them. As the projection of the 2D stationary wave functions onto the taper axis closely agrees with the 1D solutions as shown in the Section 7.2, the calculation of the time evolution of the quantum system is carried out using the 1D model potential. Such an approach was computationally feasible within the framework of this thesis.

The time evolution of the quantum system is calculated by solving the time-dependent Schrödinger equation

$$i\hbar\frac{\partial}{\partial t}\psi(x,t) = \left(-\frac{\hbar^2}{2m}\frac{\partial^2}{\partial x^2} + V(x,t)\right)\psi(x,t) \tag{7.10}$$

Here, a time-dependent part of the potential arises from the perturbation of the wave function by an ultrashort laser pulse. Its time-dependent electric field is:

$$E(t) = E_0\cos(\omega_0 t + \varphi_{CE})e^{-2\ln 2(t/\tau_{FWHM})^2} \tag{7.11}$$

Here, E_0 is the peak electric field strength, $\omega_0 = 2\pi c/\lambda_0$ is the centre carrier angular frequency, c is the speed of light, λ_0 is the centre wavelength, φ_{CE} is the CEP and τ_{FWHM} is the pulse duration.

The resulting time-dependent potential is then given by:

$$V_E(x,t) = -exE(t)s(x), \qquad x > \frac{d}{2} \tag{7.12}$$

Specific to the experiments presented in this thesis and in contrast to an extended metallic film, an incident electric field is enhanced at the apex of a metallic nanotip, as explained in Chapter 4. This feature is accounted for by including a spatial function

$$s(x) = 1 + (f-1)e^{-x/x_{nf}} \tag{7.13}$$

In particular, in the simulation it was assumed, that an incident electric field is enhanced by factor $f = 9$ for illumination with NIR laser pulses and decays over a length scale $x_{nf} = 3\ \mathrm{nm}$ [38]. Physically, the electric field should fulfil the continuity condition at the tip-vacuum boundary. However, the NIR electric field inside the nanotip is negligible as explained in Chapter 4. In the simulation, it has therefore been neglected, which is not expected to influence the results.

The combined potential is then given by $V(x,t) = V_c(x) + V_E(x,t)$. Here, $V_c(x)$ is the time-independent potential arising from the periodic potential wells representing the ionic cores matched to a Coulomb-like potential outside, as discussed in Section 7.1.

Numerical Implementation via the Crank-Nicolson Method

Numerically, the time dynamics of the quantum system is calculated using the Crank-Nicolson method [223]. In an iterative algorithm the wave function at a subsequent time step $\psi(x,t_{n+1})$ is calculated by operating on the wave function at the previous time step $\psi(x,t)$ according to:

$$\left(1 + \frac{1}{2\hbar}iH\Delta t\right)\psi(x,t_{n+1}) = \left(1 - \frac{1}{2\hbar}iH\Delta t\right)\psi(x,t) \tag{7.14}$$

Here, the Hamiltonian H is given by Equation 7.2, with the static potential there replaced by a varied potential for each time step here. In the numerical implementation it is a tridiagonal matrix, i.e. a matrix with non-zero elements on its main diagonal, subdiagonal and superdiagonal only. Hence, this set of equations is solved very efficiently using a tridiagonal matrix algorithm [223], which was implemented into the numerical simulation in this thesis.

Furthermore, Δt is the step size in time. Typically, the simulation is carried out with a numerical resolution of $\Delta x = 37.6\ \mathrm{pm}$ and $\Delta t = 5.80\ \mathrm{as}$, obeying the stability criterion $\Delta t < (\Delta x)^2/2$ [223] in atomic units, in which the simulation is run. The numerical grid was discretised into 4800 spatial and 27596 temporal elements, spanning an interval of 180 nm space and 160 fs in time. In particular, the large spatial extent was chosen, such that the electron wave function propagates for 100 fs after the peak of the laser pulse without reaching the fully reflective grid boundaries. The peak of the laser pulse was typically set at $t = 60\ \mathrm{fs}$ to include all significant optical cycles.

Comparison of the Numerical and the Analytical Solution

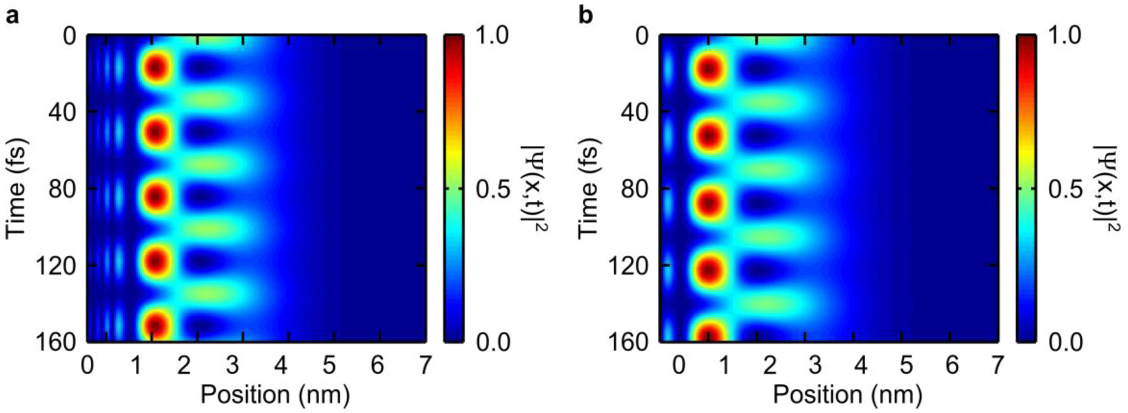

Figure 7.7: The comparison between the time evolution of an unperturbed (a) numerical and (b) analytical wave packet yields good agreement. The wave packet was prepared in a superposition of the $n = 2$ and $n = 3$ image potential states. The probability density is plotted linewise for each subsequent time step.

To check the numerical implementation, the time evolution of an unperturbed wave packet prepared in the $n = 2$ and $n = 3$ image potential states is calculated by running the Crank-Nicholson algorithm, as shown in Figure 7.7a. Here, each line in the plot represents the spatial probability density of the wave function at a subsequent step in time. It can be seen, that the amplitude of the electron wave function oscillates between two extremes corresponding to an alternating population of the $n = 2$ and the $n = 3$ image potential states. The period of this oscillatory motion is given by the energy spacing of these states according to Equation 6.7. Quantitatively, the simulation yields for the binding energies $E_2 = -0.22\ \mathrm{eV}$ and $E_3 = -0.10\ \mathrm{eV}$ corresponding to a beating frequency $\nu_{2,3} = 34\ \mathrm{fs}$. This is in excellent agreement with the analytical solution, which was calculated according to Equation 6.4 and is displayed in Figure 7.7b. Analytically, the binding energies are taken according to Equation 6.1 as $E_2 = -0.85\ \mathrm{eV}/2^2 = -0.21\ \mathrm{eV}$ and $E_3 = -0.85\ \mathrm{eV}/3^2 = -0.09\ \mathrm{eV}$, giving a beating period of $\nu_{2,3} = 34\ \mathrm{fs}$. In summary, the Crank-Nicolson scheme to solve the time-dependent Schrödinger equation implemented in this thesis can be confidentially applied to explain the experimental observations presented in Chapter 8.

Perturbation of the Quantum System by an Ultrashort Laser Pulse

To provide a background vital for the understanding of these experiments, the next step is now to gain a deeper insight into the implications of perturbing the quantum system by an ultrashort laser pulse. In particular, the temporal evolution of a released electron wave packet and its kinetic energy distribution is investigated more closely in the following. For this, the quantum system is initially prepared in the $n = 2$ state. This assumption mimics the action of a pump pulse, which is assumed to have excited an electron from the broad distribution of states near the Fermi level into an image potential state. This situation is shown in Figure 7.8a. Here, each line in the plot represents the spatial probability density of the electron wave function at a subsequent step in time. As the chosen $n = 2$ state is an eigenstate of the quantum system, the wave function is stationary and does not change in the beginning of the simulation. The quantum system is then perturbed by a 25-fs near-infrared laser (NIR) pulse centred at 1600 nm, with the maximum of its electric field set at $t = 60\ \mathrm{fs}$. This causes a freely propagating electron wave packet to separate from the bound state electron wave function and subsequently to propagate away from the surface. In particular, in each optical cycle a small fraction splits from the bound state electron wave packet. The electric field strength increases for each optical cycle until the main cycle is reached, after which it decreases again. This causes fractions of the wave packet released in different optical cycles to propagate at a different speed. Consequently, different fractions subsequently interfere with each other in space. Analysing this freely propagating electron wave packet the following conclusions arising from this situation are drawn, which are important in the framework of this thesis and for an understanding of the experimental observations to be described in Chapter 8.

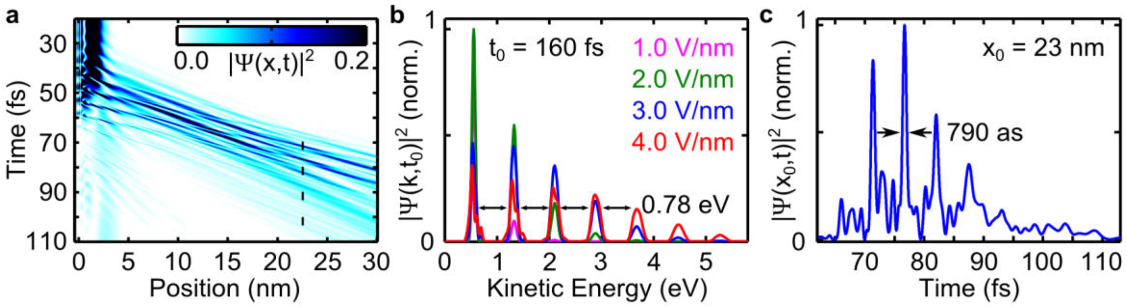

Figure 7.8: (a) Time evolution of a quantum system prepared in the $n = 2$ image potential state: A freely propagating electron wave packet separates from the bound state electron wave packet under the influence of a 25-fs NIR laser pulse. (b) The kinetic energy distribution of the released electron wave packet reveals up to 7 peaks separated by the NIR photon energy, which increase in number with the electric field strength. (c) Extracting the probability density at a fixed position shows a train of attosecond electron pulses. Modified from [JR5].

Photoelectron Kinetic Energy Spectra

First, the momentum ($p = \hbar k$) distribution of the freely propagating electron wave packet in space is obtained at a fixed time, typically $t_{fixed} = 160\ \mathrm{fs}$, by its Fourier transformation according to the relation

$$\widetilde{\Psi}(k, t_{fixed}) = \frac{1}{\sqrt{2\pi}} \int \Psi(x, t_{fixed})\, e^{-ikx} dx \tag{7.15}$$

Using the relation $E_{kin} = \frac{p^2}{2m_e} = \frac{\hbar^2 k^2}{2m_e}$, its probability density $\left|\tilde{\Psi}\left(k, t_{fixed}\right)\right|^2$ represents a kinetic energy spectrum. For this, a freely propagating electron wave packet is defined for positions $x \geq 25\ \mathrm{nm}$ to keep it well separated from bound electron wave packets.

In particular, as shown in Figure 7.8b, the kinetic energy spectra display distinct peaks separated by the photon energy of the perturbing 25-fs NIR laser pulse, increasing in number with the electric field strength, here calculated from $fE_0 = 1\ \mathrm{V/nm}$ to $fE_0 = 4\ \mathrm{V/nm}$. This modulation is explained in the framework of ATI discussed in Chapter 5. Here, the deep modulation contrast arises, because the quantum system was initially prepared in a discrete state, in this case an image potential state.

In the experiments presented in Chapter 8 a higher electric field strength is typically applied. To draw a comparison to this situation, a further simulation was performed. Here, the quantum system was initially prepared in the $n = 2$ state and perturbed by an 18-fs NIR laser pulse typically used in the experiments. For an electric field strength $fE_0 = 4\ \mathrm{V/nm}$ the spectra display eight peaks and do not vary considerably with the CEP as shown in Figure 7.9a. For an electric field strength $fE_0 = 7\ \mathrm{V/nm}$, 12 peaks can be discerned as shown in Figure 7.9b. Here, a more complex structure and a strong dependence on the CEP can be identified. As demonstrated in Chapter 3, our experimental setup provides a residual shot-to-shot CEP instability of ~800 mrad, which may be a limiting factor in the experiments presented in Chapter 8.

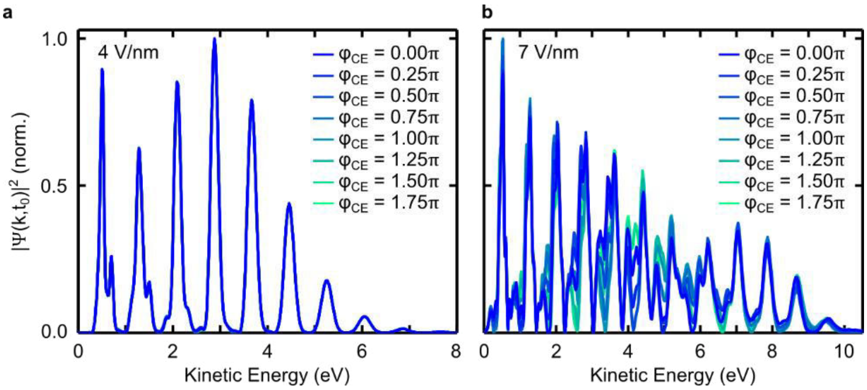

Figure 7.9: Simulated kinetic energy spectra obtained by perturbing the quantum system initially prepared in the $n = 2$ state with an 18-fs NIR pulse for eight settings of the CEP. (a) For a peak electric field strength $fE_0 = 4\ \mathrm{V/nm}$, no influence of the CEP is visible. (b) For a peak electric field strength $fE_0 = 7\ \mathrm{V/nm}$, the spectra change considerably with the CEP.

Temporal Structure of the Electron Wave Packet

Next, extracting the probability density of the wave packet at a fixed position in space, here at a distance $x = 23\ \mathrm{nm}$ in front of the surface and after perturbation of the initial $n = 2$ state with a 25-fs NIR laser pulse with electric field strength $fE_0 = 4\ \mathrm{V/nm}$, shows the release of a train of electron pulses, displayed in Figure 7.8c. Closer inspection reveals that the FWHM of an individual electron pulse is 790 as. This simulation thereby indicates, that a deeply modulated ATI spectrum as displayed in Figure 7.8b may indeed sustain a train of attosecond electron pulses, as envisaged in Chapter 5. So in summary, both a deeply modulated ATI spectrum and a train of attosecond electron pulses are obtained by assuming electron emission from a discrete initial state such as an image potential state.

Population of Image Potential States

Here, the question now arises, how image potential states may be populated, as the electrons in a metallic nanotip usually occupy states near or below the Fermi level. In fact, our 1D Schrödinger equation model, like in 2D, does not only yield weakly bound states, which may be associated with image potential states, but also states with a higher binding energy. Exemplary, the probability density of a wave function associated with such a bound state with a binding energy $E_b = -5.04\ \mathrm{eV}$ is shown in Figure 7.11a. In contrast to the probability density of wave functions associated with image potential states it is mainly located within the bulk with only a small fraction of the wave function leaking out.

Let us now consider a quantum system initially prepared in this state and perturb it by an 18-fs NIR laser pulse of variable peak electric field strength, which translates by Equation 10.5 into an intensity and by Equations 4.21 and 4.22 into a Keldysh parameter γ. Integrating over the calculated kinetic energy spectra gives the electron yield, plotted in Figure 7.10. It scales with a nonlinearity $5.04\ \mathrm{eV}/0.78\ \mathrm{eV} = 6.46$ for $\gamma \ll 1$, which is attributed to the regime of multiphoton ionisation explained in Chapter 4. However, in this case no assumption on the quantisation of the NIR light field was made. Here, this behaviour emerges in a wave picture from a quantum system obeying the Schrödinger equation. Furthermore, the transition to the strong-field regime can be identified as a soft kink in the electron yield for $\gamma \rightarrow 1$.

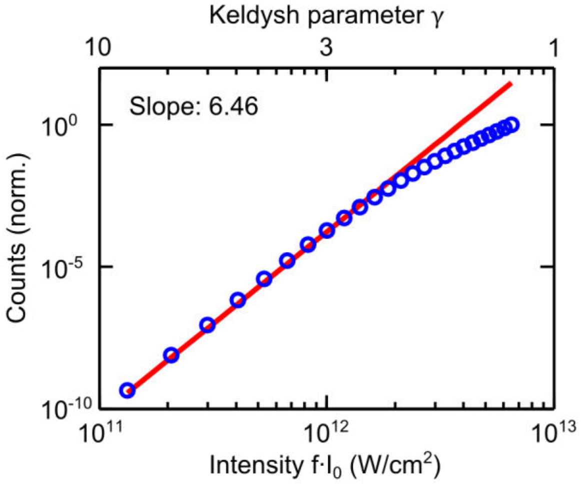

Figure 7.10: Calculated electron yield by preparing the quantum system in a bound state with binding energy $E_b = -5.04\ \mathrm{eV}$ and perturbing it with an 18-fs NIR laser pulse. The electron yield scales with a nonlinearity of 6.46 and shows a soft kink, as the Keldysh parameter explained in Chapter 4 is lowered.

Finally, let us look more closely at what happens during the presence of the NIR light field. Here, the peak electric field strength is now fixed to $fE_0 = 4\ \mathrm{V/nm}$. The incident electric field will induce an oscillatory back-and-forth motion of the wave function associated with the bound state. During the course of its oscillatory motion it will eventually overlap with wave functions associated with image potential states with their probability density located further in front of the surface as depicted in Figure 7.11a. In this way, image potential states are transiently populated. This can be quantified by calculating the coefficients of their associated wave functions $\psi_n(x)$ according to:

$$c_n = \sqrt{|\langle\psi_n(x)|\Psi(x,t)\rangle|^2} \qquad (7.16)$$

Here, n is the principal quantum number and $\Psi(x,t)$ is the total wave function. Exemplary, the evolution of the coefficients of the $n = 2$ and $n = 3$ wave functions in time is plotted in Figure 7.11b. Initially, both coefficients are zero, because the quantum system is solely prepared in the bound state with binding energy $E_b = -5.04\ \mathrm{eV}$. The action of the laser pulse then causes an oscillatory variation of the coefficients, which indicates a transient population of image potential states associated with the wave functions. After the laser pulse is over, the total wave function consists to a small fraction of wave functions associated with the image potential states with principal quantum numbers $n = 2$ and $n = 3$. In the real experiment, their coefficients would decay exponentially due to the finite lifetimes of the associated states, which are not included in this simulation.

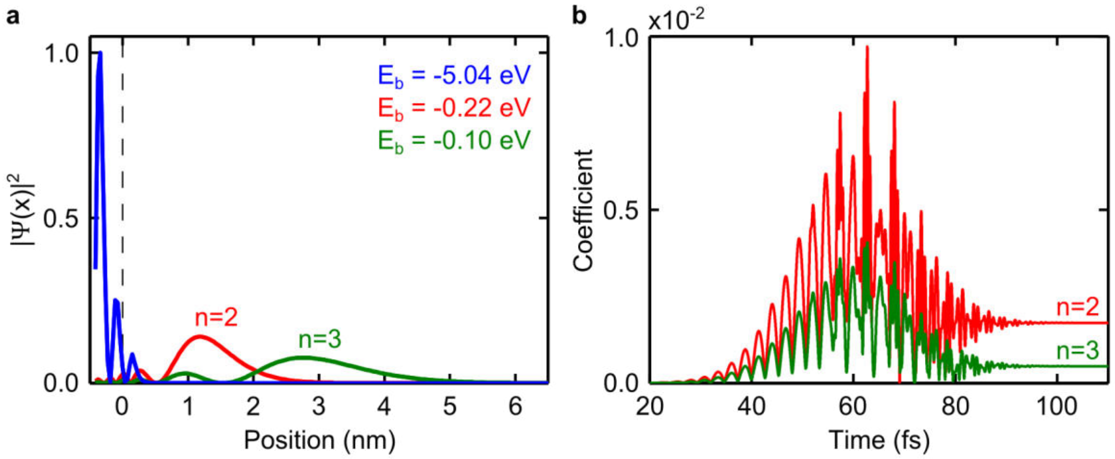

Figure 7.11: (a) The probability density of the wave function associated with a bound state with binding energy $E_b = -5.04\,\mathrm{eV}$ (blue curve) is predominantly located within the bulk, which contrasts the probability density of wave functions associated with image potential states (red and green curves). (b) The coefficients of the wave functions associated with the $n = 2$ and $n = 3$ image potential states show their transient population during the presence of an 18-fs NIR laser pulse of peak electric field strength $fE_0 = 4\,\mathrm{V/nm}$, of which a small fraction remains thereafter. The quantum system was initially prepared in the bound state with $E_b = -5.04\,\mathrm{eV}$.

The same arguments explaining the population of image potential states also hold true for another colour such as associated with a VIS or an IR laser pulse. Note, that the transient population of image potential states may provide an alternative explanation of above-threshold photoemission reported for tungsten nanotips [39,40] as explained in Chapter 4, for which, however, no further evidence was found in a follow-up two-colour photoemission study carried out with an experimental setup providing laser pulses with a duration of ~70 fs [236]. In fact, a second colour is needed to reveal the subtle population of image potential states, which would otherwise be masked by the photoemission of electrons due to a change in intensity associated with the interference of two laser pulses of the same colour. Moreover, a weaker field enhancement is expected for illuminating a gold nanotip with VIS laser pulses as explained in Chapter 4, such that weakly bound image potential states are more likely to survive in the VIS light field than in the strongly enhanced NIR light field. In this thesis, a two-colour pump-probe scheme with 9-fs VIS laser pulses and 18-fs NIR laser pulses is devised to realise the population and observation of image potential states at a single gold nanotip experimentally, which will now be presented in Chapter 8.

8. Two-Colour Pump-Probe Spectroscopy

To investigate the ultrafast dynamics of electrons photoemitted in a two-step process from a single gold nanotip introduced in Chapter 4 a two-colour pump-probe spectroscopy scheme was established as part of this thesis. In particular, the experimental strategy is to excite electrons into image potential states, discussed in Chapters 6 and 7 at the apex of the gold nanotip with a visible (VIS) pump pulse and thereby decouple them from the broad distribution of states near the Fermi level. Subsequently the electrons shall be photoionised and driven in the strongly enhanced electric field of a near-infrared (NIR) probe pulse to facilitate above-threshold ionisation (ATI), explained in Chapter 5. For this, the VIS pulses are generated in the first stage of the NOPA system discussed in Chapter 3, while the NIR pulses originate from the subsequent difference frequency generation process.

8.1. Experimental Setup

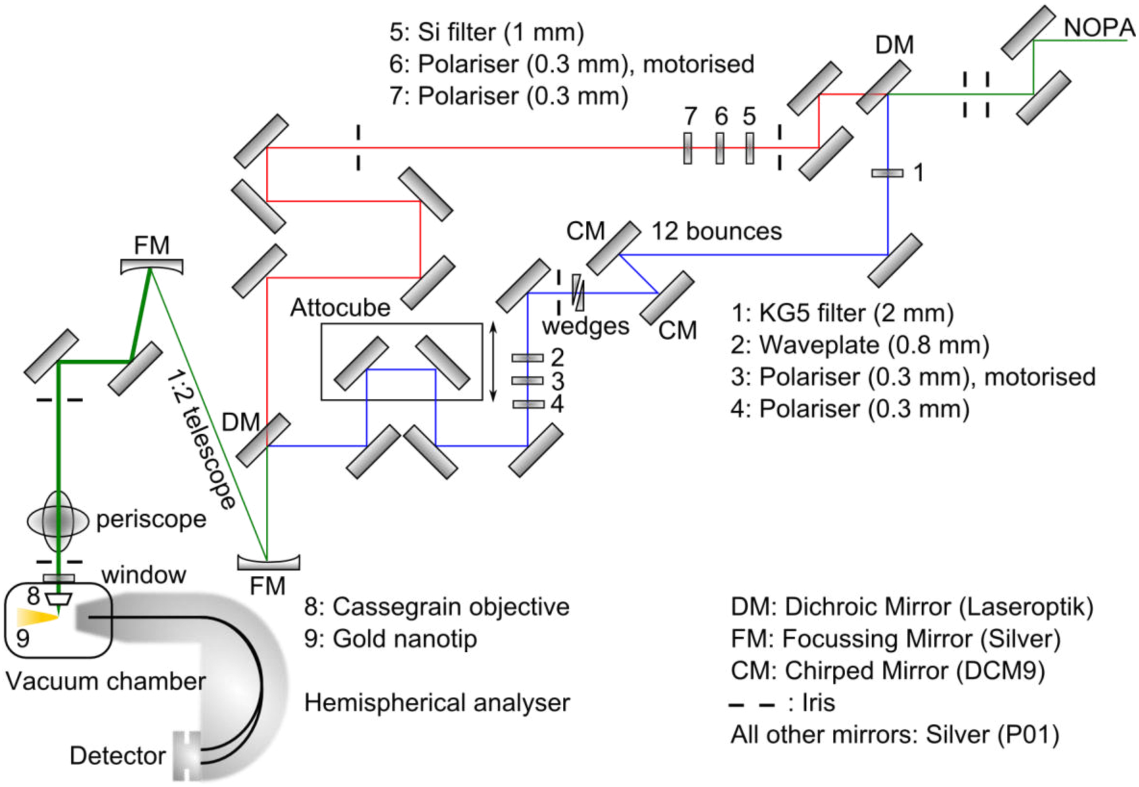
5: Si filter (1 mm)
6: Polariser (0.3 mm), motorised
7: Polariser (0.3 mm)
DM
NOPA
7 6 5
1
CM
12 bounces
FM
Attocube
wedges
CM
2
3
4
1: KG5 filter (2 mm)
2: Waveplate (0.8 mm)
3: Polariser (0.3 mm), motorised
4: Polariser (0.3 mm)
1:2 telescope
DM
periscope
window
8
9
FM
Vacuum chamber
Detector
8: Cassegrain objective
9: Gold nanotip
Hemispherical analyser
DM: Dichroic Mirror (Laseroptik)
FM: Focussing Mirror (Silver)
CM: Chirped Mirror (DCM9)
– – : Iris
All other mirrors: Silver (P01)

Figure 8.1: Two-colour pump-probe setup. The output pulses from the NOPA system are split into a NIR and a VIS path. In both arms, spectral control by optical filters and polarisation control is implemented. Additionally, dispersion management and a variable delay is introduced into the VIS arm. Spatially and temporally overlapped, the expanded pulses are focussed by a Cassegrain objective on the gold nanotip housed in a vacuum chamber. Photoemitted electrons are recorded with a photoelectron spectrometer.

The VIS and NIR laser pulses leave the NOPA system on roughly the same path, which is fixed by adjusting the VIS pulses through a pair of irises. In this way, changes to the NOPA system do not influence the following optical setup. For controllable individual manipulation as outlined below, they are separated from each other and later recombined as shown in Figure 8.1 by dichroic beam splitters (Laseroptik, HR200-900nm HT1300-2500nm). After recombination they are expanded by a telescope, such that they can be optimally focussed onto the apex of the gold nanotip by an all-reflective Cassegrain objective (Davin X36, NA=0.5) with a working distance of 8.6 mm. The technical arrangement of the mirrors in this objective results in a fraction of the laser pulses being blocked. However, in contrast to a lens or microscope objective, the use of an all-reflective Cassegrain objective avoids both chromatic dispersion, which would lengthen the pulses in time, and chromatic aberration, which would result in a wavelength-dependent location of the focal spot.

In the NIR path a silicon filter (Edmund Optics, 1.05 µm IR long pass filter, OD>3) removes the remaining VIS light. Then two polarisers (Codixx, colorPol IR 1300 BC5) facilitate the adjustment of the pulse energy allowed onto the apex of the nanotip. For this, the second polariser is fixed to transmit horizontally polarised light. The first polariser is rotatable and allows for adjusting the fraction of the horizontally polarised component. Here, an additional pair of irises ensures, that also the NIR beam path stays the same through the optical setup.

In the VIS path a 2-mm thick absorbing coloured glass filter (Schott, KG5) removes the remaining NIR light. Next, the VIS pulses are compressed by 12 bounces between a pair of chirped mirrors (Laser Quantum, DCM9) followed by a pair of fused silica wedges for fine tuning the dispersion compensation. This dispersion management is not necessary in the NIR path, as it is done in the NOPA system itself, as described in Chapter 3 and published in [JR1]. After the dispersion management an iris filters out stray light, for example, from back reflections. Next, an achromatic $\lambda/2$ wave plate (Bernhard Halle Nachfl., RAC 4.2.15L) allows for turning the polarisation of the VIS laser pulses from vertical, as emerging from the NOPA system, to horizontal, if desired. It is followed by a pair of polarisers (Codixx, colorPol VIS 600 BC4 CW01), with which the pulse energy is controlled like in the NIR path. Finally, to allow for time-resolved measurements with a controllable delay between the VIS and NIR pulses an optical delay line is introduced in the VIS path. For this, a retroreflector is mounted onto a motorised stepper positioner (Attocube, ECS3030) with a travel range of 20 mm and a minimum step size of 50 nm. It sits on top of a manual stage (Newport, M-UMR5.25) with a travel range of 25 mm. The reason for this configuration is beam pointing stability, which is explained later in this section.

Spatial and Temporal Overlap

To illuminate the apex of a gold nanotip with a controlled sequence of VIS and NIR laser pulses, both their spatial and temporal overlap need to be established. Before the temporal overlap can be found, the spatial overlap of both laser pulses is adjusted. For this, both pulses are aligned through a pair of irises over a long path in the laboratory and then even finer onto the apex of the nanotip. This second step is monitored by observing the number of photoemitted electrons from the nanotip, here with a photoelectron spectrometer explained later in this section. For this, the spatial overlap of the apex of the nanotip with the focal spot of the laser pulses needs to be found. In this alignment procedure, the nanotip is positioned coarsely by DC motors and in finer steps over a distance of up to 100 µm by a three-dimensional piezo scanner (PI Nanocube). First, for a newly installed nanotip low-intensity light from the VIS pulses is used to observe a shadow image of the nanotip by visual inspection on a piece of paper outside the vacuum chamber. Second, low-intensity light from the NIR pulses is taken to find the apex of the nanotip by observing the transmitted light on a power meter. Third, the intensity of the NIR pulses is increased, such that electron emission localised to the apex of the nanotip occurs. The electron count is observed with the photoelectron spectrometer and optimised to its maximum value. Blocking the NIR path and now allowing the VIS laser pulses onto the apex of the nanotip should result in a similar electron signal, which may need to be optimised by slightly readjusting the VIS laser pulses.

Having established the spatial overlap of the laser pulses, the next step is to find their temporal overlap. As the VIS and NIR laser pulses do not interfere with each other, the usual approach of observing interference fringes in adjusting a Mach-Zehnder interferometer does not work. Therefore, a different approach has to be found for a two-colour setup. One simplification in solving this problem arises from the geometrical layout of the beam paths. Ideally, this layout resembles a square, such that the optical paths will naturally be equal. This requirement is also fulfilled, if the laser pulses never travel backwards. However, this cannot be ensured in two instances. First, the VIS pulses need to be recompressed by a pair of chirped mirrors, between which the VIS pulses bounce back and forth. Second, a delay is introduced in the VIS path, which involves a retroreflector. The extra path length travelled by the VIS pulses in these parts of the setup can, however, be measured. It is compensated for by introducing a fixed delay line in the NIR path.

In this way, the path lengths are now similar and can be made roughly equal by carefully moving the manual stage beneath the retroreflector in the VIS path. In the temporal overlap of both laser pulses the electron signal as monitored for finding the spatial overlap with the apex of the nanotip should increase significantly. For this, the integration time of the CCD camera of the photoelectron spectrometer is set to 1 s and the manual stage is moved in steps of about 500 µm. If both pulses were temporally overlapped during moving the manual stage, an increase in the electron signal would be observed on the detector, as the CCD camera integrates over the duration of moving the stage. In this way, the time overlap may be roughly found. The fine tuning can now be done by moving the motorised stepper positioner, which is controlled by a software.

The next task is now to check that driving the motorised stepper positioner does not change the beam pointing in such a way, that the spatial overlap between the focal spot of the laser pulses and the apex of the nanotip would be lost. The accuracy of movement of the motorised stepper positioner over a length of travel of 10 mm is specified by a pitch angle of <100 µrad. This means, that a laser beam travelling over a distance of 1 m after the retroreflector mounted on the motorised stepper positioner would become displaced by <100 µm. Clearly, keeping a laser focus, which is ~2 µm in diameter, overlapped with the nanometre-sized apex of the gold nanotip is not a trivial task. Therefore, the motorised stepper positioner is operated around its centre position only. Any coarse adjustment of the delay is done by moving the manual stage, onto which the motorised stepper positioner is mounted. To exclude the possibility, that an increase in electron yield attributed to the temporal overlap of the VIS and NIR laser pulses did not accidently occur by moving the focal spot of the VIS laser pulses across the nanotip, a wide scan and a fine scan were performed. They are carried out by illuminating the apex of the gold nanotip with a time-delayed sequence of VIS and NIR laser pulses.

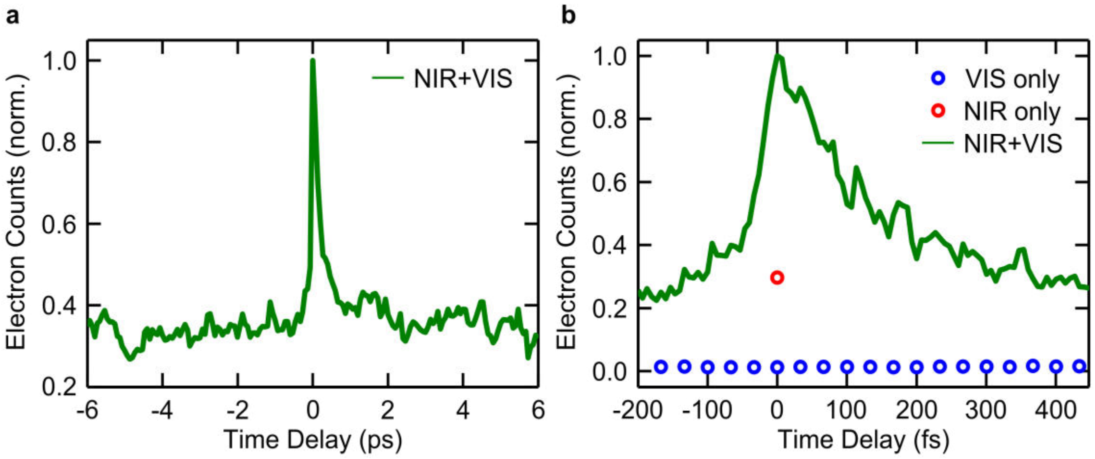

Figure 8.2: Finding the time overlap by illuminating a gold nanotip with a sequence of time delay VIS and NIR laser pulses (green curves). (a) A wide scan reveals, that the increase in electron yield is the only outstanding signal within a time range of 12 ps, and may be attributed to the temporal overlap of the VIS and NIR pulses. (b) The exact time overlap is found via a fine scan. Measuring the electron yield due to the delayed VIS laser pulses (blue circles) shows, that the increase in electron yield is not an artefact due to moving the motorised stepper positioner. For comparison, the electron yield due to the NIR laser pulses (red circle) is also shown.

As shown in Figure 8.2a, for a wide scan a distinct increase in the electron yield is found at one position of the motorised stepper positioner only. To determine a more exact position of the time overlap, the motorised stepper positioner is moved around this position in a fine scan. The NIR laser pulses are then blocked, and the gold nanotip is illuminated with the delayed VIS laser pulses only to check, that moving the motorised stepper positioner has not caused the increase in electron yield. As can be seen in Figure 8.2b, the electron signal from VIS illumination only (blue circles) did not change significantly while moving the motorised stepper positioner. A discussion of the experimental features present in this measurement signal will be given in Section 8.2.

For comparison, a time delay of 6.7 fs corresponds to moving the motorised stepper positioner by a distance of 1 µm, which the light beam travels twice due to the retroreflector on the motorised stepper positioner. During a typical fine scan over a time interval of ~1 ps, the motorised stepper positioner travels only ~150 µm around its centre position, such that beam pointing instability does not influence the measurement.

Electron Detection

Having established photoemission from the gold nanotip with a controllable sequence of VIS and NIR laser pulses, the next part of the setup is the analysis of the photoemitted electrons. This task is carried out with a photoelectron spectrometer (Phoibos 100, Specs), operated in a medium magnification mode, which gives access to both the number and the kinetic energy of the electrons. It consists of three main parts.

First, a system of electromagnetic lenses focusses the electrons via an intermediate image onto an entrance slit. For proper focussing of the electrons, the nanotip has to be placed 40 mm away from the first lens, such that the electrons originate from the focal plane of the electromagnetic lens system. To ensure that electrons enter the lens system on a well-defined axis, the perpendicular component of the Earth's magnetic field deflecting the photoemitted electrons is cancelled by a pair of Helmholtz coils. Furthermore, the nanotip is held at a small DC bias voltage of -50 V to assist the electrons in their propagation towards the photoelectron spectrometer.

Second, after passing the entrance slit the electrons are deflected into elliptical trajectories in a hemispherical analyser. Here, only electrons with a specified pass energy will travel around the whole half sphere towards the detector. Slow electrons will approach the inner part of the hemisphere, while high energy electrons hit the outer hemisphere.

Third, having passed the hemispherical analyser electrons are distributed according to their kinetic energy onto different regions of the detector. It consists of an assembly of two micro-channel plates (MCP) in chevron configuration and a phosphor screen. In an MCP thin conductive glass capillaries act as secondary electron multipliers. The capillaries are about 10 µm in diameter and aligned at an angle to the plate. Electrons will therefore hit the walls of the capillaries and eject further electrons by impact ionisation. This happens in the presence of a strong electric field by applying a voltage of 1300 V between both sides of the plate. After passing the MCP assembly the original electron signal has been amplified by several orders of magnitude. This bunch of electrons now impinges on a phosphor screen, which is held at a potential of 3000 V. Here, the impact of the accelerated electrons causes the emission of light via phosphorescence.

8.2. Above-Threshold Ionisation of Rydberg Electrons

The two-colour pump-probe spectroscopy scheme described in the previous section is now applied to investigate the ultrafast dynamics of electrons photoemitted from a single gold nanotip with the experimental strategy outlined in the introduction to this chapter. The discussion in this section closely follows the manuscript prepared for publication in a peer-reviewed journal [JR5].

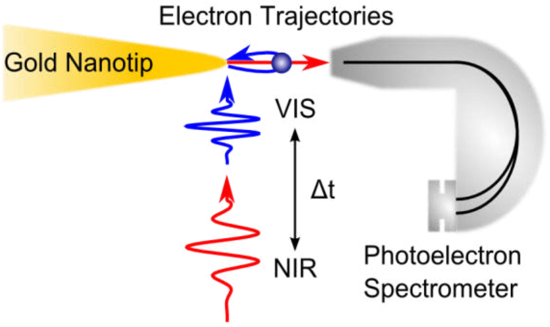

Figure 8.3: The apex of a single gold nanotip is illuminated with a precisely time sequence of a visible (VIS) and a near-infrared (NIR) femtosecond laser pulse. Photoelectron kinetic energy spectra are recorded with a photoelectron spectrometer. Modified from [JR5].

In particular, as shown schematically in Figure 8.3 the apex of a single gold nanotip ($R = 10\ \mathrm{nm}$, $\theta = 20°$), further discussed in Chapter 4, was illuminated with a precisely timed sequence of VIS and NIR laser pulses, as characterised in Chapter 10. The 9-fs VIS pulses are centred in wavelength around ~600 nm and perpendicularly polarised with respect to the axis of the nanotip. Their task is to decouple electrons from the broad distribution of states near the Fermi level by multiphoton absorption and excite them into long-lived image potential states in a process elucidated in a wave picture in Chapter 7. To achieve an efficient population of image potential states, but to suppress electron photoemission in this step as much as possible, the VIS pulse energy is adjusted to the point, at which photoemission starts to set in. Subsequently, 18-fs NIR pulses centred in wavelength around ~1600 nm and polarised parallel to the axis of the nanotip then induce strong-field photoionisation, exploiting the enhancement of the electric field in the apex region of the gold nanotip. Here, a trade-off between a pulse energy as low as possible to supress one-colour electron emission, but as high as possible to induce strong-field phenomena is required. Furthermore, a high pulse energy may induce a variation in the nanotip‘s radius of curvature and thereby affect the field enhancement factor. This effect may be reduced by improving the vacuum conditions as outlined in Section 9.2 and may need further investigation.

To distinguish the experimental features of electron photoemission in this two-step from a one-step process, photoelectron kinetic energy spectra were first obtained by illuminating the apex of the gold nanotip with the individual laser pulses only, as shown in Figure 8.4.

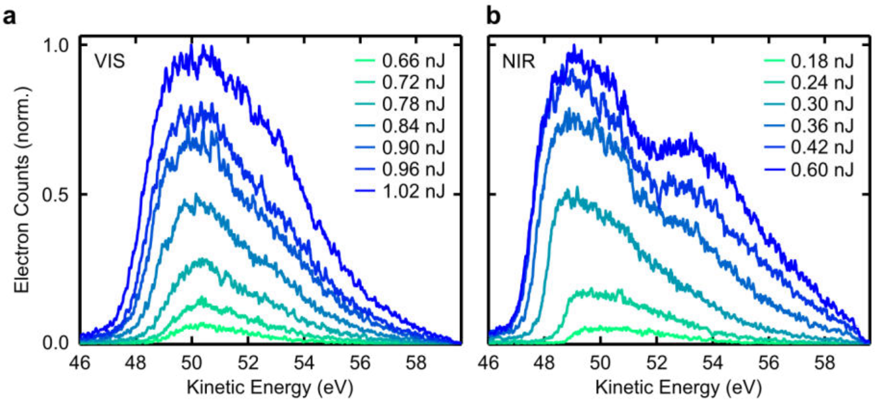

Figure 8.4: One-colour photoelectron kinetic energy spectra. (a) Illuminating the apex of a gold nanotip with 9-fs VIS pulses centred around ~600 nm results in Gaussian-like shaped spectra, which broaden with increasing pulse energy and show a single peak. (b) Illuminating the apex of a gold nanotip with 18-fs NIR pulses centred around ~1600 nm results in spectra, which broaden with increasing pulse energy and show a plateau-like second peak indicating strong-field acceleration of electrons in the optical near-field at the apex of the gold nanotip as explained in Chapter 4. Taken from [JR5].

The photoelectron kinetic energy spectra obtained by illuminating the apex of a gold nanotip with the 9-fs VIS pulses of variable pulse energy show a single peak and display a Gaussian-like shape with a slower decay towards higher kinetic energies. Both the electron yield and the width increase with the pulse energy up to a width of 6 eV (FWHM) at the maximum pulse energy 1.02 nJ. Such spectra are characteristic of the regime of multiphoton ionisation as explained in Chapter 4.

The photoelectron kinetic energy spectra obtained by illuminating the apex of a gold nanotip with the 18-fs NIR pulses of variable pulse energy show a distinct plateau-like feature towards higher kinetic energies. Both the electron yield and the width increase with the pulse energy up to a width of 7.5 eV (FWHM) at the maximum pulse energy 0.6 nJ. Such spectra indicate the sub-cycle regime of strong-field photoemission as explained in Chapter 4.

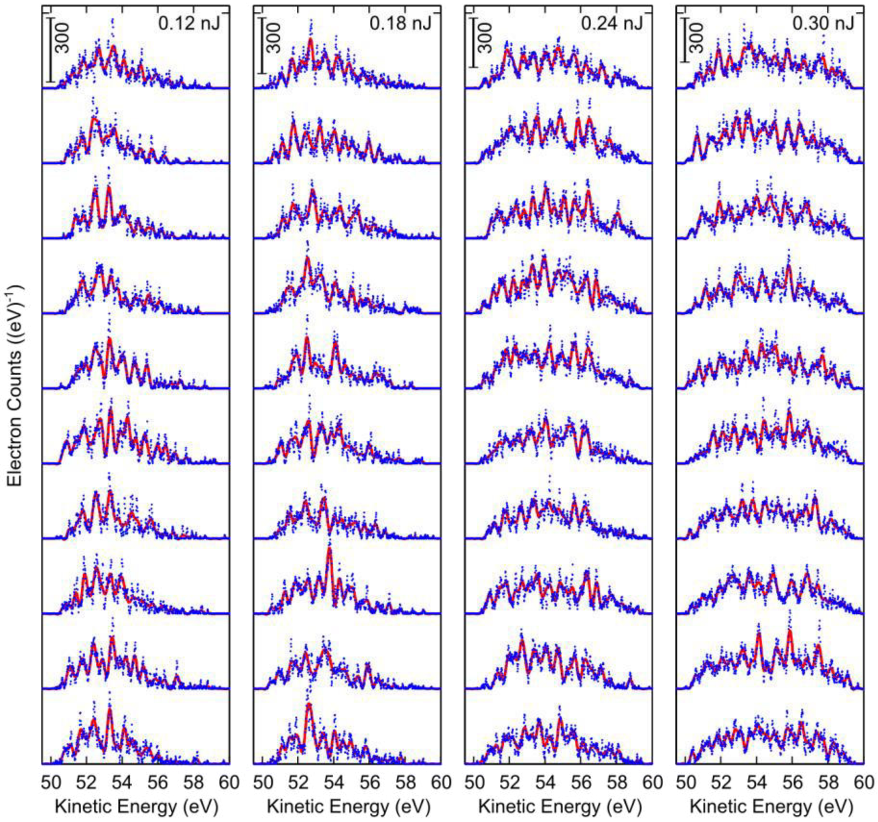

Figure 8.5: Selection of photoelectron kinetic energy spectra (blue symbols) recorded at an integration time of 100 ms in the time overlap of the VIS and NIR laser pulses. The VIS pulse energy was kept constant and the NIR pulse energy was varied. The red curves are the experimental data low-pass filtered with a cut-off frequency $(h/0.41\ \mathrm{eV})^{-1}$. Taken from [JR5].

Next, 400 individual spectra were recorded at an integration time of 100 ms in the time overlap of VIS and NIR laser pulses. In this measurement, the VIS pulse energy was kept constant at 0.75 nJ and the NIR pulse energy was varied in four steps from $E_{pulse} = 0.12\ \mathrm{nJ}$ to $E_{pulse} = 0.30\ \mathrm{nJ}$, corresponding to electric field strengths from $fE_0 = 6.5\ \mathrm{V/nm}$ to $fE_0 = 10\ \mathrm{V/nm}$ as estimated from the in situ laser pulse characterisation discussed in Chapter 10. A selection of 10 spectra for each setting of the NIR pulse energy is shown in Figure 8.5. Here, the electron yield increases from about 550 electrons per spectrum for the lowest NIR pulse energy 0.12 nJ to about 1300 electrons per spectrum for the highest NIR pulse energy 0.30 nJ. In contrast to the photoelectron kinetic energy spectra obtained by illuminating the apex of a gold nanotip with either VIS or NIR pulses individually, these spectra display an apparent modulation. Importantly, considering the signature of an individual electron as discussed in Chapter 10, the peaks apparent in these spectra do not arise from a shot-noise limited distribution of electrons.

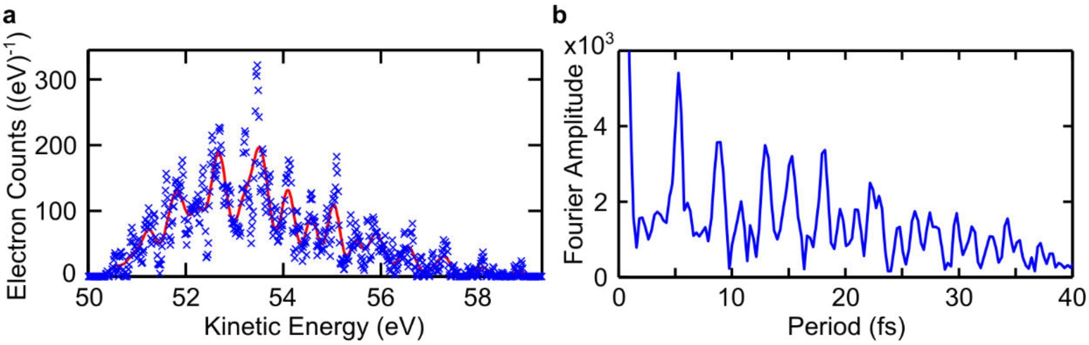

Figure 8.6: (a) Photoelectron kinetic energy spectrum (blue circles), recorded at an integration time of 100 ms in the time overlap of both VIS and NIR laser pulses for the lowest NIR pulse energy 0.12 nJ. The red curve is the experimental data low-pass filtered with a cut-off frequency $(h/0.41\ \mathrm{eV})^{-1}$. (b) The Fourier amplitude of the spectrum shows a strong period of $h/0.78\ \mathrm{eV} = 5.28\ \mathrm{fs}$.

To investigate the apparent modulation further, let us look at an individual spectrum shown in Figure 8.6a in more depth, obtained for the lowest NIR pulse energy of 0.12 nJ. A Fourier transform of this spectrum displayed in Figure 8.6b reveals a strong period of $h/0.78\ \mathrm{eV} = 5.28\ \mathrm{fs}$ and possibly weaker periods.

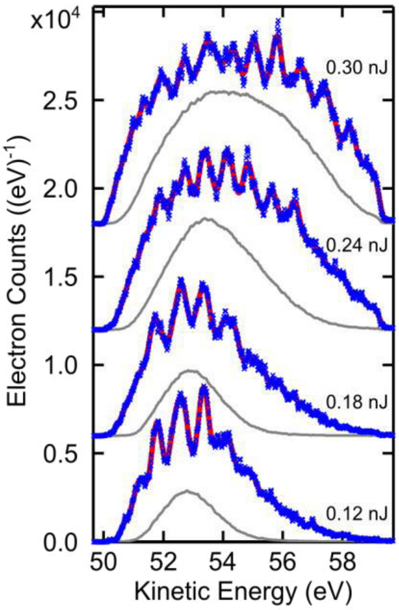

Figure 8.7: Sum of 50 photoelectron kinetic energy spectra (blue circles) recorded in the time overlap of the VIS and NIR laser pulses at four different settings of the NIR pulse energy. The red curves are the experimental data low-pass filtered with a cut-off frequency $(h/0.41\ \mathrm{eV})^{-1}$. The grey curves display the one-colour background recorded for a large interpulse delay. Taken from [JR5].

To distinguish whether this apparent modulation of the individual spectra shown in Figure 8.5 is significant or whether these spectra are dominated by noise, 50 of such spectra were selected for each of the four settings of the NIR pulse energy and summed up. The so obtained photoelectron kinetic energy spectra are displayed in Figure 8.7. These spectra show an increasing number of up to 12 distinct peaks and broaden by increasing the NIR pulse energy, which is in close agreement to the calculations presented in Chapter 7. They display a Gaussian-like shape with a slowly decaying tail towards higher kinetic energies rather than a plateau-like feature as shown in Figure 8.4b for the spectra obtained by illuminating the apex of a gold nanotip with NIR laser pulses only. In particular, the modulation apparent in the individual spectra did not average out. To quantify this modulation, a Fourier transform was performed for each of the individual spectra. The resulting Fourier amplitudes were then summed up for each setting of the NIR pulse energy as displayed in Figure 8.8.

This analysis reveals, that the individual spectra carry a dominant modulation period $h/5.28\ \mathrm{fs} = 0.78\ \mathrm{eV}$, which corresponds to the photon energy of the NIR laser pulses.

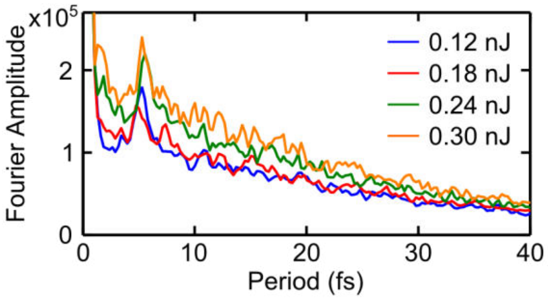

Figure 8.8: The sums of the Fourier amplitudes of the 50 selected individual spectra comprising the spectra displayed in Figure 8.7 for each of the four settings of the NIR pulse energy show a dominant modulation period $h/5.28\ \mathrm{fs} = 0.78\ \mathrm{eV}$.

From these observations we therefore conclude the observation of ATI from a gold nanotip, which has not been published so far. In distinction from the ATI spectra reported from tungsten nanotips before [39,40] the modulation contrast amounts up to 30%, even in the presence of a background, which stems from the featureless one-colour electron yield, here recorded for a large intrapulse delay (grey curves in Figure 8.7). Specifically, this modulation contrast is also achieved in the low-energy part of the spectra and thereby renders these spectra more atomic-like than the weakly modulated ATI spectra observed from tungsten nanotips. There, electron emission was assumed to originate from a broad distribution of states near the Fermi level in a one-step process, as explained in Chapter 4, which is mapped onto the photoelectron kinetic energy spectrum and washes out sharp features such as ATI peaks. Here, the two-step process appears to result in a different mechanism of photoemission.

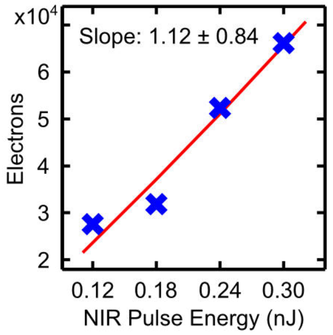

Figure 8.9: The measured integrated two-colour electron yield from the apex of a gold nanotip increases linearly with the NIR pulse energy. Modified from [JR5].

A further indication for this stems from the observation, that the integrated two-colour spectra reveal an electron count, which depends linearly on the NIR pulse energy. In particular, a slope of $N = 1.12 \pm 0.84$ is measured rather than $N = 7.1$ as expected from multiphoton photoemission as explained in Chapter 4. This observation is indicative of photoemission from weakly bound intermediate states, effectively reducing the work function of the gold nanotip. This mechanism would also enable access to the strong-field regime and support the occurrence of the strong-field phenomenon ATI at the low NIR pulse energies used here. Specifically, they would only yield a Keldysh parameter $\gamma > 1$ for typical laser parameters characterised in Chapter 10, if electron emission had occurred from the Fermi level at $E_F \approx 5.5\ \mathrm{eV}$. It changes to $\gamma \approx 0.6$ for the lowest NIR pulse energy 0.12 nJ, if electron emission from a weakly bound state with, for example, $E_b = 0.85\ \mathrm{eV}$ is assumed.

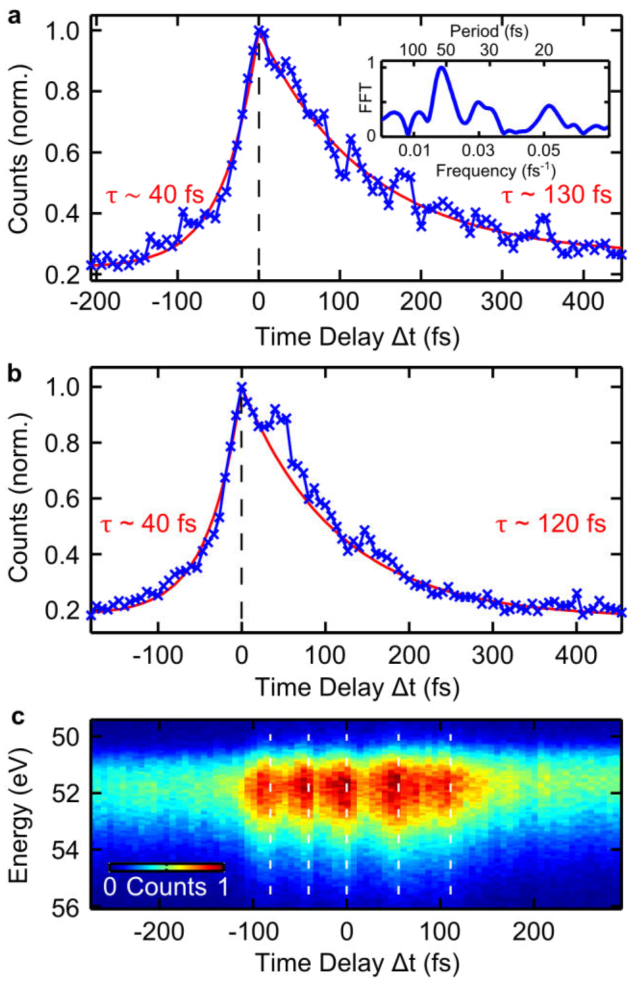

Figure 8.10: Time-resolved two-colour photoemission. (a) The two-colour electron yield decays within ~130 fs (~40 fs) for positive (negative) delays. Inset: A Fourier transform reveals beating periods for positive delays (VIS precedes NIR). (b) Similarly, the two-colour electron yield decays within ~120 fs (~40 fs) for positive (negative) delays in a control measurement performed with a different nanotip. Additionally, horizontally polarised VIS laser pulses were applied in this measurement. (c) An oscillatory pattern with dominant periods of 54 fs for positive and 39 fs for negative delays persists over a time interval of ~200 fs indicating photoemission from discrete, long-lived intermediate states. Modified from [JR5].

To further investigate the nature of the apparently populated intermediate states, the time delay between the VIS and NIR laser pulses was varied. In the measurement shown in Figure 8.10a the pulse energies are chosen as 0.30 nJ (VIS) and 0.36 nJ (NIR). Under these conditions, a five-fold increase in electron yield is observed in the time overlap of both laser pulses. The electron yield decays mono-exponentially with a long time constant of ~130 fs for positive delays corresponding to the VIS laser pulses preceding the NIR laser pulses and a short time constant of ~40 fs for negative delays. Similar decay constants are reproduced as shown Figure 8.10b for a different nanotip, for which the pulse energies were chosen as 0.54 nJ (VIS) and 0.48 nJ (NIR). In addition, in this measurement horizontally polarised VIS laser pulses were chosen, for which no difference to using vertically polarised VIS laser pulses is observed. In this case the electron wave packet is more likely driven away from the surface. Yet, the enhancement of the electric field is expected to be weak in the VIS spectral range and not localised at the apex, as discussed in Chapter 4. Consequently, a substantial part of the electron wave packet may still not overcome the attractive Coulomb-like potential and become trapped in front of the surface.

These measured decay times agree well with the lifetimes of the $n = 2$ and the $n = 3$ image potential states estimated from bulk studies [43,221]. They contrast short-lived excitations in the gold nanotip such as an electron-hole-pair excitation, which would be screened within $t = s/v = d/\sqrt{2\phi/m_e} \approx 0.2\ \text{fs}$. Here, $v = \sqrt{2\phi/m_e}$ is the Fermi velocity, $\phi \approx 5.5\ \text{eV}$ the work function taken to be equal to the Fermi level, m_e the mass of an electron and $d = 0.29\ \text{nm}$ the nearest-neighbour distance in gold. The measured long decay times further contrast electron emission from deeper lying surface states associated with an electron wave function with a greater spatial overlap with the bulk such as the Shockley surface state [203].

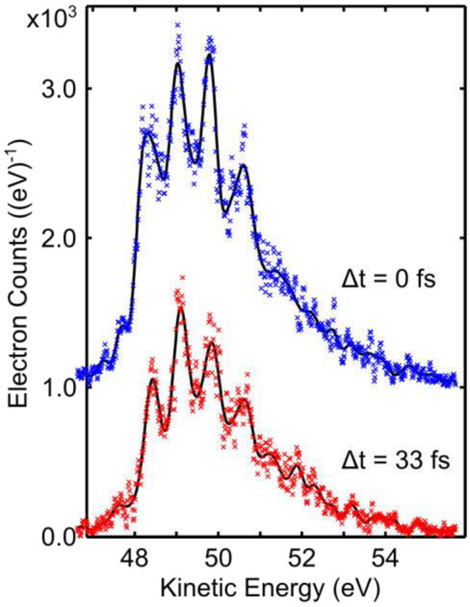

Figure 8.11: Sums of 50 photoelectron kinetic energy spectra recorded at an integration time of 100 ms each, both for a time delay between the VIS and the NIR laser pulses of $\Delta t = 0\ \mathrm{fs}$ (blue symbols) and $\Delta t = 33\ \mathrm{fs}$ (red symbols). The spectra display a Gaussian-like shape with a slowly decaying high-energy tail and a similar modulation with peaks separated by the photon energy as the spectra in Figure 8.7. The black curves are the experimental data low-pass filtered with a cut-off frequency $(h/0.41\ \mathrm{eV})^{-1}$. Taken from [JR5].

With our extended knowledge of the long lifetime of the apparently populated intermediate states, we may now repeat the measurement of photoelectron kinetic spectra, which led to the data presented in Figure 8.7, but now as a function of time delay. For this, 300 photoelectron kinetic spectra were recorded at an integration time of 100 ms each, of which again 50 spectra were selected as before. This procedure was carried out both in the time overlap of the VIS and NIR laser pulses as well as at a time delay of 33 fs, which is greater than the sum of the measured pulse durations of 9 fs (VIS) and 18 fs (NIR). Furthermore, this measurement is conducted with a different nanotip. Here, the pulse energies of the laser pulses illuminating its apex were chosen as 0.54 nJ (VIS) and 0.42 nJ (NIR).

As shown in Figure 8.11 the modulation in the photoelectron kinetic energy spectra with at least five peaks separated by the NIR photon energy is reproduced, both in the time overlap of the laser pulses as before, but now also outside the overlap of both laser pulses. In the latter case, the electron yield has decreased by a factor of ~1.7, likely due to partial decay of the populated intermediate states. The overall spectral shape is similar in both cases, displaying a Gaussian-like shape with a slowly decaying tail for higher kinetic energies pointing to a quiver regime rather than a plateau-like feature, which would indicate sub-cycle dynamics, as explained in Chapter 4.

So far, we have concluded the existence of long-lived intermediate states from different types of measurements. The next step is now to identify likely candidates for intermediate states. For this, the time-resolved measurements shown in Figure 8.10 hold a further clue. For example, superimposed on the exponentially decaying electron yield displayed in Figure 8.10a an oscillatory pattern is measured. A Fourier transform reveals periods of 34 fs and 54 fs for positive delays, for which the VIS pulses precede the NIR pulses. This oscillatory pattern is even more pronounced in a further measurement shown in Figure 8.10c, in which similar periods of 54 fs for positive delays and 39 fs for negative delays can be identified, persisting for time delays >100 fs. Here, the NIR pulse energy of 0.24 nJ was the lowest of all three measurements displayed in Figure 8.10. This may explain the survival of long-lived coherences at the apex of the gold nanotip, which are least pronounced for the highest NIR pulse of 0.48 nJ corresponding to the measurement in Figure 8.10b and weakly pronounced, but still discernible for an intermediate setting of the NIR pulse of 0.36 nJ in the measurement displayed in Figure 8.10a.

Such a beating pattern is reminiscent of quantum beats observed on extended metallic films [41] as explained in Chapter 6 and supports the population of discrete intermediate states. It contrasts a mechanism of electron emission from a continuous, possibly hot distribution of electrons [28], which might occur on a similar time scale as the observed decay constants of the time-resolved electron yield [174,175].

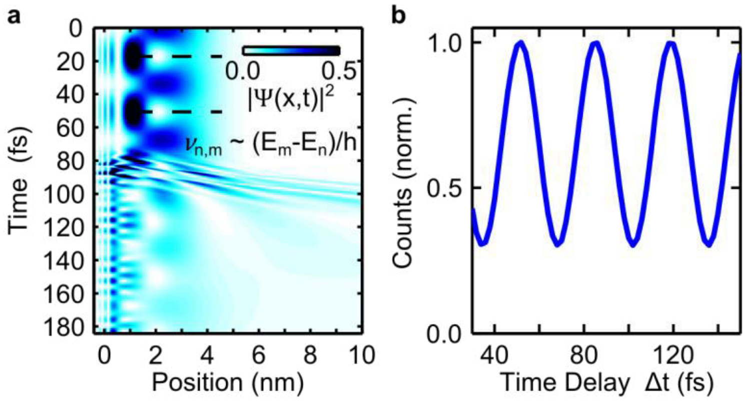

Figure 8.12: (a) Time evolution of a wave packet initially prepared in a superposition of the $n = 2$ and $n = 3$ states under the influence of a 10-fs NIR laser pulse: A freely propagating electron wave packet separates from the bound state electron wave packet. After the interaction with the laser pulse the superposition state is substantially altered. Modified from [JR5]. (b) The time-resolved electron yield displays a modulation with a period $\nu_{2,3} = 34$ fs given by the energy spacing of the states.

The population of image potential states may further be supported by turning again to our time-dependent Schrödinger equation model discussed in Chapter 7. For this, the quantum system is now prepared in a superposition of the $n = 2$ and the $n = 3$ state. These states are chosen, because the lifetimes of the $n = 2$ and the $n = 3$ image potential states estimated from bulk studies [43,221] agree well with the observed decay times at positive (~ 130 fs) and negative time delays (~ 40 fs). The time evolution is calculated by running a Crank-Nicolson algorithm. The outcome of this calculation is displayed in Figure 8.12a, in which each line represents the probability density of the electron wave function at a subsequent step in time.

Initially, the electron wave packet alternates between the $n = 2$ and the $n = 3$ Rydberg electron wave functions with a period of 34 fs. Perturbing the quantum system with a 10-fs near-infrared laser pulse centred at 1600 nm causes a freely propagating electron wave packet to split from the bound state electron wave packet. The oscillatory motion of the bound state wave function is substantially changed with respect to its initial oscillatory motion, indicating an altered superposition state. Specifically, a much shorter period, pointing to the population of the lower lying $n = 1$ image potential state, is seen. In the real experiment, however, this state would not be observed due to its extremely short lifetime of ~4 fs [43,221], which is not included in this simulation.

Importantly, the time-resolved electron yield shown in Figure 8.12b obtained by integrating the time-resolved photoelectron kinetic spectra displays a period of 34 fs, which arises from the oscillatory wave packet motion. It compares remarkably well with one of the dominant experimentally observed beating periods. It may be linked to the predominant population of the $n = 2$ and $n = 3$ image potential states, while the other dominant beating period of 54 fs may point to the simultaneous population of the $n = 3$ and $n > 4$ states. However, facetting at the apex as discussed in Chapter 7 may lead to electron emission from image potential states with slightly different binding energies and therefore affect the measured beating periods, which would need to be further investigated. Moreover, the occurrence of higher angular momentum quantum numbers at the apex of a metallic nanotip as discussed in Chapter 7 points to a more complex origin of such quantum beats, which calls for spatially resolving the associated wave functions by further experimental techniques such as velocity map imaging [228,229]. Moreover, the broadband nature of the ultrashort laser pulses used here adds to this complexity, as a huge number of closely spaced states can be excited at once. This problem may be resolved by selective excitation of image potential states using phase-locked ultrashort laser pulses generated in a TWINS (translating wedge-based identical pulse encoding system) interferometer [237].

A further improvement of the experimental setup concerns the modulation contrast of the ATI spectra, which vanishes at longer integration times, such that currently the selection of individual spectra recorded a short integration times is required. As explained in Chapters 4 and 5, the features of an ATI spectrum critically depend on the CEP, both for metallic nanostructures [40] and atomic systems [81]. In particular, the final kinetic energy of an electron is determined by the electric field strength at its birth time, by which it is subsequently accelerated [38]. As such, the residual shot-to-shot CEP instability of ~800 mrad as measured as part of this thesis [JR1], though comparing favourably to other systems employing passive CEP stabilisation as shown in Chapter 3, will cause a wash-out of sharp features such as ATI peaks. The critical dependence on the CEP has also been confirmed by the time-dependent Schrödinger equation calculations discussed in Chapter 7. Consequently, these measurements need to be repeated with an actively CEP stabilised laser system, which was not available as part of this thesis.

The reduced modulation contrast may also hint at a substructure in the observed ATI spectra due to resonant excitation of intermediate states known as Freeman resonances as explained in Chapter 5. However, they are not resolvable with the photoelectron spectrometer in our current experimental setup. This question may, however, be investigated with further experimental techniques as velocity map imaging [228,229] or with a delay line detector, which is currently set up as part of another project in our group to continue the experimental observations advanced in this thesis.

9. Outlook

9.1. Charge Transfer in Solar Cell Materials

In this thesis, the ultrafast dynamics of electrons in a single gold nanotip have been investigated by two-colour pump-probe spectroscopy. However, ultrafast electron dynamics also play an important role in, for example, organic materials [238,239]. For example, previous studies in our group on a blend of a light-harvesting, electron donating polymer P3HT and an electron accepting fullerene PCBM elucidated several aspects of this model system for an organic solar cell material [239]. An atomic force microscopy image of this blend has established the structure of this material as an arrangement of the polymer and the fullerene into separate domains [240]. Its function was then further investigated in an ultrafast all-optical pump-probe spectroscopy experiment using a similar NOPA system as presented in Chapter 3. It was found that the differential transmission signal displayed as oscillatory pattern with a period of about ~23 fs. A theoretical study explained this observation as vibronic coupling between electronic and nuclear degrees of freedom enabling charge transfer, periodically oscillating on the observed timescale of ~23 fs between the polymer and the fullerene. It was suggested theoretically that this charge transfer occurs between the lowest unoccupied molecular orbitals (LUMO). To look deeper into this phenomenon, it might be interesting to measure the charge transfer directly in an experiment.

Two-Colour Pump-Probe Spectroscopy on P3HT-PCBM with Electrons

This may be facilitated, for example, by extending the two-colour optical pump-probe scheme developed for the investigation of ultrafast dynamics of electrons in a gold nanotip to the detection of photoemitted electrons from a P3HT-PCBM sample. In such an experiment, one would first excite the HOMO-LUMO transition in P3HT. As in the study described before [239] this might be done by one-photon absorption with an ultrashort laser pulse centred around 540 nm, which is readily available from the NOPA system presented in Chapter 3. The next step would then be to probe electron emission from the LUMO, which might be done with a near-infrared laser pulse from the same laser system, to which the P3HT-PCBM sample is transparent. As the LUMO is at an energy level of ~3 eV, this would be a four-photon process.

Charge Transfer in a Novel Dyad

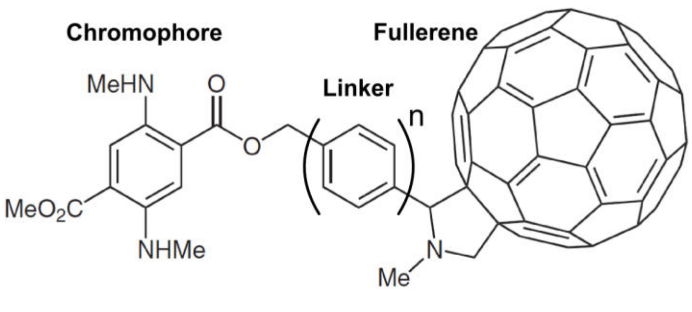

Figure 9.1: Dyad, modified from [241]. The chromophore and electron donor is a diaminoterephthalate, to which a fullerene is attached as an electron acceptor via a pyrrolidine linker consisting of n units.

To enhance the understanding of charge transfer in an organic solar cell material between the light-harvesting electron donating part and the electron accepting fullerene, a further step from merely observing it would be its control. For this purpose, a novel material, shown in Figure 9.1, was synthesised by our colleagues from the organic chemistry group of Professor Jens Christoffers [241]. Here, a diaminoterephthalate derivative was selected as the electron donating, light harvesting chromophore. This is a fluorescent scaffold, which may be functionalised with up to four effector groups [242]. For example, an alkyne or azide group allows for binding of the diaminoterephthalate to a protein [243], which might additionally be immobilised on a thin gold film by the simultaneous presence of a thiol group as another effector group. The fullerene is attached to the diaminoterephthalate via a pyrrolidine linker [241]. The length of the linker may be varied and thereby provides a switch to control charge transfer. A short linker favours charge transfer from the donor to the acceptor. The material should therefore behave like a good solar cell material. In contrast, a long linker inhibits charge transfer from the donor to the acceptor. Thus, the optical excitation of the donor would more likely decay via the emission of a fluorescence photon. Indeed, increasing the linker size from $n = 1$ to $n = 2$ caused an increase in the fluorescence quantum yield from 0.1% [241] to 2%. The chemical synthesis of the $n = 3$ compound, which might continue this trend, was, however, not successful so far.

Optical Properties of the Dyad

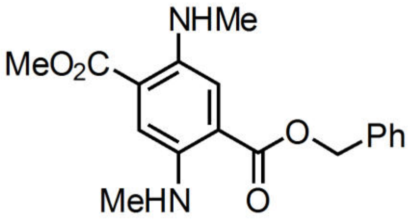

Figure 9.2: Synthetic precursor of the dyad. It does neither contain the linker nor the fullerene, but is terminated by a phenyl (Ph) ring.

Even the synthesis of the $n = 1$ dyad proved to be difficult, which was assisted as part of this thesis and published in [JR2]. In this synthesis an intermediate step is the precursor shown in Figure 9.2. This precursor does neither contain the linker nor the fullerene, but is terminated by a phenyl ring. This compound appears red in the solid form of a powder and orange when dissolved in dichloromethane. It has a pronounced absorption maximum near 485 nm, a fluorescence maximum near 584 nm and a fluorescence quantum yield of 3% [241].

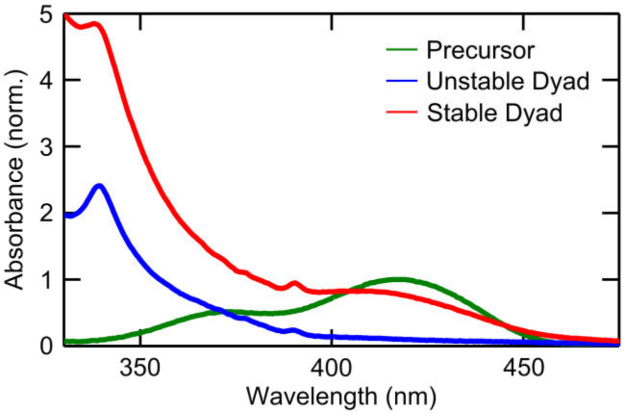

Figure 9.3: Absorption spectra of the precursor (green), the unstable compound (blue) and the stable dyad (red). The spectra are normalised to the absorption maximum of the precursor near 485 nm.

However, adding the fullerene to this compound caused the pronounced absorption maximum to disappear, as shown in Figure 9.3, whereas peaks appeared near 330 nm and 430 nm. These absorption maxima belong to the fullerene. This measurement was an important step in the synthesis of the dyad, because it revealed that the initial compound was unstable. The protocol for the chemical synthesis could therefore be modified to yield a stable dyad. Here, the absorption spectrum now shows both the peaks corresponding to the chromophore and the fullerene. In solution, the dyad appears brownish.

As can be seen from Figure 9.4, increasing the number of linker units from $n = 1$ to $n = 2$ does not significantly alter the absorption spectrum in this spectral region. In both cases, an absorption maximum near 488 nm is observed. The fluorescence spectrum, measured for the dyad with $n = 2$ linker units due to its higher fluorescence quantum yield, peaks near 583 nm, corresponding to a Stokes shift of 95 nm. It therefore resembles the fluorescence properties of the synthetic precursor, with a slightly quenched fluorescence quantum yield due to presence of the fullerene moiety. This quenching is much stronger in case of $n = 1$ linker unit, with the fullerene being closer to the chromophore.

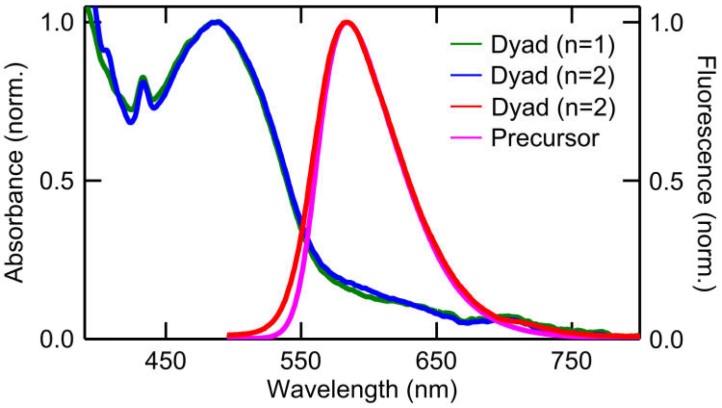

Figure 9.4: Absorption spectra of the dyad with $n = 1$ linker units (green), $n = 2$ linker units (blue), and fluorescence spectra of the dyad with $n = 2$ linker units (red) and the precursor (magenta).

Theoretical Study of Charge Transfer in the Dyad

An interesting experiment would now be to investigate charge transfer in this novel dyad by optical pump-probe spectroscopy similar to the established study of the P3HT-PCBM blend, but here as a function of linker size. A theoretical study of the dyad performed by our colleagues from the group of Carlo Andrea Rozzi based on density functional theory (DFT) and its time-dependent generalisation (TDDFT) has already elucidated the process of charge transfer in this material [JR2]. First, the optical absorption spectrum was calculated and the two experimentally observed excitation pathways were confirmed. An optical excitation in the UV would affect both the chromophore and the fullerene, while excitation in the visible spectral region may selectively excite the chromophore, as desired. Second, it was found that charge may oscillate between the chromophore and the fullerene with a period of ~45 fs. However, this process is negligible, if the positions of the nuclei are fixed. The aim would now be to investigate samples with different linker size and observe an inhibition of charge transfer by increasing the linker size. Such an experiment might establish this novel dyad as a model system to control ultrafast charge transfer in an organic material.

9.2. Ultrafast Point Projection Electron Microscopy

A natural extension of the theoretical considerations presented in this thesis suggesting the formation of a train of attosecond electron pulses emerging from the apex of a gold nanotip would be its experimental demonstration by ultrafast electron microscopy or diffraction [136,137], which was further discussed in the introduction to Chapter 4. Here, we will take a closer look on the concept of point projection microscopy [33,34], which was realised in our group as part of the ultrafast electron microscopy project [JR3]. In such a setup, depicted in Figure 9.5, a metallic nanotip is placed in front of a sample, for example, a thin nanowire. Electrons are deflected around this nanowire and detected on a phosphor screen behind the sample. The magnification in this setup is essentially given by the tip-sample distance. Decreasing this distance increases the magnification. This can be done as long as the focal spot of the laser pulse facilitating electron emission from the metallic nanotip does not overlap with the sample. After this point the laser intensity enabling electron emission from the nanotip must be decreased to avoid undesired excitation of the sample. This requires, for example, increasing the bias voltage on the metallic nanotip, eventually reaching a regime, in which electron emission becomes a one-photon process [35].

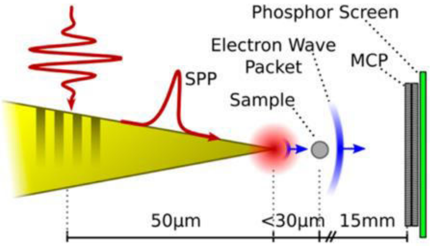

Figure 9.5: Schematic illustration of the point projection microscopy setup as realised in our group as part of the ultrafast electron microscopy project, described in the main text. Taken from [JR3].

To solve the problem of undesired sample excitation in a cleaner way one can remotely trigger electron emission [JR3],[164,165], as depicted Figure 9.5, and thereby spatially separate the focal spot of the laser pulse required for electron photoemission from the interaction region of the electrons with the sample. This was achieved by the technique of adiabatic nanofocussing [244,245] in our group as part of the ultrafast electron microscopy project. Here, a grating coupler is milled into the metallic nanotip to overcome the k-vector mismatch between the incident light and the surface plasmon polariton (SPP) on the shaft of the metallic nanotip. In this way, the SPP wave packet can travel down the shaft to the apex of the metallic nanotip, where it is re-emitted as a nano-localised spot of light. This illumination of the apex causes the photoemission of electrons just as for direct apex illumination. However, for direct apex illumination most of the light misses the apex. A circle with a typical tip radius of 10 nm will have an area, which is 10.000 times smaller than a typical diffraction-limited focal spot size of radius 1 μm. Thus, a greater efficiency may be achieved using the technique of adiabatic nanofocussing, provided that coupling and propagation losses are kept low by using a metallic nanotip with a clean and smooth surface as achieved in our home-built electrochemical etching setup described in Chapter 4.

Using the femtosecond laser system presented in Chapter 3 it was shown in our group as part of the ultrafast electron microscopy project that the electron emission efficiency increased by a factor of 50 [JR3]. A proof-of-principle experiment was carried out, in which a silver nanowire, fabricated by our colleagues from the optoelectronic organics group of Manuela Schiek, was imaged. Electrons were indeed emitted from the apex region of the metallic nanotip. Furthermore, the propagation of the SPP wave packet along the shaft of the nanotip did not lengthen the pulse duration considerably and the plasmon lifetime at the apex was short enough to initiate a 27-fs electron pulse.

This setup may be extended to prove the generation of a train of attosecond electron pulses as suggested in this thesis. In particular, to fully exploit its formation at a distance of 23 nm in front of the apex of the gold nanotip in an ultrafast electron microscopy setup, a solution might be binding a single molecule such as the novel dyad discussed in Section 9.1 to the nanotip or placing another sample such as a quantum dot close to it. Especially, for a molecule containing a thiol group, either naturally, by chemical synthesis or by point mutation, direct attachment to the nanotip may be conveniently realised. One route of exciting the molecule may again be adiabatic nanofocussing [244,245], such that the molecule would be exposed to a low light intensity localised to the apex region of the nanotip only. For visible excitation wavelengths usually required in organic materials, however, this would require the use of silver or aluminium nanotips [246]. Following optical excitation, a redistribution of charge may occur within the molecule on an ultrafast time scale, to which an attosecond electron pulse would be sensitive. This scheme may further by extended to an ultrafast diffraction setup to obtain structural information [31,32,247]. However, this may prove extremely challenging due to the low scattering intensity from a single or small periodic arrangement of molecules, especially in the ultra-dim electron emission operation mode.

Ultrahigh Vacuum Chamber

Finally, a technical advancement to increase the lifetime of a gold nanotip and facilitate long-term measurements in the ultra-dim regime in such an electron microscopy setup was placing it inside an ultrahigh vacuum chamber. This was initiated as part of this thesis and successfully embedded and further developed as part of the ultrafast electron microscopy project in our group. Using exclusively copper gaskets, an oil-free dry-scroll pump and limiting the size of the chamber, a vacuum of $2 * 10^{-9}\ \mathrm{mbar}$ was achieved. This is assisted by avoiding a breadboard at the base plate. Equipment such as a phosphor screen to detect photoemitted electrons is mounted directly to the flanges. A special feature of this vacuum chamber is a re-entrant window. It allows optics such as a Cassegrain objective, which might need regular adjustment, to be placed inside the boundaries of a cube defining the chamber, yet outside the vacuum. This improved vacuum concept may also be applied to the Rydberg electron experiments and might allow for a clearer observation of quantum beats, especially of weakly bound image potential states particularly sensitive to their local environment.

9.3. High Harmonic Generation from a Metallic Nanotip

The strong-field phenomenon ATI investigated in this thesis is closely linked to the concept of HHG, which has enabled the generation of attosecond optical pulses [12,13] and opened a pathway to investigate ultrafast phenomena at an unprecedented time scale. Most of these methods at the cutting edge of modern attosecond science have been established for atomic systems [14-16], while there exists an increasing number of experiments to transfer these concepts to solid state materials [17,19,20,22,23]. The conceptually new approach involving image potential states suggested in this thesis contributes to these developments, as it gives access to electrons originating both from a well-defined set of discrete energy levels like in an atomic system and from a well-defined point-like location like in a solid-state nanotip. In particular, in addition to the possibility of an attosecond electron pulse sustained by atomic-like ATI as suggested in this thesis a metallic nanotip may also provide a nano-localised solid state source of high harmonics [44] and thereby possibly an attosecond optical pulse. The localisation to the apex of a metallic nanotip is in stark contrast to a μm-sized gaseous ensemble of atoms, in which high harmonics are usually generated in a wide area defined by the focal spot of the driving laser pulses. Furthermore, a metallic nanotip may be positioned very accurately to investigate a sample of interest.

Mechanism of High Harmonic Generation

In particular, HHG is closely linked to ATI as described by the three-step model [8], of which the first two steps are identical to the Simple Man's Model already explained in the context of ATI. The third step, depicted in Figure 9.6, is the recombination of the quivering electron with its parent ion during the course of its oscillatory motion, in which high harmonic radiation is emitted. This process occurs every half cycle, i.e. with a periodicity equal to half of the optical period of the driving laser pulses, that is $T_{laser}/2$. Consequently, (odd) harmonics spaced by twice the photon energy of the driving laser pulses are observed.

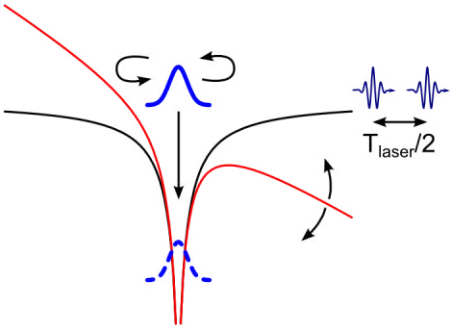

Figure 9.6: HHG. An electron wave packet (blue curve) released from an atomic potential (black curve) and quivering in the oscillatory potential (red curve) created by a light field may recombine in each half cycle with its parent ion to yield a bound state electron wave packet (dashed blue curve). In this process, high harmonic radiation is emitted in temporal slits spaced by half of the optical period of the driving laser pulses, $T_{laser}/2$.

High Harmonics and Attosecond Optical Pulses from Atomic Systems

High harmonic spectra are characterised by rapidly decreasing low-order harmonics followed by a plateau-like distribution of higher-order harmonics [155]. The low-order region of the spectrum can be described in the perturbative picture, in which the intensity of the harmonics scales with the nonlinearity of the driving multiphoton process. The plateau of higher-order harmonics marks the transition into the non-perturbative strong-field regime, in which the scaling of the intensity of the harmonics becomes closer to linear [155]. As the returning electron reaches the parent ion with a maximum velocity of $3.17\ U_p$, the harmonic spectra terminate at this energy, which is known as the high harmonic cut-off [8,9].

In the energy domain the process of HHG results in a comb-like distribution of high harmonics. Fourier transformation into the time domain would yield a pulse train with an individual pulse duration given roughly by $T_{laser}/2N$, where N is the number of phase-locked harmonics. This is in analogy to mode-locking [67,115] in a laser cavity, in which the constructive interference of phase-locked longitudinal modes results in an ultrashort pulse [11,115], as also described in the context of generating ultrashort laser pulses in Chapter 3. Provided phase-locking of the high harmonics, attosecond optical pulses originate from HHG [12,13]. Nowadays, exploiting HHG the pulse duration in the XUV spectral range has been pushed below 100 as [248].

High Harmonics from Solid State Systems

High harmonics may not only be obtained from atomic systems, but also from solids [19,22,23]. For example, in a semiconductor the valence and conduction band may be seen in analogy to the ground and excited state of an atomic system. Exciting electrons from the valence to the conduction band gives rise to a build-up of polarisation. The resulting electron-hole pair is driven apart by the strong laser field and eventually recombines to yield a harmonic photon. In fact, for ZnO crystal high harmonics up to the 25th order extending well above the band gap have been demonstrated [19]. Their non-perturbative character was shown by a decrease in the non-linear dependence of the amplitudes of the harmonics for increasing laser intensity, distinguishing their origin from other mechanisms of generating higher order harmonics further discussed below. Only odd harmonics were observed for parallel alignment of the optic axis of the non-centrosymmetric uniaxial ZnO crystal with the laser polarisation, whereas also even harmonics could be produced by rotating the crystal. This suggests, that the high harmonics indeed originated from the periodic bulk solid. Notably, the efficiency did not depend strongly on the ellipticity of the laser polarisation. This contrasts the reduction in the higher-order HHG efficiency by about two orders of magnitude in atomic systems for an ellipticity of only 4%, as the returning electron may miss its parent ion in this way [249-251]. It indicates that in contrast to a gaseous medium ionisation and recombination need not to occur at the same site in a solid. Furthermore, recent unpublished pioneering experiments by the group of Professor Paul Corkum carried out on a ZnO diffraction grating with sharp, tip-like bars suggest in their early stages of development the generation of odd harmonics up to the 7th order.

In fact, careful attention has to be paid to the exact mechanism of the generation of higher harmonics. Second and third harmonic generation, for example, have been observed from a gold nanotip [252] and a gold bow-tie nano-antenna [253]. The origin of these low-order harmonics is most likely due to the discontinuity of the bulk at the surface, which permits an induced nonlinear polarisation [254,255]. However, for a gold bow-tie antenna the observation of high harmonics up to the 17th order has also been reported [256]. This experiment sparked a lot of controversy [257]. Instead of resulting from high harmonic generation the appearance of extreme-ultraviolet radiation was assigned to atomic line emission from noble gases present in the gap of the bow-tie antenna [258]. It was concluded, that this incoherent fluorescence process is favoured in the enhanced electric field and that the nanoscopic interaction volume is too small to sustain the build-up of coherent high harmonic radiation.

High Harmonics from a Metallic Nanotip

If such experiments were to be carried out on a single metallic nanotip, a first difficulty will naturally arise from the expected measurement signal. Here, a single electron will be driven in front of a single nanostructure. In contrast, in HHG from atomic systems many atoms from an ensemble contribute to the overall signal, coherently adding up high harmonics. This scenario may be transferred to solid state nanostructures, for example, by nano-engineering an array of (metallic) nanotips [259].

A further challenge is then to prove HHG from atomic-like image potential states as presented in this thesis and distinguish it from other processes such as surface harmonic generation. The aim would therefore be to observe high-order harmonics, which form the plateau part of a high harmonic spectrum, and prove the transition into the non-perturbative regime by measuring the intensity dependence of each harmonic on the laser intensity as shown in [19]. This would require a dedicated detection setup extending far into the ultraviolet region of the spectrum, even if NIR laser pulses from the femtosecond laser system discussed in Chapter 3 are employed.

Tomography

If high harmonics are observed at a metallic nanotip, a wealth of new experiments currently carried out on atomic systems may become feasible. Especially, high harmonics are not only useful for generating attosecond optical pulses, but contain valuable information themselves. This allows for a much deeper insight into atomic matter, for example, via tomographic imaging of molecular orbitals, as for example shown for N_2 molecules [14]. This technique is based on the concept that the returning freely propagating electron wave packet interferes coherently with the bound electron wave function corresponding to the state(s), from which it tunnelled. This process generates an oscillating distribution of charge emitting high harmonics. Their relative intensity depends on the phase of the electronic states involved, such that the time-evolution of a bound state electron wave function is mapped onto the harmonic spectrum. In extension to the experiments presented in this thesis, this technique may be used to gain insight into the nature of wave functions associated with image potential states.

Chronoscopy

With its ability to gain deep insights into atomic matter attosecond metrology has further enabled atomic chronoscopy. This sub-field includes measuring the delay in photoemission from different atomic orbitals. In an exemplary experiment neon atoms were photoionised with CEP stable sub-200-as XUV pulses. The photoemitted electrons were then streaked [260,261] by sub-4-fs infrared pulses and recorded with a time-of-flight spectrometer. A delay of ~20 as between photoemission from the 2p and the 2s orbitals was observed [16]. Similarly, attosecond chronoscopy may further shed light on the migration of an electron wave packet excited inside the bulk before its actual photoemission at the surface. Illuminating a tungsten crystal by ~300-as XUV pulses and streaking the photoemitted electrons by 5-fs near-infrared laser pulses, a delay of ~100 as was found between photoemission of electrons from localised core states of the metal and delocalised conduction-band states [17]. In the extension to the experiments presented in this thesis, such techniques may be used, for example, to distinguish between electron emission from weakly bound image potential states and states close to the Fermi level.

9.4. Coherent Coupling of Nanostructures

The long lifetimes of image potential states presented in this thesis are a direct consequence of the large spatial extent of the electron wave function in front of the surface. This particular feature bears a similarity to Rydberg atoms [262], whose single outer valence electron orbits its parent nucleus at a large distance, while still being bound to it. The associated large electric dipole moment allows for strong interactions with nearby atoms, such that high fidelity quantum logic gates have been realised [263-265]. Access to specific Rydberg atoms, however, requires storing them in relatively shallow optical dipole traps, which restricts coherent control by laser excitation. In contrast, a sharply etched solid state nanostructure directly provides a nano-localised source of Rydberg electrons, which may similarly be used in quantum information processing.

The power of quantum information processing resides in the principles of quantum superposition and entanglement [266]. While in a classical computer data is represented by one of the binary numbers 0 or 1, it may be stored in the superposition of states in a two-level quantum system. Thus, a register of n entangled qubits holds 2^n quantum states, allowing for parallel processing of data and an exponential increase in computational speed. Specifically, the requirements for quantum computing are laid out by the DiVincenzo criteria [266]. In particular, a scalable system of well-defined qubits and long coherence times exceeding gate operations are necessary. These requirements are fulfilled, for example, by trapped ions, atoms in optical lattices and superconducting solid-state qubits [267], while the lack of scalability has ruled out NMR qubits, with which the first realisation of a quantum algorithm has been demonstrated [268].

In the case of Rydberg electrons from metallic nanostructures the requirement of scalability may be achieved by nano-engineering an array of bow-tie antenna structures [253,269], of which each side may additionally be equipped with a grating structure as proposed by our group in the context of realising a photonic transistor [253,270]. In this way, Rydberg electrons could be prepared in the gap region by remotely applying the required laser intensity via the concept of adiabatic nanofocussing [244], as explained in Section 9.2. This would avoid directly illuminating the gap and thereby separate the preparation laser pulses from the envisaged interaction region.

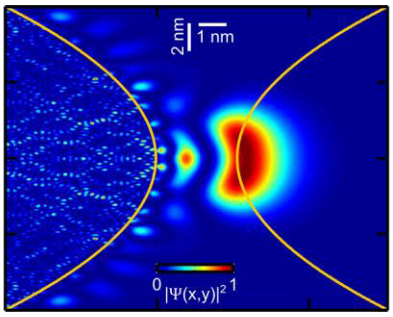

Figure 9.7: Coherent coupling of nanostructures. The probability density of the $n = 3$ wave function excited in one nanotip on the left overlaps with a second nanotip placed on the opposite side. The gap size is ~3 nm. The yellow curves mark the surfaces of the nanotips.

A first experiment of putting the suggested geometry to work would be the induction of an electron current across the gap region of the bow-tie antenna or between two opposing nanotips, as depicted in Figure 9.7. For this, one would have to nano-engineer a gap size matched to the spatial extent of the Rydberg electron wave functions. In this way, a Rydberg electron wave packet prepared on one side might have a significant probability of dephasing into the other side.

A further, yet highly advanced experiment would be the realisation of a quantum logic gate with Rydberg electrons prepared on either side of the gap. Here, one side would act as a control qubit and the other as a target qubit [265]. The length of gate operations on the Rydberg electrons located in front of the nanostructures would, however, be limited by the lifetime of the populated image potential states, which may limit the applicability of this concept in quantum information processing. Nevertheless, as may be seen from the experiments suggested in this chapter, Rydberg electrons from metallic nanotips provide many fascinating perspectives for experiments both in the short term and far-fetched future.

10. Appendix

10.1. In Situ Laser Pulse Characterisation

In interpreting the outcome of an experiment as presented in Chapter 8 an important quantity is the peak electric field strength E_0 of an ultrashort laser pulse. However, in an experiment usually its average power is accessible by measuring it with a power meter. It is therefore important to relate a measured average power to an electric field strength. This requires a characterisation of the ultrashort laser pulse at the site of the actual experiment.

For this, we assume the electric field strength of an ultrashort laser pulse in the time domain to be described by a sinusoidal wave, multiplied by a temporal envelope function $A(t)$:

$$E(t) = A(t)\cos(\omega_0 t + \varphi_{CE}) \qquad (10.1)$$

Here, φ_{CE} is the carrier-envelope phase, $\omega_0 = 2\pi c/\lambda_0$ is the centre carrier angular frequency, c is the speed of light and λ_0 is the centre wavelength. Assuming a Gaussian temporal envelope, this takes the form:

$$E(t) = E_0\cos(\omega_0 t + \varphi_{CE})e^{-2\ln 2(t/\tau_{FWHM})^2} \qquad (10.2)$$

Here, E_0 is the peak electric field strength and τ_{FWHM} is the pulse duration, defined as the intensity FWHM.

Assuming linear polarisation, the electric field strength in a plane perpendicular to the direction of propagation of the ultrashort laser pulse is assumed to be given by a Gaussian spatial profile:

$$E(x,y) = e^{-2\ln 2\left(\sqrt{x^2+y^2}/w_1\right)^2} \qquad (10.3)$$

Here, w_1 denotes the beam waist at FWHM.

The integration over the temporal and spatial profile of the ultrashort laser pulse then gives an expression for the pulse energy E_{pulse}:

$$E_{pulse} = I_0 \iint_{-\infty}^{\infty} [E(x,y,t)]^2\, dx\, dy\, dt = I_0 * \tau_{FWHM} * w_1^2 * (\pi/4\ln 2)^{3/2} \qquad (10.4)$$

Here,

$$I_0 = \frac{1}{2}\varepsilon_0 c n E_0^2 \qquad (10.5)$$

is the cycle-averaged intensity, where ε_0 is the permittivity of free space and n is the refractive index, usually taken as $n = 1$ for propagation in air.

Combining Equations 10.4 and 10.5 yields

$$E_0 = \sqrt{\frac{2}{c\varepsilon_0}\frac{E_{pulse}}{\tau_{FWHM} * w_1^2 * (\pi/4\ln 2)^{3/2}}} \qquad (10.6)$$

Here, the pulse energy E_{pulse}, the pulse duration τ_{FWHM} and the beam waist w_1 are measurable quantities, which will be characterised in the following.

Pulse Energy

For a pulsed laser system operating at a repetition rate f_{rep} the measured average power P can be converted into a pulse energy E_{pulse} by the relationship:

$$E_{pulse} = T\frac{P}{f_{rep}} \tag{10.7}$$

Here, T is a transmission coefficient, which accounts for a possible loss of power from the point of measurement to the point of interest. In our experimental setup, the repetition rate of the laser system is usually set to $f_{rep} = 5\ \mathrm{kHz}$ and the transmittance from the point of measurement to the apex of the nanotip is $T = 0.3$. This value arises from the following experimental situation. The ultrashort laser pulses are focussed onto the apex of a gold nanotip by an all-reflective Cassegrain objective as outlined before, which transmits only a fraction of the incident light due to its technical design described in Chapter 8. Furthermore, both the gold nanotip and the Cassegrain objective are housed in a vacuum chamber. To maintain the vacuum conditions, the measurement of the average power is carried out in front of the vacuum chamber.

Pulse Duration

The pulse duration τ_{FWHM} is determined by an interferometric autocorrelation as explained in Chapter 3, but now with the photoemission of electrons as the nonlinear process of order N. The measurement signal is fitted to:

$$I(\Delta t) = \left|\int_{-\infty}^{+\infty} \big(E(t) + E(t-\Delta t)\big)^N \, dt\right|^2 \tag{10.8}$$

Here, the pulse duration τ_{FWHM} enters via the electric field

$$E(t) \propto \cos(\omega_0 t) e^{-2\ln 2 (t/\tau_{FWHM})^2} \tag{10.9}$$

into the recorded signal. However, there are two further parameters, which need to be fixed independently, before fitting the pulse duration. One parameter is the nonlinearity N of the photoemission process. The other parameter is the centre wavelength $\lambda_0 = 2\pi c/\omega_0$.

Centre Wavelength

The centre wavelength λ_0 is determined from the spacing of the fringes. Here, $\boldsymbol{\lambda_{VIS} = 600\ \mathrm{nm}}$ for a VIS laser pulse and $\boldsymbol{\lambda_{NIR} = 1550\ \mathrm{nm}}$ for a NIR laser pulse yield good agreement with the recorded signals, shown in Figure 10.3. The centre wavelength can further be supported by the optical spectrum of a laser pulses, shown in Figure 10.1. These measurements would yield $\lambda_{NIR} = 1660\ \mathrm{nm}$ and $\lambda_{VIS} = 600\ \mathrm{nm}$. The slight discrepancy between the centre wavelength of the optical spectrum and the fitted centre wavelength for the NIR laser pulse can be explained by a spatial chirp resulting from the NOPA and the subsequent DFG process, such that the nanotip probes a slightly different part of the laser pulse than the spectrometer.

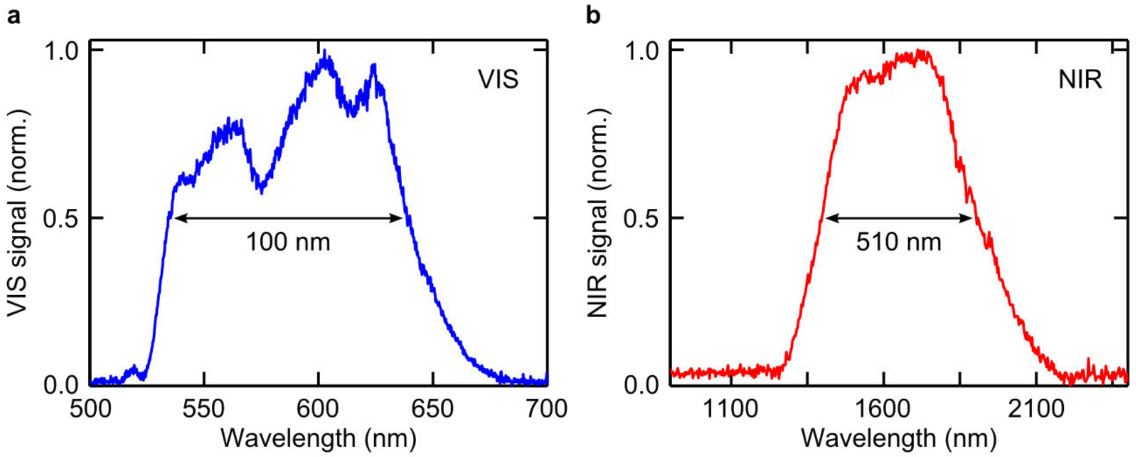

Figure 10.1: Optical laser spectra. (a) The VIS spectrum is centred at 600 nm, with a FWHM of 100 nm. (b) The NIR spectrum is centred at 1660 nm, with a FWHM of 510 nm. Modified from [JR5].

Nonlinearity

The nonlinearity N of the photoelectron emission process is simultaneously obtained while recording the interferometric autocorrelation. Due to interference of the laser pulse pair generated in the Mach-Zehnder interferometer the instantaneous laser intensity I incident at the apex of the gold nanotip changes as a function of time delay. As a consequence, the electron yield changes simultaneously and can be fitted, as explained in Chapter 4, to a power law given by Equation 4.9, revisited in this context:

$$P(I) \propto I^N$$

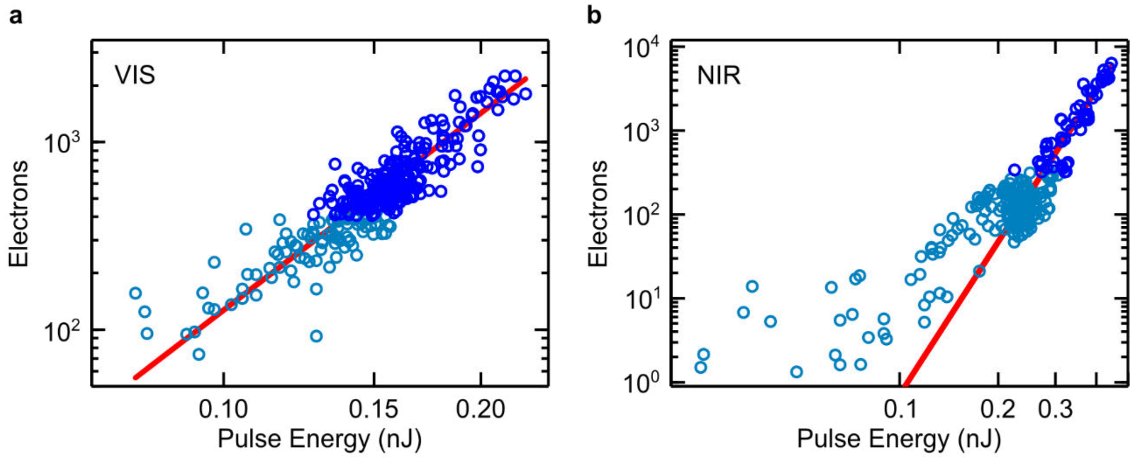

Figure 10.2: Measured electron yield (blue circles) from the apex of a sharply etched gold nanotip as a function of pulse energy on a double-logarithmic plot. (a) For illumination of the apex with VIS light the slope of the red line indicates a non-linearity of 3.49, obtained by fitting to the data with sufficient electron counts (dark blue circles). (b) Likewise, for illumination with NIR light a non-linearity of 6.04 is deduced. Modified from [JR5].

A plot of the electron yield from the apex of a gold nanotip against the measurable pulse energy, which scales linearly with the intensity, is shown in Figure 10.2. The fit yields good agreement with the experimental data for $\boldsymbol{N_{VIS}} = \mathbf{3.49} \pm 0.23$ for the VIS laser pulses and $\boldsymbol{N_{NIR}} = \mathbf{6.04} \pm 0.74$ for the NIR laser pulses. The nonlinearity for NIR illumination is lower than expected due to the possible onset of strong-field photoemission as explained in Chapter 4 despite using a pulse energy as low as possible.

This leaves the pulse duration τ_{FWHM} as the only variable parameter in Equation 10.8. As can be seen from Figure 10.3, good agreement with the experimental data is obtained for $\boldsymbol{\tau_{VIS} = 9\ \mathrm{fs}}$ for the VIS laser pulse and $\boldsymbol{\tau_{NIR} = 18\ \mathrm{fs}}$ for the NIR laser pulse. Note, that in this model, possible chirp has not been included.

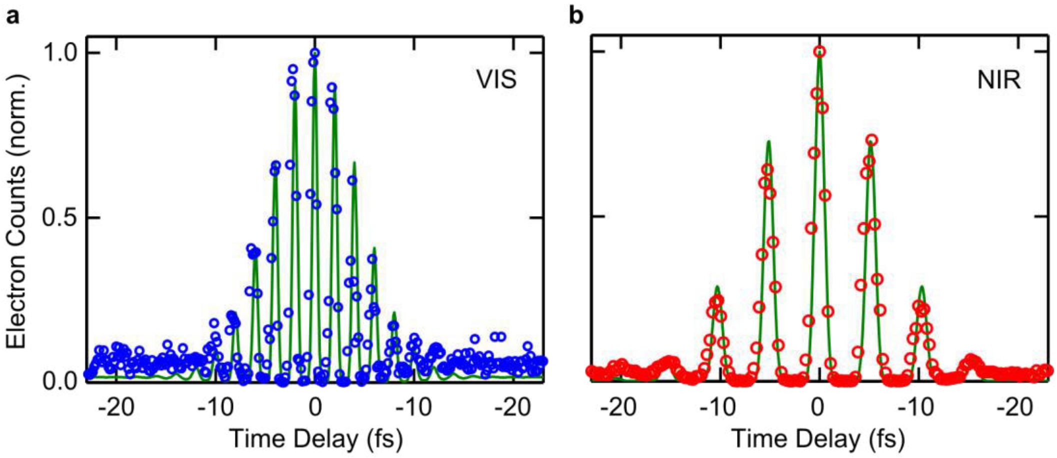

Figure 10.3: Interferometric electron autocorrelation obtained by illuminating the apex of a gold nanotip with (a) VIS and (b) NIR laser pulses. The simulations (green curve) yield good agreement with the data (blue and red circles) for a pulse duration of 9 fs and 18 fs, respectively. Modified from [JR5].

Beam Waist

Finally, the beam waist w_1 needs to be measured. For this, the spatial profile of the laser pulse can be mapped out by scanning the apex of the gold nanotip through the focal plane of the laser pulse and recording the number of photoemitted electrons at each position. For both the VIS and the NIR laser pulses, the experimental data plotted in Figure 10.4 shows electron emission confined to an area described by a two-dimensional Gaussian distribution:

$$E(x,y) = e^{-2\ln 2\left(\sqrt{x^2+y^2}/w\right)^2} \tag{10.10}$$

To quantify the extent of this distribution a Gaussian fit to the experimental data was performed, both at constant height of the gold nanotip and constant side. The fit yields a mean extent of $w_{mean,VIS} = 0.92\ \mu m$ for the VIS laser pulses and $w_{mean,NIR} = 1.17\ \mu m$ for the NIR laser pulses. As the electron yield $P(I) \propto I^N$, these values need to be scaled by a factor $\sqrt{N}$, which was obtained previously. This yields a beam waist (FWHM) $\boldsymbol{w_{1,VIS} = 1.72\ \mu\mathrm{m}}$ for the VIS laser pulses and $\boldsymbol{w_{1,NIR} = 2.87\ \mu\mathrm{m}}$ for the NIR laser pulses.

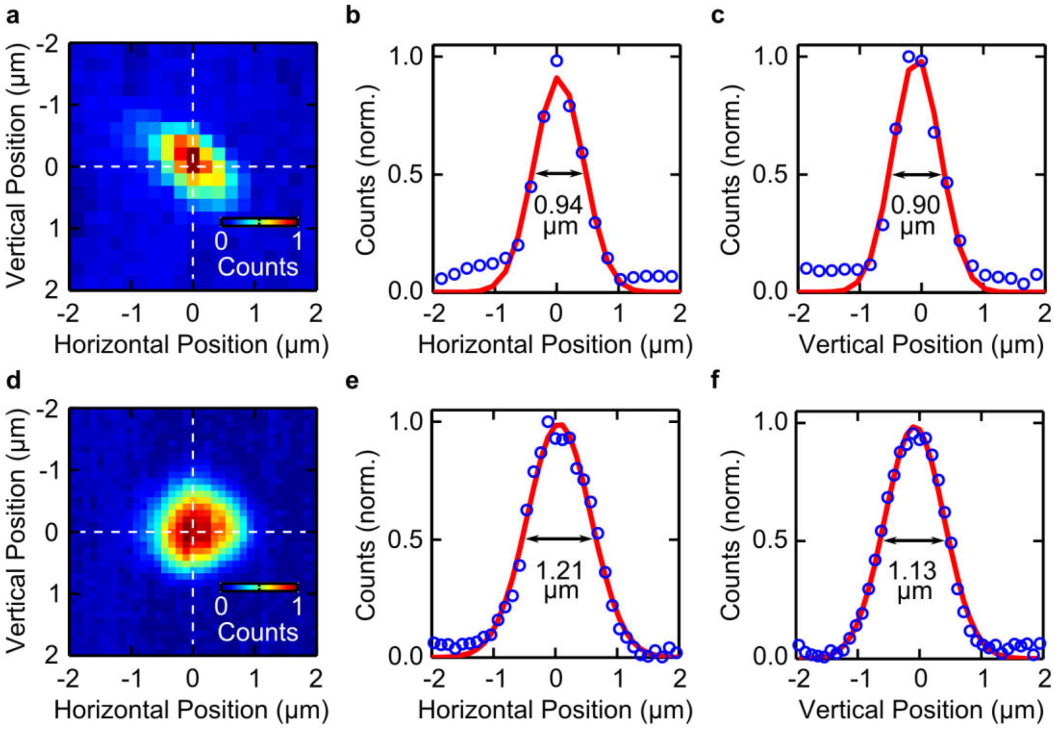

Figure 10.4: Scanning a gold nanotip through the focal plane of the laser pulse yields a Gaussian-shaped distribution of electron counts for (a-c) VIS and (d-f) NIR illumination. The dashed lines indicate cuts through the data (blue dots), which were fitted to a Gaussian distribution (red curves). They reveal an average FWHM of 0.92 µm for VIS illumination and 1.17 µm for NIR illumination.

10.2. Image Correction

A crucial part of the experimental setup described in Chapter 8 is the acquisition of images, on which the position of an electron signal impinging on a phosphor screen is recorded. This yields information on the number and kinetic energy of electrons photoemitted from the gold nanotip. Each electron signal ideally corresponds to a Gaussian spot of light, which is subsequently recorded on a CCD camera. The recorded images, however, do not only contain signal from electrons, but also several sources of background. To separate the wanted signal from this unwanted background, the images are corrected by an image correction procedure outlined in this section. This enables the recording of images at a short integration time, such that information can be extracted, which might otherwise average out due to, for example, residual CEP instabilities of the laser system as discussed in Chapter 7.

The CCD camera has 1392x1024 pixels. In the following, the 1392 pixels are called the energy axis, while the 1024 pixels are called the spatial axis. Integrating over the spatial axis corresponds to a photoelectron kinetic energy spectrum. The camera is mounted with its energy axis vertical and its spatial axis horizontal. Here, an image is always shown in its transposed form, i.e. with the energy axis oriented horizontally and the spatial axis vertically. Images recorded by the CCD camera are saved in the uint16 format. To allow for negative values the images are converted to the double format.

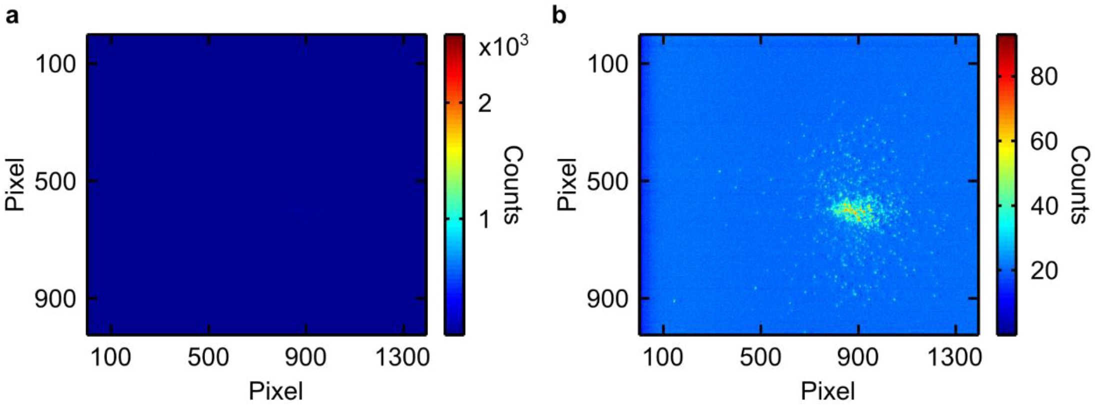

Figure 10.5: (a) In the raw image electrons are not visible due to the scaling of the colour bar by hot pixels or cosmic rays. (b) Fixing this type of artefact reveals the electron signal in the image.

Hot Pixel Correction

A typical raw image is shown in Figure 10.5a. No electrons are visible, because in the raw image few pixels with comparatively high counts are reported. These pixels do not represent electrons, but are either hot pixels of the camera or, for example, due to a cosmic ray. They are corrected for by the following procedure. Each pixel is compared to its neighbouring pixels. If the value of the pixel exceeds its neighbouring pixels by a factor of 2, the pixel is set to the value of its neighbouring pixels. After applying this hot pixel correction, the electrons in the image can now be seen in Figure 10.5b. Furthermore, it can be identified that the first 150 columns on the left and the upper 50 rows of the image appear to be less sensitive. As there will never be electrons in this region of the image, they will be ignored in the following analysis of the image to prevent bias due to these less sensitive regions.

Background Quantification

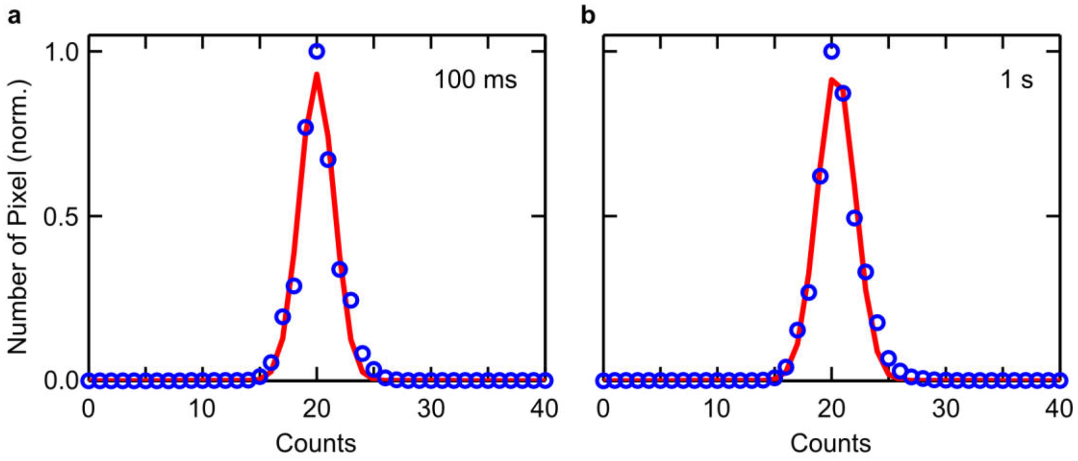

Figure 10.6: Histograms of counts (blue circles) for images without electron signal, recorded at an integration time of (a) 100 ms and (b) 1 s. The counts follow a Gaussian distribution (red curve) with a mean value of about 20 counts and a FWHM of about 3.5 counts.

The next step is to distinguish between signal and background. There are two types of background counts [258]. One type of background count has a constant value. An example is dark current, which depends on the temperature of the camera and may be subtracted from the image. The other type of background count is fluctuating. This corresponds to, for example, dark current shot noise. To quantify this background an image without any electron signal is taken.

Figure 10.6 shows the average of 250 histograms of counts (blue circles) reported by each pixel for background images recorded either with an integration time of 100 ms (a) or 1 s (b). In both cases the histogram can be fitted to a Gaussian distribution (red curve). For an integration time of 100 ms the mean value is 19.99 counts with a FWHM of 3.53 counts, which is approximately $\sqrt{20}$ as expected for dark current shot noise. For an integration time of 1 s both values are slightly higher, i.e. the mean value is 20.41 counts with a FWHM of 3.89 counts.

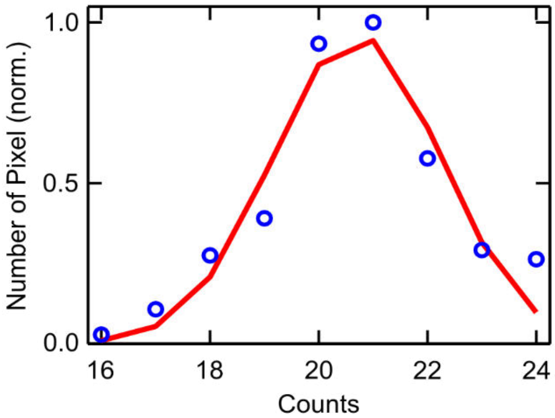

Figure 10.7: Histogram of counts (blue circles) for an image with electron signal, showing a Gaussian distribution of counts (red curve), with a mean of 20.7 counts and a FWHM of 3.6 counts.

With this information, the background for an image including an electron signal can now be quantified. Figure 10.7 shows a histogram of counts for an image with few electrons recorded at an integration of 1 s. The histogram is limited to count values between 16 and 24 (blue circles). This gives a reasonable quantification of the background (red curve) and prevents bias from count values due to electrons. The mean value is 20.70 counts and the FWHM is 3.63 counts. The mean value is taken as a constant offset. The standard deviation is a measure of the noise. For example, 99.999% of all counts will fall into the interval defined by 4.5 times the standard deviation. Only 0.001*1242*974, that is about 1200 pixel, will have counts outside this interval. In this example, this interval is 6.93 counts. This value is taken as a threshold value for noise.

Offset Subtraction

The analysis of the image has shown that the CCD camera has an offset of 20(+1) counts, which is now subtracted from the image.

Shadow Image Correction

As can be seen in Figure 10.9 by zooming into an image, the CCD camera has an artefact. Each recorded electron is accompanied by a shadow electron. This effect was quantified by recording an image with randomly emitted electrons from a pressure gauge at an integration time of 100 ms and subtracting the constant offset from that image. Then, 69 electrons were manually selected and averaged over. As shown in Figure 10.8, it was found, that the shadow electron appears with an amplitude corresponding to -0.1 times the original amplitude at a positon 26 pixels to the right of and 1 pixel below the recorded electron.

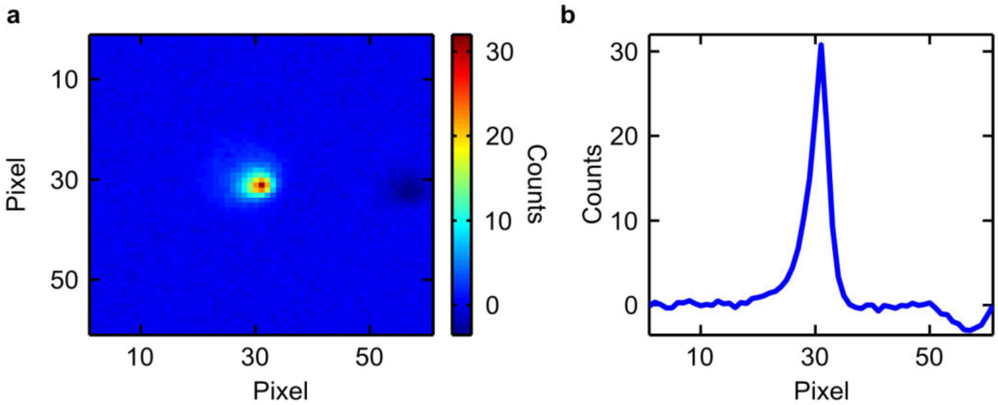

Figure 10.8: (a) The sum of 69 selected electrons reveals a shadow electron. (b) A cut shows, that the shadow electron has a negative amplitude of about 10% of the electron signal and occurs 26 pixels to the right and 1 pixel below.

Therefore, a shadow image is calculated in the next step according to $Image(x, y) = a_0 * Image(x + x_0, y + y_0)$ with $a_0 = 0.1$, $x_0 = 26$ and $y_0 = 1$ and added to the original image. Thereby, this artefact is reduced considerably, but cannot be fully compensated. A comparison between an image with and without this shadow image correction is shown in Figure 10.9.

In Matlab the calculation of the shadow image is performed with the help of the function circshift(), which shifts an array circularly, i.e. the last columns and rows will appear at the beginning of the image. Therefore, this calculation is done with the full image and the first x_0 columns and first y_0 rows of the shadow image are set to zero. These rows and columns will never appear in the region of interest.

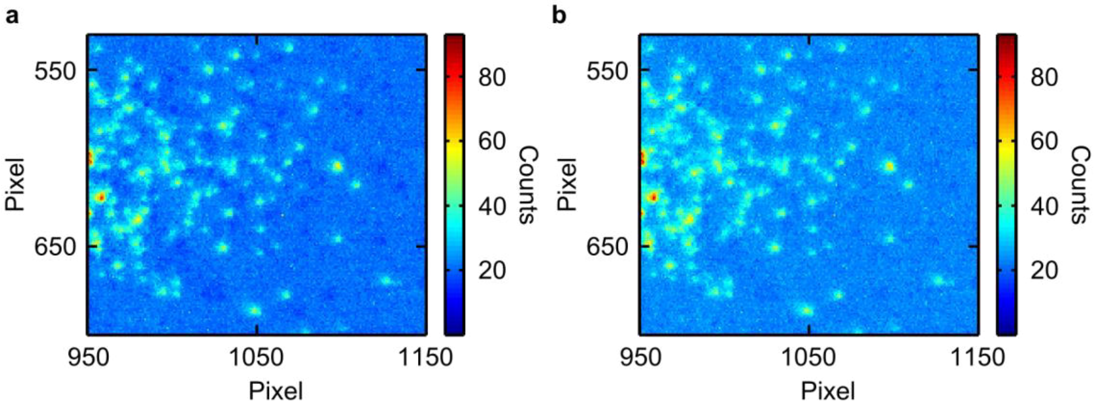

Figure 10.9: (a) The uncorrected image shows shadow electrons. (b) This artefact is reduced by applying the shadow image correction, as can be seen on the image with the same scale bar as in (a).

Cut to a Region of Interest (ROI)

Now, the image can be cut to the ROI to speed up computation and exclude regions, in which there will never be a reasonable electron signal. Usually, the ROI will span from pixel 301 to pixel 1392 on the energy axis and pixel 201 to pixel 1024 on the spatial axis.

Noise Correction

Now, the noise will be removed from the image. This is done by setting each pixel below or equal to the threshold value obtained from the histogram of counts to zero, or keeping the value of the pixel otherwise. The result of the noise correction is shown in Figure 10.10.

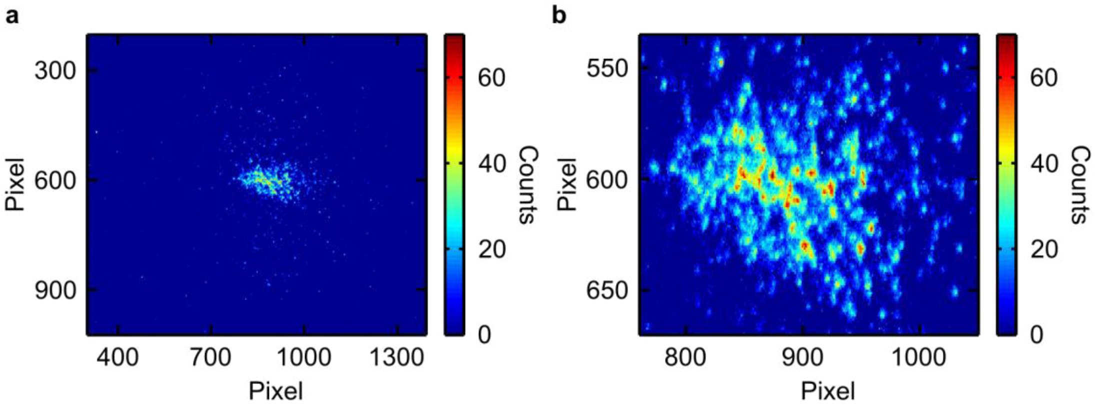

Figure 10.10: (a) After noise correction the counts in the image are predominantly due to the electron signal. (b) A magnified region of the image reveals that the background counts have been largely removed.

Isolated Pixel Correction

As can be seen by zooming into the right part of the image, as shown in Figure 10.11a, there are still individual pixels, which are unlikely electrons, if all its four direct neighbours are zero. Therefore, these pixels are additionally set to zero. As can be seen in Figure 10.11b the image quality can be improved by this procedure even further.

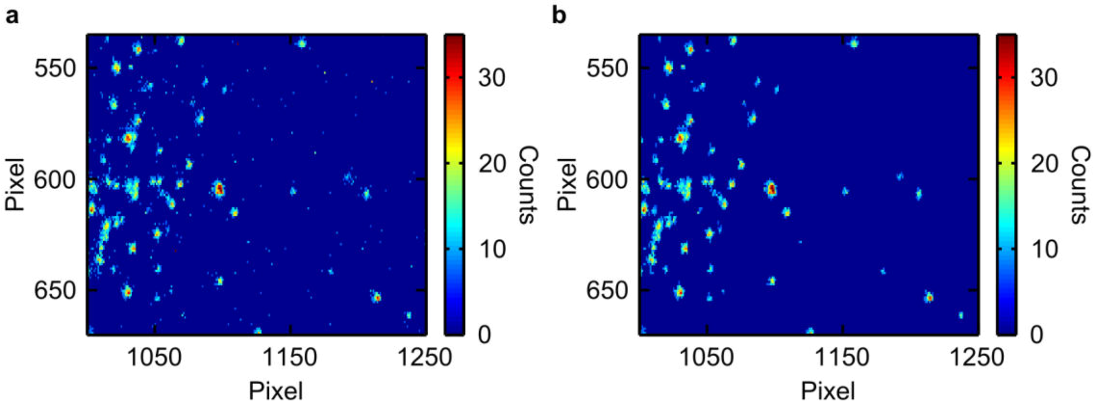

Figure 10.11: (a) The image corrected for noise still shows individual pixels, which are unlikely electrons. (b) These pixels are additionally set to 0 by applying the isolated pixel correction. For better visualisation of the isolated pixels, the colour bar has been limited.

Quantification of an Electron

After applying this image correction procedure, the region around the light spot induced by an electron signal is free of noise, as can be seen by selecting a single spot from an image, shown in Figure 10.12a. It can be described by a Gaussian distribution with a FWHM of 3.2 pixels.

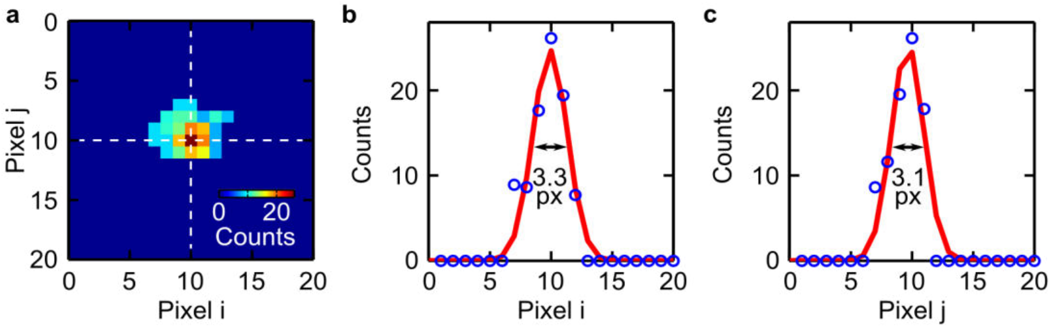

Figure 10.12: (a) An individual electron signal is represented by a Gaussian-shaped distribution of counts, with its maximum at 26 counts. (b-c) Cuts through the image (blue dots), taken at the dashed lines, were fitted to a Gaussian distribution (red curves). The FWHM of an individual electron signal is about 3.2 pixels.

On the energy axis one pixel corresponds to $\Delta E = 14.4\ \mathrm{meV}$. Integrated over the spatial axis, an electron appears in a kinetic energy spectrum with a width (FWHM) of about $\sim 46\ \mathrm{meV}$ peaking at 84 counts, as displayed in Figure 10.13a. Furthermore, by analysing 50 selected electrons it is found, that an electron signal corresponds on average to about 225 counts on the detector, as shown in Figure 10.13b This allows for the conversion of the signature of an electron into the units of counts per eV, as displayed in Figure 10.13a such that integration over the energy axis gives the number of electrons.

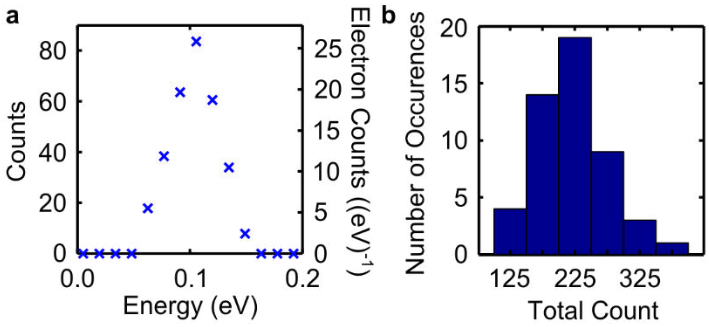

Figure 10.13: (a) Integrated over the spatial axis an electron is described by a width (FHWM) of ~46 meV and peaks at ~84 counts or ~26 counts per eV. (b) A histogram of the total counts of 50 single electrons yields an average of 225 counts per electron. Modified from [JR5].

10.3. Numerical Implementation of the Schrödinger Equation

Numerically, the eigenvalue problem of Equation 7.1, i.e. the time-independent Schrödinger equation, is efficiently solved using the software package Matlab and its internal eigenvalue solver eig() as done in this thesis, provided that the Hamiltonian is given in matrix form. For this, the Hamiltonian is discretised by the method of finite differences [223]. In this method the first-order derivative is approximated as:

$$\frac{\partial}{\partial x}\psi(x) \approx \frac{\psi(x+\Delta x) - \psi(x)}{\Delta x} \tag{10.11}$$

and consequently, the second-order derivative as:

$$\frac{\partial^2}{\partial x^2}\psi(x) \approx \frac{\psi(x-\Delta x) - 2\psi(x) + \psi(x+\Delta x)}{(\Delta x)^2} \quad (10.12)$$

Here, Δx is the step size in the x-direction.

Using the notation $\psi(x) = \psi_i$, the action of the Hamiltonian on the wave function in discrete space can be written as:

$$H\psi(x) \approx \frac{-\hbar^2}{2m_e(\Delta x)^2}(\psi_{i-1} - 2\psi_i + \psi_{i+1}) + V_i\psi_i \quad (10.13)$$

In matrix representation the Hamiltonian is given by:

$$H = \begin{bmatrix} V(x_1) + 2b & -b & 0 & 0 \\ -b & V(x_2) + 2b & -b & 0 \\ 0 & -b & V(x_3) + 2b & \cdots \\ 0 & 0 & \cdots & \cdots \end{bmatrix} \quad (10.14)$$

Here, $b = \frac{\hbar^2}{2m_e\Delta x^2}$.

One way of verifying the numerical implementation is calculating the stationary electron wave functions for the potential of a quantum harmonic oscillator, for which the solutions are known analytically [271]. Specifically, the potential is:

$$V(x) = \frac{1}{2}m_e\omega x^2 \quad (10.15)$$

Here, ω is the angular frequency of the oscillator. The associated energy levels are:

$$E_n = \left(n + \frac{1}{2}\right)\hbar\omega, \qquad n = 0,1,2,\ldots \quad (10.16)$$

The obtained eigenfunctions were compared to the analytic form:

$$\psi_n(x) = \frac{1}{\sqrt{2^n n!}}\left(\frac{m_e\omega}{\pi\hbar}\right)^{1/4} \exp\left(-\frac{m_e\omega x^2}{2\hbar}\right) H_n\left(\sqrt{\frac{m_e\omega}{\hbar}}x\right), \qquad n = 0,1,2,\ldots \quad (10.17)$$

with the Hermite polynomials $H_n(x) = (-1)^n \exp(x^2)\frac{d^n}{dx^n}(\exp(-x^2))$.

In the simulation, the angular frequency was arbitrarily set to $\omega = 0.2156 * 10^{15}\ \mathrm{s}^{-1}$, such that $\hbar\omega = 141.9\ \mathrm{meV}$. Figure 10.14a shows the probability density for the first six eigenfunctions, plotted on the energy axis at a height corresponding to their associated eigenvalues. The eigenvalues are evenly spaced by $141.9 \pm 0.1\ \mathrm{meV}$, with their ground state at $E_0 = 70.9\ \mathrm{meV}$, which is very close to the analytical value $E_0 = 71.0\ \mathrm{meV}$. Figure 10.14b shows the wave function for $n = 1$, which matches the analytical solution.

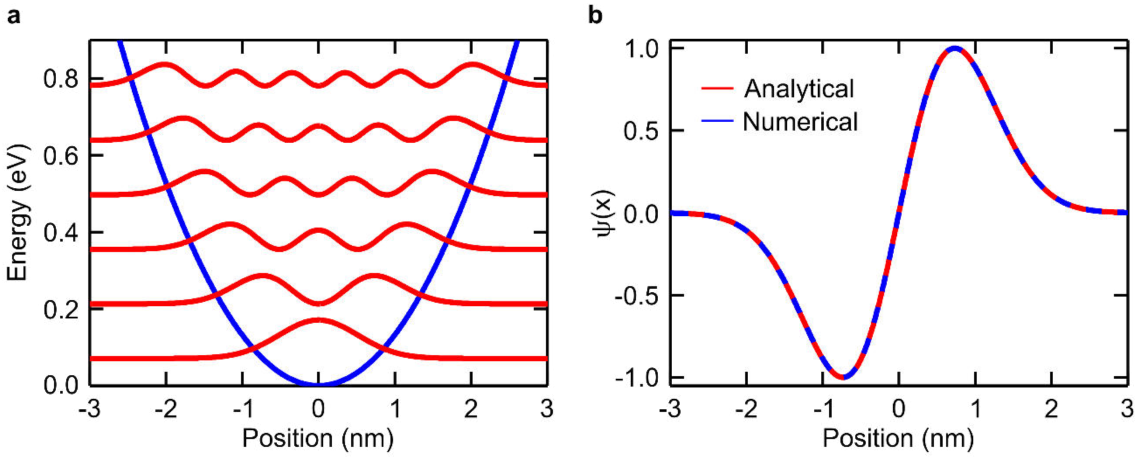

Figure 10.14: Harmonic oscillator. (a) The probability densities of the first six eigenfunctions are plotted at a height corresponding to their associated eigenvalues, revealing equally spaced energy levels as expected for a harmonic oscillator potential (blue curve). (b) A comparison between the analytical (red) and the calculated (blue) real part of the wave function for $n = 1$ yields excellent agreement.

Similarly, in two dimensions the derivatives are discretised as [223]:

$$\begin{gathered}\left(\frac{\partial^2}{\partial x^2}+\frac{\partial^2}{\partial y^2}\right)\psi(x,y)\approx \\ \frac{\psi(x-\Delta x,y)-2\psi(x,y)+\psi(x+\Delta x,y)}{(\Delta x)^2} \\ +\frac{\psi(x,y-\Delta y)-2\psi(x,y)+\psi(x,y+\Delta y)}{(\Delta y)^2}\end{gathered} \tag{10.18}$$

Here, Δy is the step size in the y-direction.

Setting $\Delta x = \Delta y$ and using the notation $\psi(x,y) = \psi_{i,j}$, the action of the Hamiltonian on the wave function in 2D discrete space can be written as:

$$\begin{gathered}H\psi(x,y)\approx \\ \frac{-\hbar^2}{2m_e(\Delta x)^2}\left(\psi_{i-1,j}+\psi_{i,j-1}-4\psi_{i,j}+\psi_{i+1,j}+\psi_{i,j+1}\right)+V_{i,j}\psi_{i,j}\end{gathered} \tag{10.19}$$

In matrix representation, and with $\psi(x,y)$ written as column vector, the Hamiltonian becomes, here exemplary for $n\times m = 3\times 3$:

$$\begin{gathered}H\psi(x,y)\approx \\ \left(\begin{bmatrix} 4b & -b & 0 & -b & 0 & 0 & 0 & 0 & 0 \\ -b & 4b & -b & 0 & -b & 0 & 0 & 0 & 0 \\ 0 & -b & 4b & 0 & 0 & -b & 0 & 0 & 0 \\ -b & 0 & 0 & 4b & -b & 0 & -b & 0 & 0 \\ 0 & -b & 0 & -b & 4b & -b & 0 & -b & 0 \\ 0 & 0 & -b & 0 & -b & 4b & 0 & 0 & -b \\ 0 & 0 & 0 & -b & 0 & 0 & 4b & -b & 0 \\ 0 & 0 & 0 & 0 & -b & 0 & -b & 4b & -b \\ 0 & 0 & 0 & 0 & 0 & -b & 0 & -b & 4b \end{bmatrix}+V_{i,j}\right)\begin{pmatrix}\psi_{1,1}\\ \psi_{2,1}\\ \psi_{3,1}\\ \psi_{1,2}\\ \psi_{2,2}\\ \psi_{3,2}\\ \psi_{1,3}\\ \psi_{2,3}\\ \psi_{3,3}\end{pmatrix}\end{gathered} \tag{10.20}$$

with $b = \frac{\hbar^2}{2m_e \Delta x^2}$. In this way, again a matrix is obtained, which Matlab's eigenvalue solver can deal with. The 2D wave functions are then found by reshaping the associated eigenvector.

For the results presented in this thesis, the calculation of eigenvalues was carried out and sped up using the alternative eigenvalue solver eigs(). This function can deal with a sparse matrix, which may be stored into computational memory more efficiently, as most of its elements are zero. In Matlab, this task is carried out by the function sparse(). This allows for using an increased number of data points and hence a finer grid. Furthermore, the function eigs() allows for the calculation of a limited number of eigenvalues. Here, the option of specifying a concrete number and calculating the nearest 250 eigenvalues proved to be the fastest way to cover the region of the eigenvalue spectrum containing solutions corresponding to image potential states.

Again, the numerical implementation was checked with a harmonic oscillator potential, for which the solutions are known [271]. In two dimensions,

$$V(x) = \frac{1}{2} m_e \omega (x^2 + y^2) \tag{10.21}$$

The associated eigenvalues are

$$E_{n_x,n_y} = (n_x + n_y + 1)\hbar\omega, \qquad n_x = 0,1,2,\ldots \text{ and } n_y = 0,1,2,\ldots \tag{10.22}$$

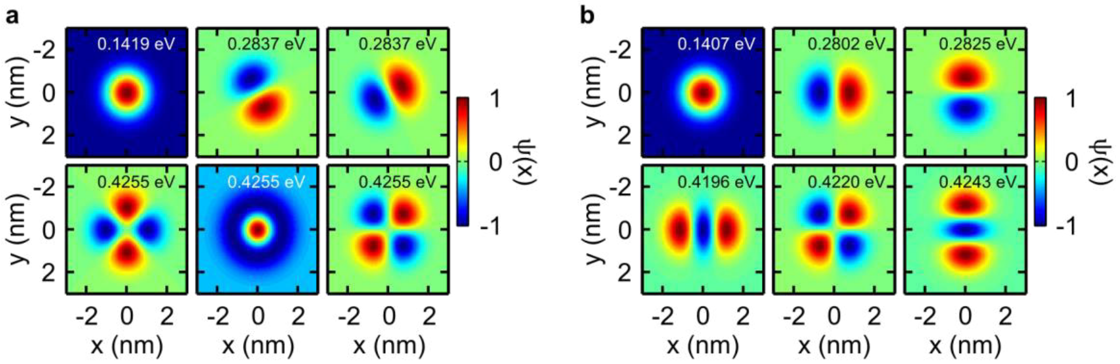

Figure 10.15: (a) First six eigenfunctions associated with a harmonic oscillator potential and their associated (degenerate) eigenvalues for a symmetric spatial resolution. (b) In the same potential, the first six eigenfunctions appear as expected for a slightly asymmetric spatial resolution, with the degeneracy of the eigenvalues now broken.

In this simulation, the numerical grid spanned from -3 nm to +3 nm in both directions, discretised into 121x121 points. The angular frequency was again arbitrarily set to $\omega = 0.2156 * 10^{15}\ \mathrm{s}^{-1}$. Numerically, the ground state energy eigenvalue $E_{0,0} = 0.1419\ \mathrm{eV}$ is equal to the analytical value $E_{0,0} = 0.1419\ \mathrm{eV}$. The next energy levels are then doubly and triply degenerate, as expected. However, the obtained wave functions, as shown in Figure 10.15a, do not appear as the expected wave functions, but rather represent a linear combination of them. The expected wave functions, shown in Figure 10.15b, are obtained by choosing an asymmetric spatial resolution, that is changing the number of grid points to 121x123. In this way, one axis is numerically preferred over the other. In consequence, the degeneracy is broken.

11. References

[1] P. B. Corkum and F. Krausz, Nature Physics **3**, 381 (2007).

[2] F. Krausz and M. Ivanov, Reviews of Modern Physics **81**, 163 (2009).

[3] F. Krausz and M. I. Stockman, Nature Photonics **8**, 205 (2014).

[4] E. Goulielmakis, V. S. Yakovlev, A. L. Cavalieri, M. Uiberacker, V. Pervak, A. Apolonski, R. Kienberger, U. Kleineberg, and F. Krausz, Science **317**, 769 (2007).

[5] P. Agostini, F. Fabre, G. Mainfray, G. Petite, and N. K. Rahman, Physical Review Letters **42**, 1127 (1979).

[6] R. R. Freeman and P. H. Bucksbaum, Journal of Physics B: Atomic, Molecular and Optical Physics **24**, 325 (1991).

[7] D. B. Milošević, G. G. Paulus, D. Bauer, and W. Becker, Journal of Physics B: Atomic, Molecular and Optical Physics **39**, R203 (2006).

[8] P. B. Corkum, Physical Review Letters **71**, 1994 (1993).

[9] J. L. Krause, K. J. Schafer, and K. C. Kulander, Physical Review Letters **68**, 3535 (1992).

[10] H. Niikura, F. Legare, R. Hasbani, A. D. Bandrauk, M. Y. Ivanov, D. M. Villeneuve, and P. B. Corkum, Nature **417**, 917 (2002).

[11] P. Antoine, A. L'Huillier, and M. Lewenstein, Physical Review Letters **77**, 1234 (1996).

[12] M. Hentschel *et al.*, Nature **414**, 509 (2001).

[13] P. M. Paul, E. S. Toma, P. Breger, G. Mullot, F. Augé, P. Balcou, H. G. Muller, and P. Agostini, Science **292**, 1689 (2001).

[14] J. Itatani, J. Levesque, D. Zeidler, H. Niikura, H. Pepin, J. C. Kieffer, P. B. Corkum, and D. M. Villeneuve, Nature **432**, 867 (2004).

[15] O. Smirnova, Y. Mairesse, S. Patchkovskii, N. Dudovich, D. Villeneuve, P. Corkum, and M. Y. Ivanov, Nature **460**, 972 (2009).

[16] M. Schultze *et al.*, Science **328**, 1658 (2010).

[17] A. L. Cavalieri *et al.*, Nature **449**, 1029 (2007).

[18] A. Einstein, Annalen der Physik **322**, 132 (1905).

[19] S. Ghimire, A. D. DiChiara, E. Sistrunk, P. Agostini, L. F. DiMauro, and D. A. Reis, Nature Physics **7**, 138 (2011).

[20] M. Hohenleutner, F. Langer, O. Schubert, M. Knorr, U. Huttner, S. W. Koch, M. Kira, and R. Huber, Nature **523**, 572 (2015).

[21] O. Schubert *et al.*, Nature Photonics **8**, 119 (2014).

[22] G. Ndabashimiye, S. Ghimire, M. Wu, D. A. Browne, K. J. Schafer, M. B. Gaarde, and D. A. Reis, Nature **534**, 520 (2016).

[23] S. Ghimire, G. Ndabashimiye, A. D. DiChiara, E. Sistrunk, M. I. Stockman, P. Agostini, L. F. DiMauro, and D. A. Reis, Journal of Physics B: Atomic, Molecular and Optical Physics **47**, 204030 (2014).

[24] A. Schiffrin *et al.*, Nature **493**, 70 (2013).

[25] M. Schultze *et al.*, Nature **493**, 75 (2013).

[26] L. Novotny and S. J. Stranick, Annual Review of Physical Chemistry **57**, 303 (2006).

[27] N. Behr and M. B. Raschke, The Journal of Physical Chemistry C **112**, 3766 (2008).

[28] C. Ropers, D. R. Solli, C. P. Schulz, C. Lienau, and T. Elsaesser, Physical Review Letters **98**, 043907 (2007).

[29] P. Hommelhoff, C. Kealhofer, and M. A. Kasevich, Phys Rev Lett **97**, 247402 (2006).

[30] B. Barwick, C. Corder, J. Strohaber, N. Chandler-Smith, C. Uiterwaal, and H. Batelaan, New Journal of Physics **9**, 142 (2007).

[31] B. J. Siwick, J. R. Dwyer, R. E. Jordan, and R. J. D. Miller, Science **302**, 1382 (2003).
[32] T. Ishikawa *et al.*, Science **350**, 1501 (2015).
[33] E. Quinonez, J. Handali, and B. Barwick, Review of Scientific Instruments **84**, 103710 (2013).
[34] M. Müller, A. Paarmann, and R. Ernstorfer, Nature Communications **5** (2014).
[35] D. Ehberger, J. Hammer, M. Eisele, M. Krüger, J. Noe, A. Högele, and P. Hommelhoff, Physical Review Letters **114**, 227601 (2015).
[36] G. Herink, D. R. Solli, M. Gulde, and C. Ropers, Nature **483**, 190 (2012).
[37] D. J. Park, B. Piglosiewicz, S. Schmidt, H. Kollmann, M. Mascheck, and C. Lienau, Physical Review Letters **109**, 244803 (2012).
[38] B. Piglosiewicz, S. Schmidt, D. J. Park, J. Vogelsang, P. Groß, C. Manzoni, P. Farinello, G. Cerullo, and C. Lienau, Nature Photonics **8**, 37 (2014).
[39] M. Schenk, M. Krüger, and P. Hommelhoff, Physical Review Letters **105**, 257601 (2010).
[40] M. Krüger, M. Schenk, and P. Hommelhoff, Nature **475**, 78 (2011).
[41] U. Höfer, I. L. Shumay, C. Reuß, U. Thomann, W. Wallauer, and T. Fauster, Science **277**, 1480 (1997).
[42] P. M. Echenique and J. B. Pendry, Progress in Surface Science **32**, 111 (1989).
[43] T. Fauster and W. Steinmann, in *Electromagnetic Waves: Recent Developments in Research*, edited by P. Halevi (Elsevier, Amsterdam, 1995), pp. 347.
[44] M. Ciappina, A. J. Pérez-Hernández, T. Shaaran, and M. Lewenstein, The European Physical Journal D **68**, 1 (2014).
[45] E. N. Pugh and T. D. Lamb, Handbook of Biological Physics **3**, 183 (2000).
[46] J. N. Tinsley, M. I. Molodtsov, R. Prevedel, D. Wartmann, J. Espigule-Pons, M. Lauwers, and A. Vaziri, Nature Communications **7** (2016).
[47] R. Schoenlein, L. Peteanu, R. Mathies, and C. Shank, Science **254**, 412 (1991).
[48] D. Polli *et al.*, Nature **467**, 440 (2010).
[49] R. D. Burgoyne, Nature reviews. Neuroscience **8**, 182 (2007).
[50] K.-W. Koch and D. Dell’Orco, ACS Chemical Neuroscience **4**, 909 (2013).
[51] M. J. Berridge, P. Lipp, and M. D. Bootman, Nat Rev Mol Cell Biol **1**, 11 (2000).
[52] M. Ikura and J. B. Ames, Proceedings of the National Academy of Sciences of the United States of America **103**, 1159 (2006).
[53] R. D. Burgoyne and L. P. Haynes, Biochimica et Biophysica Acta (BBA) - Molecular Cell Research **1853**, 1921 (2015).
[54] G. Navarro *et al.*, Chemistry & Biology **21**, 1546.
[55] H. Kolb, E. Fernandez, and R. Nelson, *Webvision: The Organization of the Retina and Visual System* (University of Utah Health Sciences Center, Salt Lake City (UT), 1995).
[56] J. M. Berg, J. L. Tymoczko, and L. Stryer, *Biochemistry* (W. H. Freeman and Company, New York, 2002).
[57] J. K. Bowmaker and H. J. Dartnall, The Journal of Physiology **298**, 501 (1980).
[58] W. M. Oldham and H. E. Hamm, Nat Rev Mol Cell Biol **9**, 60 (2008).
[59] E. E. Fesenko, S. S. Kolesnikov, and A. L. Lyubarsky, Nature **313**, 310 (1985).
[60] K.-W. Koch and D. Dell'Orco, Frontiers in Molecular Neuroscience **8** (2015).
[61] I. V. Peshenko and A. M. Dizhoor, Journal of Biological Chemistry **281**, 23830 (2006).
[62] K.-W. Koch, FEBS Letters **587**, 2055 (2013).
[63] R. Stephen, G. Bereta, M. Golczak, K. Palczewski, and M. C. Sousa, Structure **15**, 1392 (2007).

[64] J. B. Ames, R. Ishima, T. Tanaka, J. I. Gordon, L. Stryer, and M. Ikura, Nature **389**, 198 (1997).
[65] G. T. Hermanson, *Bioconjugate Techniques* (Elsevier Science, 2013).
[66] W. Chiuman and Y. Li, Nucleic Acids Research **35**, 401 (2007).
[67] A. Weiner, *Ultrafast Optics* (Wiley, 2011).
[68] J. R. Lakowicz, *Principles of Fluorescence Spectroscopy* (Springer US, 2006).
[69] V. Sundström and T. Gillbro, Chemical Physics **61**, 257 (1981).
[70] K. Suhling, D. M. Davis, and D. Phillips, Journal of Fluorescence **12**, 91 (2002).
[71] T. Förster and G. Hoffmann, Zeitschrift für Physikalische Chemie **75**, 63 (1971).
[72] V. Buschmann, K. D. Weston, and M. Sauer, Bioconjugate Chemistry **14**, 195 (2003).
[73] S. J. Strickler and R. A. Berg, The Journal of Chemical Physics **37**, 814 (1962).
[74] P. Selényi, Physical Review **56**, 477 (1939).
[75] A. Einstein, Annalen der Physik **322**, 549 (1905).
[76] G. F. Schröder, U. Alexiev, and H. Grubmüller, Biophysical Journal **89**, 3757 (2005).
[77] M. Wahl, *Technical Note: Time-Correlated Single Photon Counting* (PicoQuant GmbH, 2014).
[78] S. Sulmann, D. Dell'Orco, V. Marino, P. Behnen, and K.-W. Koch, Chemistry – A European Journal **20**, 6756 (2014).
[79] V. Marino, S. Sulmann, K.-W. Koch, and D. Dell'Orco, Biochimica et Biophysica Acta (BBA) - Molecular Cell Research **1853**, 2055 (2015).
[80] H. Kollmann, S. F. Becker, J. Shirdel, A. Scholten, A. Ostendorp, C. Lienau, and K.-W. Koch, ACS Chemical Biology **7**, 1006 (2012).
[81] G. G. Paulus, F. Lindner, H. Walther, A. Baltuška, E. Goulielmakis, M. Lezius, and F. Krausz, Physical Review Letters **91**, 253004 (2003).
[82] A. Hartschuh, Angewandte Chemie International Edition **47**, 8178 (2008).
[83] R. L. Fork, B. I. Greene, and C. V. Shank, Applied Physics Letters **38**, 671 (1981).
[84] P. Moulton, Optics News **8**, 9 (1982).
[85] P. F. Moulton, J. Opt. Soc. Am. B **3**, 125 (1986).
[86] D. E. Spence, P. N. Kean, and W. Sibbett, Opt. Lett. **16**, 42 (1991).
[87] M. T. Asaki, C.-P. Huang, D. Garvey, J. Zhou, H. C. Kapteyn, and M. M. Murnane, Opt. Lett. **18**, 977 (1993).
[88] D. Strickland and G. Mourou, Optics Communications **56**, 219 (1985).
[89] S. Backus, C. G. Durfee, M. M. Murnane, and H. C. Kapteyn, Review of Scientific Instruments **69**, 1207 (1998).
[90] J. A. Giordmaine and R. C. Miller, Physical Review Letters **14**, 973 (1965).
[91] R. W. Boyd, *Nonlinear Optics* (Elsevier Science, 2013).
[92] M. Bradler, P. Baum, and E. Riedle, Applied Physics B **97**, 561 (2009).
[93] R. R. Alfano and S. L. Shapiro, Physical Review Letters **24**, 584 (1970).
[94] P. Russell, Science **299**, 358 (2003).
[95] J. C. Knight, Nature **424**, 847 (2003).
[96] G. Cerullo and S. De Silvestri, Review of Scientific Instruments **74**, 1 (2003).
[97] E. Riedle, M. Beutter, S. Lochbrunner, J. Piel, S. Schenkl, S. Spörlein, and W. Zinth, Applied Physics B **71**, 457 (2000).
[98] D. Brida, C. Manzoni, G. Cirmi, M. Marangoni, S. Bonora, P. Villoresi, S. D. Silvestri, and G. Cerullo, Journal of Optics **12**, 013001 (2010).
[99] T. Wilhelm, J. Piel, and E. Riedle, Opt. Lett. **22**, 1494 (1997).
[100] D. Eimerl, L. Davis, S. Velsko, E. K. Graham, and A. Zalkin, Journal of Applied Physics **62**, 1968 (1987).
[101] D. Zhang, Y. Kong, and J.-y. Zhang, Optics Communications **184**, 485 (2000).

[102] F. J. Furch, S. Birkner, F. Kelkensberg, A. Giree, A. Anderson, C. P. Schulz, and M. J. J. Vrakking, Opt. Express **21**, 22671 (2013).

[103] I. Nobuhisa, K. Kenta, K. Teruto, W. Shuntaro, and I. Jiro, Applied Physics Express **4**, 022701 (2011).

[104] S. T. Cundiff, Journal of Physics D: Applied Physics **35**, R43 (2002).

[105] T. Fuji *et al.*, Opt. Lett. **30**, 332 (2005).

[106] O. D. Mücke, R. Ell, A. Winter, J.-W. Kim, J. R. Birge, L. Matos, and F. X. Kärtner, Opt. Express **13**, 5163 (2005).

[107] S. Rausch, T. Binhammer, A. Harth, E. Schulz, M. Siegel, and U. Morgner, Opt. Express **17**, 20282 (2009).

[108] G. Cerullo, A. Baltuška, O. D. Mücke, and C. Vozzi, Laser & Photonics Reviews **5**, 323 (2011).

[109] A. Baltuška, T. Fuji, and T. Kobayashi, Physical Review Letters **88**, 133901 (2002).

[110] G. Krauss, D. Fehrenbacher, D. Brida, C. Riek, A. Sell, R. Huber, and A. Leitenstorfer, Opt. Lett. **36**, 540 (2011).

[111] C. Manzoni, G. Cerullo, and S. De Silvestri, Opt. Lett. **29**, 2668 (2004).

[112] C. Vozzi *et al.*, Opt. Express **14**, 10109 (2006).

[113] C. Homann, M. Bradler, M. Förster, P. Hommelhoff, and E. Riedle, Opt. Lett. **37**, 1673 (2012).

[114] M. Bradler, C. Homann, and E. Riedle, Applied Physics B **113**, 19 (2013).

[115] A. E. Siegman, *Lasers* (University Science Books, 1986).

[116] G. Stibenz and G. Steinmeyer, Opt. Express **13**, 2617 (2005).

[117] R. Trebino, K. W. DeLong, D. N. Fittinghoff, J. N. Sweetser, M. A. Krumbügel, B. A. Richman, and D. J. Kane, Review of Scientific Instruments **68**, 3277 (1997).

[118] C. Iaconis and I. A. Walmsley, Opt. Lett. **23**, 792 (1998).

[119] V. Petrov, F. Seifert, O. Kittelmann, J. Ringling, and F. Noack, Journal of Applied Physics **76**, 7704 (1994).

[120] P. A. Franken, A. E. Hill, C. W. Peters, and G. Weinreich, Physical Review Letters **7**, 118 (1961).

[121] N. Bloembergen and P. S. Pershan, Physical Review **128**, 606 (1962).

[122] F. Shimizu, Physical Review Letters **19**, 1097 (1967).

[123] R. R. Alfano and S. L. Shapiro, Physical Review Letters **24**, 592 (1970).

[124] R. H. Stolen and C. Lin, Physical Review A **17**, 1448 (1978).

[125] J. E. Midwinter and J. Warner, British Journal of Applied Physics **16**, 1135 (1965).

[126] P. Kumbhakar and T. Kobayashi, Journal of Applied Physics **94**, 1329 (2003).

[127] G. Cerullo, M. Nisoli, S. Stagira, and S. De Silvestri, Opt. Lett. **23**, 1283 (1998).

[128] A. Baltuska *et al.*, Nature **421**, 611 (2003).

[129] M. Kakehata, H. Takada, Y. Kobayashi, K. Torizuka, Y. Fujihira, T. Homma, and H. Takahashi, Opt. Lett. **26**, 1436 (2001).

[130] T. Wittmann, B. Horvath, W. Helml, M. G. Schatzel, X. Gu, A. L. Cavalieri, G. G. Paulus, and R. Kienberger, Nature Physics **5**, 357 (2009).

[131] B. Borchers, A. Anderson, and G. Steinmeyer, Laser & Photonics Reviews **8**, 303 (2014).

[132] A. Guandalini, P. Eckle, M. Anscombe, P. Schlup, J. Biegert, and U. Keller, Journal of Physics B: Atomic, Molecular and Optical Physics **39**, S257 (2006).

[133] M. Knoll and E. Ruska, Zeitschrift für Physik **78**, 318 (1932).

[134] R. Erni, M. D. Rossell, C. Kisielowski, and U. Dahmen, Physical Review Letters **102**, 096101 (2009).

[135] P. E. Batson, N. Dellby, and O. L. Krivanek, Nature **418**, 617 (2002).

[136] A. H. Zewail, Science **328**, 187 (2010).

[137] B. Barwick and A. H. Zewail, ACS Photonics **2**, 1391 (2015).

[138] J. C. Williamson and A. H. Zewail, Proceedings of the National Academy of Sciences **88**, 5021 (1991).

[139] J. C. Williamson, J. Cao, H. Ihee, H. Frey, and A. H. Zewail, Nature **386**, 159 (1997).

[140] H. Ihee, V. A. Lobastov, U. M. Gomez, B. M. Goodson, R. Srinivasan, C.-Y. Ruan, and A. H. Zewail, Science **291**, 458 (2001).

[141] C. Gerbig, A. Senftleben, S. Morgenstern, C. Sarpe, and T. Baumert, New Journal of Physics **17**, 043050 (2015).

[142] P. Baum and A. H. Zewail, Chemical Physics **366**, 2 (2009).

[143] P. Baum and A. H. Zewail, Proceedings of the National Academy of Sciences **103**, 16105 (2006).

[144] P. Baum, Chemical Physics **423**, 55 (2013).

[145] M. Aidelsburger, F. O. Kirchner, F. Krausz, and P. Baum, Proceedings of the National Academy of Sciences **107**, 19714 (2010).

[146] M. Gao *et al.*, Nature **496**, 343 (2013).

[147] L. Wimmer, G. Herink, D. R. Solli, S. V. Yalunin, K. E. Echternkamp, and C. Ropers, Nature Physics **10**, 432 (2014).

[148] P. Baum and A. H. Zewail, Proceedings of the National Academy of Sciences **104**, 18409 (2007).

[149] A. Feist, K. E. Echternkamp, J. Schauss, S. V. Yalunin, S. Schafer, and C. Ropers, Nature **521**, 200 (2015).

[150] W. Kaiser and C. G. B. Garrett, Physical Review Letters **7**, 229 (1961).

[151] F. H. M. Faisal, *Theory of Multiphoton Processes* (Springer US, New York, 1987).

[152] T. H. Maiman, Nature **187**, 493 (1960).

[153] A. L. Schawlow and C. H. Townes, Physical Review **112**, 1940 (1958).

[154] G. G. Paulus, W. Nicklich, H. Xu, P. Lambropoulos, and H. Walther, Physical Review Letters **72**, 2851 (1994).

[155] M. Ferray, A. L. Huillier, X. F. Li, L. A. Lompre, G. Mainfray, and C. Manus, Journal of Physics B: Atomic, Molecular and Optical Physics **21**, L31 (1988).

[156] T. Popmintchev *et al.*, Science **336**, 1287 (2012).

[157] S. Luan, R. Hippler, H. Schwier, and H. O. Lutz, Europhysics Letters **9**, 489 (1989).

[158] G. Farkas and C. Tóth, Physical Review A **41**, 4123 (1990).

[159] W. S. Fann, R. Storz, and J. Bokor, Physical Review B **44**, 10980 (1991).

[160] M. Aeschlimann, C. A. Schmuttenmaer, H. E. Elsayed-Ali, R. J. D. Miller, J. Cao, Y. Gao, and D. A. Mantell, The Journal of Chemical Physics **102**, 8606 (1995).

[161] F. Banfi, C. Giannetti, G. Ferrini, G. Galimberti, S. Pagliara, D. Fausti, and F. Parmigiani, Physical Review Letters **94**, 037601 (2005).

[162] F. Bisio, M. Nývlt, J. Franta, H. Petek, and J. Kirschner, Physical Review Letters **96**, 087601 (2006).

[163] G. Saathoff, L. Miaja-Avila, M. Aeschlimann, M. M. Murnane, and H. C. Kapteyn, Physical Review A **77**, 022903 (2008).

[164] B. Schröder, M. Sivis, R. Bormann, S. Schäfer, and C. Ropers, Applied Physics Letters **107**, 231105 (2015).

[165] M. Müller, V. Kravtsov, A. Paarmann, M. B. Raschke, and R. Ernstorfer, ACS Photonics **3**, 611 (2016).

[166] D. J. Park, B. Piglosiewicz, S. Schmidt, H. Kollmann, M. Mascheck, P. Groß, and C. Lienau, Annalen der Physik **525**, 135 (2013).

[167] S. V. Yalunin, G. Herink, D. R. Solli, M. Krüger, P. Hommelhoff, M. Diehn, A. Munk, and C. Ropers, Annalen der Physik **525**, L12 (2013).
[168] R. Bormann, M. Gulde, A. Weismann, S. V. Yalunin, and C. Ropers, Physical Review Letters **105**, 147601 (2010).
[169] M. I. Stockman and P. Hewageegana, Applied Physics A **89**, 247 (2007).
[170] S. Thomas, G. Wachter, C. Lemell, J. Burgdörfer, and P. Hommelhoff, New Journal of Physics **17**, 063010 (2015).
[171] L. Novotny, R. X. Bian, and X. S. Xie, Physical Review Letters **79**, 645 (1997).
[172] C. Kealhofer, S. M. Foreman, S. Gerlich, and M. A. Kasevich, Physical Review B **86**, 035405 (2012).
[173] G. Herink, L. Wimmer, and C. Ropers, New Journal of Physics **16**, 123005 (2014).
[174] W. S. Fann, R. Storz, H. W. K. Tom, and J. Bokor, Physical Review B **46**, 13592 (1992).
[175] H. Petek and S. Ogawa, Progress in Surface Science **56**, 239 (1997).
[176] P. G. Etchegoin, E. C. Le Ru, and M. Meyer, The Journal of Chemical Physics **125**, 164705 (2006).
[177] N. Talebi, W. Sigle, R. Vogelgesang, M. Esmann, S. F. Becker, C. Lienau, and P. A. van Aken, ACS Nano **9**, 7641 (2015).
[178] R. Gomer, Surface Science **299**, 129 (1994).
[179] C. Kittel, *Introduction to Solid State Physics* (Wiley, 2004).
[180] R. W. Wood, Physical Review (Series I) **5**, 1 (1897).
[181] R. H. Fowler and L. Nordheim, Proceedings of the Royal Society of London A: Mathematical, Physical and Engineering Sciences **119**, 173 (1928).
[182] R. G. Forbes, Applied Physics Letters **89**, 113122 (2006).
[183] H. Hertz, Annalen der Physik **267**, 983 (1887).
[184] W. Hallwachs, Annalen der Physik **269**, 301 (1888).
[185] P. Lenard, Annalen der Physik **313**, 149 (1902).
[186] M. Planck, Annalen der Physik **309**, 553 (1901).
[187] R. A. Millikan, Physical Review **7**, 355 (1916).
[188] G. Grynberg, A. Aspect, C. Fabre, and C. Cohen-Tannoudji, *Introduction to Quantum Optics: From the Semi-classical Approach to Quantized Light* (Cambridge University Press, 2010).
[189] M. Göppert-Mayer, Annalen der Physik **401**, 273 (1931).
[190] R. R. Freeman, P. H. Bucksbaum, H. Milchberg, S. Darack, D. Schumacher, and M. E. Geusic, Physical Review Letters **59**, 1092 (1987).
[191] L. Veisz, G. Kurkin, K. Chernov, V. Tarnetsky, A. Apolonski, F. Krausz, and E. Fill, New Journal of Physics **9**, 451 (2007).
[192] B. Barwick, D. J. Flannigan, and A. H. Zewail, Nature **462**, 902 (2009).
[193] S. T. Park, M. Lin, and A. H. Zewail, New Journal of Physics **12**, 123028 (2010).
[194] L. Piazza, T. T. A. Lummen, E. Quiñonez, Y. Murooka, B. W. Reed, B. Barwick, and F. Carbone, Nature Communications **6** (2015).
[195] F. J. García de Abajo, A. Asenjo-Garcia, and M. Kociak, Nano Letters **10**, 1859 (2010).
[196] G. G. Paulus, W. Becker, and H. Walther, Physical Review A **52**, 4043 (1995).
[197] L. V. Keldysh, Soviet Physics JETP **20**, 1307 (1965).
[198] F. V. Bunkin and M. V. Fedorov, Soviet Physics JETP **21**, 896 (1965).
[199] S. Larochelle, A. Talebpour, and S. L. Chin, Journal of Physics B: Atomic, Molecular and Optical Physics **31**, 1201 (1998).
[200] G. G. Paulus, W. Becker, W. Nicklich, and H. Walther, Journal of Physics B: Atomic, Molecular and Optical Physics **27**, L703 (1994).

[201] W. Denk and D. W. Pohl, Journal of Vacuum Science & Technology B **9**, 510 (1991).
[202] E. L. Murphy and R. H. Good, Physical Review **102**, 1464 (1956).
[203] F. Sirotti, N. Beaulieu, A. Bendounan, M. G. Silly, C. Chauvet, G. Malinowski, G. Fratesi, V. Véniard, and G. Onida, Physical Review B **90**, 035401 (2014).
[204] G. G. Paulus and D. Bauer, in *Time in Quantum Mechanics - Vol. 2*, edited by G. Muga, A. Ruschhaupt, and A. Campo (Springer Berlin Heidelberg, Berlin, Heidelberg, 2009), pp. 303.
[205] W. Becker, F. Grasbon, R. Kopold, D. B. Milošević, G. G. Paulus, and H. Walther, in *Advances In Atomic, Molecular, and Optical Physics*, edited by B. Bederson, and H. Walther (Academic Press, 2002), pp. 35.
[206] P. H. Bucksbaum, R. R. Freeman, M. Bashkansky, and T. J. McIlrath, J. Opt. Soc. Am. B **4**, 760 (1987).
[207] J. H. Eberly, J. Javanainen, and K. Rzążewski, Physics Reports **204**, 331 (1991).
[208] F. H. M. Faisal, J. Z. Kamiński, and E. Saczuk, Physical Review A **72**, 023412 (2005).
[209] U. Höfer, Applied Physics B **68**, 383 (1999).
[210] P. M. Echenique, R. Berndt, E. V. Chulkov, T. Fauster, A. Goldmann, and U. Höfer, Surface Science Reports **52**, 219 (2004).
[211] M. Marks, C. H. Schwalb, K. Schubert, J. Güdde, and U. Höfer, Physical Review B **84**, 245402 (2011).
[212] V. M. Silkin, J. Zhao, F. Guinea, E. V. Chulkov, P. M. Echenique, and H. Petek, Physical Review B **80**, 121408 (2009).
[213] N. Armbrust, J. Güdde, and U. Höfer, New Journal of Physics **17**, 103043 (2015).
[214] M. Zamkov, N. Woody, S. Bing, H. S. Chakraborty, Z. Chang, U. Thumm, and P. Richard, Physical Review Letters **93**, 156803 (2004).
[215] M. Feng, J. Zhao, T. Huang, X. Zhu, and H. Petek, Accounts of Chemical Research **44**, 360 (2011).
[216] G. Gumbs, A. Balassis, A. Iurov, and P. Fekete, The Scientific World Journal **2014**, 6, 726303 (2014).
[217] V. Kasperovich, K. Wong, G. Tikhonov, and V. V. Kresin, Physical Review Letters **85**, 2729 (2000).
[218] P. Rinke, K. Delaney, P. García-González, and R. W. Godby, Physical Review A **70**, 063201 (2004).
[219] E. V. Chulkov, V. M. Silkin, and P. M. Echenique, Surface Science **391**, L1217 (1997).
[220] E. V. Chulkov, V. M. Silkin, and P. M. Echenique, Surface Science **437**, 330 (1999).
[221] E. V. Chulkov, M. Machado, and V. M. Silkin, Vacuum **61**, 95 (2001).
[222] J. Güdde and U. Höfer, Progress in Surface Science **80**, 49 (2005).
[223] W. H. Press, *Numerical Recipes: The Art of Scientific Computing* (Cambridge University Press, 2007).
[224] J. Crank and P. Nicolson, Mathematical Proceedings of the Cambridge Philosophical Society **43**, 50 (1946).
[225] M. Esmann, PhD Thesis, Carl von Ossietzky Universität Oldenburg, 2016.
[226] P. Groß, M. Esmann, S. F. Becker, J. Vogelsang, N. Talebi, and C. Lienau, Advances in Physics: X **1**, 297 (2016).
[227] W. P. Davey, Physical Review **25**, 753 (1925).
[228] A. T. J. B. Eppink and D. H. Parker, Review of Scientific Instruments **68**, 3477 (1997).

[229] A. R. Bainbridge and W. A. Bryan, New Journal of Physics **16**, 103031 (2014).
[230] C. C. King, Quanta **3**, 16 (2014).
[231] P. Hohenberg and W. Kohn, Physical Review **136**, B864 (1964).
[232] C. Attaccalite, S. Moroni, P. Gori-Giorgi, and G. B. Bachelet, Physical Review Letters **88**, 256601 (2002).
[233] P. A. M. Dirac, Mathematical Proceedings of the Cambridge Philosophical Society **26**, 376 (1930).
[234] F. Bloch, Zeitschrift für Physik **57**, 545 (1929).
[235] N. D. Lang and W. Kohn, Physical Review B **1**, 4555 (1970).
[236] M. Förster, T. Paschen, M. Krüger, C. Lemell, G. Wachter, F. Libisch, T. Madlener, J. Burgdörfer, and P. Hommelhoff, Physical Review Letters (2016).
[237] D. Brida, C. Manzoni, and G. Cerullo, Opt. Lett. **37**, 3027 (2012).
[238] G. S. Engel, T. R. Calhoun, E. L. Read, T.-K. Ahn, T. Mancal, Y.-C. Cheng, R. E. Blankenship, and G. R. Fleming, Nature **446**, 782 (2007).
[239] S. M. Falke *et al.*, Science **344**, 1001 (2014).
[240] S. Falke, P. Eravuchira, A. Materny, and C. Lienau, Journal of Raman Spectroscopy **42**, 1897 (2011).
[241] L. Freimuth, C. A. Rozzi, C. Lienau, and J. Christoffers, Synthesis **47**, 1325 (2015).
[242] R. Pflantz and J. Christoffers, Chemistry – A European Journal **15**, 2200 (2009).
[243] S. Sulmann, M. Wallisch, A. Scholten, J. Christoffers, and K.-W. Koch, Biochemistry **55**, 2567 (2016).
[244] M. I. Stockman, Physical Review Letters **93**, 137404 (2004).
[245] C. Ropers, C. C. Neacsu, T. Elsaesser, M. Albrecht, M. B. Raschke, and C. Lienau, Nano Letters **7**, 2784 (2007).
[246] W. L. Barnes, A. Dereux, and T. W. Ebbesen, Nature **424**, 824 (2003).
[247] M. Gulde, S. Schweda, G. Storeck, M. Maiti, H. K. Yu, A. M. Wodtke, S. Schäfer, and C. Ropers, Science **345**, 200 (2014).
[248] E. Goulielmakis *et al.*, Science **320**, 1614 (2008).
[249] P. B. Corkum, N. H. Burnett, and M. Y. Ivanov, Opt. Lett. **19**, 1870 (1994).
[250] M. Ivanov, P. B. Corkum, T. Zuo, and A. Bandrauk, Physical Review Letters **74**, 2933 (1995).
[251] I. J. Sola *et al.*, Nature Physics **2**, 319 (2006).
[252] S. Schmidt, B. Piglosiewicz, D. Sadiq, J. Shirdel, J. S. Lee, P. Vasa, N. Park, D.-S. Kim, and C. Lienau, ACS Nano **6**, 6040 (2012).
[253] H. Kollmann *et al.*, Nano Letters **14**, 4778 (2014).
[254] T. Y. F. Tsang, Physical Review A **52**, 4116 (1995).
[255] Y. R. Shen, Nature **337**, 519 (1989).
[256] S. Kim, J. Jin, Y.-J. Kim, I.-Y. Park, Y. Kim, and S.-W. Kim, Nature **453**, 757 (2008).
[257] M. Sivis, M. Duwe, B. Abel, and C. Ropers, Nature **485**, E1 (2012).
[258] M. Sivis, M. Duwe, B. Abel, and C. Ropers, Nature Physics **9**, 304 (2013).
[259] M. E. Swanwick, P. D. Keathley, A. Fallahi, P. R. Krogen, G. Laurent, J. Moses, F. X. Kärtner, and L. F. Velásquez-García, Nano Letters **14**, 5035 (2014).
[260] R. Kienberger *et al.*, Nature **427**, 817 (2004).
[261] J. Itatani, F. Quéré, G. L. Yudin, M. Y. Ivanov, F. Krausz, and P. B. Corkum, Physical Review Letters **88**, 173903 (2002).
[262] G. Alber and P. Zoller, Physics Reports **199**, 231 (1991).
[263] D. Jaksch, J. I. Cirac, P. Zoller, S. L. Rolston, R. Côté, and M. D. Lukin, Physical Review Letters **85**, 2208 (2000).
[264] T. Wilk, A. Gaëtan, C. Evellin, J. Wolters, Y. Miroshnychenko, P. Grangier, and A. Browaeys, Physical Review Letters **104**, 010502 (2010).

[265] M. Saffman, T. G. Walker, and K. Mølmer, Reviews of Modern Physics **82**, 2313 (2010).
[266] D. P. DiVincenzo, Fortschritte der Physik **48**, 771 (2000).
[267] T. D. Ladd, F. Jelezko, R. Laflamme, Y. Nakamura, C. Monroe, and J. L. O'Brien, Nature **464**, 45 (2010).
[268] L. M. K. Vandersypen, M. Steffen, G. Breyta, C. S. Yannoni, M. H. Sherwood, and I. L. Chuang, Nature **414**, 883 (2001).
[269] T. Rybka, M. Ludwig, M. F. Schmalz, V. Knittel, D. Brida, and A. Leitenstorfer, Nature Photonics **10**, 667 (2016).
[270] P. Vasa, W. Wang, R. Pomraenke, M. Lammers, M. Maiuri, C. Manzoni, G. Cerullo, and C. Lienau, Nature Photonics **7**, 128 (2013).
[271] C. Cohen-Tannoudji, B. Diu, and F. Laloe, *Quantenmechanik* (De Gruyter, Berlin, 2007), Vol. 1.

12. Publications and Conference Contributions

Peer-Reviewed Journals

[JR1] J. Vogelsang*, J. Robin*, B. Piglosiewicz, C. Manzoni, P. Farinello, S. Melzer, P. Feru, G. Cerullo, C. Lienau, and P. Groß, *High passive CEP stability from a few-cycle, tunable NOPA-DFG system for observation of CEP-effects in photoemission*, Optics Express **22**, 25295 (2014), *contributed equally

[JR2] S. Pittalis, A. Delgado, J. Robin, L. Freimuth, J. Christoffers, C. Lienau, and C. A. & Rozzi, *Charge separation dynamics and opto-electronic properties of a diaminoterephthalate-C60 dyad*, Advanced Functional Materials **25**, 2047 (2014)

[JR3] J. Vogelsang, J. Robin, B. J. Nagy, P. Dombi, D. Rosenkranz, M. Schiek, P. Groß, and C. Lienau, *Ultrafast Electron Emission from a Sharp Metal Nanotaper Driven by Adiabatic Nanofocusing of Surface Plasmons*, Nano Letters **15**, 4685 (2015)

[JR4] J. Robin, J. Brauer, S. Sulmann, V. Marino, D. Dell'Orco, C. Lienau, and K.-W. Koch, *Differential Nanosecond Protein Dynamics in Homologous Calcium Sensors*, ACS Chemical Biology **10**, 2344 (2015)

[JR5] J. Robin, J. Vogelsang, J. Solanpäa, P. Wopperer, U. di Giovanni, B. J. Nagy, P. Dombi, E. Räsänen, A. Rubio, C. Lienau, and P. Groß, *Strong-Field Above-Threshold Ionization of Rydberg Electrons Localized to a Single Gold Nanotip*, submitted (2016)

Peer-Reviewed Conference Contributions

[C1] P. Groß, B. Piglosiewicz, S. Schmidt, D. Park, J. Vogelsang, J. Robin, C. Manzoni, P. Farinello, G. Cerullo, and C. Lienau, *Controlling the motion of strong-field, few-cycle photoemitted electrons in the near-field of a sharp metal tip*, in 19th International Conference on Ultrafast Phenomena, OSA Technical Digest (online), paper 10.Thu.B.5 (2014)

[C2] J. Robin, J. Vogelsang, B. J. Nagy, P. Groß, and C. Lienau, *Ultrafast coherent dynamics of Rydberg electrons bound in the image potential near a single metallic nano-object*, in Proc. SPIE 9547, Plasmonics: Metallic Nanostructures and Their Optical Properties XIII, 954708 (Presentation Recording), doi:10.1117/12.2190722 (2015) [invited]

[C3] J. Robin, J. Vogelsang, B. J. Nagy, P. Dombi, P. Groß, and C. Lienau, *Strong Field Above Threshold Ionization of Rydberg Electrons Localized to a Gold Nanotip*, in Conference on Lasers and Electro-Optics, OSA Technical Digest (online), paper FTh4B.1 (2016)

[C4] J. Vogelsang, J. Robin, B. J. Nagy, P. Dombi, D. Rosenkranz, M. Schiek, P. Groß, and C. Lienau, *Remotely Driven Electron Emission for Ultrafast Electron Microscopy*, in Conference on Lasers and Electro-Optics, OSA Technical Digest (online), paper FTh4B.3 (2016)

[C5] J. Robin, J. Vogelsang, B. J. Nagy, P. Dombi, C. Lienau, and P. Groß, *A Road toward Attosecond Physics in Solids - Atomic-Like Rydberg States Localized at a Nanotip*, in 20th International Conference on Ultrafast Phenomena, OSA Technical Digest (online), paper UTu5A.3 (2016)

[C6] J. Vogelsang, J. Robin, B. J. Nagy, P. Dombi, P. Groß, and C. Lienau, *Efficient Emission of Ultrafast Electron Bursts by Plasmonic Nanofocusing of Light*, in 20th International Conference on Ultrafast Phenomena, OSA Technical Digest (online), paper UW1A.6 (2016)

Conference Talks

[T1] J. Robin, J. Vogelsang, K. Strahlendorff, P. Groß, and C. Lienau, *Passively carrier-envelope phase stabilised few-cycle laser pulses in the near-infrared*, DPG, Dresden (2014)

[T2] J. Robin, J. Brauer, S. Sulmann, K.-W. Koch, and C. Lienau, *Conformational Change of Calcium Sensor Protein GCAP1*, 1st German-Iraqi Summer School on Nanophotonics, Delmenhorst (2014)

[T3] J. Robin, J. Brauer, S. Sulmann, C. Lienau, and K.-W. Koch, *Conformational Change of the Neuronal Calcium Sensor GCAP1*, DPG, Berlin (2015)

[T4] J. Robin, J. Vogelsang, C. Lienau, and P. Groß, *Passively CEP stabilised few-cycle laser pulses in the near-infrared*, DPG, Heidelberg (2015)

[T5] J. Robin, J. Vogelsang, P. Groß, and C. Lienau, *Ultrafast Dynamics of Rydberg Electrons from a Metallic Nanotip*, 2nd German-Iraqi Summer School on Nanophotonics, Delmenhorst (2015)

[T6] J. Robin, J. Vogelsang, B. J. Nagy, P. Groß, and C. Lienau, *Above threshold ionization of Rydberg electrons localized to a gold nanotip*, DPG, Hannover (2016)

[T7] J. Robin, J. Vogelsang, B. J. Nagy, P. Groß, and C. Lienau, *Above threshold ionization of Rydberg electrons localized to a gold nanotip*, DPG, Regensburg (2016)

[T8] J. Robin, J. Vogelsang, B. J. Nagy, P. Dombi, P. Groß, and C. Lienau, *Towards Attosecond Physics in Solids: Strong-Field Above Threshold Ionization of Rydberg Electrons from a Gold Nanotip*, DPG, Regensburg (2016) [post-deadline]

[T9] J. Robin, J. Vogelsang, P. Groß, and C. Lienau, *Strong-Field Above Threshold Ionization of Rydberg Electrons Localized to a Gold Nanotip*, Ultrafast Phenomena at Nanostructures: Attosecond Physics Meets Plasmonics, Les Houches (2016) [poster prize]

Patents

[P1] J. Vogelsang, J. Robin, C. Lienau, and P. Groß, *Elektronenquelle und Verfahren zum Erzeugen eines Elektronenstrahls, Verfahren zum Herstellen einer solchen Elektronenquelle sowie deren Verwendung,* DE 102015108893 B3

[P2] C. Lienau, P. Groß, J. Vogelsang, and J. Robin, *Verfahren zum Erzeugen eines Elektronenstrahls und/oder Elektronenpulses sowie eine Elektronenquelle und deren Verwendung,* DE 102016110301 B3

Differential Nanosecond Protein Dynamics in Homologous Calcium Sensors

Jörg Robin[1,2], Jens Brauer[1,2], Stefan Sulmann[3], Valerio Marino[4],
Daniele Dell'Orco[4,5], Christoph Lienau[1,2], and Karl-Wilhelm Koch[2,3]

[1] Ultrafast Nano-Optics, Institute of Physics, Faculty V,
University of Oldenburg, D-26111 Oldenburg, Germany
[2] Center of Interface Science,
University of Oldenburg, D-26111 Oldenburg, Germany
[3] Biochemistry, Department of Neurosciences, Faculty VI,
University of Oldenburg, D-26111 Oldenburg, Germany
[4] Department of Life Sciences and Reproduction, Section of Biological Chemistry,
University of Verona, Verona, Italy
[5] Center for BioMedical Computing (CBMC),
University of Verona, Verona, Italy

ACS Chemical Biology **10**, 2344 (2015)

DOI: 10.1021/acschembio.5b00278

Copyright © 2015 American Chemical Society

Reprinted with kind permission from the American Chemical Society (ACS).

Differential Nanosecond Protein Dynamics in Homologous Calcium Sensors

Jörg Robin,[†,‡] Jens Brauer,[†,‡] Stefan Sulmann,[§] Valerio Marino,[∥] Daniele Dell'Orco,[∥,⊥] Christoph Lienau,[†,‡] and Karl-Wilhelm Koch*[,‡,§]

[†] Ultrafast Nano-Optics, Institute of Physics, Faculty V, University of Oldenburg, D-26111 Oldenburg, Germany
[‡] Center of Interface Science, University of Oldenburg, D-26111 Oldenburg, Germany
[§] Biochemistry, Department of Neurosciences, Faculty VI, University of Oldenburg, D-26111 Oldenburg, Germany
[∥] Department of Life Sciences and Reproduction, Section of Biological Chemistry, University of Verona, Verona, Italy
[⊥] Center for BioMedical Computing (CBMC), University of Verona, Verona, Italy

S *Supporting Information*

ABSTRACT: Shaping the temporal response of photoreceptors is facilitated by a well-balanced second messenger cascade, in which two neuronal Ca^{2+}-sensor proteins operate in a sequential relay mechanism. Although they share structurally similar sensing units, they differentially activate the same target protein. Here, as a prototypical case in Ca^{2+}-mediated signal processing, we investigate differential cellular responsiveness in protein conformational dynamics on a nanosecond time scale. For this, we have site-specifically labeled cysteine residues in guanylate cyclase-activating protein GCAP1 by the fluorescent dye Alexa647 and probed its local environment via time-resolved fluorescence spectroscopy. Fluorescence lifetime and rotational anisotropy measurements reveal a distinct structural movement of the polypeptide chain around position 106 upon release of Ca^{2+}. This is supported by analyzing the diffusional dye motion in a wobbling-in-a-cone model and by molecular dynamics simulations. We conclude that GCAP1 and its cellular cognate GCAP2 operate by distinctly different switching mechanisms despite their high structural homology.

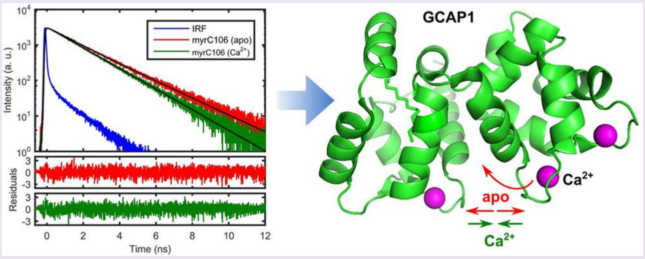

Spatial and temporal variations in intracellular Ca^{2+} signals are key phenomena in physiological processes like, for example, fertilization, apoptosis, muscle contraction, and sensory perception.[1−3] A general open question in Ca^{2+}-mediated signal processing is how physiological specificity is achieved by unique forms of target interaction and activation. For example, the ubiquitous Ca^{2+} sensor calmodulin can adopt different three-dimensional structures depending on target binding,[2] whereas members of the neuronal Ca^{2+} sensor (NCS) protein family share common structural features like EF-hand Ca^{2+}-binding sites but are more specific in target regulation.[3] However, all these signaling pathways have in common that a Ca^{2+}-induced conformational change in the specific Ca^{2+} sensor triggers subsequent protein−protein interaction modes and different target regulatory features.

Photoreceptor cells are remarkable single photon detectors, in which Ca^{2+} transport and Ca^{2+}-sensor systems fulfill key functions for temporally precise responses. Utilizing the second messengers cGMP and Ca^{2+}, these cells respond to changing light conditions on a millisecond time scale.[4] Negative feedback loops further control and shape photoreceptor responses, thereby involving NCS proteins like guanylate cyclase-activating proteins (GCAP) that target membrane guanylate cyclases.[5−7] GCAPs harbor three functional EF-hands and operate in a Ca^{2+}-relay mode fashion in photoreceptor cells,[8−10] which is evident by differences in Ca^{2+}-sensing and catalytic efficiency of target regulation,[8−16] electrophysiological recordings,[9,17] and computational modeling.[18]

The response to fluctuating Ca^{2+}-concentrations by GCAPs is assumed to be mediated by conformational changes.[11−16] For GCAP2, this conformational change was found, in an earlier time-resolved fluorescence study, to reflect a piston-like movement[19] of the α-helix situated between positions C111 and C131. This raises the interesting question of whether the structurally related GCAP1 protein undergoes a similar or even identical conformational transition, even though it differs significantly in its Ca^{2+}-signaling properties. Specifically, one may ask whether these functional differences are already manifesting in early stages of Ca^{2+}-controlled protein dynamics. Previous studies of GCAP1 did not yet conclusively address those questions. Static studies of tryptophan fluorescence quantum yield and Ca^{2+}-induced modifications of cysteines showed conformational transitions without, however, providing insight into structural dynamics.[14,23,24] An amide hydrogen−

Received: April 17, 2015
Accepted: July 23, 2015
Published: July 23, 2015

© 2015 American Chemical Society

DOI: 10.1021/acschembio.5b00278
ACS Chem. Biol. 2015, 10, 2344−2352

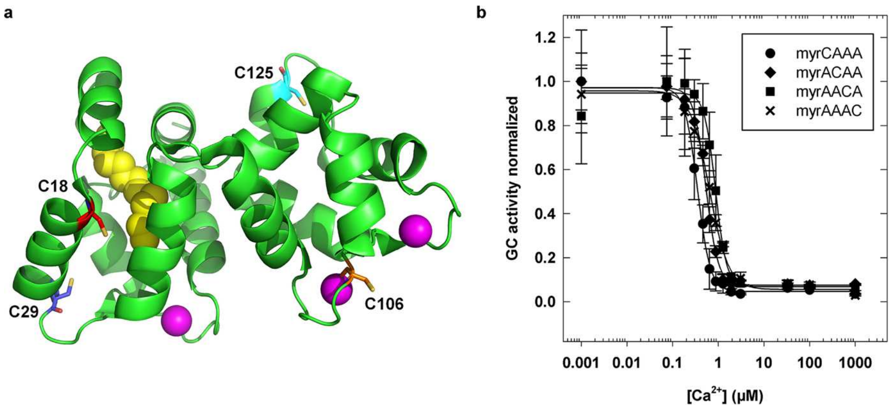

Figure 1. (a) Three-dimensional structural model of GCAP1. The position of each cysteine is highlighted. The myristoyl group (yellow) is layered in a hydrophobic crevice, and the three functional EF-hand motifs have each a bound Ca^{2+} (magenta). (b) Ca^{2+}-sensitive activation of ROS-GC1 by myristoylated GCAP1 mutants as indicated. The IC_{50} values are the following (three to four data sets): 336 nM (Alexa647-labeled CAAA), 529 nM (Alexa647-labeled ACAA), 832 nM (Alexa647-labeled AACA), and 659 nM (Alexa647-labeled AAAC).

deuterium exchange study indicated movements of the *N*-terminal and *C*-terminal fragment upon Ca^{2+}-dissociation.[25] Employing a GCAP1 mutant with an inactive EF-hand 4 in an NMR spectroscopy approach suggested a remote control mechanism, in which EF-hand 4 influences EF-hand 1 for switching the protein form the activator to the inhibitor state.[26,27]

Here, we study the conformational dynamics of GCAP1 by time-resolved fluorescence spectroscopy. Mutants of GCAP1 were expressed with all but one of its four cysteine residues replaced, checked for functionality, and then site-specifically labeled with the fluorescent dye Alexa647. The local environment of the dye was probed by time-resolved fluorescence spectroscopy in the apo-state and with either Ca^{2+} or Mg^{2+} bound to the protein. A major conformation rearrangement of the polypeptide chain around amino acid position 106 is revealed upon release of Ca^{2+}. These results are supported by a wobbling-in-a-cone model analysis and by molecular dynamics simulations, which overall suggest distinctly different switching mechanisms for GCAP1 and GCAP2 upon Ca^{2+} release.

■ RESULTS AND DISCUSSION

Biochemical Properties of Labeled GCAP1 Mutants. Native GCAP1 contains four cysteine residues at positions C18, C29, C125, and C106 (Figure 1a). In previous work we constructed and thoroughly analyzed the biochemical properties of isolated cysteine mutants of nonmyristoylated (nmyr) GCAP1 revealing that all mutants are functional.[22] In the present work, nmyr and myristoylated (myr) mutants with one C left were expressed in *E. coli*, purified, and biochemically analyzed. The remaining cysteine in mutants annotated CAAA (C18), ACAA (C29), AACA (C106), and AAAC (C125) allowed site-specific labeling with the fluorescent dye Alexa647 (see Table 1). Degree of myristoylation was high for all mutants as routinely observed for wildtype GCAP1 (88 to 95%). Labeling with Alexa647 was also successful for all mutants yielding (84 to 95%), except for nmyrC125 and myrC125, where 78% and 63% were obtained, respectively. Attachment of Alexa647 did not impair the Ca^{2+}-sensitive activating properties of GCAP1, since all labeled GCAP1 forms activated native rod outer segment guanylate cyclase 1 (ROS-GC1) with similar IC_{50} values, i.e. defining the free Ca^{2+} concentration of half-maximum guanylate cyclase activation (Figure 1b). In addition, we labeled nmyrGCAP1 variants and determined their Ca^{2+}-sensitive activation profiles. All curves were similar but shifted to slightly higher free Ca^{2+}-concentrations (Supporting Information Figure S1). This difference between the myristoylated and nonmyristoylated form is a characteristic feature of wildtype GCAP1[7,27] and demonstrates that mutants labeled with Alexa647 undergo the critical Ca^{2+}-dependent conformational changes in a nearly identical manner as the nonlabeled wildtype protein and, therefore, are well suited for subsequent fluorescence studies.

Table 1. Labelling of Myristoylated and Non-myristoylated GCAP Mutants with Alexa647-C2-maleimide[a]

	myr GCAP		nonmyr GCAP
	degree of myristoylation (%)	degree of labeling (%)	degree of labeling (%)
CAAA	91.4	90.2	84.5
ACAA	91.0	88.5	89.8
AACA	87.8	95.2	94.9
AAAC	95.1	78.5	63.5

[a] The degree of myistoylation for the D6S mutants was determined by rp-HPLC.

Fluorescence Lifetime. For each mutant, the fluorescence lifetime was measured for the Ca^{2+}-bound, the Mg^{2+}-bound, a mixed Ca^{2+}/Mg^{2+} bound, and the apo-state of the protein. A representative fluorescence decay curve is displayed in Figure 2a showing fluorescence decay of myrC106 in the presence of Ca^{2+} (green curve) or EGTA (red curve) and the instrument response function (blue curve). A biexponential fit results in equally distributed residuals, indicating a good agreement with the experimental data.

Such an acceptable biexponential modeling was observed for all mutants when assuming a fast component ranging from 0.6 to 1.2 ns and a slow component ranging from 1.3 to 2.0 ns. Typically, the amplitude of the slow component exceeded that of the fast component by a factor of 3. Therefore, a summary of deduced lifetimes for the dominating slow component τ_1 is given in Figure 2b, exhibiting similar features for both myristoylated and nonmyristoylated mutants. Specifically, fluorescence lifetimes differed significantly among cysteine positions. The longest fluorescent lifetimes were observed for the dye at positions C18 and C29 located in the interior of the protein. In contrast, the fluorescence lifetime was shortest for

DOI: 10.1021/acschembio.5b00278
ACS Chem. Biol. 2015, 10, 2344−2352

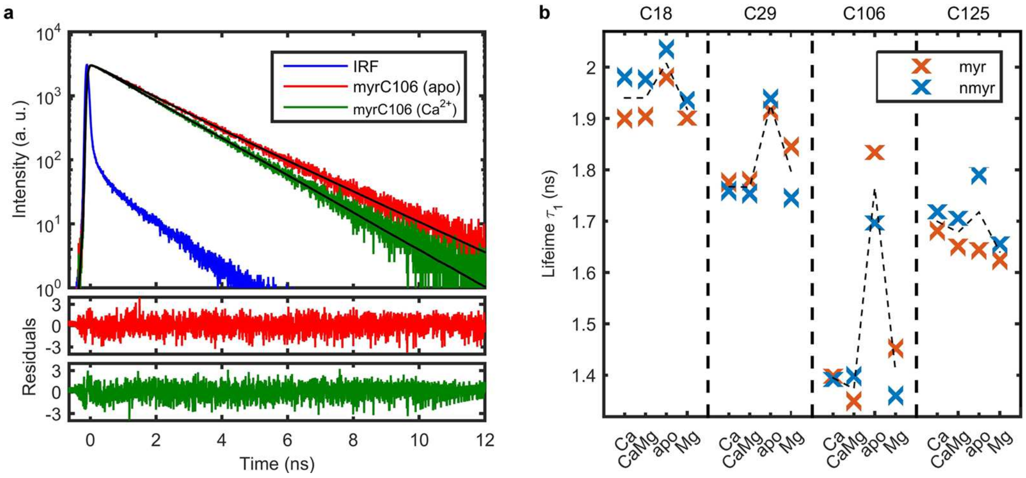

Figure 2. (a) Representative fluorescence decay curves of the mutant myrC106 in the apo (red) and Ca^{2+} bound (green) state and corresponding residuals for biexponentially fitted curves (black). The instrument response function (IRF) is shown in blue. (b) Summary of the high amplitude lifetime component for all mutants. Each section corresponds to one mutant, either myristoylated (red) or nonmyristoylated (blue), in all cation configurations. Each data point corresponds to the weighted average of 10 measurements with a weighted fitting error <5 ps. Error bars are smaller than the data point symbols.

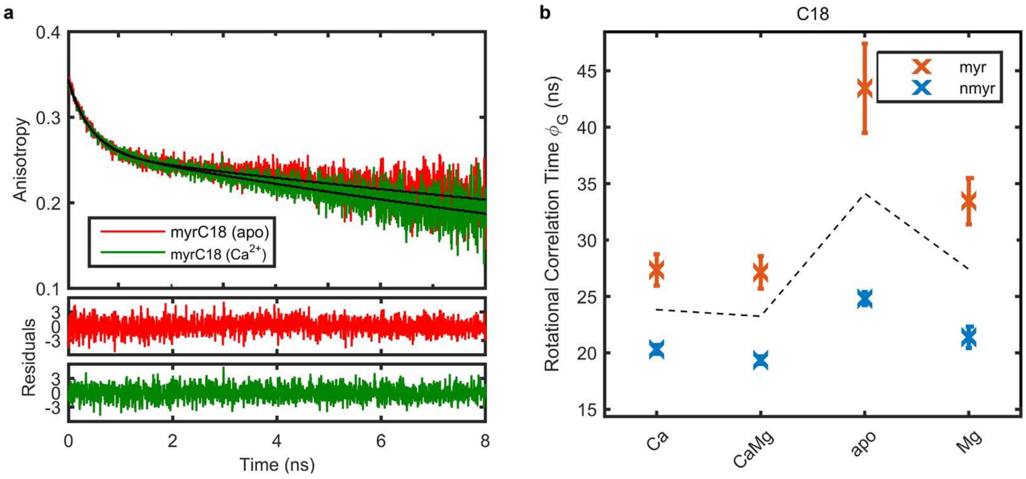

Figure 3. (a) Representative anisotropy decay curves of mutant myrC18 in the apo (red) and Ca^{2+} bound (green) state and corresponding residuals for biexponentially fitted curves (black). (b) Summary of the slow rotational correlation time component for the mutant C18, either myristoylated (red) or nonmyristoylated (blue), in all cation configurations. Each data point corresponds to the weighted average of 10 measurements with weighted fitting errors ranging from 0.33 to 4.0 ns, depending on excess of rotational correlation time over fluorescence lifetime.

the positions C106 and C125 corresponding to regions exposed to the solvent.

Most prominently, binding of either Ca^{2+}, Mg^{2+}, or a mixture thereof did hardly affect the fluorescence lifetimes. In stark contrast, in the apo-state, i.e. in the presence of the chelating agent EGTA, the fluorescence lifetime of the dye increased significantly at each of the dye positions. This increase in fluorescence lifetime is most pronounced for dye labeling at C106. Here, lifetime increases by more than 30% from 1.4 ns with either Ca^{2+} or Mg^{2+} bound to 1.8 ns in the apo-state of the myristoylated protein.

Fluorescence Anisotropy. Similarly, the fluorescence anisotropy was measured for each of the eight mutants in each of the four cation configurations. A representative anisotropy decay curve is shown in Figure 3a for myrC18 in the presence of Ca^{2+} (green curve) or for the apo-state (red curve). Again, a biexponential model gives a statistical distribution of residuals indicating a good agreement with the experimental data for the fluorescence anisotropy of the protein−dye complex. Therefore, we can identify two distinct two rotational correlation times, which can be distinguished into a fast component ranging from 0.43 to 0.82 ns for all mutants and a slow component ranging from 19 to 43 ns for the mutants C18 and C29 with the dye located in the interior of the protein−dye complex. For the mutants C106 and C125 with the dye facing the exterior of the protein, the rotational correlation times of the protein−dye complex greatly exceeded the fluorescence lifetime and only lower limits of several hundreds of nanoseconds could be estimated (results not shown).

For the mutant C18, the slow component is shown in Figure 3b for all cation configurations. In the myristoylated protein, we find similar rotational correlation times from 27 to 33 ns in the case of Ca^{2+} or Mg^{2+} binding and a slight increase to 43 ns in the apo-state. Under all conditions, the rotational correlation time of the nonmyristoylated protein is significantly faster than in the myristoylated case, and again the correlation time in the apo-state is slightly longer than in the case of Ca^{2+} or Mg^{2+} binding.

Change in Local Environment of the Dye. The fluorescence lifetime τ of a dye is related to the local viscosity η of its environment via $\tau \propto \eta^{\beta}$, where β is a positive number.[28] In the interior of the protein, the diffusive rotational motion of the dye is constrained, and the local viscosity of the environment therefore is large. This gives rise to a comparatively long fluorescence lifetime. In contrast, an exposure of the dye to the solvent buffer will reduce the local viscosity and hence fluorescence lifetime. The observed pronounced increase in fluorescence lifetime of the dye in the apo-state therefore necessarily reflects a tighter confinement of the dye in the interior of the protein than in the Ca^{2+}- or Mg^{2+}-bound state and thus indicates that the loop region around position C106 moves toward the interior of the protein, when GCAP1 releases its Ca^{2+}.

Motional Restriction by Wobbling-in-a-Cone. This local movement at position C106 is further supported by analyzing the diffusional dye motion in a phenomenological wobbling-in-a-cone model (see Figure 4).[19,29−31] This model separates a rapid diffusive rotational motion of the dye within its local environment from the much slower global rotational motion of the protein−dye complex and hence naturally accounts for the two distinct decay times in the experimentally measured anisotropy curves. The geometric constraint of the dye motion due to the surface of the protein is taken into account by restricting the dye rotation to the interior of a cone with semicone angle

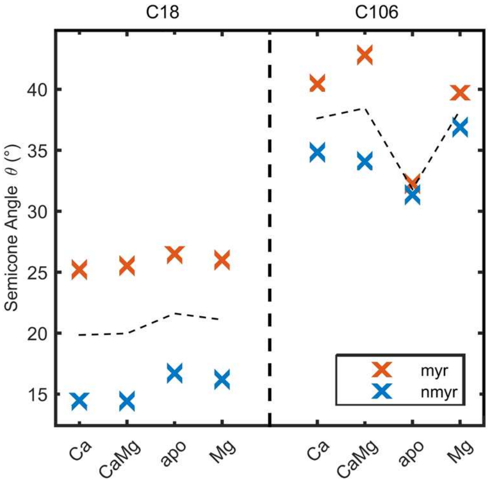

Figure 4. Semicone angle obtained from a wobbling-in-a-cone model for mutants C18 and C106, either myristoylated (red) or non-myristoylated (blue), in all cation configurations. Each data point corresponds to the weighted average of 10 evaluations with weighted errors ranging from 0.15° to 0.57°. Error bars are smaller than the data point symbols.

$$\theta = \cos^{-1}\left(\sqrt{2\left(\frac{r_D}{r_G}+1\right)^{-1/2}+\frac{1}{4}}-\frac{1}{2}\right)$$

Here, the amplitudes of the fast and slow components, r_D and r_G, are the amplitudes of the fast and slow components of the anisotropy decay.

An analysis of our experimental data within the framework of this model suggests that at dye position C106 this semicone angle decreases markedly from 41° in the Ca^{2+}-bound state to 32° in the apo-state of the myristoylated protein. Clearly, a dye closer to the interior of the protein should be more restricted in its motion than a dye more exposed to the solvent. Therefore, the analysis of both our fluorescence and anisotropy measurements strongly indicates a movement of the loop region around position C106 toward the interior of the protein, when GCAP1 releases its Ca^{2+}. Rebinding of Ca^{2+} or Mg^{2+} reverses this movement. This is consistent with the notion that the binding of cations to an EF hand loop, where C106 is located, results in a structural transition from an open conformation in the apo-state to a more closed conformation in the case of cation binding. When switching from open to closed conformation, a covalently bound dye molecule would therefore necessarily move outward with respect to the protein interior.

In contrast, the diffusional dye motion is similar in all cation configurations of the mutant C18 but differs strongly between the myristoylated and nonmyristoylated form. The distance between the cysteine sulfur in C18 and the end-standing carbon of the myristoyl group is ∼1.03 nm and is located at the end of the hydrophobic crevice harboring the fatty acyl chain. One would expect a larger semicone angle due to larger spatial freedom, if the myristoyl group is missing. However, we deduce a reduction in the semicone angle from 26° in the myristoylated protein to 15° in the nonmyristoylated protein, which is accompanied by an increase in lifetime by ∼0.1 ns (Figure 2b). This indicates a movement of the region around C18 into the hydrophobic pocket, thereby constraining its circular movement.

Global Rotation of the Protein−Dye Complex. Our anisotropy measurements further indicate that the local conformational change upon release of Ca^{2+} or Mg^{2+} at position C106 results in an increase in the slow, global rotational correlation time ϕ_G, which is directly related to the hydrodynamic radius r_{st} of the protein by the Stokes−Einstein−Debye equation

$$\phi_G = \frac{4\pi\eta r_{st}^3}{3k_B T}$$

Here, $k_B T$ is the Boltzmann factor and $\eta = 1$ mNs/m^2 is the viscosity of water at a temperature $T = 293.15$ K. In our measurements, we necessarily probe the rotational motion of the protein−dye complex. To extract information on the rotational correlation time of the unlabeled protein, the presence of the dye molecule must not enlarge the hydrodynamics radius of the protein. This requirement is met for a dye located in the interior of the protein, i.e. for a motionally restricted dye showing the longest fluorescence lifetimes. From our fluorescence lifetime measurements, the most suitable mutant to probe the rotational correlation time of GCAP1 is C18. The increase in rotational correlation time from 27 ns (Ca^{2+}-bound) to 43 ns (apo) therefore corresponds to an increase in hydrodynamic radius from $r_{st} = 2.98 \pm 0.05$ nm (Ca^{2+}-bound) to $r_{st} = 3.48 \pm 0.10$ nm (apo). This global enlargement of the mutated protein upon release of Ca^{2+} agrees with dynamic light scattering measurements on myristoylated, wild type GCAP1,[32] in which the hydrodynamic radius was determined as $r_{st} = 3.35 \pm 0.02$ nm for the Ca^{2+}-bound state and $r_{st} = 3.75 \pm 0.10$ nm for the apo-state.

Molecular Dynamics Simulations. To gain further structural insights into the local movement at position C106, as compared to the global enlargement of the protein observed

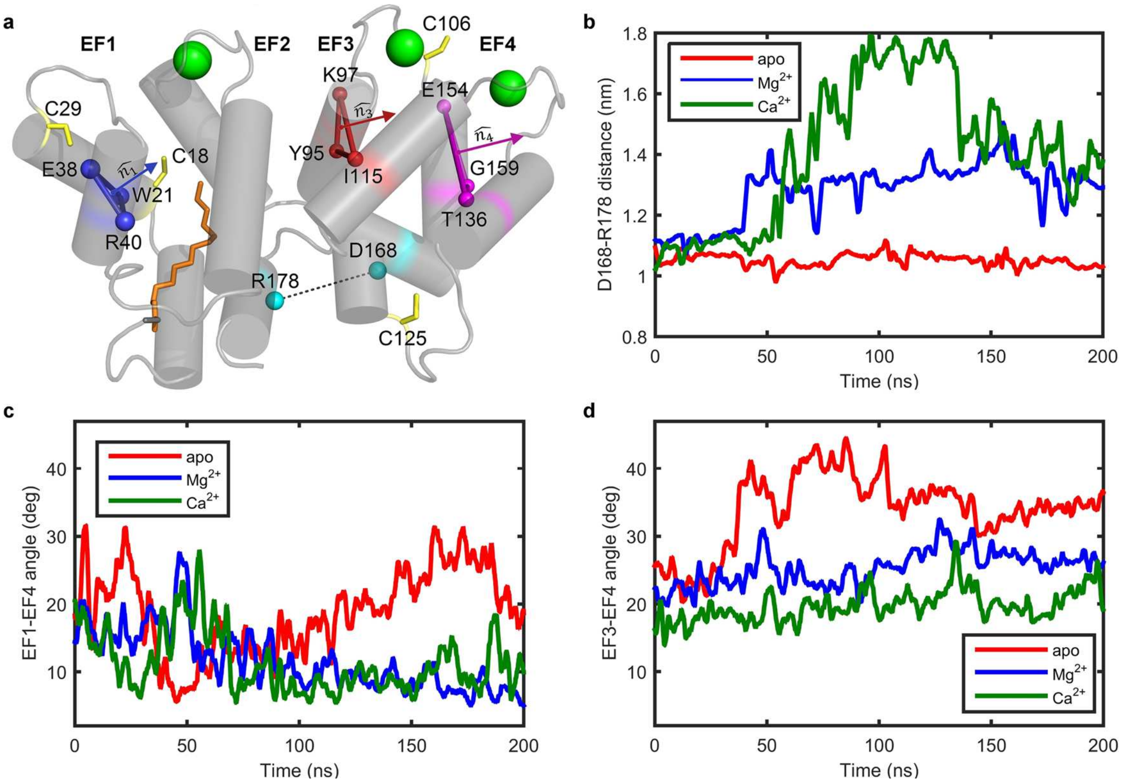

Figure 5. Structural descriptors of myrGCAP1 dynamical features calculated on the trajectories obtained by carrying out 200 ns all-atom molecular dynamics simulations. (a) Cartoon structural model of myrGCAP1 in the Ca^{2+}-bound form with the myristoyl moiety (orange), cysteine side chains (yellow), Ca^{2+} ions (green), as well as C_α atoms of key residues belonging to EF1 (blue), EF3 (red), EF4 (purple), and defining the distance between the *N*- and *C*-terminal domains (cyan). (b) Evolution of the distance between C_α of D168 and R178: apo (red), Mg^{2+}-EF2 (blue), Ca^{2+}-loaded (green). (c) Evolution of the angle between EF1 and EF4: apo (red), Mg^{2+}-EF2 (blue), Ca^{2+}-loaded (green). (d) Evolution of the angle between EF3 and EF4: apo (red), Mg^{2+}-EF2 (blue), Ca^{2+}-loaded (green).

upon Ca^{2+} and/or Mg^{2+} release, we analyzed the results from a previous 200 ns molecular dynamics (MD) study[33] of myristoylated GCAP1 in the light of the time-resolved fluorescence measurements presented here (Figure 5). Although the dye was not explicitly included in MD simulations, the biochemical assays performed in this study (Figure 1b) suggest that the dye exerts only minimal perturbations to the GCAP1 structure/function.

The analysis of MD trajectories focused on selected regions representative for those structural elements, in which the dye was experimentally bound as a probe for the structural dynamics. At the same time, it allowed us to assess global dynamical properties of the GCAP1 tertiary structure, which is characterized by two lobes, each consisting of two EF-hand regions (EF1−EF2 and EF3−EF4).[20]

The distance between these lobes is well represented by the distance between the $C\alpha$ atoms of D168 and R178, which are both located in the *C*-terminal region, but in the two different lobes. As D168 and R178 form a salt bridge, this distance remains nearly constant at 1.03 ± 0.02 nm in the apo-state (Figure 5b) but is dynamically disturbed upon Ca^{2+} (~32% salt bridge presence) or Mg^{2+} binding (~72% salt bridge presence) increasing the distance to 1.38 ± 0.07 nm and 1.31 ± 0.04 nm, respectively. In consequence, formation of the salt bridge in the apo-state enables the protein to open up near the Ca^{2+}-binding sites, which should be accompanied by an increased separation between the EF-hands.

To elucidate this feature the EF-hand motifs are conveniently represented by planes, which stand at an angle with respect to each other. For example, EF1 and EF4 are nearly parallel in the Ca^{2+} and Mg^{2+} bound state (6.8 ± 0.9°) but are significantly tilted (19.5 ± 1.8°) against each other in the apo-state. Similarly, the angle between EF3 and EF4 increases from 23.3 ± 1.7° in the Ca^{2+} bound state to 34.8 ± 0.8° in the apo-state (Figure 5c,d).

Therefore, molecular dynamics simulations point to two main reorganizing movements in the GCAP1 structure during the transition from the cation-bound to the apo-state: decreasing the distance between the two lobes by forming a salt bridge and a concomitant slight but significant expulsion of the EF4 region with respect to other regions (EF1 and EF3). These parallel movements lead to a slight increase in the radius of gyration of the protein in the apo-state (1.711 ± 0.009 nm) as compared to the Ca^{2+}-bound state (1.68 ± 0.01 nm) and to an overall more important increase in the hydrodynamic volume of GCAP1, which is in agreement with previous theoretical[33] and experimental[32] observations. Additionally, the increased angles between the EF-hand motifs upon release of Ca^{2+} open a cavity for the loop region around position C106 to move toward the interior of GCAP1. Pictorially, this dynamic process can be illustrated as a "twisted accordion"-like movement.

The large-scale motions described above are in fact in line with principal component analysis (PCA) performed on the whole 200 ns MD trajectory. Analysis of the first two principal components (PCs) describing the large-scale movements indeed shows that, in the apo-state, EF1, EF2, EF3, and *C*- and *N*-termini move in a concerted fashion along the direction

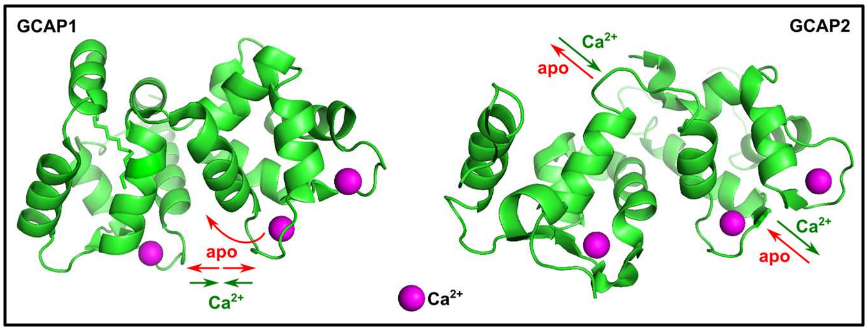

Figure 6. Comparison of the three-dimensional structures of GCAP1 and GCAP2 showing distinctly different switching mechanisms upon Ca^{2+} release. Structural model of GCAP2 is based on the NMR structure (PDB ID: 1JBA).[21]

of the first PC (Supporting Information Figure S2). Projection of the concerted trajectories over the second PC of the apo-state suggests that the loop connecting EF1 and EF2 as well as the highly flexible 121−133 region and the loops of EF-hands 2, 3, and 4 are collectively moving along the same direction, orthogonal to that defined by the first PC, which is substantially in line with the "twisted accordion" model described above. On the other hand, the first two PCs describing large scale motions of the Ca^{2+}-bound state of GCAP1 show a concerted motion of the *C*- and *N*-termini and of the highly flexible 121−133 loop, while the movement along the longitudinal axis of the "accordion" is much less pronounced.

Summary and Conclusions. In conclusion, our model of a twisted accordion-like movement for GCAP1 upon a changing Ca^{2+} concentration distinctly contrasts the piston-like movement deduced from a previous time-resolved fluorescence study on its structurally similar cognate GCAP2 (see Figure 6 for a comparison).[18] Recently, another pair of related NCS proteins, NCS-1 and calneuron-1, was found to differentially modulate by selective Ca^{2+} sensing a signaling pathway involving the heterodimeric adenosine/dopamine receptor.[34] Thus, our results constitute an example of a more general concept beyond retina specific Ca^{2+} sensors. Previously, the variability of target recognition and regulation by NCS proteins despite their structural similarities has been related in the past to differences in the number and location of Ca^{2+}-binding sites, in surface charge distribution, and in Ca^{2+}-sensitive dimerization.[2,8−11,32,35] Here, we present a new concept, in which differential cellular responsiveness mediated by two structurally similar proteins is directly mirrored by a difference in protein conformational dynamics, which tunes their physiological specificity.

■ METHODS

Cloning of GCAP1 Cysteine Mutants. The cloning of the single cysteine mutants of bovine GCAP1, in which three cysteine residues are replaced by alanine, namely C18AAA, AC29AA, AAC106A, and AAAC125, was described in detail before.[22] To facilitate myristoylation of GCAP1 variants at the *N*-terminus, an additional point mutation at position 6 (D6S) is necessary for creating a consensus sequence for the yeast *N*-myristoyltransferase (NMT). It was shown earlier that this point mutation has virtually no effect on the biochemical and biophysical properties of wildtype GCAP1.[36] Accordingly, we prepared the D6S mutants employing the following primers 5′-AAACAT-ATGGGGAACATTATGTCCGGTAAGTCG-3′ and 3′-TTTGAA-TTCTCAGCCGTCGGCCTCCGC-5′ and used the respective cysteine mutant as a template. The amplified PCR product was cut with *NdeI* and *NheI* and ligated in an analogous treated template clone. All sequences were verified by DNA sequencing (LGC Genomics).

Expression and Purification of GCAP1, Wild-Type, and Cysteine Mutants. GCAP1 mutants were overexpressed in BL21 *E. coli* cells as described before.[8,15,22] In order to myristoylate GCAP1, mutants cells were cotransformed with the plasmid pBB131 containing a gene for the yeast (*S. cerevisiae*) NMT. After cell lysis, the myristoylated and nonmyristoylated GCAP1 mutants were isolated from the insoluble fraction.[8,15,22] Briefly, the insoluble material was homogenized in 6 M guanidinium hydrochloride and afterward dialyzed against Tris-buffer (20 mM Tris-HCl, 150 mM NaCl, 1 mM DTT pH 7.5). Prior to chromatographic steps, the volume of the protein solution was reduced by ammonium sulfate precipitation. Subsequently, the protein was resolved and applied onto a size exclusion column (Superdex 75, GE Healthcare) equilibrated in Tris-buffer. Fractions containing the respective GCAP form were further purified with an anion exchange column (HiLoad 26/10 Q Sepharose; GE Healthcare) equilibrated in Tris-buffer with 2 mM EGTA. Chromatography was performed with a gradient of 200−550 mM NaCl in 40 mL.

The purity of the obtained GCAP forms was verified by sodium dodecyl-sulfate polyacrylamide gel electrophoresis. The myristoylation degree of the D6S mutants was determined by a reversed phase HPLC on a silica based C-18 column (Luna 5 μm C18, Phenomenex).[37]

Labeling with the Fluorescent Dye Alexa647 and Validation of Protein Function. GCAP1 mutants with one reactive cysteine were labeled with the fluorescent dye Alexa647-C2-maleimide (Life Technologies) using the following protocol: the respective lyophilized GCAP1 form was dissolved in 10 mM Hepes-KOH pH 7.0 to a final concentration of 30 μM. The Alexa647 dye was added in 5-fold molar excess in a final volume of 0.5 mL. The reaction mixture was incubated for 1−3 h in a light-protected vial at room temperature, before the reaction was terminated by adding 2 mM DTT.

Removal of the excessive dye was done by passing the reaction mixture over a NAP5 column (GE Healthcare) equilibrated in fluorescence buffer (125 mM NaCl, 25 mM Tris-HCl pH 7.4). If excessive dye was still present, it was removed by dialysis against the same buffer.

For the calculation of the labeling efficiency, the concentration of the bound dye was determined by UV−VIS spectrophotometry at 650 nm (ε = 265 000 M^{-1} cm^{-1}) and the protein concentration by the Coomassie Blue assay.

A critical point for further use of fluorescence labeled mutants was the ability to regulate the target guanylate cyclase ROS-GC1. For this purpose, we isolated membranes from bovine rod outer segments,[7,8] providing us with a native ROS-GC1 source. The cyclase activity was determined as a function of free [Ca^{2+}] exactly as described before.

Fluorescence Lifetime Measurement. Fluorescence lifetime measurements were performed by time-correlated single photon counting (TCSPC). A pulsed diode laser (PicoQuant, LDH 8−1−060 with PDL 800) operating at a repetition rate of 6 MHz provided 50 ps pulses centered at 656 nm and at an average power < 5 μW. Vertically polarized laser pulses were weakly focused into a microcuvette. Emitted fluorescence light was collected and focused by a glass objective (Nikon, NA = 0.7) onto an avalanche photodiode (ID Quantique 100).

To avoid anisotropy effects, all lifetime measurements were performed under magic angle conditions (54.7°). Fluorescence decay curves $I(t)$ were collected with a timing resolution of 4 ps (PicoQuant, PicoHarp 300) and fitted with the software FluoFit (PicoQuant) to an exponential decay model by reconvolution:

$$I(t) = \int_{-\infty}^{t} \mathrm{IRF}(t') \sum_{i=1}^{n} A_i \, e^{-(t-t')/\tau_i} \, dt'$$

Here, A_i denotes the amplitude of the decay component with fluorescence lifetime τ_i.

The instrument response function (IRF) was recorded with excitation light scattered from diluted milk and found to have a full width at half-maximum (fwhm) of about 100 ps.

Our setup yielded a monoexponential decay for free oxazine 1. However, a biexponential decay was observed for free Alexa647, which we attribute to a low but nonzero probability for the dye to take an alternative configuration due to its chemical structure. Reference measurements of free Alexa647 in the presence of Ca^{2+}, Mg^{2+}, or the chelating agent EGTA used for the apo-state measurements yielded no change in fluorescence lifetime.

For each of the four mutants, either myristoylated or nonmyristoylated, and in each of the four cation configurations, we carried out 10 measurements and calculated the weighted mean $\bar{x} = (\Sigma w_i x_i)/(\Sigma w_i)$ with $w_i = 1/(\Delta x_i)^2$ and the overall error as $\Delta x = [1/(\Sigma w_i)]^{1/2}$.

Fluorescence Anisotropy Measurement. For fluorescence anisotropy measurements, the intensity of fluorescence emission with a polarization component parallel, $I_{\parallel}(t)$, and perpendicular, $I_{\perp}(t)$, to the vertically polarized excitation light was measured. The fluorescence anisotropy $r(t)$ is then defined as

$$r(t) = \frac{I_{\parallel}(t) - G \cdot I_{\perp}(t)}{I_{\parallel}(t) + 2G \cdot I_{\perp}(t)}$$

Here, an instrument parameter G corrects for biased polarization detection efficiency and was found to be $G = (\int I_{HV}(t)\, dt / \int I_{HH}(t)\, dt) = 0.95$ for our setup.

Anisotropy decay curves were fitted with the software FluoFit (PicoQuant) to an exponential decay model

$$r_{\mathrm{fit}}(t) = r_{\infty} + \sum_{i=1}^{n} r_i \, e^{-t/\phi_i}$$

Here, r_i denotes the amplitude of the decay component with rotational correlation time ϕ_i and r_{∞} is the steady state anisotropy.

Similar to the lifetime measurements, we carried out 10 measurements for both $I_{\parallel}(t)$ and $I_{\perp}(t)$, for all mutants and in all configurations, and calculated the weighted mean accordingly.

Molecular Dynamics Simulations. Molecular dynamics simulations were set up as previously described[33] using as a starting structure the homology model of human mGCAP1 built using Ca^{2+}-bound chicken mGCAP1[20] as a template (PDB ID: 2R2I), according to a procedure previously elucidated.[12] Simulated states were modeled either by removing Ca^{2+} ions from all three EF-hand binding sites (apo) or by removing Ca^{2+} ions from EF3 and EF4 and substitution with a Mg^{2+} ion in EF2 (Mg^{2+}-EF2).

MD simulations were performed using the GROMACS 4.6.3 simulation package,[38] with the CHARMM27 all-atom force field.[39,40] Structures were subjected to energy minimization, 4 ns equilibration, and 200 ns MD production with an integration time step of 2 fs. See ref 33 for details. Values reported for distances and angles are mean values ± standard deviations calculated over the last 10 ns of MD production.

Analysis of MD Trajectories. MD trajectories generated in Marino et al.[33] were subjected to different analyses. The distance between the centers of mass of C_α of D168 (belonging to the EF3–EF4 lobe) and R178 (belonging to the EF1–EF2 lobe) was calculated over the 200 ns MD time frame with the *g_dist* function implemented in the GROMACS simulation package. The angles between the versors orthogonal to the planes cutting EF1 (represented by C_α Ca^{2+}'s of W21, E38 and R40), EF3 (represented by C_α's of Y95, K97 and I115), and EF4 (represented by C_α's of T136, E154 and G159) were calculated over the 200 ns MD time frame with the *g_sgangle* function implemented in the GROMACS simulation package, which is based on the equation $\cos \widehat{EF1EF4} = \hat{n}_1 \cdot \hat{n}_4$ and $\cos \widehat{EF3EF4} = \hat{n}_3 \cdot \hat{n}_4$.

Smoothing of distance and angle data plots was performed with the smoothing function within the SigmaPlot 12 package, by using the running average module with 10 000 intervals averaging 200 points each, corresponding to one-hundredth of the points in the original data set (2 ns frequency).

Principal component analysis was performed using the pca module of the Wordom software[41] by computing progressive comparisons every 10 ns. Radius of gyration measurement calculated on all protein atoms was performed using the rgyr module of the Wordom software.

■ ASSOCIATED CONTENT

Ⓢ Supporting Information

The Supporting Information is available free of charge on the ACS Publications website at DOI: 10.1021/acschembio.5b00278.

> Two additional figures are supplied. Figure S1: Ca^{2+}-sensitive activation of ROS-GC1 by nonmyristoylated GCAP1 mutants. Figure S2: Analysis of the first two principal components describing 200 ns all-atom molecular dynamics simulations of apo and Ca^{2+}-bound myristoylated GCAP1 (PDF)

■ AUTHOR INFORMATION

Corresponding Author

*E-mail: karl.w.koch@uni-oldenburg.de.

Author Contributions

J.R., C.L., and K.W.K. developed the concept. J.R., J.B., and S.S. designed experiments. V.M and DDO performed molecular dynamics simulations. J.R., J.B., and S.S. carried out experiments. All authors analyzed data. J.R. and K.W.K. wrote the first draft of the manuscript. All authors corrected and completed the manuscript.

Notes

The authors declare no competing financial interest.

■ ACKNOWLEDGMENTS

This work was supported by a grant from the Deutsche Forschungsgemeinschaft (GRK 1885/1) and by funds from the Italian Ministry for Research and Education via Departmental funds (FUR2013) and via support from CINECA through the Italian Super Computing Resource Allocation project (ISCRA Grant: HP10CB736X to DDO). Part of this work resulted from a Fellowship at the Hanse-Wissenschaftskolleg Delmenhorst (Germany) to DDO.

■ REFERENCES

(1) Berridge, M. J., Lipp, P., and Bootman, M. D. (2000) The versatility and universality of calcium signalling. *Nat. Rev. Mol. Cell Biol. 1*, 11–21.

(2) Ikura, M., and Ames, J. B. (2006) Genetic polymorphism an dprotein conformational plasticity in the calmodulin superfamily: Two ways to promote multifunctionality. *Proc. Natl. Acad. Sci. U. S. A. 103*, 1159–1164.

(3) Burgoyne, R. D., Haynes, L. P. (2014) Sense and specificity in neuronal calcium signalling. *Biochim. Biophys. Acta, Mol. Cell Res.* DOI: 10.1016/j.bbamcr.2014.10.029.

(4) Pugh, E. N., Jr., and Lamb, T. D. (2000) Phototransduction in Vertebrate Rods and Cones: Molecular Mechanisms of Amplification, Recovery and Light Adaptation. *Handb. Biol. Phys. 3*, 183−255.

(5) Palczewski, K., Subbaraya, I., Gorczyca, W. A., Helekar, B. S., Ruiz, C. C., Ohguro, H., Huang, J., Zhao, X., Crabb, J. W., Johnson, R. S., Walsh, K. A., Gray-Keller, M. P., Detwiler, P. B., and Baehr, W. (1994) Molecular cloning and characterization of retinal photoreceptor guanylyl cyclase-activating protein. *Neuron 13*, 395−404.

(6) Dizhoor, A. M., Olshevskaya, E. V., Henzel, W. J., Wong, S. C., Stults, J. I., Ankoudinova, I., and Hurley, J. B. (1995) Cloning,sequencing, and expression of a 24-kDa Ca2+-binding protein activating photoreceptor guanylyl cyclase. *J. Biol. Chem. 270*, 25200−25206.

(7) Bönigk, W., Müller, F., Kellner, R., Koch, K.-W., and Frins, S. (1996) Functional characterization of a guanylyl cyclase-activating protein from vertebrate rods. *J. Biol. Chem. 271*, 8022−8027.

(8) Hwang, J. Y., Lange, C., Helten, A., Höppner-Heitmann, D., Duda, T., Sharma, R. K., and Koch, K.-W. (2003) Regulatory modes of rod outer segment membrane guanylate cyclase differ in catalytic efficiency and Ca^{2+}-sensitivity. *Eur. J. Biochem. 270*, 3814−3821.

(9) Makino, C. L., Wen, X.-H., Olshevskaya, E. V., peshenko, I. V., Savchenko, A. B., and Dizhoor, A. M. (2012) Enzymatic relay mechanism stimulates cyclic GMP synthesis in rod photoresponse: biochemical and physiological study in guanyly cyclase activating protein 1 knockout mice. *PLoS One 7*, e47637.

(10) Koch, K.-W., and Dell'Orco, D. A. (2013) Calcium relay mechanism in vertebrate phototransduction. *ACS Chem. Neurosci. 4*, 909−917.

(11) Lim, S., Peshenko, I., Dizhoor, A., and Ames, J. B. (2009) Effects of Ca^{2+}, Mg^{2+}, and myristoylation on guanylyl cyclase activating protein 1 structure and stability. *Biochemistry 48*, 850−862.

(12) Dell'Orco, D., Behnen, P., Linse, S., and Koch, K.-W. (2010) Calcium binding, structural stability and guanylate cyclase activation in GCAP1 variants associated with human cone dystrophy. *Cell. Mol. Life Sci. 67*, 973−984.

(13) Otto-Bruc, A., Buczylko, J., Surgucheva, I., Subbaraya, I., Rudnicka-Nawrot, M., Crabb, J. W., Arendt, A., Hargrave, P. A., Baehr, W., and Palczewski, K. (1997) Functional reconstitution of photoreceptor guanylate cyclase with native and mutant forms of guanylate cyclase-activating protein 1. *Biochemistry 36*, 4295−4302.

(14) Sokal, I., Li, N., Klug, C. S., Filipek, S., Hubbell, W. L., Baehr, W., and Palczewski, K. (2001) Calcium-sensitive regions of GCAP1 as observed by chemical modifications, fluorescence, and EPR spectroscopies. *J. Biol. Chem. 276*, 43361−43373.

(15) Hwang, J.-Y., Schlesinger, R., and Koch, K.-W. (2004) Irregular dimerization of guanylate cyclase-activating protein 1 mutants causes loss of target activation. *Eur. J. Biochem. 271*, 3785−3793.

(16) Peshenko, I. V., Olshevskaya, E. V., and Dizhoor, A. M. (2008) Binding of guanylyl cyclase activating protein 1 (GCAP1) to retinal guanylyl cyclase (RetGC1). The role of individual EF-hands. *J. Biol. Chem. 283*, 21747−21757.

(17) Makino, C. L., Peshenko, I. V., Wen, X. H., Olshevskaya, E. V., Barrett, R., and Dizhoor, A. M. (2008) A role for GCAP2 in regulating the photoresponse. Guanylyl cyclase activation and rod electrophysiology in GUCA1B knock-out mice. *J. Biol. Chem. 283*, 29135−29143.

(18) Dell'Orco, D., Sulmann, S., Zägel, P., Marino, V., and Koch, K.-W. (2014) Impact of cone dystrophy-related mutations in GCAP1 on a kinetic model of phototransduction. *Cell. Mol. Life Sci. 71*, 3829−3840.

(19) Kollmann, H., Becker, S. F., Shirdel, J., Scholten, A., Ostendorp, A., Lienau, C., and Koch, K.-W. (2012) Probing the Ca^{2+} switch of the neuronal Ca^{2+} sensor GCAP2 by time-resolved fluorescence spectroscopy. *ACS Chem. Biol. 7*, 1006−1014.

(20) Stephen, R., Bereta, G., Golczak, M., Palczewski, K., and Sousa, M. C. (2007) Stabilizing function for myristoyl group revealed by the crystal structure of a neuronal calcium sensor, guanylate cyclase-activating protein 1. *Structure 15*, 1392−1402.

(21) Ames, J. B., Dizhoor, A. M., Ikura, M., Palczewski, K., and Stryer, L. (1999) Three-dimensional structure of guanylyl cyclase activating protein-2, a calcium-sensitive modulator of photoreceptor guanylyl cyclase. *J. Biol. Chem. 274*, 19329−19337.

(22) Hwang, J.-Y., Schlesinger, R., and Koch, K.-W. (2001) Calcium-dependent cystein reactivities in the neuronal calcium sensor guanylate cyclase-activating protein 1. *FEBS Lett. 508*, 355−359.

(23) Sokal, I., Otto-Bruc, A. E., Surgucheva, I., Verlinde, C. L. M. J., Wang, C.-K., Baehr, W., and Palczewski, K. (1999) Conformational changes in guanylyl cyclase-activating protein 1 (GCAP1) and its tryptophan mutants as a function of calcium concentration. *J. Biol. Chem. 274*, 19829−19837.

(24) Peshenko, I. V., and Dizhoor, A. M. (2006) Ca^{2+} and Mg^{2+} binding properties of GCAP-1. Evidence that Mg^{2+}-bound form is the physiological activator of photoreceptor guanylyl cyclase. *J. Biol. Chem. 281*, 23830−23841.

(25) Orban, T., Bereta, G., Miyagi, M., Wang, B., Chance, M. R., Sousa, M. C., and Palczewski, K. (2010) Conformation changes in guanylate cyclase-activating protein 1 induced by Ca^{2+} and N-terminal fatty acid acylation. *Structure 18*, 116−126.

(26) Lim, S., Peshenko, I. V., Dizhoor, A. M., and Ames, J. B. (2013) Structural insights for activation of retinal guanylate cyclase by GCAP1. *PLoS One 8* (11), e81822.

(27) Peshenko, I. V., Olshevskaya, E. V., Lim, S., Ames, J. B., and Dizhoor, A. M. (2012) Calcium-myristoyl tug is a new mechanisms for intramolecular tuning of calcium sensitivity and tarbet enzyme interaction for guanylyl cyclase-activating protein 1. *J. Biol. Chem. 287*, 13972−13984.

(28) Sundström, V., and Gillbro, T. (1981) Viscosity dependent radiationless relaxation rate of cyanine dyes. A picosecond laser spectroscopy study. *Chem. Phys. 61*, 257−269.

(29) Hovius, R., Vallotton, P., Wohland, T., and Vogel, H. (2000) Fluorescence techniques: shedding light on ligand-receptor interactions. *Trends Pharmacol. Sci. 21*, 266−273.

(30) Kinosita, K., Kawato, S., and Ikegami, A. (1977) A theory of fluorescence polarization decay in membranes. *Biophys. J. 20*, 289−305.

(31) Schröder, G. F., Alexiev, U., and Grubmüller, H. (2005) Simulation of Fluorescence Anisotropy Experiments: Probing Protein Dynamics. *Biophys. J. 89*, 3757−3770.

(32) Sulmann, S., Dell'Orco, D., Marino, V., Behnen, P., and Koch, K.-W. (2014) Conformational changes in calcium-sensor proteins under molecular crowding conditions. *Chem. - Eur. J. 20*, 6756−6762.

(33) Marino, V., Sulmann, S., Koch, K.-W., and Dell'Orco, D. (2014) Structural effects of Mg^{2+} on the regulatory states of three neuronal calcium sensors operating in vertebrate phototransduction. *Biochim. Biophys. Acta, Mol. Cell Res. 1853*, 2055−2065.

(34) Navarro, G., Aguinaga, D., Moreno, E., Hradsky, J., Reddy, P. P., Cortés, A., Mallol, J., Casadó, V., Mikhaylova, M., Kreutz, M. R., Lluís, C., Canela, E. I., McCormick, P. J., and Ferré, S. (2014) Intracellular calcium levels determine differential modulation of allosteric interactions within G protein-coupled receptor heteromers. *Chem. Biol. 21*, 1546−1556.

(35) Ames, J. B., and Lim, S. (2012) Molecular structure and target recognition of neuronal calcium sensor proteins. *Biochim. Biophys. Acta, Gen. Subj. 1820*, 1205−1213.

(36) Krylov, D. M., Niemi, G. A., Dizhoor, A. M., and Hurley, J. B. (1999) Mapping sites in guanylyl cyclase activating protein-1 required for regulation of photoreceptor membrane guanylyl cyclases. *J. Biol. Chem. 274*, 10833−10839.

(37) Hwang, J.-Y., and Koch, K.-W. (2002) The myristoylation of the neuronal Ca^{2+}-sensors guanylate cyclase-activating protein 1 and 2. *Biochim. Biophys. Acta, Proteins Proteomics 1600*, 111−117.

(38) Hess, B., Kutzner, C., Van Der Spoel, D., and Lindahl, E. (2008) GROMACS 4: Algorithms for Highly Efficient, Load-Balanced, and Scalable Molecular Simulation. *J. Chem. Theory Comput. 4*, 435−447.

(39) Bjelkmar, P., Larsson, P., Cuendet, M. A., Hess, B., and Lindahl, E. (2010) Implementation of the CHARMM force field in GROMACS: Analysis of protein stability effects from correction maps, virtual interaction sites, and water models. *J. Chem. Theory Comput. 6*, 459−466.

(40) Mackerell, A. D., Jr., Feig, M., and Brooks, C. L., 3rd. (2004) Extending the treatment of backbone energetics in protein force fields: limitations of gas-phase quantum mechanics in reproducing protein conformational distributions in molecular dynamics simulations. *J. Comput. Chem. 25*, 1400−1415.

(41) Seeber, M., Felline, A., Raimondi, F., Muff, S., Friedman, R., Rao, F., Caflisch, A., and Fanelli, F. (2011) Wordom: a user-friendly program for the analysis of molecular structures, trajectories, and free energy surfaces. *J. Comput. Chem. 32*, 1183−94.

SUPPORTING INFORMATION

Differential nanosecond protein dynamics in homologous calcium sensors

Jörg Robin,[#,§] Jens Brauer,[#,§] Stefan Sulmann,[‡] Valerio Marino, Daniele Dell’Orco, [,†]
Christoph Lienau,[#,§] and Karl-Wilhelm Koch,[§,‡,*]

[#]Ultrafast Nano-Optics, Institute of Physics, Faculty V, University of Oldenburg, D-26111 Oldenburg, Germany

[§]Center of Interface Science, University of Oldenburg, D-26111 Oldenburg, Germany

[‡]Biochemistry, Department of Neurosciences, Faculty VI, University of Oldenburg, D-26111 Oldenburg, Germany

Department of Life Sciences and Reproduction, Section of Biological Chemistry, University of Verona, Verona, Italy

[†]Center for BioMedical Computing (CBMC), University of Verona, Verona, Italy

Corresponding Author

*E-mail: karl.w.koch@uni-oldenburg.de

Content

Figure S1: Ca^{2+}-sensitive activation of ROS-GC1 by nonmyristoylated GCAP1 mutants

Figure S2: Analysis of the first two principal components describing 200 ns all-atom molecular dynamics simulations of apo and Ca^{2+}-bound myristoylated GCAP1.

Figure S1

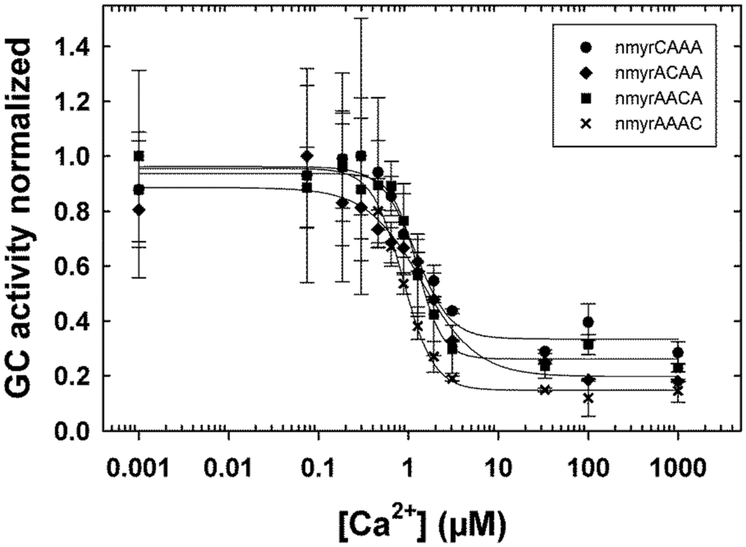

Figure S1

Ca^{2+}-sensitive activation of ROS-GC1 by nonmyristoylated GCAP1 mutants as indicated. The IC_{50} values are the following (three to four data sets): 1148 nM (Alexa647-labeled CAAA), 1547 nM (Alexa647-labeled ACAA), 1274 nM (Alexa647-labeled AACA), and 917 nM (Alexa647-labeled AAAC).

Figure S2

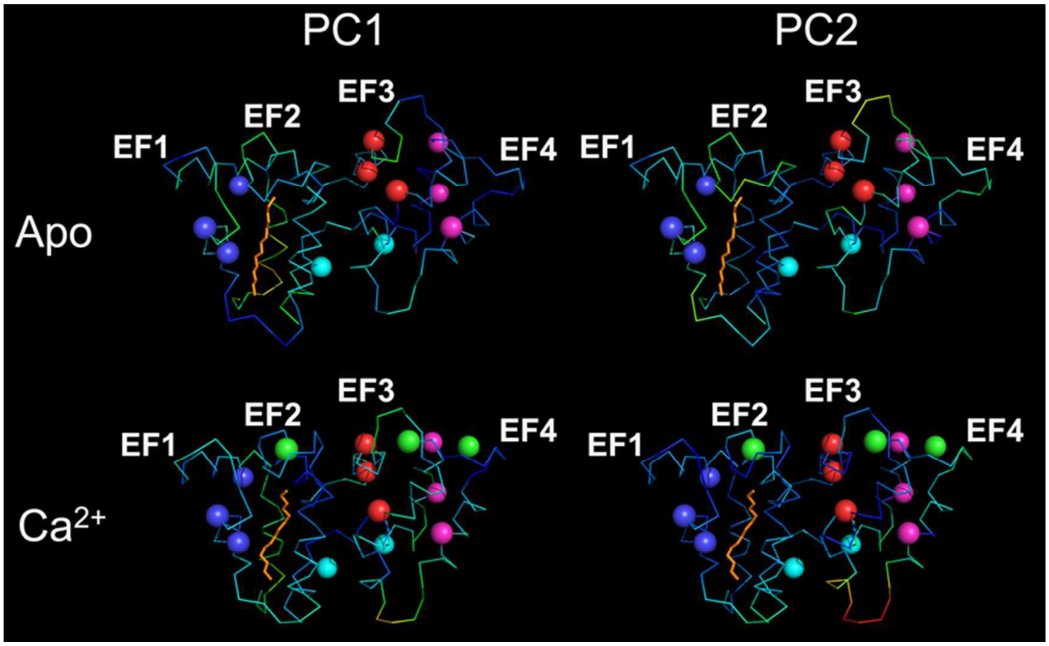

Figure S2

Analysis of the first two principal components describing 200 ns all-atom molecular dynamics simulations of apo and Ca^{2+}-bound myristoylated GCAP1. The ribbon structural model of myrGCAP1 (showing only the C_α atoms pattern) is colored according to the eigenvalues corresponding to the respective principal component in a blue-to-red (0 to 29.89) scale. The myristoyl moiety is represented in orange sticks, Ca^{2+} ions are represented as green spheres, C_α atoms of the residues implied in structural descriptors calculation are represented as spheres colored as in Figure 5, namely EF1 in blue, EF3 in red, EF4 in purple and residues D168 and R178 in cyan.

High passive CEP stability from a few-cycle, tunable NOPA-DFG system for observation of CEP-effects in photoemission

Jan Vogelsang[1,2,5], Jörg Robin[1,2,5], Björn Piglosiewicz[1,2],
Cristian Manzoni[3], Paolo Farinello[3], Stefan Melzer[4], Philippe Feru[4],
Giulio Cerullo[3], Christoph Lienau[1,2], and Petra Groß[1,2]

[1] Institut für Physik, Carl von Ossietzky Universität,
26129 Oldenburg, Germany
[2] Center of Interface Science, Carl von Ossietzky Universität,
26129 Oldenburg, Germany
[3] IFN-CNR, Dipartimento di Fisica, Politecnico di Milano,
20133 Milano, Italy
[4] Spectra-Physics,
Santa Clara, CA 95054, USA
[5] Both authors contributed equally

Optics Express **22**, 25295 (2014)

DOI: 10.1364/OE.22.025295

Copyright © 2014 Optical Society of America

Reprinted with kind permission from the Optical Society of America (OSA).

High passive CEP stability from a few-cycle, tunable NOPA-DFG system for observation of CEP-effects in photoemission

Jan Vogelsang,[1,2,5] Jörg Robin,[1,2,5] Björn Piglosiewicz,[1,2] Cristian Manzoni,[3] Paolo Farinello,[3] Stefan Melzer,[4] Philippe Feru,[4] Giulio Cerullo,[3] Christoph Lienau,[1,2] and Petra Groß[1,2,*]

[1] *Institut für Physik, Carl von Ossietzky Universität, 26129 Oldenburg, Germany*
[2] *Center of Interface Science, Carl von Ossietzky Universität, 26129 Oldenburg, Germany*
[3] *IFN-CNR, Dipartimento di Fisica, Politecnico di Milano, 20133 Milano, Italy*
[4] *Spectra-Physics, Santa Clara, CA 95054, USA*
[5] *Both authors contributed equally*
**petra.gross@uni-oldenburg.de*

Abstract: The investigation of fundamental mechanisms taking place on a femtosecond time scale is enabled by ultrafast pulsed laser sources. Here, the control of pulse duration, center wavelength, and especially the carrier-envelope phase has been shown to be of essential importance for coherent control of high harmonic generation and attosecond physics and, more recently, also for electron photoemission from metallic nanostructures. In this paper we demonstrate the realization of a source of 2-cycle laser pulses tunable between 1.2 and 2.1 μm, and with intrinsic CEP stability. The latter is guaranteed by difference frequency generation between the output pulse trains of two noncollinear optical parametric amplifier stages that share the same CEP variations. The CEP stability is better than 50 mrad over 20 minutes, when averaging over 100 pulses. We demonstrate the good CEP stability by measuring kinetic energy spectra of photoemitted electrons from a single metal nanostructure and by observing a clear variation of the electron yield with the CEP.

©2014 Optical Society of America

OCIS codes: (320.7120) Ultrafast phenomena; (190.4410) Nonlinear optics, parametric processes; (320.7110) Ultrafast nonlinear optics; (270.6620) Strong-field processes.

References and links

1. E. Goulielmakis, Z.-H. Loh, A. Wirth, R. Santra, N. Rohringer, V. S. Yakovlev, S. Zherebtsov, T. Pfeifer, A. M. Azzeer, M. F. Kling, S. R. Leone, and F. Krausz, "Real-time observation of valence electron motion," Nature **466**(7307), 739–743 (2010).
2. A. Mokhtari, P. Cong, J. L. Herek, and A. H. Zewail, "Direct femtosecond mapping of trajectories in a chemical reaction," Nature **348**(6298), 225–227 (1990).
3. R. R. Alfano and S. L. Shapiro, "Emisson in region 400 to 7000 A via 4-photon oupling in glass," Phys. Rev. Lett. **24**(11), 584–587 (1970).
4. M. Bradler, P. Baum, and E. Riedle, "Femtosecond continuum generation in bulk laser host materials with sub-μJ pump pulses," Appl. Phys. B **97**(3), 561–574 (2009).
5. J. C. Knight, "Photonic crystal fibres," Nature **424**(6950), 847–851 (2003).
6. P. Russell, "Photonic crystal fibers," Science **299**(5605), 358–362 (2003).
7. D. Brida, C. Manzoni, G. Cirmi, M. Marangoni, S. Bonora, P. Villoresi, S. De Silvestri, and G. Cerullo, "Few-optical-cycle pulses tunable from the visible to the mid-infrared by optical parametric amplifiers," J. Opt. **12**(1), 013001 (2010).
8. F. Krausz and M. Ivanov, "Attosecond physics," Rev. Mod. Phys. **81**(1), 163–234 (2009).
9. C. A. Haworth, L. E. Chipperfield, J. S. Robinson, P. L. Knight, J. P. Marangos, and J. W. G. Tisch, "Half-cycle cutoffs in harmonic spectra and robust carrier-envelope phase retrieval," Nat. Phys. **3**(1), 52–57 (2007).
10. J. Itatani, J. Levesque, D. Zeidler, H. Niikura, H. Pépin, J. C. Kieffer, P. B. Corkum, and D. M. Villeneuve, "Tomographic imaging of molecular orbitals," Nature **432**(7019), 867–871 (2004).

#220700 - $15.00 USD Received 8 Aug 2014; revised 26 Sep 2014; accepted 26 Sep 2014; published 9 Oct 2014

11. M. Nisoli, G. Sansone, S. Stagira, S. De Silvestri, C. Vozzi, M. Pascolini, L. Poletto, P. Villoresi, and G. Tondello, "Effects of carrier-envelope phase differences of few-optical-cycle light pulses in single-shot high-order-harmonic spectra," Phys. Rev. Lett. **91**(21), 213905 (2003).
12. M. Krüger, M. Schenk, and P. Hommelhoff, "Attosecond control of electrons emitted from a nanoscale metal tip," Nature **475**(7354), 78–81 (2011).
13. B. Piglosiewicz, S. Schmidt, D. J. Park, J. Vogelsang, P. Gross, C. Manzoni, P. Farinello, G. Cerullo, and C. Lienau, "Carrier-envelope phase effects on the strong-field photoemission of electrons from metallic nanostructures," Nat. Photonics **8**, 38–43 (2014).
14. P. Hommelhoff, C. Kealhofer, and M. A. Kasevich, "Ultrafast Electron Pulses from a Tungsten Tip Triggered by Low-Power Femtosecond Laser Pulses," Phys. Rev. Lett. **97**(24), 247402 (2006).
15. D. J. Park, B. Piglosiewicz, S. Schmidt, H. Kollmann, M. Mascheck, and C. Lienau, "Strong field acceleration and steering of ultrafast electron pulses from a sharp metallic nanotip," Phys. Rev. Lett. **109**(24), 244803 (2012).
16. T. Wilhelm, J. Piel, and E. Riedle, "Sub-20-fs pulses tunable across the visible from a blue-pumped single-pass noncollinear parametric converter," Opt. Lett. **22**(19), 1494–1496 (1997).
17. G. Cerullo and S. De Silvestri, "Ultrafast optical parametric amplifiers," Rev. Sci. Instrum. **74**(1), 1–18 (2003).
18. F. J. Furch, S. Birkner, F. Kelkensberg, A. Giree, A. Anderson, C. P. Schulz, and M. J. J. Vrakking, "Carrier-envelope phase stable few-cycle pulses at 400 kHz for electron-ion coincidence experiments," Opt. Express **21**(19), 22671–22682 (2013).
19. N. Ishii, K. Kitano, T. Kanai, S. Watanabe, and J. Itatani, "Carrier-Envelope-Phase-Preserving, Octave-Spanning Optical Parametric Amplification in the Infrared Based on BiB3O6 Pumped by 800nm Femtosecond Laser Pulses," Appl. Phys. Express **4**(2), 022701 (2011).
20. S. T. Cundiff, "Phase stabilization of ultrashort optical pulses," J. Phys. D Appl. Phys. **35**(8), R43–R59 (2002).
21. T. Fuji, J. Rauschenberger, A. Apolonski, V. S. Yakovlev, G. Tempea, T. Udem, C. Gohle, T. W. Hänsch, W. Lehnert, M. Scherer, and F. Krausz, "Monolithic carrier-envelope phase-stabilization scheme," Opt. Lett. **30**(3), 332–334 (2005).
22. O. D. Mücke, R. Ell, A. Winter, J. W. Kim, J. R. Birge, L. Matos, and F. X. Kärtner, "Self-referenced 200 MHz octave-spanning Ti: sapphire laser with 50 attosecond carrier-envelope phase jitter," Opt. Express **13**(13), 5163–5169 (2005).
23. S. Rausch, T. Binhammer, A. Harth, E. Schulz, M. Siegel, and U. Morgner, "Few-cycle oscillator pulse train with constant carrier-envelope- phase and 65 as jitter," Opt. Express **17**(22), 20282–20290 (2009).
24. G. Cerullo, A. Baltuška, O. D. Mücke, and C. Vozzi, "Few-optical-cycle light pulses with passive carrier-envelope phase stabilization," Laser Photonics Rev. **5**(3), 323–351 (2011).
25. A. Baltuska, T. Fuji, and T. Kobayashi, "Controlling the carrier-envelope phase of ultrashort light pulses with optical parametric amplifiers," Phys. Rev. Lett. **88**(13), 133901 (2002).
26. G. Krauss, D. Fehrenbacher, D. Brida, C. Riek, A. Sell, R. Huber, and A. Leitenstorfer, "All-passive phase locking of a compact Er:fiber laser system," Opt. Lett. **36**(4), 540–542 (2011).
27. C. Manzoni, G. Cerullo, and S. De Silvestri, "Ultrabroadband self-phase-stabilized pulses by difference-frequency generation," Opt. Lett. **29**(22), 2668–2670 (2004).
28. C. Vozzi, G. Cirmi, C. Manzoni, E. Benedetti, F. Calegari, G. Sansone, S. Stagira, O. Svelto, S. De Silvestri, M. Nisoli, and G. Cerullo, "High-energy, few-optical-cycle pulses at 1.5 μm with passive carrier-envelope phase stabilization," Opt. Express **14**(21), 10109–10116 (2006).
29. C. Homann, M. Bradler, M. Förster, P. Hommelhoff, and E. Riedle, "Carrier-envelope phase stable sub-two-cycle pulses tunable around 1.8 μm at 100 kHz," Opt. Lett. **37**(10), 1673–1675 (2012).
30. M. Bradler, C. Homann, and E. Riedle, "Broadband difference frequency mixing between visible and near-infrared pulses for few-cycle pulse generation with stable carrier-envelope phase," Appl. Phys. B **113**(1), 19–25 (2013).
31. G. Cerullo, M. Nisoli, S. Stagira, and S. De Silvestri, "Sub-8-fs pulses from an ultrabroadband optical parametric amplifier in the visible," Opt. Lett. **23**(16), 1283–1285 (1998).
32. I. Amat-Roldán, I. Cormack, P. Loza-Alvarez, E. Gualda, and D. Artigas, "Ultrashort pulse characterisation with SHG collinear-FROG," Opt. Express **12**(6), 1169–1178 (2004).
33. M. Kakehata, H. Takada, Y. Kobayashi, K. Torizuka, Y. Fujihira, T. Homma, and H. Takahashi, "Single-shot measurement of carrier-envelope phase changes by spectral interferometry," Opt. Lett. **26**(18), 1436–1438 (2001).
34. C. Feng, J. F. Hergott, P. M. Paul, X. Chen, O. Tcherbakoff, M. Comte, O. Gobert, M. Reduzzi, F. Calegari, C. Manzoni, M. Nisoli, and G. Sansone, "Complete analog control of the carrier-envelope-phase of a high-power laser amplifier," Opt. Express **21**(21), 25248–25256 (2013).
35. T. Wittmann, B. Horvath, W. Helml, M. G. Schaetzel, X. Gu, A. L. Cavalieri, G. G. Paulus, and R. Kienberger, "Single-shot carrier-envelope phase measurement of few-cycle laser pulses," Nat. Phys. **5**(5), 357–362 (2009).
36. B. Borchers, A. Anderson, and G. Steinmeyer, "On the role of shot noise in carrier- envelope phase stabilization," Laser Photonics Rev. **8**(2), 303–315 (2014).
37. A. Guandalini, P. Eckle, M. Anscombe, P. Schlup, J. Biegert, and U. Keller, "5.1 fs pulses generated by filamentation and carrier envelope phase stability analysis," J. Phys. At. Mol. Opt. Phys. **39**(13), S257–S264 (2006).

#220700 - $15.00 USD Received 8 Aug 2014; revised 26 Sep 2014; accepted 26 Sep 2014; published 9 Oct 2014

38. B. Piglosiewicz, J. Vogelsang, S. Schmidt, D. J. Park, P. Gross, and C. Lienau, "Electron Photoemission and Acceleration from Sharp Gold Nanotapers in the Strong-Field, Few-Cycle Regime," Quantum Matter **3**(4), 10 (2014).

---

1. Introduction

Ultrafast pulsed laser sources are an important tool to directly observe fundamental processes taking place on a femtosecond time scale, such as for example the motion of electron wave packets during electronic excitation of atoms or molecules [1] or during chemical processes [2]. In recent years, the focus for generating such ultrafast laser pulses has shifted from solid-state or fiber-based laser oscillators to white-light (WL) generation in bulk material [3, 4] or nonlinear fibers [5, 6] followed by parametric nonlinear optical processes. Such schemes have been shown to enable generation of few-cycle laser pulses over a wide spectral range from the visible to the far-infrared [7]. Wavelength tunability is important because it allows addressing or avoiding certain material resonances and, more specifically, to minimize local heating of metallic nanostructures by tuning the laser to the red of the onset of interband absorption of the metal. Also, wavelength tuning enables a variation of the quiver oscillation period and hence provides important control over strong field photoemission processes. Wavelenght-flexible light sources thus open the path to investigating different fundamental mechanisms from electronic excitation via vibrational motion to off-resonance strong-field effects, such as high harmonic generation (HHG), attosecond streaking or strong-field tunneling ionization [8].

In the strong-field regime, the electric field strength rather than the peak or average intensity plays a key role. Thus, for very short pulses, the phase of the carrier wave with respect to the pulse envelope, also known as carrier-envelope phase (CEP), determines the maximum strength of the electric field and has been demonstrated to be of key importance for coherent control of HHG and attosecond streaking in gases [9–11]. More recently, similar effects have been demonstrated for photoemission from metallic nanostructures: In the case of multiphoton ionization, CEP effects are ascribed to changing interferences of electron wave packets, which are emitted in subsequent cycles of the driving laser field [12], while in the case of strong-field electron emission the changing maximum field strength directly influences the electron motion [13]. The latter indicates control of electron motion via the laser field and may become an enabling step towards the generation and application of attosecond electron pulses.

Experiments as the ones described above require ultrafast laser pulses with a duration of only a few cycles, a wavelength in the near-infrared range, and with a stable CEP. Furthermore, the electric field strength must be on the order of the inner-atomic field strength to enable tunneling of the electrons through the potential barrier, however, this condition can be mitigated by exploiting the field enhancement around metallic nanostructures [14, 15]. Noncollinear optical parametric amplifiers (NOPAs) are used since more than a decade. Since then, they have been continuously improved to supply high gain over very wide bandwidths within the whole transparency range of the used nonlinear crystals [16, 17]. It has been shown that NOPAs have the capability of preserving the phase of the amplified light [18, 19], which can be used, e.g., to transfer the phase of an actively CEP-stabilized oscillator [20–23]. Recently, their ability of providing intrinsic, passive CEP stability has moved into focus [24, 25]. Such passive, all-optical schemes can be realized in different setups, but they usually rely on difference frequency generation (DFG) of two pulses with the same CEP [19, 26–30].

Here we present the realization and characterization of a source of few-cycle, passively CEP-stabilized laser pulses tunable between 1.2 and 2.1 μm for controlling photoemission and motion of electrons by the phase of a strong light field. The approach is based on DFG between the output of two NOPAs, which are seeded by the same WL and thus share the same CEP (similar to [27]). We achieve a CEP stability better than 50 mrad over time spans of seconds up to 20 minutes, when averaging over 100 pulses, which is an excellent long-term

#220700 - $15.00 USD   Received 8 Aug 2014; revised 26 Sep 2014; accepted 26 Sep 2014; published 9 Oct 2014

CEP stability. The suitability of the CEP-stable laser source for strong-field experiments is demonstrated by measuring kinetic energy spectra of photoemitted electrons from a metallic nano-taper as a function of the CEP.

2. Experimental setup

The experimental setup of the ultrafast pulse source is shown schematically in Fig. 1. Coarsely, our system can be grouped into two parallel NOPA stages followed by DFG, and it is pumped by a chirped pulse regenerative amplifier system (Spectra-Physics Spitfire Pro XP) emitting pulses of 120-fs duration at 800-nm center wavelength with a repetition rate of up to 5 kHz and a pulse energy of 800 μJ. Our approach is to generate pulses with a broad bandwidth (and short duration) at a center wavelength around 600 nm in one stage (NOPA#1), and pulses with a narrow bandwidth at 890 nm in the other stage (NOPA#2). With this choice of wavelength for NOPA#2 the spectral properties of NOPA#1 are transferred to the wavelength region around 1.6 μm by DFG between the pulse trains.

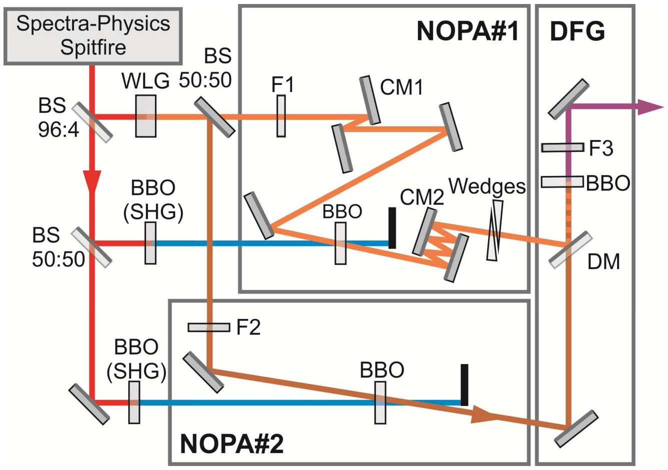

Fig. 1. Experimental setup. The system is based on pulse generation in two NOPA stages (NOPA#1, NOPA#2), which are seeded by the same white light generation (WLG) source, and subsequent difference frequency generation (DFG) of the two pulse trains. For details, see text.

A small portion of the pump light, with a pulse energy of 600 nJ, is split off and focused into a 2-mm thick sapphire plate to create a stable WL filament (white light generation, WLG in Fig. 1). The generated WL spans a spectral range from <450 nm to >1 μm and displays low power fluctuations of about 2% RMS. From the dependence of the amplification in NOPA#1 on the time delay between seed and pump, we estimate a temporal width of the WL of about 200 fs. By means of a reflective neutral density filter used as a 50:50 beam splitter (BS), the WL is split into two replicas, which serve as the seed light sources for the two NOPA stages. The major remaining fraction of the available source pulse energy serves as the pump light for the NOPAs. To this aim, the pulse train is split into two pulse trains with an energy of 220 μJ and 260 μJ, respectively, which are frequency-doubled in two 1-mm-thick β-barium borate (BBO) crystals cut for type-I phase matching. This results in two pulse trains at a center wavelength of 400 nm and with pulse energies of 110 μJ and 130 μJ, respectively.

In NOPA#1, the spectral components with wavelengths > 650 nm are suppressed by an absorptive filter (F1, 2 mm of Schott BG39), and the chirped WL is partially compressed by one reflection off a pair of chirped mirrors (CM1, Venteon DCM9) to increase the temporal overlap with the pump pulse and hence broaden the spectrum of the amplified beam. The WL and the 110-μJ second harmonic (SH) pulse train are noncollinearly overlapped in a 1-mm thick BBO crystal cut for type-I phase matching at an angle of $\theta = 32^\circ$. In order to support a parametric gain bandwidth in excess of 100 nm, the internal angle between the SH and the

Received 8 Aug 2014; revised 26 Sep 2014; accepted 26 Sep 2014; published 9 Oct 2014
(C) 2014 OSA

WL is set to $\approx 3.7°$ [31]. The WL is focused using a spherical mirror with 500 mm radius of curvature, and the SH light is focused by a lens of 300 mm focal length. The foci are positioned in front of the BBO crystal, such that the beam diameter of the SH and the WL inside the crystal are 650 μm and 320 μm, respectively. The peak intensity of the SH is $2.8 \cdot 10^{11}\,\mathrm{Wcm}^{-2}$. The output of NOPA#1, i.e., the amplified WL, is collimated using a second spherical mirror with 500 mm radius of curvature. The pulses are subsequently compressed by 3 reflections off a second pair of chirped mirrors (CM2, Venteon DCM9) and by transmission through a finely adjusted pair of fused silica wedges.

The seed of NOPA#2 is a fixed narrow-bandwidth pulse, which is extracted from the WL by a bandpass filter of 10 nm bandwidth, centered at 890 nm (F2, Thorlabs FB890-10). This spectral component and the 130-μJ SH pulse trains are noncollinearly overlapped with an internal angle of 2.5° in a 1-mm thick BBO crystal cut for type-I phase matching at an angle of $\theta = 29°$. The two pulse trains are focused by two lenses of 500 mm and 300 mm focal length, respectively. Again, the foci are positioned in front of the BBO crystal, such that the beam diameter of the SH and the WL inside the crystal are 650 μm and 320 μm, respectively. The peak intensity of the SH in the NOPA#2 BBO crystal is $3.3 \cdot 10^{11}\,\mathrm{Wcm}^{-2}$. The output of NOPA#2 is collimated using a 400-mm focal length lens.

The output pulse trains of NOPA#1 and NOPA#2 are collinearly combined by a dichroic mirror (DM) and are then focused with a spherical mirror with 200 mm radius of curvature into a 300-μm thick BBO crystal cut at $\theta = 30°$ for type-II phase-matched DFG. The generated DFG pulse train is collimated by a second spherical mirror with 200 mm radius of curvature, and the residual input light for the DFG stage is removed by spectral filtering (F3, Edmund Optics NT67-299).

3. Performance of the NOPA-DFG system

By changing the time delay between the WL and the SH pulse train in NOPA#1, the center wavelength of the amplified pulses can be adjusted within the wavelength range between 475 nm and 675 nm [see Fig. 2(a)]. The selected spectral band of the WL seed light is amplified to pulse energies between 0.1 μJ (for the shortest-wavelength spectrum) and 7.6 μJ (for the second spectrum from the left, centered at 525 nm). The broadest spectrum has a bandwidth of 100 nm centered at 600 nm with a pulse energy of 3.6 μJ. Pulse durations down to 7 fs are achieved.

The second NOPA#2 stage generates pulses with the center wavelength fixed to 890 nm [see black curve in Fig. 2(a)] and with a pulse energy of 2 μJ.

After suitable tuning of NOPA#1, the temporal pulse overlap between the two pulse trains in the DFG crystal is adjusted, and the conversion efficiency is optimized by slightly tilting the DFG crystal. With the fixed, narrow-bandwidth output of NOPA#2, the wide bandwidth and tunability of NOPA#1 are directly transferred to the NIR by the DFG process and result in a wavelength coverage from 1350 nm to 2030 nm [see Fig. 2(b)]. For the short-wavelength spectrum, centered at 1400 nm, a pulse energy of 220 nJ and a pulse duration of around 30 fs are achieved. For the long-wavelength spectrum, centered at 1800 nm, the pulse energy is 70 nJ and the pulse duration is 20 fs. The broadest spectrum, centered at 1600 nm, yields a pulse energy of 110 nJ and the shortest pulse duration. The duration of the NIR pulses is measured using interferometric frequency-resolved autocorrelation (IFRAC), which could also be described as a collinear FROG and which, like FROG, yields the full information on the complex electric field [32]. The IFRAC measurement yields a pulse duration as short as 10.6 fs [Fig. 3(a)], which is only slightly above the Fourier-limited pulse duration of 10.4 fs. This in agreement with the almost flat spectral phase [see Fig. 3(b)] and corresponds to 2 optical cycles.

#220700 - $15.00 USD Received 8 Aug 2014; revised 26 Sep 2014; accepted 26 Sep 2014; published 9 Oct 2014

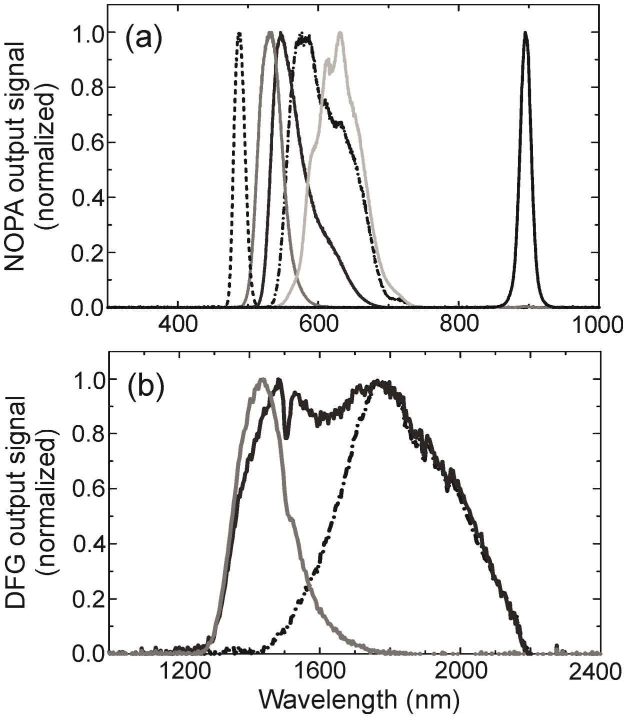

Fig. 2. Wavelength tuning of the NOPA-DFG system. (a) Output spectra of the NOPA stages. The spectra at $\lambda < 800\ \mathrm{nm}$ are generated by NOPA#1; the wavelength tuning was achieved by changing the time delay between WL and pump pulse. The spectrum at $\lambda = 890\ \mathrm{nm}$ is the output of NOPA#2. (b) DFG spectra, corresponding to the three center NOPA#1 spectra shown in (a). The detected wavelength range is limited at long wavelengths by the spectral response of the spectrometer.

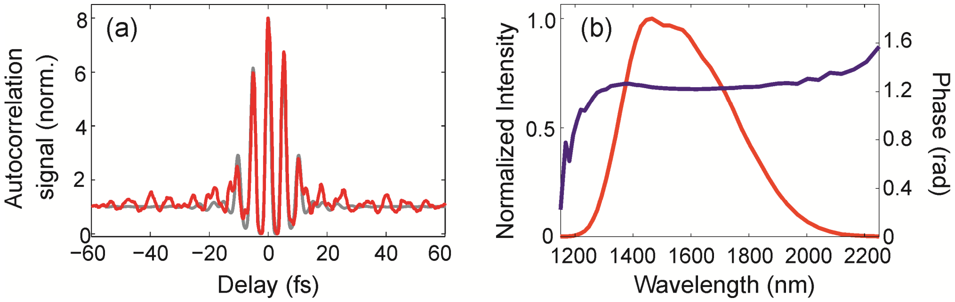

Fig. 3. (a) Interferometric autocorrelation trace distilled from an IFRAC measurement of the pulses (red curve), recorded at a center wavelength of 1.6 μm and indicating a pulse duration of 10.6 fs or 2 optical cycles. The grey curve is a simulated autocorrelation trace, calculated from the retrieved electric field strength. (b) The retrieved spectrum (red curve) indicates a Fourier-limited pulse duration of 10.4 fs, and the retrieved phase (blue curve) shows a small residual chirp.

As a measure for the beam quality, the DFG output is focused using an 0.5-NA cassegrain objective onto a sharply etched gold tip and the electron yield is measured as a function of the laser focus position on the tip. Thereby effectively the intensity distribution of the focus is measured with a near-field probe. The electron counts are displayed color-coded in Fig. 4 and show an even, almost Gaussian-shaped, and slightly elliptical distribution with a full width at half maximum of about 0.8 μm in vertical and 0.94 μm in horizontal direction. In these experiments, the electron signal scales with the fifth power of the laser intensity, $N = 5$, and

#220700 - $15.00 USD Received 8 Aug 2014; revised 26 Sep 2014; accepted 26 Sep 2014; published 9 Oct 2014

the spot size is inversely proportional to $\sqrt{N}$. The experiment thus points to a diffraction limit spot size of about 1.8 μm diameter at the fundamental.

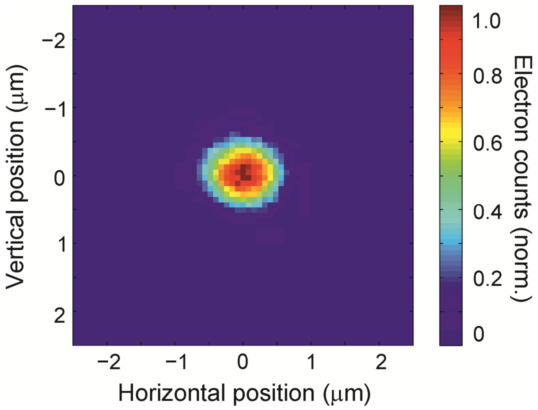

Fig. 4. Electron counts as a function of the position of the laser focus on a gold tip, with the electron count depending on the laser intensity to the fifth order. The electron counts form a slightly elliptical spot with a diameter of about 0.8 μm in vertical and 0.94 μm in horizontal direction.

4. CEP stability

Fluctuations of the CEP are measured in an f-to-2f-interferometer [33], realized as a common-path interferometer. The laser pulses are spectrally broadened to an octave-spanning bandwidth by self-phase modulation in an 8-mm thick YAG plate, followed by a 100-μm-thick BBO crystal for frequency doubling. Interference between the WL and the SH yields spectral fringes, whose period is adjusted via changing the position of the filament within the YAG crystal. A polarizer is used to project the WL and the SH to the same polarization axis and to balance their intensities. The spectral interference fringes are recorded by a monochromator equipped with a cooled CCD camera (Princeton Instruments Pro EM512B-EX), and the CEP is determined by removing high-frequency noise and by extracting the phase offset from the filtered fringe pattern.

In order to fully exploit the capability of the system to generate passively CEP-stabilized pulses, we investigated the role of different potential sources of CEP instabilities of the DFG pulses in our system. With the goal to isolate such contributions to the over-all instability, we measured time traces of different observables that could possibly act as noise sources for the CEP measurements and determined the degree of their correlation with the CEP variation by calculating the cross correlation function:

$$\phi_{sg}(\tau)=\int_{-\infty}^{\infty} s(t)\cdot g^{*}(t+\tau)dt \tag{1}$$

Here, $s(t)$ and $g(t)$ refer to the two time traces that were compared, and τ is the delay between them. $\phi_{sg}(\tau)$ was normalized by the autocorrelation functions of $s(t)$ and $g(t)$ at time delay $\tau=0$ to yield the normalized correlation function:

$$\varphi_{sg}(\tau)=\frac{\phi_{sg}(\tau)}{\sqrt{\phi_{ss}(0)\cdot\phi_{gg}(0)}} \tag{2}$$

First, we ruled out that the f-to-2f interferometer itself presents a major source of instabilities, by varying the DFG pulse energy in front of the f-to-2f interferometer. Only very small changes of the spectral fringes were observed. After that, we simultaneously recorded time series of spectral fringes and time traces of either the laser SH power (at 400 nm), the

#220700 - $15.00 USD Received 8 Aug 2014; revised 26 Sep 2014; accepted 26 Sep 2014; published 9 Oct 2014
(C) 2014 OSA

DFG power, or the duration or spectral width of the pump pulses. Varying degrees of correlations were observed. The highest degree of correlation of $\varphi(0) = 0.87$ was found between the SH power and the CEP variation. Further investigation showed that the SH and the CEP fluctuations mainly result from fluctuations in the pump pulse duration. The degree of correlation between the pump pulse duration and the CEP variation of $\varphi(0) = 0.75$ was slightly lower [see time traces in Fig. 5(a)]. Both the CEP and the SH intensity show nonlinear dependencies on the pump pulse duration: the CEP shifts with the inverse pump pulse duration, and the SH intensity is proportional to the square of the inverse pulse duration. This results in a lower degree of linear correlation $\varphi(\tau)$ between the CEP and the pump pulse duration on one hand than between the SH and the pump pulse duration on the other hand. Using a fast (~400 ms acquisition time) autocorrelator we found that the pulse duration changed slowly, on a ~2 s timescale.

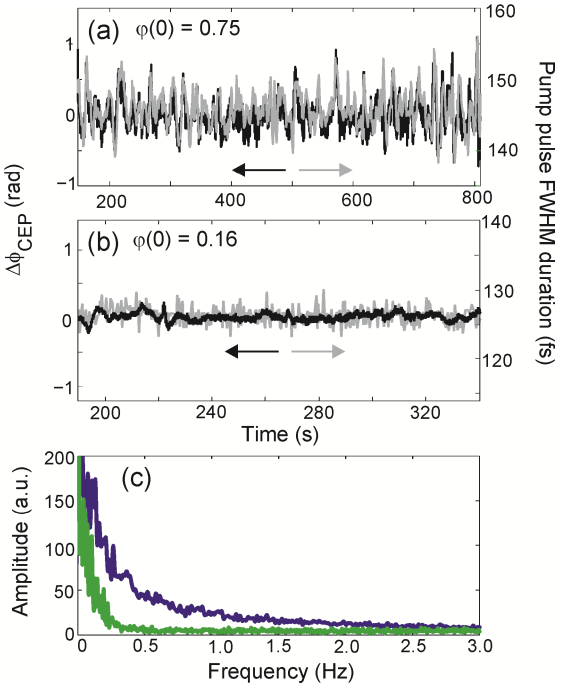

Fig. 5. (a) Initial time traces of the CEP (black curve) and of the pump pulse duration (grey curve) reveals a high grade of correlation of 0.75. (b) Measurement of the same parameters after amplifier modification show a very low grade of correlation of 0.16. (c) Fourier transforms of the CEP time traces before (blue curve) and after (green curve) amplifier modification show that slow variations in the range of 0.1 to ~3 Hz have been drastically reduced.

Heat management inside the amplifier housing emerged as a likely cause of those fluctuations. As a first attempt to improve the pulse duration stability, the amplifier was upgraded to the latest Spitfire Ace stability performance, which optimizes heat management.

After this modification of the amplifier housing we again measured the pulse duration and the CEP variation. A substantial improvement of the CEP stability was apparent: Before modification, the CEP fluctuations, when averaged over 100 ms, could be as high as ~500 mrad RMS as shown in Fig. 5(a). With the modified amplifier design, the CEP fluctuations were reduced to ~50 mrad RMS. The pump pulse duration fluctuations were reduced from 2.6 fs RMS to 1.3 fs, and the correlation between CEP noise and pump pulse duration essentially vanished [$\varphi(0) = 0.16$, Fig. 5(b)]. A Fourier transform of the CEP traces [Fig. 5(c)] shows

#220700 - $15.00 USD Received 8 Aug 2014; revised 26 Sep 2014; accepted 26 Sep 2014; published 9 Oct 2014

that mainly slow fluctuations in the range 0.1~3 Hz have been suppressed by the improved heat management.

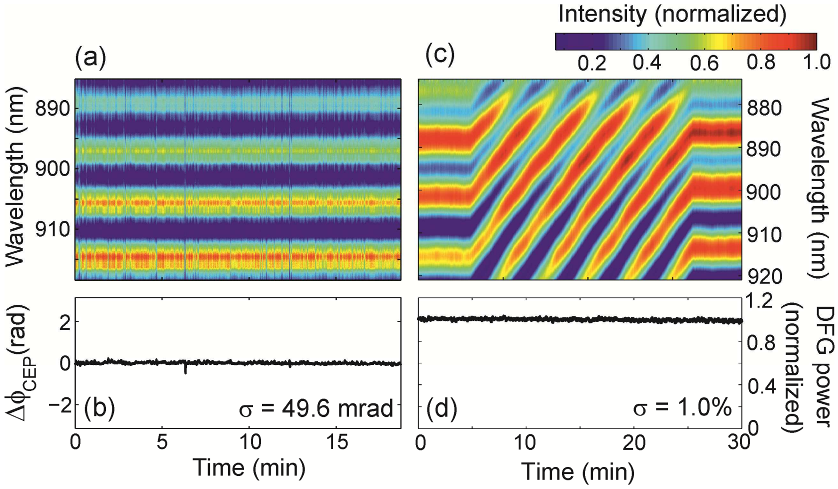

Fig. 6. (a) Interference fringes measured in the f-to-2f interferometer over a time span of 18 min when averaging over 100 pulses, showing (b) very low residual CEP fluctuations of only 49.6 mrad. (c) By inserting dispersive material, the CEP can be tuned linearly over 10π. (d) shows the power stability of the generated DFG radiation measured over 30 min, with a residual instability of about 1%.

Figure 6(a) shows spectral interference fringes recorded behind the f-to-2f interferometer over a period of 18 min. For each spectrum, the integration time was set to 100 ms (100 pulses at a repetition rate of 1 kHz). The CEP was extracted from these spectra [Fig. 6(b)], revealing low residual fluctuations of 49 mrad. This compares favorably with a previously reported measurement at a repetition rate of 100 kHz [29], and is an excellent long-term CEP stability, especially considering that it is achieved in a completely passive manner. By inserting dispersive material in the form of a pair of fused silica wedges, the CEP could be controlled and adjusted over a range of 10π [Fig. 6(c)].

So far, all characterization has been performed by temporally averaging over a series of 100 subsequent NOPA pulses and demonstrated the good long-term stability of the NOPA-DFG system. In order to be able to characterize also the short-term stability, we have also measured the CEP fluctuations from one shot to the next. For this, we recorded spectra behind the f-to-2f interferometer with the spectrometer exposure time set to 0.9772 ms, and with the laser system operating at 1 kHz repetition rate. Figure 7(a) shows a shot-to-shot measurement over 20 minutes (1200000 pulses at 1 kHz repetition rate), again displaying the good long-term CEP stability. Looking at an interval over 1 s [Fig. 7(b)] one can see, however, that there is a clear CEP fluctuation discernible between adjacent spectra. For completeness, Fig. 7(c) shows the Fourier transform of the CEP recorded over 20 minutes. One can see that the CEP noise spectrum displays a minimum at roughly 10 Hz (corresponding to averaging over 100 pulses), and is slowly increasing towards higher frequencies.

#220700 - $15.00 USD Received 8 Aug 2014; revised 26 Sep 2014; accepted 26 Sep 2014; published 9 Oct 2014

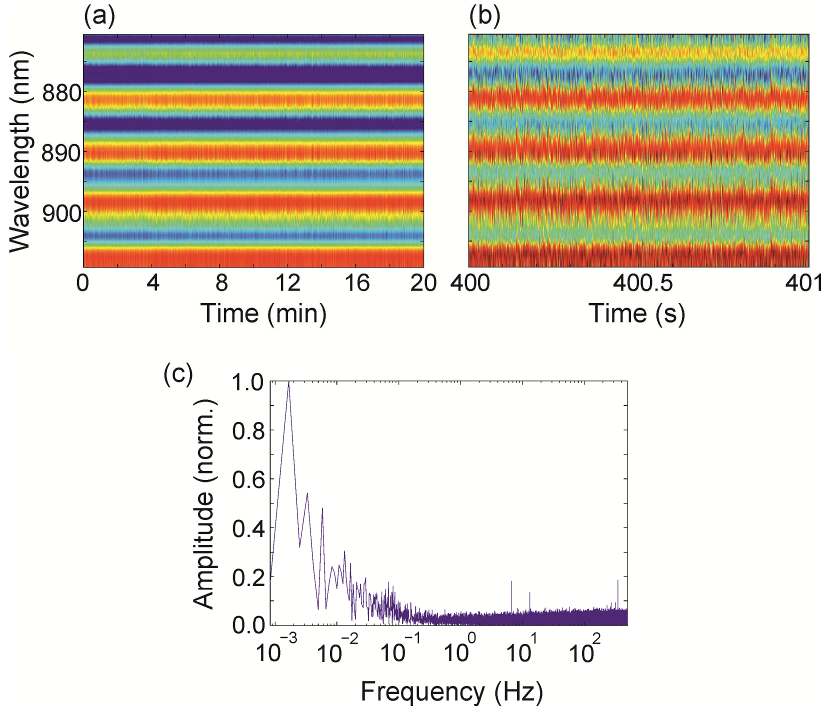

Fig. 7. Shot-to-shot CEP stability. (a) Interference fringes of single laser pulses measured in the f-to-2f interferometer over a time span of 20 minutes. (b) A zoom of a time span of 1 s makes the individual spectra visible, each recorded for a single laser pulse. (c) The Fourier transform of the CEP extracted from each spectrum shows the full CEP noise spectrum.

Thus averaging evidently suppresses high-frequency shot-to-shot fluctuations and therefore reduces the effect of CEP fluctuations on the fringes in the f-to-2f interferometer [34, 35]. To investigate high-frequency CEP fluctuations in our system, we recorded such fringes for different spectrometer exposure times. Five data sets were recorded for exposure times varying between <1 and 11 ms. In the fastest measurements, the exposure time was less than the time delay between two consecutive pulses $T = 1/f_{\text{rep}} = 1\text{ms}$. The results of these measurements are shown in Fig. 8, with different symbols corresponding to different exposure times and the utmost right data point of each set referring to the actual measurement. The data points further to the left result from post-processing each data set by averaging over 10, 100 and 1000 spectra, respectively, and then extracting the CEP RMS noise from the averaged spectra. For example, post-processing the shot-to-shot data by averaging over 100 spectra gives a similar result as a measurement with the integration time of the CCD camera set to capture 100 pulses. As expected from the law of large numbers, the values for the CEP noise reduce with the square root of the number of averaged pulses. Using a sensitive CCD camera as detector, we achieved count rates of around 15000 photons per pulse and could record spectral interference of single pulses. With this we can ensure that shot noise induced phase jitter of less than 10 mrad [36] is not a limiting factor in our measurements. Thus, we have measured the shot-to-shot CEP instability with an upper limit of ~800 mrad, which compares favorably with shot-to-shot CEP measurements of previously reported measurements at repetition rates at 100 Hz and 1 kHz [33, 37].

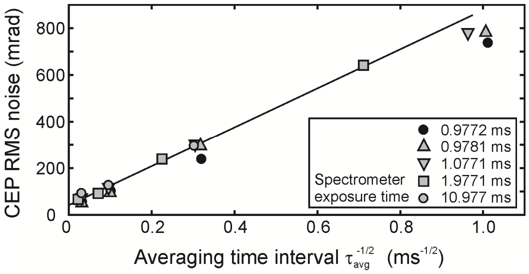

Fig. 8. Residual CEP instability extracted as a function of exposure time interval. The two utmost right data points represent shot-to-shot CEP instabilities.

We would like to note that the shot-to-shot CEP stability can also be estimated from the visibility of the fringe pattern, even when averaging over a larger number of pulses. To demonstrate this, we have simulated a large number of interference spectra with variable shot-to-shot CEP RMS noise. After averaging over 10, 100, and 1000 pulses, the average fringe visibility is plotted as the green, the red, and the blue curve in Fig. 9, respectively. In order to demonstrate the practical applicability of this method, we have extracted the fringe visibility from an experimentally measured f-to-2f interferogram, which was recorded with an exposure time of 100 ms (100 pulses). The visibility of the fringe pattern was maximized by balancing the intensity and carefully adjusting the spatial overlap of the two interfering spectral components. After careful removal of dark counts, the visibility was 0.71, which, superposed onto the red curve in Fig. 9, results in a shot-to-shot CEP RMS noise of 826 mrad. This value is in excellent agreement with the true shot-to-shot measurements presented in Figs. 7 and 8.

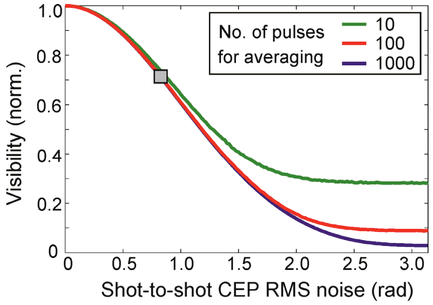

Fig. 9. Fringe visibility as a function of shot-to-shot CEP RMS noise when averaging over 10, 100, and 1000 pulses as the green, red, and blue curve, respectively. The solid curves are simulated data, and the square symbol is from a measured interference pattern, averaged over 100 pulses.

In order to demonstrate the suitability of the presented NOPA-DFG system for the observation of strong-field effects, we illuminated a sharply etched gold nanotaper with the generated NIR, CEP-controlled pulses and recorded electron kinetic energy spectra as a function of the CEP. With the pulse energy adjusted such that photoemission is governed by above-threshold ionization and the onset of strong-field emission [12, 38], the electron yield is expected to depend strongly on the maximum field strength and thus to vary with the CEP.

Figure 10 shows kinetic energy spectra of electrons that were photoemitted in this regime. The graph displays seven spectra, which were recorded, while the CEP was changed by inserting dispersive material. Between each pair of consecutively recorded spectra, the CEP was increased by $\Delta\varphi_{CEP} = \pi$. The seven recorded spectra can be clearly grouped into two sets, as indicated by the red and blue color in Fig. 10. The two sets of spectra are offset with respect to each other by a difference in CEP by $\Delta\varphi_{CEP} = \pi$. Integration of the curves yields a variation of electron counts of 50% with CEP.

#220700 - $15.00 USD Received 8 Aug 2014; revised 26 Sep 2014; accepted 26 Sep 2014; published 9 Oct 2014

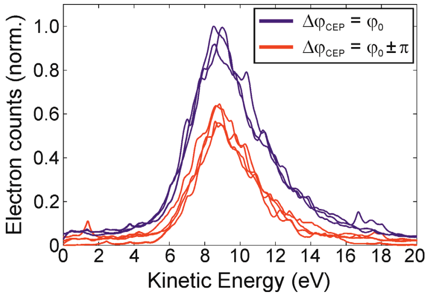

Fig. 10. Kinetic energy spectra of electrons photoemitted from a sharp gold tip. The individual curves correspond to consecutive spectra that were recorded after the CEP was increased by p. The spectra can clearly be grouped into two sets (indicated by red and blue), which are offset with respect to each other by a difference in CEP of $\Delta\varphi_{CEP} = \pi$.

At higher pulse energies, i.e., in the strong-field regime, we expect that the CEP mainly influences the field-driven acceleration of the electrons. This was confirmed by observing a cyclic variation of the cutoff energy of the kinetic energy spectra. Both observations prove that the CEP is sufficiently stable and that the pulse duration is sufficiently short to study the influence of the electric field rather than the envelope on photoemission from single nanostructures. The experiments on the CEP effect on photoemission from nanostructures in the strong-field regime can be found in [13].

5. Summary

In summary, we have realized a NOPA-DFG system as a source of few-cycle, passively CEP-stabilized NIR laser pulses. The system consists of two NOPAs, which are seeded by the same WL, followed by DFG between the outputs of the two NOPAs. The DFG output is wavelength-tunable between 1.2 and 2.1 µm and supports pulses as short as 2 cycles.

Due to the design of the system, the DFG output pulses are intrinsically CEP-stable. Furthermore, in order to reduce technical noise sources and thus to fully utilize this high potential for CEP stability, we have investigated different potential sources of CEP fluctuations. Thereby we have identified thermal fluctuations of the air within the amplifier housing as a major source, which we have suppressed successfully by improving heat management in the amplifier. This resulted in low residual CEP fluctuations of <800 mrad RMS from shot to shot, and of <50 mrad when integrating the spectra over 100 ms.

Finally, we have demonstrated the suitability of this pulsed laser source for electron photoemission from single metal nanostructures. The pulse duration was sufficiently short and the CEP sufficiently stable to clearly show a CEP dependence of electron photoemission. We believe that the development and handling of such dedicated, ultrashort pulsed laser sources is a key to observe and understand the motion of electron wave packets in solids, e. g. during electronic excitation or charge transfer processes in natural and artificial light harvesting structures.

Acknowledgments

Financial support by the Deutsche Forschungsgemeinschaft (SPP1391), by the European Union (project ‘CRONOS’, Grant number 280879-2), and the Korea Foundation for International Cooperation of Science and Technology (Global Research Laboratory project, K20815000003) is gratefully acknowledged. GC acknowledges support by the European Research Council Advanced Grant STRATUS (ERC-2011-AdG No. 291198). JV acknowledges funding from the Studienstiftung des Deutschen Volkes. JR acknowledges funding from the Deutsche Forschungsgemeinschaft (Research Training Group ‘Molecular Basis of Sensory Biology’).

#220700 - $15.00 USD Received 8 Aug 2014; revised 26 Sep 2014; accepted 26 Sep 2014; published 9 Oct 2014

Strong-field above-threshold ionization of Rydberg electrons localized to a single gold nanotip

Jörg Robin[1,2], Jan Vogelsang[1,2], Janne Solanpää[3], Philipp Wopperer[4],
Umberto De Giovannini[4], Benedek J. Nagy[5,6], Péter Dombi[5,6], Esa Räsänen[3],
Angel Rubio[4,7], Christoph Lienau[1,2,8], Petra Groß[1,2]

[1] Institut für Physik, Carl von Ossietzky Universität Oldenburg,
26129 Oldenburg, Germany
[2] Center of Interface Science, Carl von Ossietzky Universität Oldenburg,
26129 Oldenburg, Germany
[3] Tampere University of Technology, Department of Physics,
FI-33101 Tampere, Finland
[4] Universidad del País Vasco UPV/EHU, Centro de Física de Materiales CSIC-UPV and DIPC, Nano-bio Spectroscopy Group and European Theoretical Spectroscopy Facility (ETSF)
[5] Wigner Research Center for Physics,
H-1121 Budapest, Hungary
[6] ELI-ALPS, ELI-HU Nonprofit Kft.,
6720 Szeged, Hungary
[7] Max Planck Institute for the Structure and Dynamics of Matter, and Center for Free-Electron Laser Science & Department of Physics, University of Hamburg,
22761 Hamburg, Germany
[8] Forschungszentrum Neurosensorik, Carl von Ossietzky Universität Oldenburg,
26129 Oldenburg, Germany

Manuscript prepared for publication in a peer-reviewed journal (submitted)

Introduction (148 words):

In gaseous media, the ultrafast acceleration of electronic wavepackets in strong laser fields results in spectacular phenomena such as above-threshold-ionization[1-3] or high harmonic generation[4-6] and lies at the heart of modern attoscience[7,8]. In condensed matter, metallic nanotips[9] have recently emerged as model systems for exploring strong-field phenomena in single nanostructures[10,11]. Signatures of above-threshold-ionization have been observed, but so far they have remained weak[12,13] since electrons are emitted from a continuum of states near the Fermi level. Here, we demonstrate atomic-like photoemission up to the 12th photon order from a single gold nanotip. This is achieved by storing photoelectrons in a set of discrete, long-lived image potential states[14-16] and driving them by a strong near-infrared laser field, locally enhanced at the tip apex. This approach bridges the gap between atomic strong field science and solid-state nanostructures and paves the way toward the controlled generation of nanolocalized, attosecond electron pulses.

Main text (2485 words):

When exposing an atomic system to a strong laser field, an electronic wavepacket is launched, from a discrete bound state, into continuum states within a fraction of an optical cycle. It is then accelerated within the spatially homogeneous and temporally oscillating field of the laser and partially released from the atom near the outer turning points of its oscillatory motion. A small fraction of the returning wavepacket recombines upon passing the parent ion, emitting high harmonic radiation (HHG)[4,8,17]. This periodic motion continues until the end of the driving field and self-interference of the released electron wavepacket gives rise to broadened photoelectron (PE) kinetic energy spectra, modulated at the period of the photon energy and extending to high photon orders. Hence, this above threshold ionization (ATI) spectrum[1-3] is a direct signature of an attosecond electron pulse train whereas the HHG spectrum reflects the emission of attosecond optical pulses[5,7]. As such ATI and HHG have led, e.g., to measurements of the absolute phase of light pulses[18] and to new coherent sources of short-wavelength radiation[6], and have become cornerstones of attosecond atomic and molecular science.

Even though these strong-field phenomena are now well established, their counterparts in condensed matter systems have long defied experimental observation. Only recently, efficient HHG has been achieved in bulk semiconductors, e.g., by driving electron-hole pair polarizations in strong mid-infrared fields[19,20]. ATI on solid state surfaces has been limited to low photon orders[21,22], possibly due to the low damage threshold of the surfaces. Higher ATI photon orders have been demonstrated by making use of optical field enhancement at sharp metal tips. These signatures are, however, comparatively weak since electrons are released from a continuum of states near the Fermi level[12,13]. Since nanotips are interesting model systems for strong field phenomena[10,11] and serve as point-like sources for ultrafast electron and light pulses[9], with applications in ultrafast microscopy[23,24] and diffraction[25], it is important to gain control over ATI from such nanotip sources to bring their time resolution to the attosecond regime.

Conceptually, current limitations in nanotip ATI may be overcome by using strong-field photoionization from discrete, atomic-like states rather than continuum states. At extended metallic surfaces[16] such states exist in the form of long-lived image potential (IP) states[14,15] that arise from the Coulomb attraction between an electron released from the metal surface and its own image charge. So far, however, such IP states have never been observed for a single metallic nanostructure.

Here we report the first observation of atomic-like ATI from a single, sharp gold nanotip. In two-colour pump-probe photoemission experiments we excite long-lived Rydberg electron wave packets in front of the tip surface and, for the first time, induce strong-field photoemission from these discrete surface states. This bridges the gap between attosecond physics in atomic and condensed matter systems.

Strong field phenomena in photoemission are generally observed whenever the ponderomotive kinetic energy $U_P = \left(eE_{loc}^2\right)/\left(4m\omega^2\right)$, that is gained by an electron moving in an oscillating electromagnetic field at angular frequency ω and with local field strength E_{loc}, exceeds its binding energy E_b to the ionic core, or if the Keldysh parameter $\gamma = \sqrt{E_b / 2U_p}$ approaches or becomes less than 1. In all previous experiments on metallic nanostructures, photoemission was induced from a continuum of bound states near the Fermi energy and hence E_b approximately matches the work function of the metal, e.g., $\Phi = 5.5\,e\text{V}$ for gold[26]. In contrast, the idea here is to induce strong field emission from discrete, weakly bound states, close to the ionization continuum and with binding energies $E_b < 1\,e\text{V}$. For this, we first prepare these states by multiphoton absorption of electrons near the Fermi sea and then photoionize them by a second, strong laser pulse. By choosing $E_b < 2U_P < \Phi$ we prevent strong field photoemission from the large background of continuum states while strongly driving electrons in weakly bound states.

Experimentally, we illuminate a sharply etched gold nanotip with a radius of curvature of ~10 nm by a phase-locked pair of precisely timed dichromatic femtosecond laser pulses

(Fig. 1a). The pulses are focused to a few micron-sized spot at the apex of the tip (Fig. 1b) using an all-reflective objective. Electrons in the tip are excited by a ~ 9 fs visible (VIS) laser pump pulse centred at a wavelength of ~ 600 nm. This pulse is linearly polarized perpendicular to the taper axis, and its peak intensity is adjusted to the precise onset of photoemission. At this wavelength, interband absorption in gold largely suppresses field enhancement and localization at the apex and photoemission is reached at a pulse energy of $<1\,\mathrm{nJ}$. The VIS pulse is followed by an $\sim 18\,\mathrm{fs}$ near-infrared (NIR) pulse with a centre wavelength of $\sim 1600\,\mathrm{nm}$ to induce strong field photoionization. The NIR pulse is polarized along the taper axis and hence its electric field is largely enhanced, by approximately a factor $f \approx 9$, in a 10-nm region around the apex due to the strongly curved surface of the nanotip (Fig. 1c) [11]. NIR pulses with energies of up to 0.3 nJ and peak field amplitudes E_0 of up to 1.1 V/nm are used. At the tip apex, these fields are enhanced to local field strengths of up to $E_{loc} \approx f \cdot E_0$ ~ 10 V/nm, well within the strong field regime. The pulse durations of these incident pulses are measured directly by inducing multiphoton electron emission from the taper apex and recording interferometric autocorrelation traces (Figs. 1d, e).

To explore strong-field photoemission from the gold tip, kinetic energy distributions of the released electrons are measured with a photoelectron spectrometer (PES). When using a single NIR pulse of variable intensity, we observe the now well-established transition from multiphoton to subcycle photoemission[10,11] with broadened, plateau-like spectra at high pulse energies that are characteristic of the subcycle regime (Fig. S8). In contrast, distinctly different spectra are recorded when illuminating the tip with time-overlapping VIS and NIR pulses (Fig. 1f). For a VIS pulse energy of 0.75 nJ, well within the multiphoton regime and a NIR energy of 0.12 nJ, corresponding to an apex field strength of about $f \cdot E_0 = 6.5\,\mathrm{V/nm}$, we observe markedly modulated spectra with seven emission peaks, equally separated by an energy close to the NIR photon energy of 0.78 eV. When increasing the NIR energy while keeping that of the VIS pulses constant, the kinetic energy spectra broaden and strongly modulated spectra develop, showing up to 12 distinct peaks separated by the NIR photon energy. The modulation contrast is between 20% and 30%, even in the presence of the featureless one-color background (grey curves, recorded for a large interpulse delay). The integrated spectra yield a total electron count which increases roughly linearly (with a slope of 1.12 ± 0.84) with the NIR intensity (Fig. S3). This is in stark contrast to the 7th order nonlinear dependence expected in the multiphoton regime from the work function of gold[11,26] of $\sim 5.5\,\mathrm{eV}$ and an additional clear signature of strong-field photoemission[10,27].

These spectra are distinctly different from single-pulse ATI spectra recorded earlier from tungsten nanotips[12,13]. The single-pulse spectra show a much reduced contrast of the lowest order peaks and a strong suppression of the emission from higher order peaks in the plateau region. Those ATI measurements have been interpreted in terms of strong field photoemission from conduction band states in the metal with energies close to the Fermi level. In contrast, the appearance of *sharp* ATI peaks is well known from atomic and molecular systems[8], where electrons are released from a (series of) discrete, bound state(s).

This makes it likely that the ATI spectra in Fig. 1f can also be related to ionization of discrete electronic states of the nanotip, transiently populated by the VIS excitation pulse. Inherent candidates are adsorbate states at the metal surface, surface states, or IP states. For the latter, the interaction between the released electron and its image charge in the metal results in a Coulomb-like binding potential. Such IP states are known from photoemission[16,28] and scanning tunnelling spectroscopy[29] studies of planar metal surfaces. The Coulomb potential gives rise to a Rydberg-like series of states with main quantum number n and binding energies of a few hundred meV, scaling as $1/n^2$. Their wavefunctions are mainly localized a few nanometres outside the surface (Fig. 2a). Their weak overlap with the metal results in comparatively long lifetimes, ranging from few fs to several hundred fs scaling with n^3.

So far, little is known about the existence and properties of such IP states at the surface of metallic nanoparticles such as our gold nanotip. We therefore first estimate their static properties by a solution of the two-dimensional (2D) Schrödinger equation. We model the tip as a periodic array of binding potentials, confined within a hyperbolic surface and matched to a Coulomb-like potential that accounts for the image potential (see SOM for more information about the model). In the absence of a laser field, this potential leads, in addition to those electronics states that are localized within the metal tip, to a series of weakly bound electron wavefunctions which are predominantly located outside the tip and confined to its apex (Fig. 2b). Their projections onto the taper axis are very similar to the well-known, one-dimensional (1D) case (Fig. 2a). To simulate strong-field photoionization dynamics in such IP states, we solve a 1D time-dependent Schrödinger equation (1D-TDSE). We initially prepare the system in the $n = 2$ Rydberg state, mimicking the action of the VIS pulse, and then subject the system to the spatially localized and temporally varying electric field induced near the apex by the a strong ~ 25 fs NIR pulse. The decay length of the optical near field is similar to the extent of the bound state, and hence the electron is driven by a field with a strong spatial gradient, reducing the probability for recollisions[10,30]. As a result, the electron wavepacket is periodically accelerated by the few-cycle excitation pulse and, once per cycle, splits into a bound wavefunction and a freely propagating electron wavefunction (Fig. 2d). The time structure of the released wavepacket is modulated with the laser period of 5.3 fs and changes slightly over the course of the propagation. At fixed positions, an attosecond pulse train with a subpulse duration of 790 as is created (Fig. 2e). Self-interference of the released wave packet results in PE kinetic energy spectra displaying distinct ATI peaks separated by the NIR photon energy (Fig. 2f). Both the width of the spectra and the number of ATI peaks increase with electric field strength, in reasonable agreement with experiment.

To support the choice of the model potential, which inevitably has a pronounced effect on the electron dynamics, we calculated an effective, 2D Kohn-Sham potential using density functional theory (DFT). We model the nanotip as a hyperbola filled with a jellium background charge density that is set to decay smoothly into the vacuum to produce Coulomb-like asymptotics in the Kohn-Sham potential. The jellium tip hosts around 5000 electrons, which indeed results in an effective potential with a work function of ~5.5 eV. Also in this potential, a series of Rydberg-like electron states with binding energies of few tens to few hundred meV is found. The electron density of these states is mostly localized in front of the tip apex (Fig. 2c). As such, the DFT calculations confirm the existence of Rydberg-like IP states near the apex of the gold nanotips. In general, the wavefunctions show a more complex structure and extend further away from the tip surface than predicted for the model potential in Fig. 2b. To simulate strong-field photoionization, we place a single active electron (SAE) in the excited bound state shown in Fig. 2c, emulating the effect of the VIS pulse, and calculate the temporal dynamics of the light-driven electron density driven by the NIR probe pulse (see Movie S1). The resulting PE spectra (Fig. 2g) are very similar to those derived from the effective model potential (Fig. 2f).

Both models support strong-field photoionization of IP states as the origin of the ATI spectra in Fig. 1f. To validate this finding, we performed time-dependent two-colour photoemission experiments with weak NIR probe pulses (Fig. 3a). This suppresses ATI and gives rise to spectrally narrow PE spectra, characteristic for the multiphoton regime. Photoemission persists for time delays of more than 100 fs, and shows characteristic beatings of the emission intensity, with periods of 54 fs for positive (VIS precedes NIR) and 39 fs for negative delays, respectively. The observed beating pattern is quite complex and sensitively depends on the excitation conditions. This can be seen in the time trace in Fig. 3b, showing distinctly different decay times at positive time delays (~ 130 fs) and negative delays (~ 40 fs). These lifetimes agree well with the lifetimes of the $n=2$ (30 fs) and $n=3$ (110 fs) IP states estimated from bulk studies[26]. The rather complex quantum beating contains multiple Fourier components and is qualitatively quite similar to that observed in two-photon photoemission studies of IP states at bulk surfaces[16,28]. In those studies, however, ATI signatures have never been observed, possibly due to the lack of local field enhancement.

Both simulation methods can nicely account for the complex quantum beating observed experimentally. In 1D-TDSE simulations (Fig. 3c), the electron wave packet is initially prepared in a coherent superposition of Rydberg states $n = 2$ and $n = 3$ and photoionized by a strong, time-delayed 10-fs NIR pulse. The resulting time-dependent PE spectra (Fig. 3d) then display a clear beating with a period of $T = h/\left(E_3 - E_2\right) = 34$ fs, given by the energy splitting between the two states, close to one of the dominant, experimentally observed beat periods.

More complex beating patterns arise when preparing the electronic wave packet in a superposition of four excited states in the DFT-based SAE model. Here, both the delay-dependent PE spectra (Fig. 3e) as well as the total electron count rate (Fig. 3f) display multi-period beating patterns with their periods matching the three beating frequencies observed in the experiment (inset of Fig. 3a). Taken together, these arguments provide strong support that the ATI peaks in Fig. 1f are indeed induced by strong-field ionization of a coherent superposition of long-lived IP states, in which photoexcited electrons undergo a persistent orbit-like motion in front of a sharply curved metallic surface.

In summary, our results suggest that atomic-like ATI spectra of solid-state nanostructures can be observed by strong-field photoionization of long-lived, weakly bound states with rather long dephasing times such as image potential or, potentially, adsorbate states. Such spatially localized surface states thus offer exciting possibilities for transferring well-known concepts from strong-field atomic physics to solid state nano-devices. Specifically, attosecond electron pulses can be controllably generated from single metallic nanotips with high yield, providing an intriguing new source for ultrahigh time-resolution electron microscopy, in particular in conjunction with recently developed diffractive-imaging, point-projection methods[24,31]. Strong-field coherent control of the electronic motion in such Rydberg orbits can offer a conceptually new approach towards high harmonic generation from metallic nanostructures while the enormous spatial extent of these quantum states might be of interest for the coherent coupling of neighbouring nanoparticles.

Methods (582 words)

Tip fabrication. Single-crystalline gold nanotips were fabricated from polycrystalline gold wires (99.99%) with a diameter of 125 μm (commercially available from Advent Research Materials). After cleaning in ethanol, the wires were annealed at 800 °C for 8 h and then slowly (over another 8 h) cooled to room temperature. These annealed wires were then electrochemically etched in HCl (aq. 37%). For etching, rectangular voltage pulses with a frequency of 3 kHz and a duty cycle of 10% were applied between the wire and a platinum ring serving as the counter electrode. The tip shape was inspected by scanning electron microscopy.

Generation of synchronized dual-colour ultrafast pulses. Spectrally tunable, few-cycle VIS and NIR pulses were generated by two non-collinear optical parametric amplification (NOPA) stages followed by difference frequency generation (DFG). Such pulses are derived from a Ti:sapphire regenerative amplifier (Newport, spitfire pro) with a pulse energy of 0.5 mJ, duration of 120 fs, repetition rate of 5 kHz and centre wavelength of 800 nm. The output of one of the NOPA stages directly serves as the source of 600-nm VIS pulses in the dual-colour pump-probe scheme, while DFG between the output pulses from these two NOPA stages delivers the 1600-nm NIR pulses.

The output pulses of the Ti:sapphire amplifier were split into three parts to form the pump sources for white-light generation and, after frequency doubling, for the two NOPA stages. White light was generated in a 2-mm thick sapphire plate and split into two parts, each part overlapping with a pump pulse in one of the NOPA stages. Each NOPA stage consisted of a 1-mm thick, type I beta-barium borate (BBO) crystal cut to sustain amplification from 540 nm to 650 nm (for the VIS pulses), and from 870 nm to 890 nm, respectively. Both output pulses were collinearly aligned and temporally overlapped in a 0.3-mm thick, type-II cut BBO crystal to generate the DFG (NIR pulses). After the DFG stage, the VIS pulses and the NIR pulses were separated using a dichroic mirror, and all other unwanted residual spectral components were suppressed using filters. The polarization of the two pulses was then adjusted and their temporal distance controlled, before they were collinearly overlapped using a second dichroic mirror and focussed onto the gold tapers using an all-reflective Cassegrain objective.

Recording of electron kinetic energy spectra. Electrons emitted from the tip were monitored with a photoelectron spectrometer (Specs Phoibos 100) aligned along the tip axis. Electrons are energetically dispersed in a hemispherical electrostatic field and detected by a multi-channel plate (MCP) followed by a phosphor screen and a two-dimensional CCD camera. The counts on the CCD camera were integrated over one dimension and normalized to yield the kinetic energy spectra in units of electron counts per eV.

To acquire the four kinetic energy spectra shown in Fig. 1f, the tip apex was illuminated with temporally overlapped VIS and NIR pulses, with a VIS pulse energy of 0.75 nJ and an NIR pulse energy varied between 0.12 nJ and 0.30 nJ. The CCD camera integration time was set to 100 ms and for each NIR pulse energy, 300 individual spectra were recorded. Of these 300 spectra, 50 were selected manually and added together, constituting the blue symbols in Fig. 1f. The red curve plotted together with these experimental data are the measurements low-pass filtered using a 6th order Butterworth filter with a cutoff frequency of $(0.41\ \mathrm{eV})^{-1}$.

References

1 Agostini, P., Fabre, F., Mainfray, G., Petite, G. & Rahman, N. K. Free-free transitions following 6-photon ionization of Xenon atoms. *Phys. Rev. Lett.* **42**, 1127-1130 (1979).

2 Freeman, R. R. *et al.* Above-threshold ionization with subpicosecond laser pulses. *Phys. Rev. Lett.* **59**, 1092-1095 (1987).

3 Paulus, G. G., Nicklich, W., Xu, H. L., Lambropoulos, P. & Walther, H. Plateau in above-threshold ionization spectra. *Phys. Rev. Lett.* **72**, 2851-2854 (1994).

4 Corkum, P. B. Plasma perspective on strong-field multiphoton ionization. *Phys. Rev. Lett.* **71**, 1994-1997 (1993).

5 Paul, P. M. *et al.* Observation of a train of attosecond pulses from high harmonic generation. *Science* **292**, 1689-1692 (2001).

6 Popmintchev, T. *et al.* Bright Coherent Ultrahigh Harmonics in the keV X-ray Regime from Mid-Infrared Femtosecond Lasers. *Science* **336**, 1287-1291 (2012).

7 Hentschel, M. *et al.* Attosecond metrology. *Nature* **414**, 509-513 (2001).

8 Krausz, F. & Ivanov, M. Attosecond physics. *Rev. Mod. Phys.* **81**, 163-234 (2009).

9 Ropers, C., Solli, D. R., Schulz, C. P., Lienau, C. & Elsaesser, T. Localized multiphoton emission of femtosecond electron pulses from metal nanotips. *Phys. Rev. Lett.* **98**, 043907 (2007).

10 Herink, G., Solli, D. R., Gulde, M. & Ropers, C. Field-driven photoemission from nanostructures quenches the quiver motion. *Nature* **483**, 190-193 (2012).

11 Piglosiewicz, B. *et al.* Carrier-envelope phase effects on the strong-field photoemission of electrons from metallic nanostructures. *Nature Photon.* **8**, 37-42 (2014).

12 Krueger, M., Schenk, M. & Hommelhoff, P. Attosecond control of electrons emitted from a nanoscale metal tip. *Nature* **475**, 78-81 (2011).

13 Schenk, M., Krueger, M. & Hommelhoff, P. Strong-Field Above-Threshold Photoemission from Sharp Metal Tips. *Phys. Rev. Lett.* **105**, 257601 (2010).

14 Chulkov, E. V., Silkin, V. M. & Echenique, P. M. Image potential states on metal surfaces: binding energies and wave functions. *Surf. Sci.* **437**, 330-352 (1999).

15 Echenique, P. M. & Pendry, J. B. Existence and detection of Rydberg state at surfaces. *J. Phys. C: Solid State Physics* **11**, 2065-2075 (1978).

16 Hofer, U. *et al.* Time-resolved coherent photoelectron spectroscopy of quantized electronic states on metal surfaces. *Science* **277**, 1480-1482 (1997).

17 Niikura, H. *et al.* Sub-laser-cycle electron pulses for probing molecular dynamics. *Nature* **417**, 917-922 (2002).

18 Paulus, G. G. *et al.* Measurement of the phase of few-cycle laser pulses. *Phys. Rev. Lett.* **91**, 253004 (2003).

19 Ghimire, S. *et al.* Observation of high-order harmonic generation in a bulk crystal. *Nature Phys.* **7**, 138-141 (2011).

20 Hohenleutner, M. *et al.* Real-time observation of interfering crystal electrons in high-harmonic generation. *Nature* **523**, 572-575 (2015).

21 Aeschlimann, M. *et al.* Observation of surface-enhanced multiphoton photoemission from metal-surfaces in the short-pulse limit. *J. Chem. Phys.* **102**, 8606-8613 (1995).

22 Bisio, F., Nyvlt, M., Franta, J., Petek, H. & Kirschner, J. Mechanisms of high-order perturbative photoemission from Cu(001). *Phys. Rev. Lett.* **96**, 087601 (2006).

23 Gulde, M. *et al.* Ultrafast low-energy electron diffraction in transmission resolves polymer/graphene superstructure dynamics. *Science* **345**, 200-204 (2014).

24 Vogelsang, J. *et al.* Ultrafast Electron Emission from a Sharp Metal Nanotaper Driven by Adiabatic Nanofocusing of Surface Plasmons. *Nano Lett.* **15**, 4685-4691 (2015).

25 Feist, A. *et al.* Quantum coherent optical phase modulation in an ultrafast transmission electron microscope. *Nature* **521**, 200-203 (2015).

26 Fauster, T. & Steinmann, W. Two-photon photoemission spectroscopy of image states. *Electromagnetic Waves: Recent Developments in Research* **2**, 347-411 (1995).

27 Bormann, R., Gulde, M., Weismann, A., Yalunin, S. V. & Ropers, C. Tip-Enhanced Strong-Field Photoemission. *Phys. Rev. Lett.* **105**, 147601 (2010).

28 Marks, M., Schwalb, C. H., Schubert, K., Gudde, J. & Hofer, U. Quantum-beat spectroscopy of image-potential resonances. *Phys. Rev. B* **84**, 245402 (2011).

29 Wahl, P., Schneider, M. A., Diekhoner, L., Vogelgesang, R. & Kern, K. Quantum coherence of image-potential states. *Phys. Rev. Lett.* **91**, 106802 (2003).

30 Park, D. J. *et al.* Strong Field Acceleration and Steering of Ultrafast Electron Pulses from a Sharp Metallic Nanotip. *Phys. Rev. Lett.* **109**, 244803 (2012).

31 Muller, M., Paarmann, A. & Ernstorfer, R. Femtosecond electrons probing currents and atomic structure in nanomaterials. *Nature Commun.* **5**, 5292 (2014).

Acknowledgments: We acknowledge financial support by the Deutsche Forschungsgemeinschaft (SPP1391, SPP1839, SPP 1840, and DFG-NSF Materials World Network), by the European Union (project “CRONOS”, grant number 280879-2), the European Research Council (ERC-2010-AdG-267374), the Academy of Finland, the FinnishIT Center for Science for computational resources CSC, Spanish grant (FIS2013-46159-C3-1-P), Groupos Consolidados (IT578-13), and the Korea Foundation for International Cooperation of Science and Technology (Global Research Laboratory project, K20815000003). J.V., J.R., B.N., and P.D. acknowledge personal grants from the Studienstiftung des Deutschen Volkes, the Deutsche Forschungsgemeinschaft (GRK 1885), the German Academic Exchange Service (IPID4all program), the Hungarian Academy of Sciences (“Lendelüt” grant), the Campus Hungary program, and the Stiftung der Metallindustrie im Nord-Westen.

Author Contributions: C.L. initiated the project. J.R. and J.V. implemented the set-up, J.R., J.V., and B.N. carried out the experiments. J.R., P.G., and C.L. evaluated the data and implemented the TDSE model. J.S., P.W., U.D.G., E.R., and A.R. developed the DFT simulation model. J.R., J.S., P.W., P.D., C.L., and P.G. prepared the manuscript. All authors contributed to the final version of the manuscript.

Competing Financial Interests Statement: The authors declare no competing financial interests.

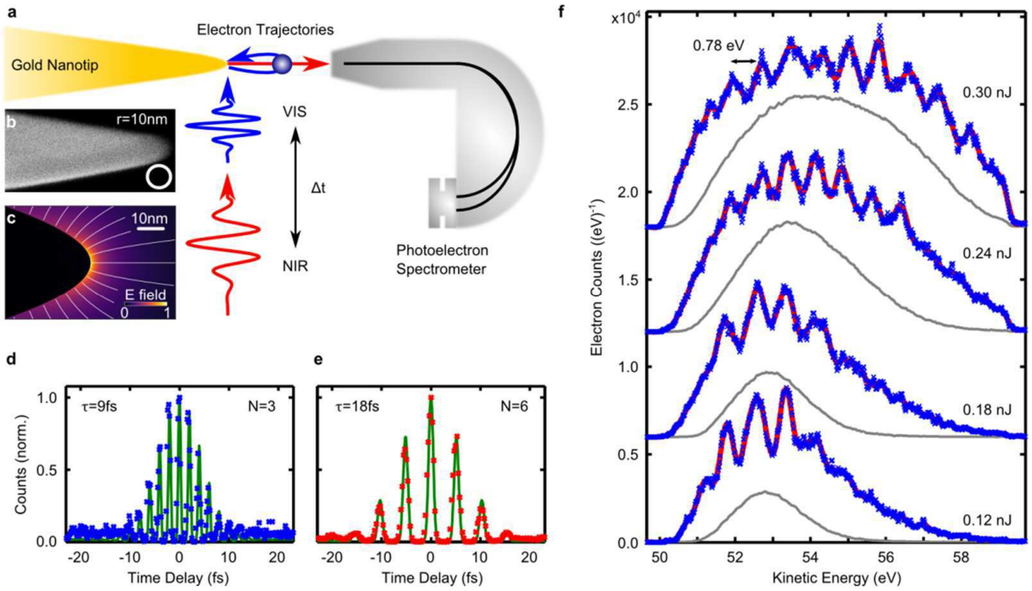

Figure 1. Two-colour photoemission from a gold nanotaper. a, A single gold nanotip is illuminated with a visible (VIS) and a time-delayed near-infrared (NIR) femtosecond laser pulse. Kinetic energy spectra of the photoemitted electrons are recorded. **b,** Scanning electron microscope (SEM) image of a nanotip with ~10 nm radius and **c,** calculated localized near-field at its apex. **d** and **e,** Interferometric autocorrelation traces, probing non-linear one-color photoelectron (PE) emission from the taper apex with VIS (blue dots) and NIR (red dots) excitations. The solid lines are simulations with different orders *N* of the optical nonlinearity, indicating pulse durations of 9 fs and 18 fs, respectively. **f,** Two-colour photoelectron (PE) kinetic energy spectra (blue symbols) recorded in the time overlap of orthogonally polarized few-cycle VIS and NIR pulses, showing a comb-like series of emission peaks as a signature of strong-field photoemission from discrete bound states. With increasing NIR laser intensity up to 12 ATI peaks separated by the NIR photon energy are observed. The red lines are low-pass-filtered guides to the eye. The grey lines shows corresponding two-colour PE spectra recorded for an interpulse delay of 500 fs.

(187 words)

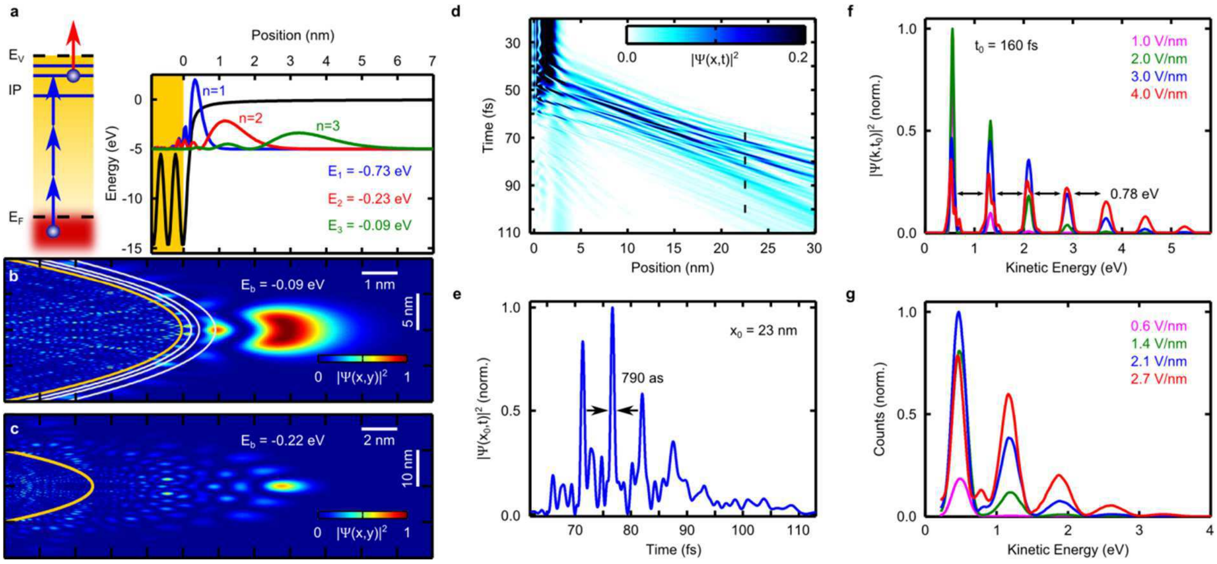

Figure 2. Theoretical modelling of strong-field photoemission from surface states localized to a gold nanotip. a, Schematic energy diagram for weakly bound image potential (IP) states. The probability densities and binding energies E_B of the three lowest IP states are depicted with the effective potential in black[14]. **b,** Probability density of IP state $n=3$ with $E_B=$ 0.1 eV in a 2D model potential. The state is mostly localized outside of the nanotip, with its borders in brown. White: Equipotential lines of the Coulomb potential. **c,** As in b, for a selected excited Kohn-Sham state calculated from a 2D DFT model. **d,** Time evolution of an electron wave packet, initially prepared in state n = 2 and driven by a strong, 25-fs NIR laser pulse. **e,** Time evolution of the electron density at a position $x_0=$ 22.5 nm (dashed line in d), showing the release of a sub-fs electron pulse train. **f,** Kinetic energy spectra of the released wavepacket at t = 160 fs, revealing distinct ATI peaks spaced by the NIR photon energy. **g,** Kinetic energy spectra from the DFT model display ATI peaks for similar field strengths as in f.

(184 words)

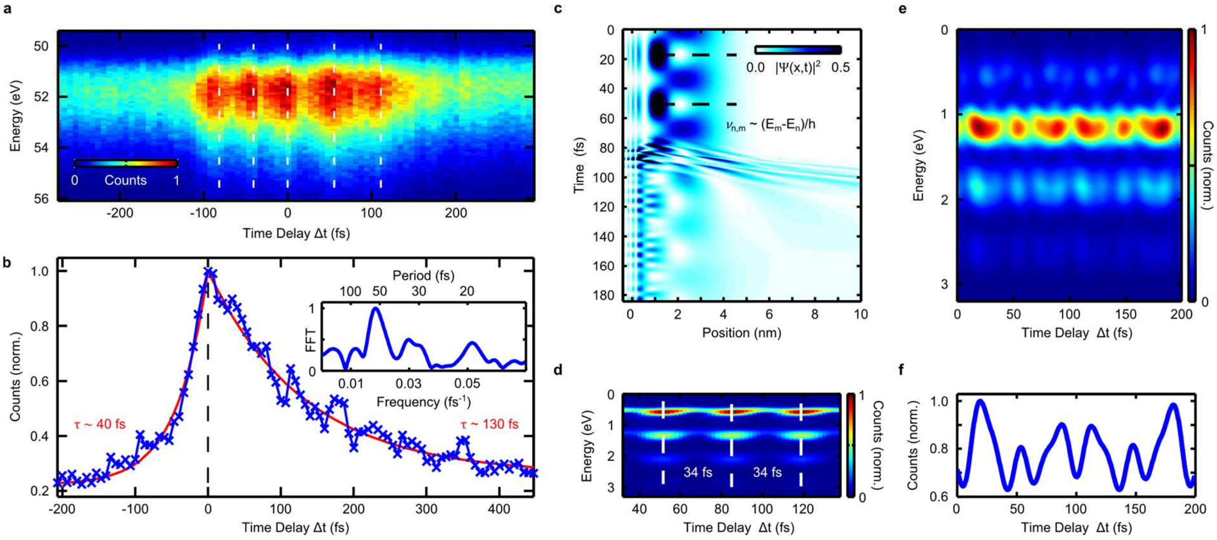

Figure 3. Quantum beats in the dynamics of long-lived surface states localized to a gold nanotip. a, Photoelectron spectra from a single gold nanotip as a function of time delay Δt between orthogonally polarized VIS and NIR excitation pulses. Photoemission persists for more than 150 fs and shows an oscillatory beating with dominant periods of 54 fs for positive (VIS precedes NIR) and 39 fs for negative delays, respectively. These are signatures for multiphoton excitation of discrete, long-lived IP states of the gold tip. **b,** Time-dependence of two-colour photoemission yield. The decay time of 130 fs (40 fs) for negative (positive) delays suggests predominant population of the $n = 3$ ($n = 2$) IP state. Inset: Beating periods at negative delays. **c,** 1D TDSE simulation showing the strong-field photoionization of a wavepacket initially prepared in a superposition of the $n = 2$ and $n = 3$ states and driven by strong 10-fs NIR laser pulse. **d,** Resulting time-dependent PE spectra, modulated by a similar beating as observed experimentally. **e,** Time-dependent PE spectra deduced from the DFT SAE model when preparing a coherent superposition of four weakly bound IP states. **f** Cross-section through e at an energy of 2 eV, showing the resulting multiperiod beating pattern.

(203 words)

Supplementary Information for

Strong-Field Above-Threshold Ionization of Rydberg Electrons Localized to a Single Gold Nanotip

Jörg Robin, Jan Vogelsang, Janne Solanpää, Philipp Wopperer, Umberto De Giovannini, Benedek J. Nagy, Péter Dombi, Esa Räsänen, Angel Rubio, Christoph Lienau, Petra Groß

correspondence to: christoph.lienau@uni-oldenburg.de, petra.gross@uni-oldenburg.de

Contents:

A Materials and Methods
A1 Experimental setup, nanotip preparation, and measurement method
A2 Numerical model: Time-dependent Schrödinger equation
A3 Numerical model: DFT with a single active electron

B Supplementary Information
B1 Additional measured kinetic energy spectra
B2 Eigenstates and wavefunctions of 1D-TDSE and 2D-SE

Captions for Movie S1

A Materials and Methods

A1 Experimental setup, nanotip preparation, and measurement method

A1.1 Generation of synchronized dual-colour femtosecond pulses

In our experiments, few-cycle pulses at centre wavelengths of 600 nm and 1600 nm, termed VIS and NIR, respectively, are used for the excitation and probing of image potential states localized to a sharp gold nanotaper. Such pulses are derived from a regenerative Ti:sapphire amplifier (Spectra Physics Spitfire) with a repetition rate of 5 kHz. They are generated in two non-collinear optical parametric amplifier (NOPA) stages, which are seeded by the same white light. The output of one of the NOPA stages (NOPA#1) directly serves as a source of VIS pulses in our two-colour pump-probe scheme. Subsequently, difference frequency generation (DFG) between the output pulses from these two NOPA stages delivers the NIR pulses.

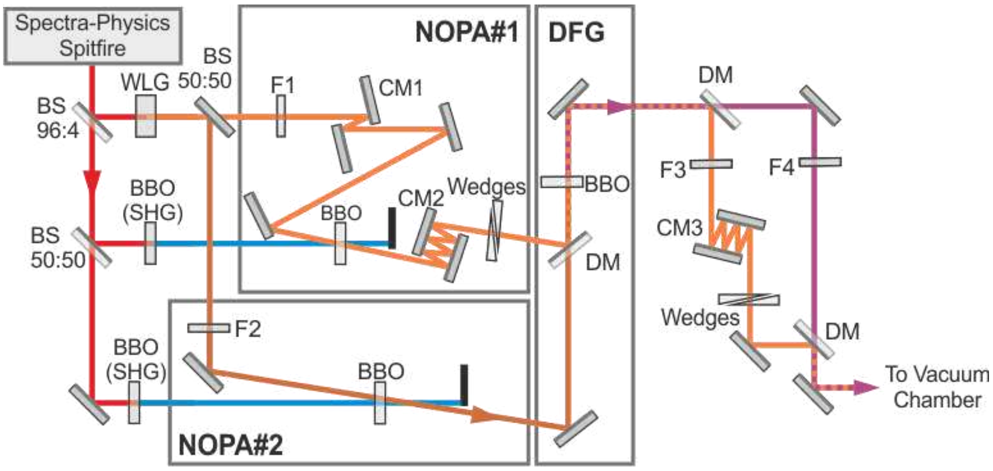

Fig. S1. Experimental setup of the laser system. The system is based on pulse generation in two NOPA stages (NOPA#1, NOPA#2), which are seeded by the same white light generation (WLG) source and subsequent difference frequency generation (DFG) of the two pulse trains. Filters F1 and F2 are used to select the spectral ranges for the two NOPA stages. The VIS pulses are compressed before and after NOPA#1 by chirped mirror pairs (CM1 and CM2, respectively). After DFG, the VIS and the NIR pulses are separated by a dichroic mirror (DM), residual unwanted frequency components are removed by a silicon plate (F3) and a long-pass filter (F4), and the VIS pulses are again recompressed (CM3). Finally, the VIS and NIR pulse trains are temporally adjusted and overlapped again by a dichroic mirror before the vacuum chamber containing the gold nanotip.

The first NOPA stage (NOPA#1) supports amplification of a broad spectral range from 530 nm to 640 nm (see spectrum in Fig. S2a) and yields a pulse energy of about 3.6 µJ. The pulses are compressed using chirped mirrors and the pulse duration is measured by interferometric autocorrelation using the electron yield from illumination of the sharp gold tapers. These measurements, shown in Fig. 1d of the main document, indicate a nearly transform-limited pulse duration of 9 fs.

The seed for the second NOPA stage (NOPA#2) is filtered to a narrow bandwidth of 10 nm, centred at 890 nm. The output pulses of both NOPA stages are spatially and temporally overlapped in a third BBO crystal cut for DFG. With the fixed, narrow-bandwidth output of NOPA#2, the wide bandwidth of NOPA#1 is directly transferred to the NIR by the DFG process. The DFG process supplies pulses of up to 110 nJ energy with a bandwidth in excess of 500 nm centred at 1600 nm (Fig. S2b). After compression, we measure a pulse duration of 18 fs by interferometric autocorrelation using the electron yield of the gold nanotaper (shown in Fig. 1e of the main text).

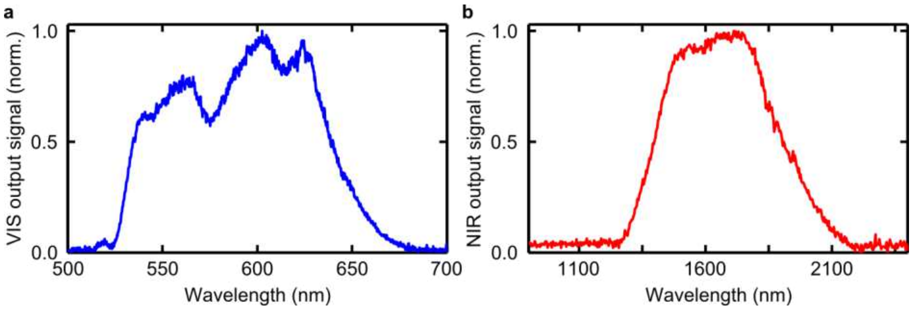

Fig. S2. Measured spectra of the VIS and NIR laser pulses. a. The output spectrum of the NOPA#1 stage spans a spectral range from 530 to 640 nm. **b.** The output spectrum of the DFG stage reaches from 1400 to >1900 nm. The detected wavelength range is limited at long wavelengths by the spectral response of the spectrometer.

Since the two NOPA stages are seeded by the same WL, they inherently share the same carrier-envelope phase (CEP). Thus, by DFG of the two NOPA output pulse trains, the resulting NIR pulses are passively CEP-stabilized[1,2]. We have previously demonstrated a shot-to-shot CEP RMS noise of about 800 mrad as well as an excellent long-term CEP stability of this source of better than 50 mrad over time spans up to 20 minutes, when averaging over 100 pulses[3].

A1.2 Production of sharp gold nanotips and plasmonic properties

The single-crystalline gold nanotips were fabricated from polycrystalline gold wires (99.99%) with a diameter of 125 µm (commercially available from Advent Research Materials). After cleaning in ethanol, the wires were annealed at 800 °C for 8 h and then slowly over another 8 h cooled to room temperature. These annealed wires were then electrochemically etched in HCl (aq. 37%). For etching, rectangular voltage pulses with a frequency of 3 kHz and a duty cycle of 10% were applied between the wire and a platinum ring serving as the counter electrode. The tip shape was inspected by scanning electron microscopy.

In the following, we give estimates for the electric field strengths that drive electron emission at the apex of the nanotaper. For this, we measured the order of nonlinearity of the photoemission process at the respective laser wavelengths of VIS and NIR pulses and the focus diameter, which is explained briefly in the following paragraphs.

The nanotips were side-illuminated with a sequence of VIS and NIR pulses incident at an angle of 90° with respect to the tip axis. The VIS pulse was linearly polarized perpendicular to the tip axis, while the linear polarization of the NIR pulse was chosen along the tip axis. The laser repetition rate was 5 kHz and the pulses were focused onto the tip using an all-reflective Cassegrain objective with 0.5 numerical aperture (NA), which transmitted about

30% of the incident light. Further pulse characterization, as the pulse duration measurement shown in Figs. 1d and e in the main document and the determination of the focus diameter and electric field strength at the tip apex were carried out directly using the photoemission yield of electrons from the nanotip. In order to use the yield as measure for intensity, we first determined the order of nonlinearity of the photoemission process for the VIS and the NIR pulse.

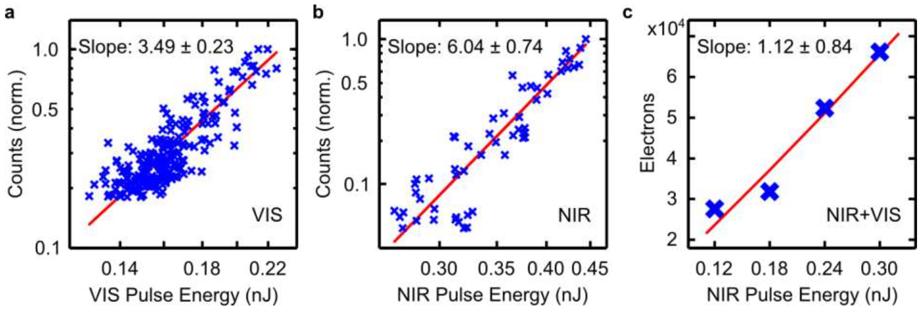

Fig. S3. Order of nonlinearity of the photoemission from the gold nanotip. The blue crosses show the measured electron count as a function of pulse energy incident on the nanotip on a double logarithmic scale. The red lines are linear fit functions to determine the slope. **a.** When illuminating the tip solely with the VIS pulses with a centre wavelength of 600 nm, the electron count increases with the pulse energy with the nonlinear order of 3.5, yielding a nonlinearity of $N_{VIS} = 3.5$. **b.** Same for tip illumination with the NIR pulse centred at a wavelength of 1600 nm, yielding a nonlinearity $N_{NIR} = 6.0$. **c.** When illuminating the tip with a combination of VIS and NIR pulses arriving simultaneously, and keeping the VIS pulse energy constant at 0.75 nJ, the dependence of the electron yield on the NIR pulse energy decreases to a nonlinearity $N_{NIR} = 1.1$.

The results of these measurements are shown in Fig. S3. For three different cases, we varied the pulse energy incident on the gold nanotip and measured the electron yield. First, the tip was illuminated with VIS laser pulses. The average laser power was varied between 2 µW and 3.7 µW, measured in front of the vacuum chamber. With the laser repetition rate of 5 kHz and the Cassegrain objective transmission, this translates to a pulse energy between 0.12 nJ and 0.22 nJ at the gold nanotip. The measured electron yield varies over almost one order of magnitude (crosses in Fig. S3a), and linear regression reveals a dependence of photoemission with roughly the VIS pulse energy to the order $N_{VIS} = 3.5$ (red line in Fig. S3a). Repeating the measurement with illumination by only the NIR pulses leads to a nonlinearity of $N_{NIR} = 6.0$ (Fig. S3b). For the measurements shown in Fig. 1f, the nanotip was illuminated with VIS and NIR pulses arriving simultaneously. Here the VIS power was set to the precise onset of photoemission, which for this tip was reached for an average power of 12.5 µW, measured in front of the vacuum chamber, and correspondingly for a pulse energy of 0.75 nJ at the nanotip. Keeping the VIS pulse energy constant and increasing the NIR pulse energy, a dependence of photoemission yield on the NIR pulse energy with nonlinearity $N_{NIR} = 1.1$ was measured (Fig. S3c).

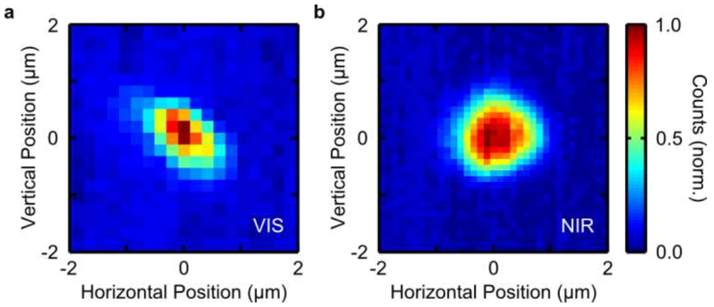

Fig. S4. Focus spot sizes of the VIS and NIR laser pulses. a. The intensity profile of the VIS pulse focus was measured by raster-scanning the nanotip through the focus. The electron count rate, measured as a function of nanotip position, is proportional to the laser intensity to the power of the nonlinearity of the electron emission process, i. e., $I(x,y)^{3.5}$, and yields a beam diameter at the focus of $w_{VIS} = 1.7\,\mu m$. **b.** Same as A, but for the NIR laser pulse. Here the nonlinearity is $N = 6$, yielding a beam diameter at the focus of $w_{NIR} = 2.9\,\mu m$.

The beam diameter at the focus was determined for both the VIS and the NIR pulses by raster-scanning the nanotip through the focus created by the Cassegrain objective and by measuring the electron yield. The electron yield as a function of the nanotip position is shown for illumination with the VIS pulse in Fig. S4a. The FWHM diameter of the electron image is $0.92\,\mu\mathrm{m}$, which, taking into account the previously determined nonlinearity of the process $N_{VIS} = 3.5$, yields the focus diameter (intensity FWHM) $w_{VIS} = 1.7\,\mu\mathrm{m}$. The same measurement carried out with nanotip illumination by the NIR pulse (Fig. S4b) gives a diameter of $1.2\,\mu\mathrm{m}$ of the electron image. With the higher nonlinearity $N_{NIR} = 6.0$ this results in a NIR focus diameter of $w_{NIR} = 2.9\,\mu\mathrm{m}$.

For the VIS pulses, with the incident pulse energy of 0.75 nJ at the tip and with a measured pulse duration of 9 fs and a focus diameter of 1.7 µm (temporal and spatial intensity FWHM, respectively) this yields a peak electric field strength of $E_0 = 4.2\,\mathrm{V/nm}$ or a peak intensity of the incident pulse of $I_0 = 2.4\,\mathrm{TW/cm^2}$. This intensity was chosen to be sufficiently low to avoid significant photoemission of electrons by the VIS pulse alone.

The NIR average power as measured in front of the vacuum chamber was varied between 2 and 5 µW, translating into a pulse energy of 0.12 to 0.30 nJ at the nanotip. The pulse duration was measured to be 18 fs FWHM, and the focus diameter was 2.9 µm. With these values we determine the peak electric field strength to be between $E_0 = 0.7\,\mathrm{V/nm}$ and $E_0 = 1.1\,\mathrm{V/nm}$. Taking into account a field enhancement factor of $f = 9$,[4] this results in values between $f \cdot E_0 = 6.5\,\mathrm{V/nm}$ and $f \cdot E_0 = 10\,\mathrm{V/nm}$. Accordingly, the (enhanced) peak intensity is varied between $f^2 \cdot I_0 = 5.5\,\mathrm{TW/cm^2}$ and $f^2 \cdot I_0 = 14\,\mathrm{TW/cm^2}$.

To confirm that the NIR pulse parameters enable the transition from multi-photon to the strong-field regime, we calculate the Keldysh parameter γ, which decreases to values $\gamma < 1$ when the multi-photon to tunnel transition occurs[5-7]:

$$\gamma = \sqrt{\frac{\Phi}{2U_P}}\,. \tag{1}$$

Here $\Phi = 5.5\,\mathrm{eV}$ is the work function of gold[8,9], and U_P is the ponderomotive energy,

$$U_P = \frac{e^2 \cdot f^2 \cdot E^2}{4 m_e \omega^2}, \tag{2}$$

where e is the charge and m_e the mass of the electron, and ω the laser field oscillation frequency. For the lowest electric field strength, this gives a Keldysh parameter above unity, $\gamma = 1.5$, and for the highest electric field strength just below, $\gamma = 0.94$. However, the situation changes drastically if we consider electron emission not from the Fermi level, but from a high-lying, weakly bound surface state. For example, assuming $E_b = 0.85\,e\mathrm{V}$ as was found for the $n = 1$ Rydberg state on extended gold surfaces, we derive a Keldysh parameter in the range from $\gamma = \sqrt{E_b / \left(2U_P\right)} = 0.59$ down to $\gamma = 0.37$, i. e., well below unity for all applied pulse energies. Hence preparation of such surface states gives easy access to the study of strong-field effects presented in the main text.

A1.3 Acquisition of electron kinetic energy spectra

Electrons emitted from the tip were monitored with a photoelectron spectrometer (PES, Specs Phoibos 100) aligned along the tip axis. Electrons are energetically dispersed in a hemispherical electrostatic field and detected by a multi-channel plate (MCP) followed by a phosphor screen and a two-dimensional CCD camera. The PES is operated in a medium magnification mode, spreading the incoming electrons on the CCD screen according to their kinetic energy along the x-(energy-) axis and according to their vertical impact position on the entrance slit of the spectrometer along the y-axis.

To extract the kinetic energy spectra, the images of the CCD camera are processed as follows. We record the counts of each pixel over a region of interest of 870 by 800 pixels, $S_{i,j}$, where *i* denotes the pixel number along the energy axis and *j* the pixel number along the y-axis. After subtracting a small, constant background signal from each pixel, the counts are added together over the y-axis, yielding the counts on the CCD as a function of energy: $S_i' = \sum_{j=1}^{800} S_{i,j}$. Typically these are 870 values that span an energy interval of 12.5 eV with adjustable centre energy. One pixel thus corresponds to an energy interval ΔE of 14.4 meV.

To calibrate the counts on the CCD camera, we have analysed the images of 50 single electrons that were incident on the MCP. An example of such a single electron measurement is shown in Fig. S5. The counts on the CCD camera, $S_{i,j}$ (Fig. S5a), appear as a roughly circular feature with a maximum count of $S_{i,j}^{\max} = 26$ and a diameter (full width of half maximum) of about 3 pixels. The distribution S_i' for this example electron is shown in Fig. S5b. It has a maximum value of 84 and a width of 3.6 pixels or 52 meV. The total count for this electron is $S'' = \sum_{i,j} S_{i,j} = 306$.

The distribution of counts on the CCD, $S_{i,j}$, can be well approximated by a continuous Gaussian distribution as function on the x- and y-axis $S\left(x, y\right)$:

$$S\left(x, y\right) = S_{\max} \cdot e^{-4\ln 2 \frac{x^2}{w_x^2}} \cdot e^{-4\ln 2 \frac{y^2}{w_y^2}} \tag{3}$$

where $S_{\max}$ is the average maximum count, $S_{\max} = \bar{S}_{i,j}^{\max} = 21.5$, and $w_x = 3.05$ and $w_y = 3.04$ are the average FWHM in the x- and the y-direction, respectively. These numbers have been determined by fitting a Gaussian distribution to each of the 50 electrons individually and by averaging over the obtained fitting parameters. For the projection onto the x-axis, we obtain

$$S'(x) = \int_{y=-\infty}^{\infty} S(x,y)\,dy = S'_{\max} \cdot e^{-4\ln 2 \frac{x^2}{w_x^2}} \tag{4}$$

with $S'_{\max} = S_{\max} \cdot \frac{\sqrt{\pi}}{\sqrt{4\ln 2}} w_y = 69.6$. With the energy interval of a pixel $\Delta E = 14.4\,\mathrm{m}e\mathrm{V}$ the width on the x-axis of $w_x = 3.05$ corresponds to a kinetic energy spread of a single electron of 44 m*e*V, which we can take as a lower limit for the energy resolution in our measurements.

The area under the Gaussian distribution Eq. 4 corresponds to the total counts on the CCD for a single electron: $S'' = \int_{-\infty}^{\infty} S'(x)\,dx = S'_{\max} \cdot \frac{\sqrt{\pi}}{\sqrt{4\ln 2}} w_x = 226$. This is in very good agreement with the total number of counts derived by summing up the counts on the CCD camera for each individual electron (see histogram in Fig. S5c). The measured kinetic energy spectra have been renormalized by dividing the measured counts on the CCD camera by division by $S'' = 226$. This results in a conversion of the counts on the CCD camera into electron counts per eV, such that integration over the energy axis directly gives the number of detected electrons (right axis in Fig. S5b). Throughout the manuscript and these supplementary materials, kinetic energy spectra are displayed as electron counts per eV. All kinetic energy spectra shown in the main manuscript or in the supplementary text are experimental data that have been treated as described above and that have not been filtered further.

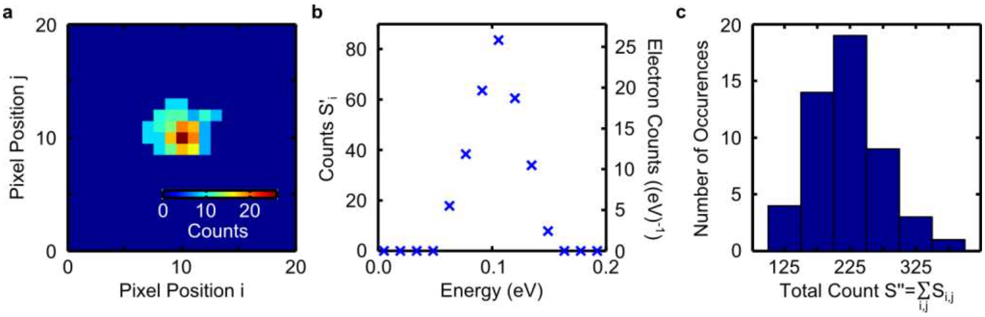

Fig. S5. Measured counts of single electrons. a. Representative signature of a single electron on the phosphor screen, as imaged by the CCD camera. The maximum count on the center pixel is in this case 26. **b.** Adding together the counts on the CCD camera over the axis perpendicular to the energy axis yields the counts as a function of energy, peaking at 84 and with a width of 3.6 pixels or 52 eV. **c.** The histogram of the total counts of 50 single electrons has its maximum at 225 counts.

To acquire the four kinetic energy spectra shown in Fig. 1f, the tip apex was illuminated with temporally overlapped VIS and NIR pulses, with a VIS pulse energy of 0.75 nJ and an NIR pulse energy varied between 0.12 nJ and 0.30 nJ. The camera integration time was set to 100 ms and for each NIR pulse energy, 300 individual spectra were recorded.

The visibility of the modulation varies strongly for the individual spectra, which we mainly ascribe to the variation of the NIR pulse CEP for long measurement times (this is elaborated in more detail in Sec. B1.2). To visualize the modulation more clearly, 50 spectra were selected manually and added together. The result constitutes the experimental data shown as blue symbols in Fig. 1f. The red curve plotted together with the experimental measurements are the measurements low-pass filtered using a 6th order Butterworth filter with a cutoff frequency of $\left(0.41\,\mathrm{eV}\right)^{-1}$.

To determine the modulation contrast of the 50 added together experimental (unfiltered) spectra, background spectra were measured with the same pulse parameters and integration time, but with a large delay of 500 fs between the VIS and NIR pulses. These background spectra (shown as the grey curves in Fig. 1f) were subtracted from the measured spectra recorded with the respective NIR pulse energy, and the modulation contrast was determined as

$$K = \frac{S_{\max} - S_{\min}}{S_{\max} + S_{\min}} \tag{5}$$

with the maximum and the minimum electron count rates, $S_{\max}$ and $S_{\min}$, respectively.

A2 Numerical Model: Time-dependent Schrödinger Equation

A2.1 One-dimensional model

In the 1D time-dependent Schrödinger equation (1D TDSE) model, the nanotip is described as periodically arranged potential wells inside the metal that represent the ionic cores of the bulk metal, given by

$$V_C\left(x\right) = \Phi + \frac{V_C - \Phi}{2} \cdot \left[1 - \cos\left(\frac{2\pi}{d} x\right)\right], \qquad x \le \frac{d}{2}. \tag{6}$$

Here $\Phi = -5.5\,e\mathrm{V}$ is the Fermi level, taken as the work function of gold[8,9], and $V_C = -14.6\,e\mathrm{V}$ is the crystal potential [9]. The spacing between the potential wells is the nearest neighbour distance $d = a/\sqrt{2} = 0.29\,\mathrm{nm}$ in gold (FCC lattice with lattice constant $a = 407.82\,\mathrm{pm}$). The gold surface is defined by the last ionic core potential well, which is placed at $x = d/2$. For coordinates $x > d/2$ the potential is matched to a Coulomb-like potential that accounts for the image potential[9,10]:

$$V_C\left(x\right) = -\frac{1}{4}\frac{1}{4\pi\varepsilon_0}\frac{e^2}{x}, \qquad x > \frac{d}{2} \tag{7}$$

where e is the elementary charge and ε_0 is the permittivity of free space.

This stationary system is perturbed by a time-dependent potential V_E due to the pulsed, and spatially non-uniform, strong laser field $E\left(x,t\right)$:

$$V_E\left(x,t\right) = -exE\left(x,t\right) \tag{8}$$

The temporal function of the electric field is given by its oscillation with the carrier frequency ω under a Gaussian envelope with the intensity full width at half maximum τ. An electric field incident on a sharp metal nanotip is spatially strongly inhomogeneous, i. e., the electric field strength is locally enhancement due to the strongly curved tip apex. The enhanced field has its maximum at the surface and exponentially decreases with increasing distance down to its non-enhanced level. In total, the temporally and spatially varying electric field strength can be written

$$E(x,t)=\frac{1}{2}\left\{ f\cdot E_0\cdot e^{i(\omega t+\varphi_{CE})}\cdot e^{-2\ln 2\frac{t^2}{\tau^2}}\cdot e^{-\frac{(x-d/2)}{l_{nf}}}+c.c.\right\},\quad x\geq\frac{d}{2} \tag{9}$$

Here $f=9$ is the near-field enhancement factor due to the nanostructure[4], and E_0 is the maximum field strength of the incident laser pulse. For the near-field decay length we take $l_{nf}=3\,\text{nm}$, which has been determined experimentally earlier for such sharply etched tips[4]. The absolute phase of the electric field strength is determined by the carrier-envelope (CE) phase φ_{CE}. In the bulk material, the electric field is of opposite sign[11], but its penetration depth is very short, on the order of 1 Å. Furthermore, its absolute value is much smaller than outside the material, due to the large real part of the dielectric function of gold at a wavelength of 1600 nm: $\varepsilon_r=-123.02+12.259\,i$.[12] Here we have neglected this small electric field inside the bulk material and set $E(x,t)=0$ for $x<d/2$.

The time evolution of the wavefunction $\Psi(x,t)$ in this system is simulated by numerically solving the 1D-TDSE:

$$i\hbar\frac{\partial}{\partial t}\Psi(x,t)=-\frac{\hbar^2}{2m_e}\frac{\partial^2}{\partial x^2}\Psi(x,t)+V(x,t)\cdot\Psi(x,t) \tag{10}$$

with Planck's constant $\hbar$ and the electron mass m_e. The potential $V(x,t)=V_C(x)+V_E(x,t)$ is here the sum of the time-independent potential $V_C(x)$ as defined by Eqs. 6 and 7 inside and outside the material, respectively, and of the time-dependent potential $V_E(x,t)$ due to the action of the laser pulse as given in Eqs. 8 and 9.

The numerical integration of Eq. 10 is carried out by employing the Crank-Nicolson method[13] with a typical step size of $\Delta t=5.80\,\text{as}$. The spatial step size was chosen to be $\Delta x=37.6\,\text{pm}$ to obey the stability criterion $\Delta t<(\Delta x)^2/2$ in atomic units[13]. In addition we verified that the simulation did not show numerical artefacts by repeatedly varying both step sizes.

The simulation was implemented using MATLAB[14] and was typically carried out on a numerical grid of 4800 spatial by 27596 temporal elements, thereby spanning a length of 180 nm and a time interval of 160 fs. The maximum field strength of the laser pulse is set at $t=60\,\text{fs}$ to ensure that all significant cycles are well within the time frame of calculation. The spatial boundaries are fully reflective. However, the large number of grid elements together with an appropriate choice of the spatio-temporal starting point enables the electron wavefunction to propagate for 100 fs after the peak of the laser pulse without reaching the spatial grid boundary.

In the main document we show the temporal evolution of electron wavepackets under the influence of an NIR laser pulse simulated as described here in Figs. 2d and 3c. As a result of the of the laser pulse action the initial stationary wavefunction splits into a bound wavefunction and a freely propagating wavefunction. The temporal structure of the electron pulse is determined by calculating the absolute square of the wavefunction $\left|\Psi(x_{fixed},t)\right|^2$ at a fixed position $x_{fixed} \geq 10\,\text{nm}$, such that the bound and the free parts of the wavepacket are well separated (Fig. 2e of the main text). To extract the simulated photoelectron kinetic energy spectra the released electron wavepacket is Fourier transformed at a fixed time of $t_{fixed} = 160\,\text{fs}$, yielding the wavefunction as a function of momentum k:

$$\tilde{\Psi}\left(k, t_{fixed}\right) = \frac{1}{\sqrt{2\pi}} \int_{-\infty}^{\infty} \Psi\left(x, t_{fixed}\right) e^{-ikx}\, dx \tag{11}$$

Using $E_{kin} = \dfrac{\hbar^2 k^2}{2m_e}$ the probability density $\left|\tilde{\Psi}\left(k, t_{fixed}\right)\right|^2$ is plotted as a function of kinetic energy to represent kinetic energy spectra.

A2.2 Two-dimensional model potential and eigenstates

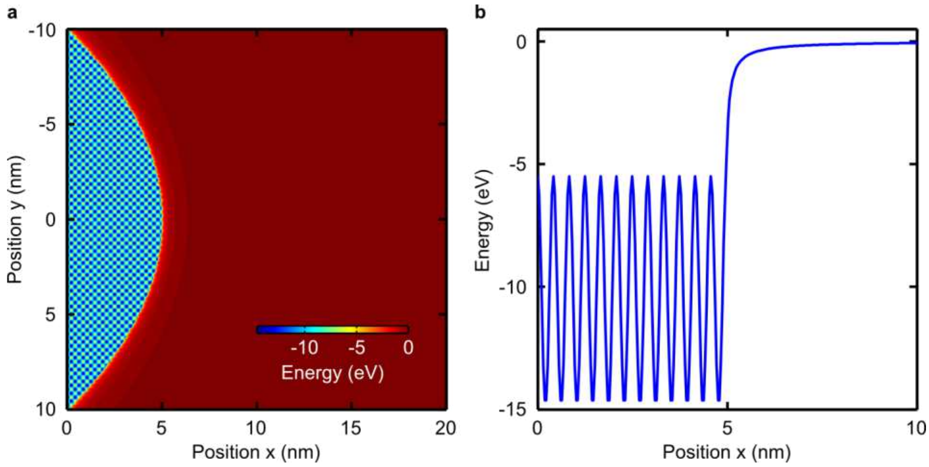

Fig. S6. Potential for 2D-SE simulations. a. Potential energy calculated for a two-dimensional array of ionic cores in a 2D fcc lattice **b.** The cut along the tip axis, for $x = 0$ resembles the potential assumed for the 1D-TDSE simulations with atomic spacing of the lattice constant a.

The wavefunctions and the binding energies of the eigenvalues were also numerically determined in 2D using the MATLAB software packet[14]. However, in 2D we only considered the stationary case:

$$E\Psi\left(x, y\right) = -\frac{\hbar^2}{2m_e}\left(\frac{\partial^2}{\partial x^2} + \frac{\partial^2}{\partial y^2}\right)\Psi\left(x, y\right) + V\left(x, y\right) \cdot \Psi\left(x, y\right). \tag{12}$$

To model the nanotip in two dimensions the periodic potential wells were expanded to a 2D array (see Fig. S6):

$$V_C\left(x, y\right) = \Phi + \frac{V_C - \Phi}{2} \cdot \left[1 - \cos\left(\frac{2\pi}{a} x\right) \cdot \cos\left(\frac{2\pi}{a} y\right)\right]. \tag{13}$$

Here the periodicity along the x- and the y-axis is the lattice constant a. Multiplication of the two cosine-functions results in a 2D fcc lattice structure with the nearest neighbour distance $d = a/\sqrt{2}$ along the diagonal. The 2D periodic potential is terminated by a hyperbolic surface [15], where it is matched to a Coulomb-like potential with isopotential lines parallel to the surface.

A3 Numerical Model: DFT with a single active electron

A3.1 2D Jellium ground-state

We describe the electronic ground state of the two-dimensional model by means of density-functional theory (DFT). In these calculations, the electron density of the many-body system is obtained from an auxiliary system of non-interacting fermions coupled to a one-body potential[16]. The single-particle equations are

$$\left[\frac{-\hbar^2}{2m}\nabla^2 + V_{\mathrm{KS}}(\vec{r})\right]\phi_i = \varepsilon_i \phi_i \tag{14}$$

with

$$V_{\mathrm{KS}}(\vec{r}) = V_{\mathrm{Ext}}(\vec{r}) + V_{\mathrm{Hartree}}[n](\vec{r}) + V_{\mathrm{XC}}[n](\vec{r}) \tag{15}$$

where ϕ_i are the single-particle orbitals in the Kohn-Sham potential V_{KS}, and ε_i are the corresponding auxiliary single-particle energies. The Kohn-Sham potential V_{KS} is a sum of three terms: V_{Ext} is an external potential describing the gold ions in the nanotip, V_{Hartree} is the Hartree potential formed by the electron density $n(\vec{r}) = \sum_{i=1}^{\#\,\text{of particles}} |\phi_i|^2$, and V_{XC} is the exchange-correlation potential which accounts for the many-body effects beyond the Hartree interaction. For V_{XC}, we use the local density approximation[17-19]. The binding potential V_{Ext} is described by the jellium model [see, e.g., Ref. 20], where the ionic background is smeared out to a constant positive background charge inside the tip with a smooth transition at the tip-vacuum interface. The shape of the nanotip is modelled by a hyperbola with apex radius of 7 nm and full opening angle of 20°. The background charge density is given by

$$\rho(x,y) = \left\{1 - \left[1 + \exp\left(-\frac{\frac{x^2}{a^2} - \left(\frac{y}{b}+1\right)^2 + 1}{\sigma_1}\right)\right]^{-1}\right\} \frac{1}{1 + \exp\left(-\frac{y^2 - L^2}{\sigma_2}\right)} \tag{16}$$

where x and y are the spatial coordinates; $a \approx 39.7\,\mathrm{nm}$ and $b \approx 225.1\,\mathrm{nm}$ define the hyperbola; $L = 28\,\mathrm{nm}$ is the simulated tip length; and σ_1, σ_2, and Δ are the softening parameters chosen as

$$\Delta = 3.18\,\mathrm{nm}$$

$$\sigma_1 = \frac{\Delta}{4b}, \text{ and}$$

$$\sigma_2 = \sigma_1 a^2.$$

The softening is introduced into the model to account for the expected Coulomb-like decay of the binding potential for the surface-state electrons.

The number of electrons, $N = 5350$, (and correspondingly the total charge of the jellium background) is chosen such that the work function of the simulated tip, i.e., the single-particle energy ε_i of the highest occupied Kohn-Sham orbital [see, e. g., Refs. 21-23], matches the negative of the measured work function of gold, 5.5 eV.[4,8]

The upper panel of Figure S7 shows an image of the electron density $n(\vec{r})$ derived from the Kohn-Sham orbitals (in orange). The typical Friedel oscillations of the electron density which can be observed, for instance, in steep jellium models [see, e.g., Ref. 20] are damped due to a smooth decay of the background charge at the tip-vacuum interface. In return, the Kohn-Sham potential V_{KS} decays like ${}^{1}\!/_{r}$ perpendicular to the surface, as shown in the lower panel of Fig. S7 for the apex direction.

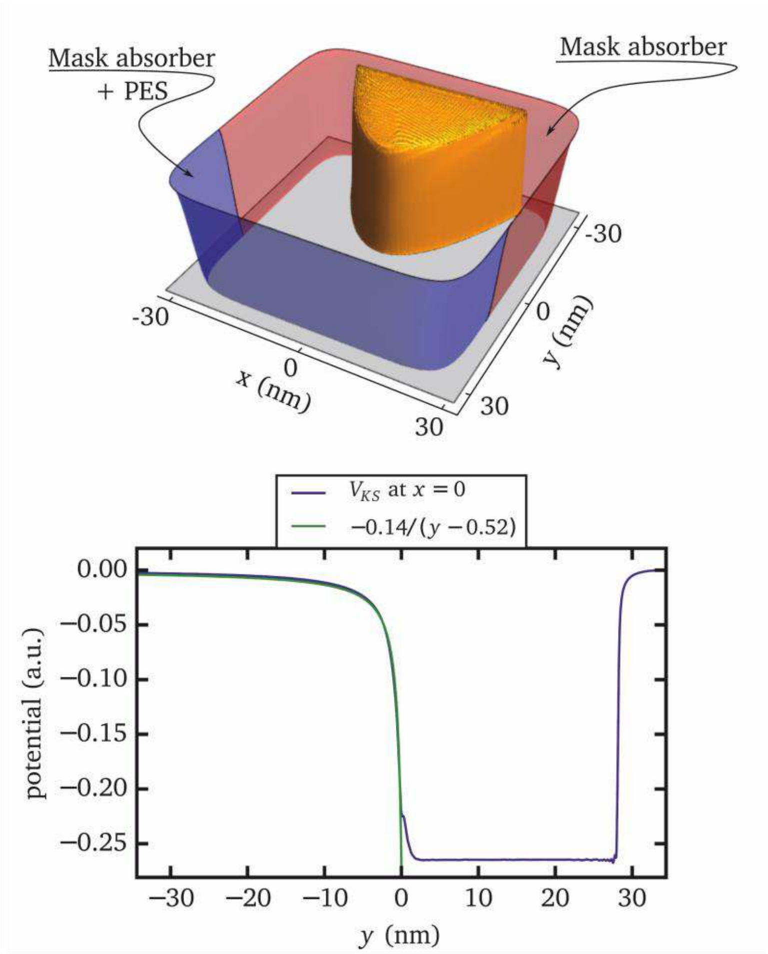

Fig. S7: Ground-state properties of the two-dimensional jellium model. Upper panel: Electron density (orange) showing damped Friedel oscillations. The regular mask absorbing boundary is shown in red, and the mask detecting the photoelectrons is shown in blue. Lower panel: A cut of V_{KS} along the taper axis (x=0) is Coulomb-like outside the nanotip.

A3.2 2D single-active electron model

Electron emission of surface states is modelled by a single-active electron (SAE) approach, where only one electron is propagated in the effective (Kohn-Sham) potential given by the many-body ground-state. The electron wavefunction is constructed as a superposition of 1–4 Kohn-Sham states with low binding energies (between 0.36 and 0.14 eV). The electron densities of the selected states are shown in Fig. S8. The states are chosen so that (1) there is a significant amount of the electron wavefunction outside the tip apex, (2) they have roughly equal coupling to the laser field, and (3) their energies match the experimentally observed beating frequencies. This construction of the initial state emulates the excitation by the VIS pulse arriving before the NIR pulse. We note that our choice of the single-particle states is not unique, but selecting other states (with significant part of the wavefunction outside the tip apex) yields similar results.

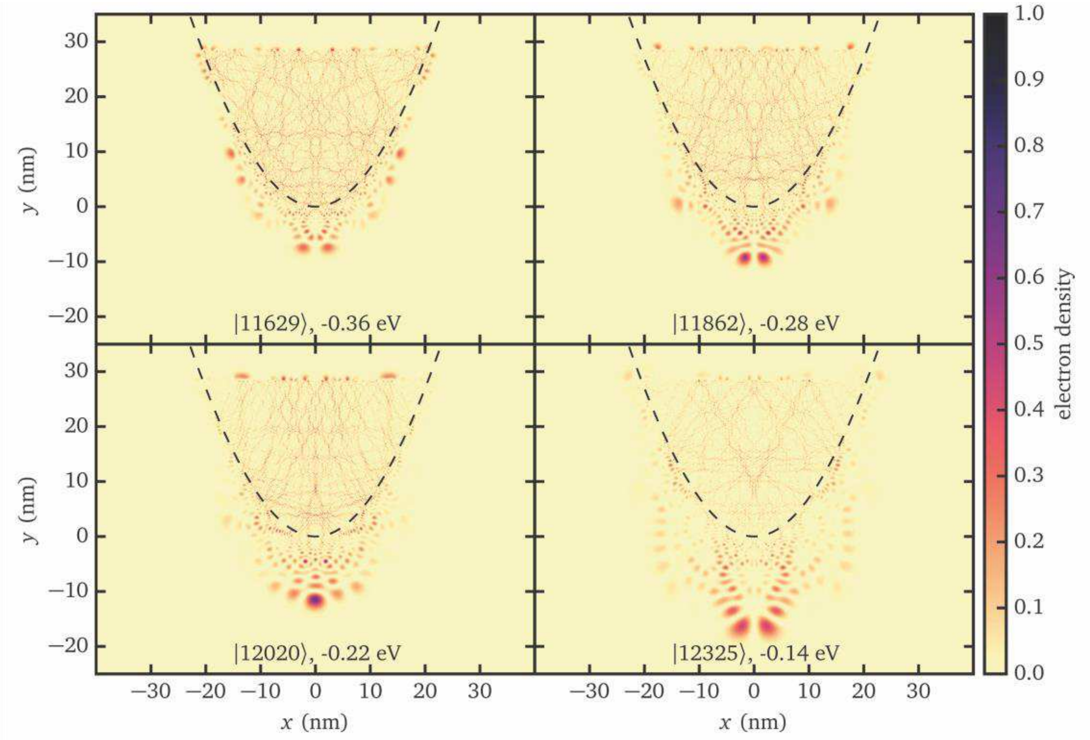

Fig. S7: Weakly bound excited surface states of the jellium model. Electron densities of the single-particle states which were used to construct the initial state in the time-dependent simulations.

The constructed state is next propagated in a space- and time-dependent electric near-field resulting from the action of the NIR pulse around the apex. The near-field is modelled by the quasi-static approach given in Ref. 15, i. e.,

$$E(\vec{r},t) = E_{\max} E_0(\vec{r}) \sin^2\left(\frac{\pi}{T}t\right) \cos(\omega t) \tag{17}$$

where $T = 23\,\text{fs}$ is the pulse length, $\omega/\left(2\pi\right) = 187.5\,\text{THz}$ (1.6 μm) is the carrier frequency, E_0 is the normalized spatial form of the near field (see Ref. 22), and $E_{\max}$ is the maximum of the (enhanced) electric field observed in front of the apex. We calculate $E_{\max}$ as

$$E_{\max} = f \cdot E_{\text{incident field}} \tag{18}$$

where $f = 9$ is the experimentally deduced enhancement factor of the near field, and $E_{\text{incident field}}$ is the peak amplitude of the incident field.

The laser excitation leads to electron emission from the tip. The emission process can be followed in the movie S1. Emitted electrons are absorbed at the boundaries of the simulation box with mask functions (blue and red) shown in the lower panel of Fig. S6. At the sides and back of the tip, we employ a regular absorbing mask of width $\approx 4\,\text{nm}$ shown as a red surface. In front of the tip, we retrieve photoelectron spectra of the escaping electrons with the method presented in Ref. 24 with a mask shown as a blue surface in Fig. S6.

To collect even the slowest electrons, we propagate the system up to 4 times the duration of the laser pulse. However, the very low-energy spectra may not be entirely reliable due to minor back-reflection of the wavefunction at the boundary.

All simulations were executed using the *Octopus* software[25-30].

B Supplementary Information

B1 Additional measured kinetic energy spectra

B1.1 One-color photoemission kinetic energy spectra

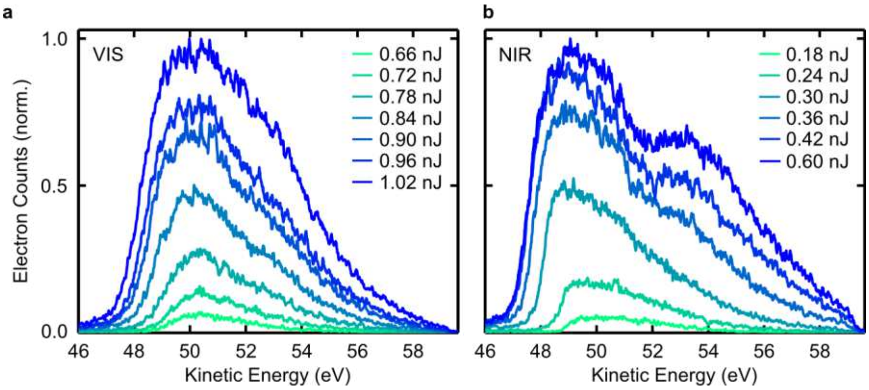

Fig. S8. One-color photoelectron kinetic energy spectra. a. Spectra recorded when the nanotip was illuminated with 9-fs pulses at a centre wavelength of 600 nm show a single peak that increases and broadens with increasing pulse energy. **b.** Spectra recorded for 18-fs pulses at a centre wavelength of 1600 nm similarly increase and broaden with increasing pulse energy and in addition develop a plateau-like second peak that indicates strong-field acceleration of the electrons in the near field of the tip.

We have measured the kinetic energy spectra when illuminating the gold nanotip with VIS pulses and with NIR pulses alone, respectively. When illuminating the nanotip with 9-fs VIS pulses, centred at a wavelength of 600 nm, the measured kinetic energy spectra show a single peak (Fig. S8a). Its maximum electron count as well as the width increase with increasing pulse energy, until at the maximum pulse energy of 1.02 nJ the FWHM is about 6 eV. The shape remains roughly Gaussian with a slower decay at the high-kinetic energy edge. These kinetic energy spectra are typical for photoelectron emission in the multi-photon regime.

Similarly, for photoelectron emission induced by 18-fs NIR pulses with a centre wavelength of 1600 nm, the measured kinetic energy spectra increase in maximum electron count and in width with increasing pulse energy (Fig. S8b). At the highest NIR pulse energy of 0.6 nJ the spectrum has a width of 7.5 eV, slightly wider than in the case of tip illumination with VIS pulses. Furthermore, when the tip is illuminated with high NIR pulse energies, the spectrum develops a distinct plateau-like feature on the high-kinetic energy side. This is an indication of the onset of strong-field acceleration in the near field of the sharply etched nanotip.

In both cases of one-color illumination the measured kinetic energy spectra are similar to previously measured photoelectron emission spectra from single metal nanostructures[5,12]. Specifically they do not show any finer spectral features or modulation as observed for two-colour photoemission.

B1.2 ATI spectra measured in the temporal overlap of VIS and NIR pulses

To generate the four kinetic energy spectra shown in Fig. 1f, the tip apex was illuminated with temporally overlapped VIS and NIR pulses, with a VIS pulse energy of 0.75 nJ and an NIR pulse energy varied between 0.12 nJ and 0.30 nJ. The electrons emitted from the tip were detected with a photoelectron spectrometer with kinetic energy resolution of 44 meV as described above. For the spectra recorded in the time overlap of the two pulses, shown in the main manuscript in Fig. 1f, we recorded for each NIR pulse energy 300 individual kinetic energy spectra with the camera integration time set to 100 ms. These individual spectra thus contain electrons released within 500 laser pulses.

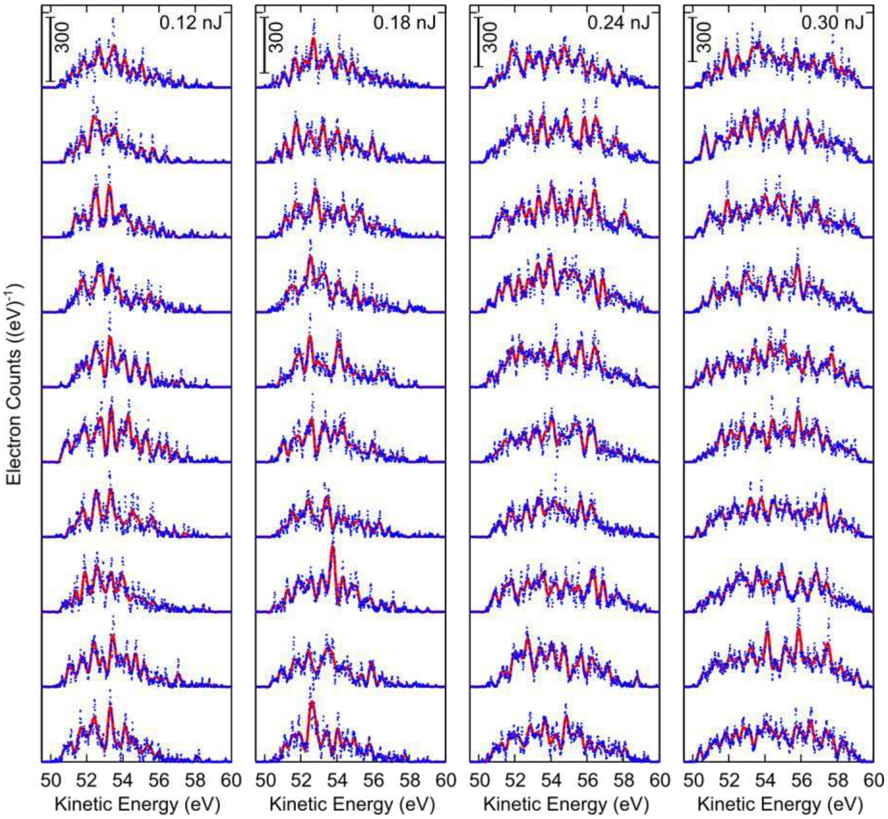

Fig. S9. Individual recorded kinetic energy spectra. For constant VIS pulse energy and for each of four different adjusted NIR pulse energies, a selection of 10 individual kinetic energy spectra is displayed. The blue symbols are raw experimental data and the red lines are the same data low-pass filtered with a cutoff frequency of $(0{,}41\,\mathrm{eV})^{-1}$. A strong modulation of the individual spectra is apparent.

A selection of 10 of these individual recorded spectra is shown in Fig. S9 for each NIR pulse energy. Each of the displayed spectra shows a marked modulation. On average, spectra recorded at the lowest NIR pulse energy of 0.12 nJ are composed of about 550 electrons and spectra recorded at the highest pulse energy of 0.30 nJ are composed of 1300 electrons. These high electron numbers, together with a comparison with the signature of an individual electron (in Fig. S5, Sec. 1.3), show that the peaks that can be discerned in the spectra in Fig. S9 are not due to a shot-noise-based distribution of electrons but are already a signature of ATI. Possibly the spectra also display a considerable substructure (Freeman resonances)[31], which cannot be resolved in our experiments. This becomes even more evident when 50 of these spectra are added up to yield the kinetic energy spectra shown in the main manuscript in Fig. 1f.

In general, the individual spectra shown in Fig. S9 display a high modulation contrast that reaches up to 100%. However, the visibility of the modulation varies strongly for the individual spectra, which results in a reduced visibility of about 30% for the added together spectra shown in Fig. 1f in the main text.

We ascribe this variation in visibility to a number of possible causes. Firstly, fluctuations of the laser pulse energies inevitably result in variations of the excitation conditions resulting in changes in the shape of the PE spectra. Secondly and most importantly, the variation of the NIR pulse CEP for long measurement times may result in substantial modifications of the photoelectron spectra. Qualitatively this can be understood as follows: The electrons are released from an image potential state and have thus a precisely defined starting energy at the time of emission, given by the binding energy of the respective state and a multiple of the NIR photon energy. Subsequently, they are accelerated in the spatially and temporally varying electric field of the laser pulse. After propagation to the detector the kinetic energy is measured. The acceleration and hence the change in kinetic energy the electrons experience during this process depends on the exact time of emission as well as on the temporal shape of the electric field strength. For very short, few-cycle pulses it has been shown that the change of the temporal field shape with varying CEP has a distinct effect on the final kinetic energy of the electrons emitted from sharp gold nanotips[4].

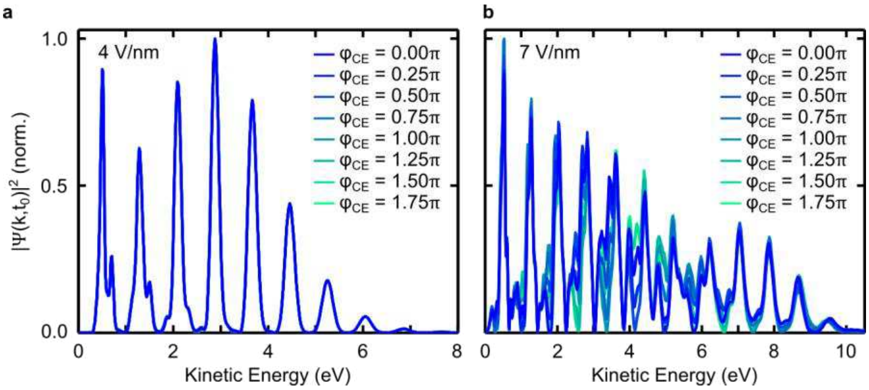

Fig. S10. Influence of the CEP on the kinetic energy spectra. a. Kinetic energy spectra simulated by TDSE when the system was prepared in the $n = 2$ state and perturbed with a 18-fs NIR pulse with a peak electric field strength of $f \cdot E_0 = 4\,\mathrm{V/nm}$. The absolute phase of the laser field was varied in eight steps and the resulting kinetic energy spectra are plotted on top of each other. There is no influence of the CEP apparent. **b.** Same as a, but for a higher peak electric field strength of $f \cdot E_0 = 7\,\mathrm{V/nm}$. Here the simulated kinetic energy spectra change considerably with the CEP, indicating that such measurements with strong electric fields require a stable laser CEP.

In order to estimate the impact of this effect we have simulated kinetic energy spectra as a function of the NIR pulse CEP, as described above in Sec. A2.1. The system was prepared in the $n = 2$ state and perturbed with an 18-fs NIR laser pulse. After propagation the kinetic energy spectrum of the freely propagating wavepacket was calculated. This was repeated for a total of eight cases with the laser pulse modelled with different CE phases, equally spaced by $\pi/4$. In Fig. S10 the eight resulting kinetic energy spectra are all plotted on top of each other to show the variation. These simulations show that for relatively low electric field strengths of $f \cdot E_0 = 4\,\mathrm{V/nm}$ (Fig. S10a) there is hardly any change of kinetic energy spectra with CEP discernible. This changes drastically when the electric field strength is increased to $f \cdot E_0 = 7\,\mathrm{V/nm}$ (Fig. S10b): Here a substantial change is visible. In an experiment, when measuring kinetic energy spectra with integration times during which the NIR laser pulse CEP is changing, this would lead to a strong wash-out of spectral features.

A further possible cause for the variation in visibility could be the variation of the relative phase between VIS and NIR pulses. However, the VIS pulse populates the image potential states, which do not change after the VIS pulse. Hence, in continuation of the line of argument given above, the CEP of the VIS pulse should not have any effect, and neither should the timing between the pulses or their relative CEP. We have tested this also using the simulation, by preparing the system in a state with a binding energy of $E_B = -5.04\,e\mathrm{V}$ and then perturbing it with a 9-fs VIS pulse followed after a delay of 40 fs with an 18-fs NIR pulse. Then we have again varied the VIS pulse CEP with respect to the (fixed) NIR pulse CEP. We have observed no changes in the simulated ATI peaks.

Summarizing these investigations, we have established using 1D-TDSE simulations that the NIR pulse CEP can have a strong effect of the kinetic energy spectra. Together with fluctuations of the laser pulse energy the NIR pulse CEP this explains the variation of the modulation between different spectra recorded with an integration time of 100 ms as well as the decrease of the visibility when either adding together these spectra or when integrating over longer measurement times. Experimentally, we find that the modulation in contrast in the PE spectra decreases and virtually vanishes when increasing the integration time to 1 s or longer.

B1.3 Kinetic energy spectra as function of time delay between VIS and NIR pulses

To ensure that the appearance of ATI peaks in the kinetic energy spectra of photoemitted electrons was not due to an interference effect of the VIS and the NIR pulse, but due to the population of long-lived discrete atomic-like states, we have repeated the measurements presented in Sec. B1.2 with temporally delayed pulses. For the measurements shown in Fig. S11, the tip was illuminated with a fixed VIS pulse energy of 0.5 nJ and a fixed NIR pulse energy of 0.4 nJ. Spectra were recorded in the time overlap of the two pulses (blue symbols), as well as with a finite delay between the VIS and the NIR pulse of $\Delta t = 33\,\mathrm{fs}$ (red symbols). The chosen time delay of $33\,\mathrm{fs}$ is longer than the combined pulse durations of the VIS and the NIR pulses of $9\,\mathrm{fs} + 18\,\mathrm{fs} = 27\,\mathrm{fs}$ and thus ensures that the temporal overlap of the pulses is negligible. At each time delay, 300 individual kinetic energy spectra were recorded with the camera integration time set to 100 ms. The spectra were treated as described above in Sec. A1.3. The symbols shown in Fig. S11 were obtained by adding together 50 manually selected spectra, and the black curves plotted together with the experimental measurements are the measurements low-pass filtered using a 6th order Butterworth filter with a cutoff frequency of $(0.41\,\mathrm{eV})^{-1}$

The spectrum recorded just outside the time overlap of the pulses displays a somewhat (by a factor ~1.7) decreased total electron count in comparison with the spectrum recorded in the time overlap, but very similar over-all shape: Both spectra are strongly modulated and in each spectrum, at least five peaks can be discerned, which are separated by the photon energy.

The observation of strongly modulated spectra is thus not limited to the pulse overlap, thus excluding interference of the VIS and NIR pulses as cause for our observations. This measurement furthermore excludes ponderomotive acceleration of electrons by the interference of the combined VIS and NIR fields. It is thus another strong indication that our observations are caused by the population of long-lived image potential states with discrete energies.

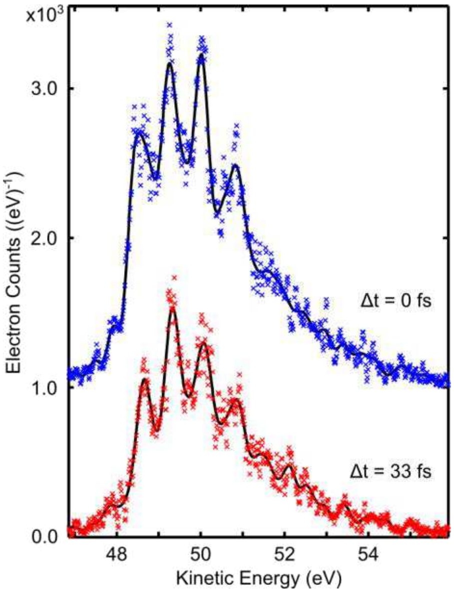

Fig. S11. Photoelectron kinetic energy spectra recorded outside the pulse overlap. The spectra recorded for a time delay between the VIS and the NIR pulse of $\Delta t = 0\,\text{fs}$ (blue symbols) and $\Delta t = 33\,\text{fs}$ (red symbols) all are modulated with peaks separated by the photon energy, verifying the population of a discrete, long-lived intermediate state. The black curves are the low-pass-filtered measurements.

To study the laser-driven dynamics of electrons in image potential states, we have recorded time-dependent two-colour photoemission spectra at relatively weak pulse energies to suppress ATI. The VIS pulse energy was kept in the range of 0.3-05 nJ to avoid single-color multiphoton emission, which is well below the energy used for measuring the ATI spectra shown in Fig. S9 above and in Fig. 1f of the main text, and even lower than the lowest pulse energy in Fig. S8. Some examples of time-dependent measurements that have been recorded for low, but slightly varying NIR pulse energies are shown in the following. Note that all these kinetic energy spectra were recorded with an integration time of 1 s. As demonstrated above, at this long integration time leads to a wash-out of finer spectral features such as ATI peaks. However, these measurements allow observing the dynamics of the spectral shape and electron counts over a longer time delay.

The time-dependent measurement of kinetic energy spectra shown in the first example, Fig. S12 has been performed for the highest NIR pulse energy of 0.48 nJ. The kinetic energy spectra (Fig. S12a) are spectrally narrow as expected for such low pulse energies and for photoemission in the multi-photon regime. In the time overlap, however, the spectra show a significant increase in intensity as well as width. The total electron count (Fig. S12b) is enhanced roughly by a factor 5 in the time overlap with respect to far delayed VIS and NIR pulses. The enhancement with respect to the photoemission solely due to the NIR pulses (i. e., electron count when the VIS pulses are blocked, not shown in Fig. S12) is 20, and with respect to photoemission by only the VIS pulses (NIR pulses blocked) is more than 30. The total count rate as a function of delay follows very closely a double-sided exponential decay, with a decay time of ~40 fs for negative delays and a much longer decay time of ~120 fs for positive delays. Apart from a secondary maximum that is just discernible at a time delay of about 40 fs, the total electron count decay is very smooth and there is hardly any modulation visible.

The shape of the kinetic energy spectra does not change significantly when the pulses coincide, and the mean kinetic energy of the released electrons is increased slightly, by about

0.4 eV (Fig. S12c). The width of the spectra, however, increases significantly: The very narrow spectra of about 2.5 eV width for delayed pulses double their width to 5 eV (Fig. S12d).

We have repeated this time-delayed measurement for a lower NIR pulse energy of 0.36 nJ, shown in Fig. S13. Again, the spectrally narrow kinetic energy spectra show a significant increase in intensity as well as width in the time overlap (Fig. S13a). The total electron count (Fig. S13b) is enhanced roughly by a factor 5 in the time overlap with respect to far delayed VIS and NIR pulses. Like in the previous example, the total count rate as a function of delay follows a double-sided exponential decay, with a decay time of ~40 fs for negative delays and a much longer decay time of ~130 fs for positive delays. However, in comparison to the previous example, here the total electron count decay is less smooth and more strongly modulated. Note that Fig. S13b is also shown as Fig. 3b of the main document, were the strong modulation is further analysed by Fourier transform, shown in the inset of Fig. 3b.

The mean kinetic energy of the released electrons again is increased slightly, by about 0.4 eV (Fig. S13c), and the increase in spectral spread is less pronounced than in the first example: the width increases by about 1 eV from 3.3 eV to 4.3 eV (Fig. S13d).

For the final example, shown in Fig. S14, we have further reduced the NIR pulse energy to 0.24 nJ. For this low NIR pulse energy the dynamics displayed by the kinetic energy spectra change considerably: instead of a clear, single maximum and a (more or less modulated) exponential decay we now see a distinct beating pattern (see Fig. S14a). This beating pattern expands over more than 200 fs and exhibits dominant beating periods of 54 fs for positive and 39 fs for negative delays. The beating pattern is reflected in the total electron count as a function of delay (Fig. S14b), where the count remains at a high level over the time span of more than 200 fs, that by far exceeds the duration of pulse overlap. For even longer delay times the electron count decreases by about 60% down to level for far detuned VIS and NIR pulses. During the time interval of increases electron emission the mean kinetic energy of the released electrons is increased only slightly, by about 0.2 eV (Fig. S14c), and the increase in spectral spread is about 0.5 eV (Fig. S14d), which is even less pronounced than in the previous examples.

The extended electron emission over such a long time span, during which the total electron counts remained at an elevated level, is a clear signature of photoemission from discrete, long-lived image potential states. The beating pattern seen in Figs. S14a and b furthermore reflects the electron wavepacket motion that has its origin in the coherent superposition of several states. From the comparison of Figs. S12 to S14 it appears that in the first two examples emission from the long-lived image potential states was overcast by multiphoton emission from the Fermi level, and that photoemission from image potential states is dominant only for very low pulse energies.

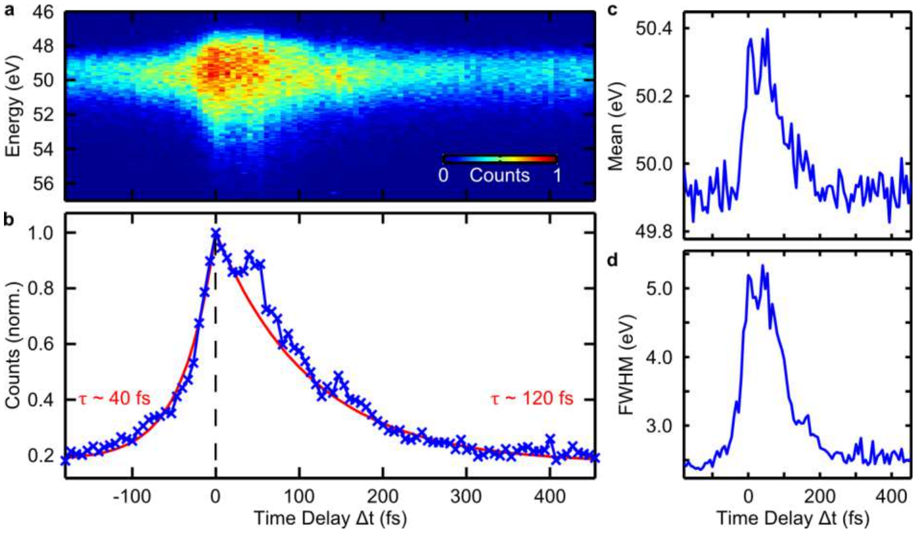

Fig. S12. Time-dependent two-colour photoemission recorded for an NIR pulse energy of 0.48 nJ. a. Kinetic energy spectra as a function of time delay between the VIS and the NIR pulse. **b.** The total count shows a clear maximum at the time overlap, which is about 5 times enhanced with respect to far delayed pulses. The electron count decays exponentially over a time of ~40 fs for negative delays and over ~120 fs for positive delays. **c.** The mean kinetic energy of the released electrons increases slightly in the time overlap, while **d.** the increase in width is significant when the pulses coincide.

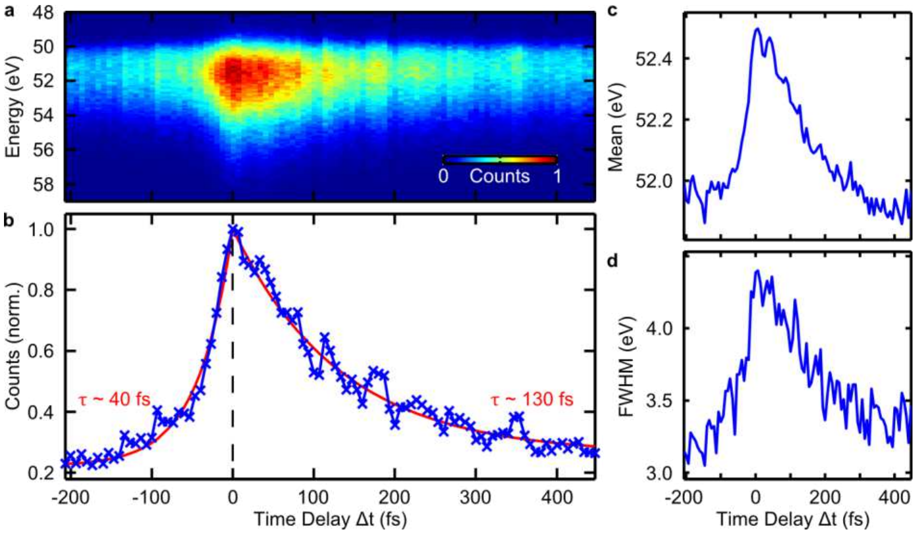

Fig. S13. Time-dependent two-colour photoemission recorded for an NIR pulse energy of 0.36 nJ. a. Kinetic energy spectra as a function of time delay between the VIS and the NIR pulse. **b.** The total count shows a clear maximum at the time overlap, which is about 5 times enhanced with respect to far delayed pulses. The electron count decays exponentially over a time of ~40 fs for negative delays and over ~130 fs for positive delays. **c.** The mean kinetic energy of the released electrons increases slightly in the time overlap, while **d.** the increase in width is significant when the pulses coincide.

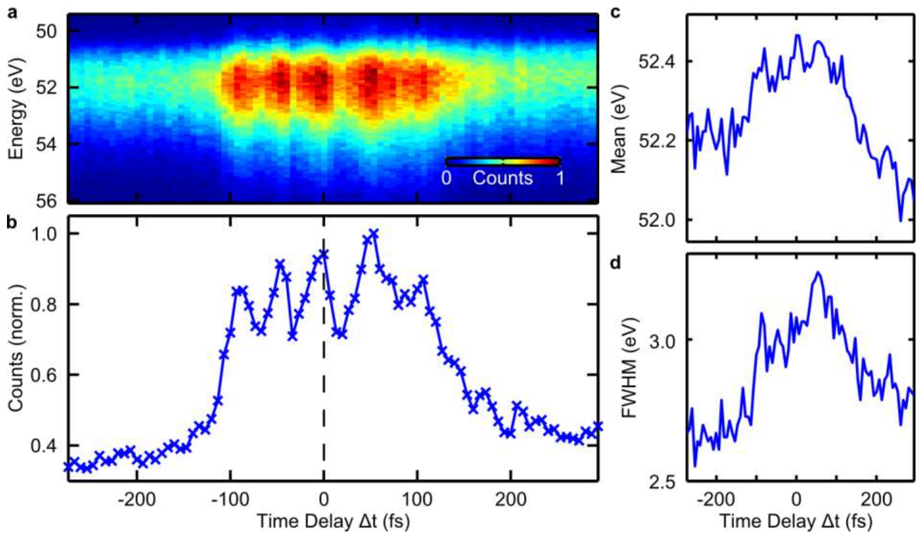

Fig. S14. Time-dependent two-colour photoemission recorded for an NIR pulse energy of 0.24 nJ. a. The kinetic energy spectra as a function of time delay between the VIS and the NIR pulse show a distinct beating pattern over a time interval of about 200 fs. **b.** The total count also reflects the beating pattern and an exponential decay for longer time delays. **c.** The mean kinetic energy of the released electrons and **d.** the width of the spectra both increase slightly in the time overlap.

B2. Eigenstates and wavefunctions of 1D-TDSE and 2D-SE

The solution of the 2D-SE yields a large number (~1000) of bound states with different wavefunctions and binding energies. Among these, surface states are easily identified by the location of the centre of mass of their wavefunctions being outside the tip. These surface states constitute as small subset of the 2D-SE solutions. Their binding energies roughly follow the relation $E_n = -0.85\,e\mathrm{V}\cdot\frac{1}{n^2}$ with the principal quantum number $n = 1, 2, 3, ...$ as known from image potential states on extended surfaces[9,10,32]. Examples for the spatial probability density of the four wavefunctions associated with the four lowest quantum numbers are shown in the upper four panels of Fig. S14. In each case, one can see a fine structure of low electron probability density inside the tip with the surface indicated by the yellow line. Most significant, however, is a clearly discernible maximum of the probability density that is located outside the tip and axially centred directly at the apex. The probability density maximum shifts with increasing quantum number n to farther distances from the surface, which is accompanied by the evolution of an increasing number $(n-1)$ of nodes between the surface and the maximum. Note that the probability densities are determined mainly by the coulomb potential originating from the image charge. By varying the shape and periodicity of the potential inside the tip we have verified that its influence on the electron wavefunction is minor, as should be expected by the small overlap of the surface state wavefunctions with the tip material.

We have calculated the projection of the probability densities shown in Figs. S15a-d onto the taper axis in the spheroidal coordinate system[15]. These projections (red curves in Figs. S15e-h) closely follow the respective probability densities derived from the 1D-TDSE model in the stationary case, i. e., with no laser field applied (blue curves). Both, the 1D probability densities and the projection of the 2D probability densities, closely resemble hydrogenic radial wavefunctions scaled by a factor 4 and multiplied with the distance from the surface[10].

This similarity implies that the curvature of the surface does not crucially influence the electron axial spatial probability density as compared to that of an extended metallic film. Its effect is mainly a variation of the probability density in the direction parallel to the surface, i. e., a contraction of the wavefunction and its localization at the apex. Hence we expect the 1D TDSE model to yield realistic electron wavefunctions despite the rotationally symmetric 2D geometry of the tip. The temporal evolutions shown in Figs. 2d and 3c in the main text have been derived from the 1D-TDSE model and can be understood to resemble the electron wavepacket motion along the taper axis.

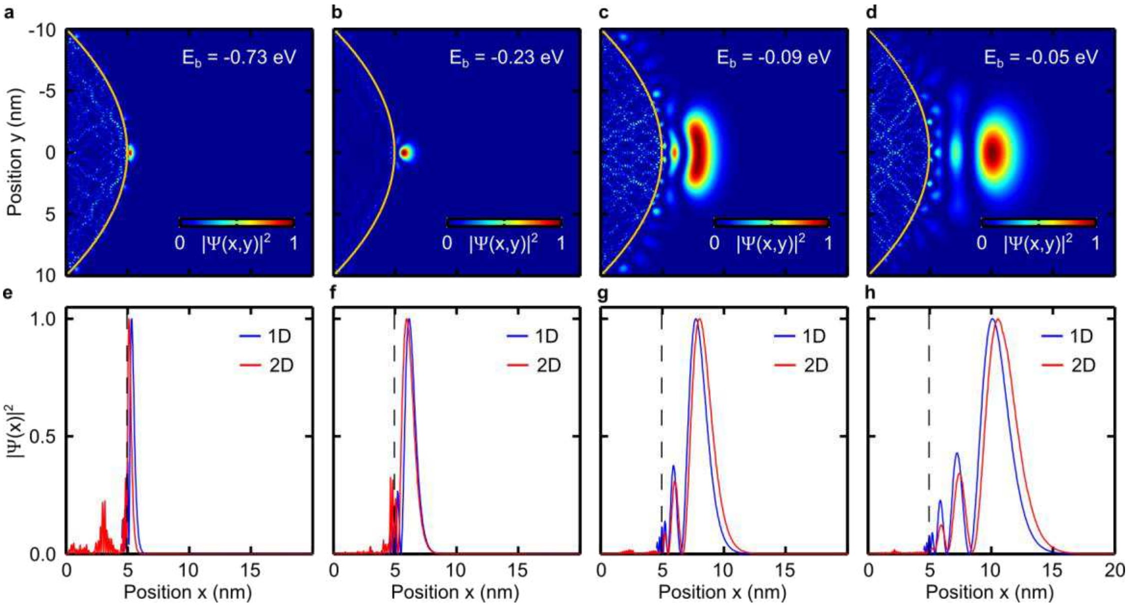

Fig. S15. Wavefunctions of image potential states. a-d. Example solutions of the 2D-SE with a periodic potential representing the atomic lattice structure and a Coulomb potential caused by the image charge. Plotted is the spatial probability density, i. e., the absolute square of the electron wavefunction color-coded with the spheroid tip surface given by the yellow line. From left to right, the number of nodes outside the tip along the tip axis increases from 0 to 3. **e-f.** Corresponding projections of the probability density in the spheroidal coordinate system onto the tip axis (red), plotted together with the solution of the 1D-SE (blue), showing good agreement. From left to right, the number of nodes increases from 0 to 3, while the spatial probability density is the highest at the outermost maximum.

The solutions of the 2D-SE shown in Fig. S15 show a specific symmetry: they have a high probability density along the tip axis and a quick decay in the direction perpendicular to the axis. There are different solutions that satisfy our requirements for image potential states that vary in the number of nodes of the wavefunctions outside the tip along the tip axis. We have associated these solutions with an energy quantization and the principal quantum number *n* as expected from image potential states.

For the case of image potential states on an extended surface, however, the potential is constant along the surface. Hence, the solution of the wavefunction in the directions perpendicular to the surface normal is that of a plane wave and one would not expect further quantization. For the case of a metal nanotip, the situation is quite different: here one should expect to find at least two more quantum numbers, one resulting from the tip's circular symmetry, and one resulting from the variation of the potential with the distance from the apex along tip's surface. The circular symmetry around the tip axis is not contained in our 2D model potential, however, the potential variation with the distance from the apex is. Indeed, we also find eigenstates with wavefunctions that are modulated not only along the tip axis but also perpendicular. Some representative examples are shown in Fig. S16. The top row again shows the probability density of wavefunctions that can be associated with the principal quantum numbers $n = 2,3,4$ (same as in Fig. S15). Below these, the absolute square of wavefunctions is shown with increasing number of nodes (0,1,2,3) perpendicular to the taper axis. This is an indication that in this model quantization along a second axis is seen. We have found that the binding energies of these states increase by roughly 10% of the binding energies $E_n = -0.85\,e\mathrm{V}\cdot\frac{1}{n^2}$.

While we have thus found indication of further quantization in the model, the verification is currently beyond the capabilities of the current experimental setup. The energy splitting observed in the simulations is typically below the energy resolution of the kinetic energy spectra, and as yet we have no way to image the spatial electron distribution around the nanotips. However, we are currently planning experiments to directly image the Rydberg wavefunctions of image potential states localized to the apex of gold nanotips by velocity map imaging. This should in the near future enable to image the spatial electron density around the nanotip and to disentangle the quantization of Rydberg states localized to a single gold nanotip.

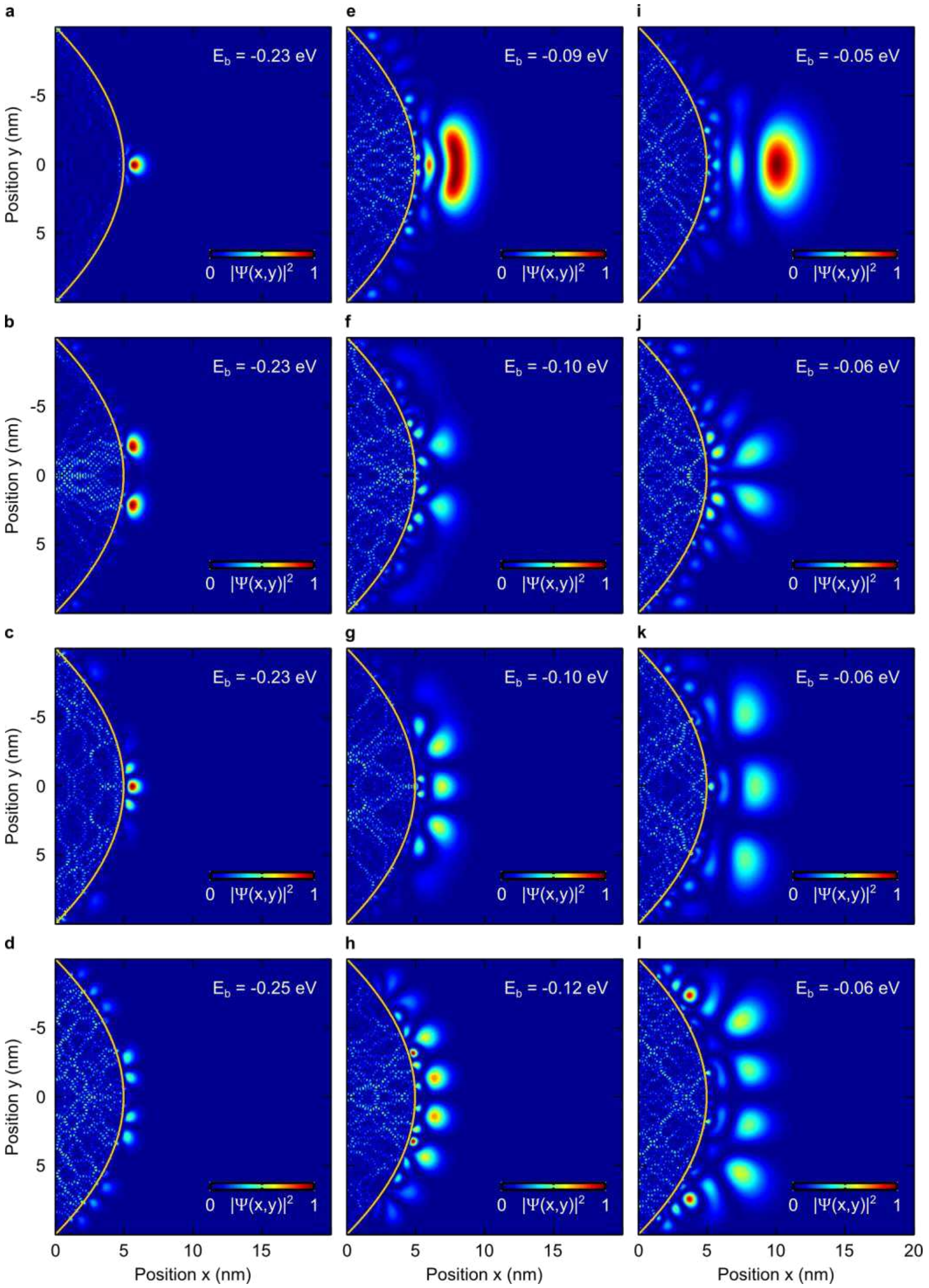

Fig. S16. Quantization perpendicular to the tip axis. In all panels, the probability density of image potential states is color-coded, with the tip surface depicted as the yellow line. The top row shows the wavefunctions associated with the principal quantum numbers **a** $n=2$, **e**, $n=3$, and **i**, $n=4$. In the rows below, we show wavefunctions with increasing numbers of nodes perpendicular to the tip axis. **a-d:** wavefunctions with one node along the tip axis and with 0,1,2,3 nodes perpendicular. **e-h:** the same with two nodes and **i-l:** with three nodes along the tip axis and with 0,1,2,3 nodes perpendicular.

References

1 Cerullo, G., Baltuška, A., Mücke, O. D. & Vozzi, C. Few-optical-cycle light pulses with passive carrier-envelope phase stabilization. *Laser Photonics Rev.* **5**, 323-351 (2011).

2 Manzoni, C., Cerullo, G. & De Silvestri, S. Ultrabroadband self-phase-stabilized pulses by difference-frequency generation. *Opt. Lett.* **29**, 2668-2670 (2004).

3 Vogelsang, J. *et al.* High passive CEP stability from a few-cycle, tunable NOPA-DFG system for observation of CEP-effects in photoemission. *Opt. Express* **22**, 25295-25306 (2014).

4 Piglosiewicz, B. *et al.* Carrier-envelope phase effects on the strong-field photoemission of electrons from metallic nanostructures. *Nature Photon.* **8**, 37-42 (2014).

5 Herink, G., Solli, D. R., Gulde, M. & Ropers, C. Field-driven photoemission from nanostructures quenches the quiver motion. *Nature* **483**, 190-193 (2012).

6 Keldysh, L. V. Ionization in field of a strong electromagnetic wave. *Soviet Physics Jetp-Ussr* **20**, 1307-1314 (1965).

7 Piglosiewicz, B. *et al.* Electron Photoemission and Acceleration from Sharp Gold Nanotapers in the Strong-Field, Few-Cycle Regime. *Quantum Matter* **3**, 297-396 (2014).

8 Sachtler, W. M., Dorgelo, G. J. H. & Holscher, A. A. Work function of gold. *Surf. Sci.* **5**, 221-229 (1966).

9 Fauster, T. & Steinmann, W. Two-photon photoemission spectroscopy of image states. *Electromagnetic Waves: Recent Developments in Research* **2**, 347-411 (1995).

10 Echenique, P. M. & Pendry, J. B. Theory of image states at metal surfaces. *Progr. Surf. Sci.* **32**, 111-172 (1989).

11 Stockman, M. I. & Hewageegana, P. Absolute phase effect in ultrafast optical responses of metal nanostructures. *Appl. Phys. A* **89**, 247-250 (2007).

12 Park, D. J. *et al.* Strong Field Acceleration and Steering of Ultrafast Electron Pulses from a Sharp Metallic Nanotip. *Phys. Rev. Lett.* **109**, 244803 (2012).

13 Press, W. H. *Numerical recipes 3rd edition: The art of scientific computing*. (Cambridge University Press, 2007).

14 MATLAB Release 2013b (The MathWorks, Inc., Natick, Massachusetts, United States).

15 Behr, N. & Raschke, M. B. Optical antenna properties of scanning probe tips: Plasmonic light scattering, tip-sample coupling, and near-field enhancement. *J. Chem. Phys. C* **112**, 3766-3773 (2008).

16 Kohn, W. & Sham, L. J. Self-Consistent Equations Including Exchange and Correlation Effects. *Phys. Rev.* **140**, A1133-A1138 (1965).

17 Attaccalite, C., Moroni, S., Gori-Giorgi, P. & Bachelet, G. B. Correlation energy and spin polarization in the 2D electron gas. *Phys. Rev. Lett.* **88**, 256601 (2002).

18 Bloch, F. Bemerkung zur Elektronentheorie des Ferromagnetismus und der elektrischen Leitfähigkeit. *Z. Phys.* **57**, 545-555 (1929).

19 Dirac, P. A. in *Mathematical Proceedings of the Cambridge Philosophical Society.* **26**, 376-385 (Cambridge Univ Press, 1930).

20 Lang, N. & Kohn, W. Theory of metal surfaces: charge density and surface energy. *Phys. Rev. B* **1**, 4555-4568 (1970).

21 Casida, M. E. Correlated optimized effective-potential treatment of the derivative discontinuity and of the highest occupied Kohn-Sham eigenvalue: A Janak-type theorem for the optimized effective-potential model. *Phys. Rev. B* **59**, 4694-4698 (1999).

22 Perdew, J. P. & Levy, M. Comment on "Significance of the highest occupied Kohn-Sham eigenvalue". *Phys. Rev. B* **56**, 16021-16028 (1997).

23 Perdew, J. P., Parr, R. G., Levy, M. & Balduz Jr, J. L. Density-functional theory for fractional particle number: derivative discontinuities of the energy. *Phys. Rev. Lett.* **49**, 1691-1694 (1982).

24 Giovannini, U., Larsen, A. & Rubio, A. Modeling electron dynamics coupled to continuum states in finite volumes with absorbing boundaries. *Eur. Phys. J. B* **88**, 56 (2015).

25 Andrade, X. *et al.* Time-dependent density-functional theory in massively parallel computer architectures: the octopus project. *J. Phys.: Cond. Mat.* **24**, 233202 (2012).

26 Andrade, X. *et al.* Real-space grids and the Octopus code as tools for the development of new simulation approaches for electronic systems. *Phys. Chem. Chem. Phys.* **17**, 31371-31396 (2015).

27 Castro, A. *et al.* octopus: a tool for the application of time-dependent density functional theory. *physica status solidi (b)* **243**, 2465-2488 (2006).

28 Castro, A., Marques, M. A. & Rubio, A. Propagators for the time-dependent Kohn–Sham equations. *J. Chem. Phys.* **121**, 3425-3433 (2004).

29 Marques, M. A., Castro, A., Bertsch, G. F. & Rubio, A. Octopus: a first-principles tool for excited electron–ion dynamics. *Comput. Phys. Commun.* **151**, 60-78 (2003).

30 Marques, M. A., Oliveira, M. J. & Burnus, T. Libxc: A library of exchange and correlation functionals for density functional theory. *Comput. Phys. Commun.* **183**, 2272-2281 (2012).

31 Freeman, R. R. & Bucksbaum, P. H. Investigations of above-threshold ionization using subpicosecond laser pulses. *J. Phys. B* **24**, 325-347 (1991).

32 Hofer, U. *et al.* Time-resolved coherent photoelectron spectroscopy of quantized electronic states on metal surfaces. *Science* **277**, 1480-1482 (1997).

Movie S1: Electron emission in the 2D single-active electron model

Electron density for a single-active electron model for a weakly bound surface-dominant state is ionized by the quasi-static near field. Absorbing boundaries reduce the reflections from the grid boundaries, and the reflection from the back of the tip does not significantly affect the collected kinetic energy spectrum. The spectrum is collected by the absorbing mask only in front of the tip (see Fig. S7) to collect only the electron density emitted towards the detector.

Acknowledgments: We acknowledge financial support by the Deutsche Forschungsgemeinschaft (SPP1391, SPP1839, SPP 1840, and DFG-NSF Materials World Network), by the European Union (project “CRONOS”, grant number 280879-2), the European Research Council (ERC-2010-AdG-267374), the Academy of Finland, the FinnishIT Center for Science for computational resources CSC, Spanish grant (FIS2013-46159-C3-1-P), Groupos Consolidados (IT578-13), and the Korea Foundation for International Cooperation of Science and Technology (Global Research Laboratory project, K20815000003). J.V., J.R., B.N., and P.D. acknowledge personal grants from the Studienstiftung des Deutschen Volkes, the Deutsche Forschungsgemeinschaft (GRK 1885), the German Academic Exchange Service (IPID4all program), the Hungarian Academy of Sciences (“Lendelüt” grant), the Campus Hungary program, and the Stiftung der Metallindustrie im Nord-Westens.

Author Contributions: C.L. initiated the project. J.R. and J.V. implemented the set-up, J.R., J.V., and B.N. carried out the experiments. J.R., P.G., and C.L. evaluated the data and implemented the TDSE model. J.S., P.W., U.D.G., E.R., and A.R. developed the DFT simulation model. J.R., J.S., P.W., P.D., C.L., and P.G. prepared the manuscript. All authors contributed to the final version of the manuscript.

Acknowledgements

First of all, I would like to thank my supervisor Professor Christoph Lienau for his continuous support throughout my three years of work, which have led to this thesis. During this time, I have learned a lot of new physics, which I could share with other experts in the field on various international conferences, including presenting my work as an invited talk in San Diego, winning a poster prize in Les Houches and contributing to the traditional post-deadline session of the surface science division at the DPG spring meeting in Regensburg. I am also grateful for two patents and valuable insights into the industry through a mentorship with the founder of attocube systems, Professor Khaled Karrai.

I would also like to thank Professor Walter Pfeiffer for co-refereeing this thesis and acknowledge his role as a coordinator of the DFG priority programme 1391 “Ultrafast Nanooptics”, which introduced me to this field of research.

Furthermore, I would like to thank Privatdozentin Petra Groß for her continuous support throughout my three years of work, especially in preparing the manuscripts associated with this thesis and in the early stages of this thesis itself.

A special thanks goes to all members of the working group Ultrafast Nano-Optics, who introduced me to the equipment, supported me in my experiments and gave me a place for fruitful discussions, and all collaborators from other research groups, who contributed to the success of my work.

I owe a particular debt of gratitude to my funding agencies, especially the Deutsche Forschungsgemeinschaft (DFG), which supported this thesis in the framework of the research training group “Molecular Basis of Sensory Biology” (GRK 1885/1). I further acknowledge support from the DFG priority programme 1840 “Quantum Dynamics in Tailored Intense Fields”, which will enable follow-up studies of the experimental findings advanced in this thesis.

I would also like to thank the research training group “Molecular Basis of Sensory Biology”, in particular its speaker Professor Karl-Wilhelm Koch and its coordinator Dr. Beate Grünberg, for their support. The associated lecture series and seminar gave me a sound knowledge of research topics addressed by my fellow PhD students in the disciplines of biology and chemistry, whereas our excursions to places such as Helgoland, Spiekeroog, Barcelona, Hamburg and Frankfurt strengthened our team building leading to an increasingly stronger bond between a group of students from a diverse range of backgrounds.

In particular, I would like to thank Dr. Beate Grünberg for encouraging me to take part in Science Slam, in which an advanced scientific topic is concisely communicated to a general audience, and Professor Henrik Mouritsen for his course on advanced presentation techniques. It was beyond my wildest dreams to perform in front of an audience of over 1000 spectators in a concert hall at the German Championship, travel across the country thereafter and become a mentor of Science Slam myself helping others to shine.

I would not be in this position, if it wasn’t for my family, who supported me throughout my life and, despite coming from a non-academic background, granted me access to a number of amazing places throughout my career. Thank you!

Lebenslauf

Persönliche Daten

Adresse: Gotthelfstraße 7, 26131 Oldenburg
Telefon: 0441 35069777
Geboren am: 14.09.1983 in Haselünne
Familienstand: Ledig
Nationalität: Deutsch

Schulbildung

1990 – 1994	Grundschule Ober-Niederlangen
1994 – 1996	Orientierungsstufe Lathen
1996 – 2003	Hümmling-Gymnasium Sögel

Bachelorstudium

2005 – 2009	Open University, Milton Keynes, Großbritannien • Bachelor of Science (Honours) Open, First-class Honours • Bachelorarbeit: „Quantum Information Transfer between Qubits Stored in Trapped Ions“ • Allgemeine Hochschulzugangsberechtigung (1,0)

Masterstudium

2009 – 2010	University of Oxford (St Hugh's College), Großbritannien • MPhys-Prüfungen in Laser Science & Quantum Information Processing und Condensed Matter Physics • MPhys-Projekt: „Laser Intensity Stabilisation by a PID Controller on a FPGA“ (Dr. David Lucas)
2011 – 2012	Ludwig-Maximilians-Universität, München • Master of Science in Physik, Gesamtnote: sehr gut (1,11) • Masterarbeit: “Laser Cooling of Beryllium Ions in a Segmented Linear RF Trap” (Prof. Theodor W. Hänsch)

Promotionsstudium

Seit 2013	Carl von Ossietzky Universität, Oldenburg • Doktorand in der Arbeitsgruppe Ultraschnelle Nano-Optik (Prof. Christoph Lienau) • Stipendiat im Graduiertenkolleg „Molecular Basis of Sensory Biology“ (GRK 1885/1, Sprecher: Prof. Karl-Wilhelm Koch)

Universitäre Lehre

WS 2013/14	Tutorium zur Vorlesung Atom- und Molekülphysik
WS 2014/15	Fortgeschrittenen-Praktikum Ultraschnelle Photolumineszenz
WS 2015/16	Fortgeschrittenen-Praktikum Ultraschnelle Photolumineszenz

Selbstständigkeitserklärung

Hiermit versichere ich, dass ich die vorliegende Arbeit selbstständig verfasst und nur die angegebenen Hilfsmittel verwendet habe. Außerdem versichere ich, dass ich die allgemeinen Prinzipien wissenschaftlicher Arbeit und Veröffentlichung, wie sie in den Leitlinien guter wissenschaftlicher Praxis der Carl von Ossietzky Universität Oldenburg festgelegt sind, befolgt habe.

Oldenburg, den ______________

____

(Jörg Robin)